Performance Enhancement and Corrosion Studies of Metal–Air Batteries

Von der Fakultät für Ingenieurwissenschaften
Abteilung Elektrotechnik und Informationstechnik
der Universität Duisburg-Essen

zur Erlangung des akademischen Grades

Doktor der Ingenieurwissenschaft

genehmigte Dissertation

von

Saúl Said Montiel Guerrero
aus
Tepeji del Río de Ocampo, Hidalgo, Mexico

Gutachter: Prof. Dr.–Ing. Stefan van Waasen
Gutachter: Prof. Dr. rer. nat. Rüdiger–A. Eichel
Tag der mündlichen Prüfung: 04.08.2023

Abstract

Metal-air batteries (MABs) are an attractive and promising alternative energy storage system to existing batteries due to their high energy density, cost efficiency, and intrinsic safety. They have potential applications in both the electromobility sector and stationary energy storage. This thesis examines the possible uses of MABs, in specific silicon, aluminum, zinc and their alloys, and proposes strategies for performance improvement.

One of the main focusses in this research is the potential applications of alkaline and non-aqueous Si-air batteries in low-power electronics. As a proof–of–concept, the use of a Si–air battery with an integrated circuit (IC) on the anode to power an LED is demonstrated. Additionally, the self–destructive capability of the Si–IC is also examined. The study also surveys the potential improvement of Si electrodes through alloying with Al, which show a slight increase in the anodic current densities without passivating the electrode.

This work further extends the investigations from the primary Si–air battery to secondary Zn-air batteries (ZABs). ZABs have the advantage that the zinc electrodes can be cycled in several types of electrolytes, including neutral solutions. By doing so, the prejudicial high corrosion of Zn in the alkaline electrolytes is avoided. However, the potentials of zinc in neutral electrolytes are relatively low in comparison to alkaline solutions. To increase the discharge potential of Zn, alloying it with more electronegative materials is proposed, such as Zn–Al alloy. The tested Zn–10 wt.%Al electrodes require, however, an initial cathodic pulse to reveal the more negative potential, which is also limited over time.

This study finds that the potential enhancement can be further improved and prolonged by the introduction of the chelating agent ethylenediaminetetraacetic acid (EDTA). Such beneficial effect is present under discharge conditions even after applying relatively high anodic current densities on Zn electrodes. The cycling of the ZABs was possible in both electrolyte formulations but could be slightly extended in presence of EDTA, which also showed higher discharge voltages in comparison to the neat 2M NaCl electrolyte.

Zusammenfassung

Metall-Luft-Batterien (Englisch: MABs) sind eine interessante und vielversprechende Alternative zu bestehenden Batterien aufgrund ihrer hohen Energiedichte, des guten Preis–Leistungs–Verhältnisses, und ihrer intrinsischen Sicherheit. Sie haben mögliche Anwendungen sowohl im Elektromobilitätssektor als auch in der stationären Energiespeicherung. Diese Arbeit untersucht die möglichen Verwendungen von MABs, insbesondere Silizium, Aluminium, Zink, sowie deren Legierungen und schlägt Strategien zur Leistungsverbesserung vor.

Einer der Hauptfokusse dieser Forschung sind die möglichen Anwendungen von alkalischen und nicht–wässrigen Si–Luft-Batterien für Elektronik mit geringem Strombedarf. Als Beweis des Konzepts wird die Verwendung einer Si–Luft–Batterie mit einem integrierten Schaltkreis (IC) auf der Anode gezeigt, um eine LED zu betreiben. Darüber hinaus wird die selbstzerstörende Fähigkeit des Si–IC untersucht. Die Studie erforscht auch die Verbesserung des Potenzials von Si-Elektroden durch Legierung mit Al, die eine leichte Erhöhung der Anoden–Stromdichte ohne Passivierung der Elektrode zeigt.

Diese Arbeit erweitert die Untersuchungen von der primären Si-Luftbatterie zu sekundären Zn-Luftbatterien (Englisch: ZABs). ZABs haben den Vorteil, dass die Zink–Elektroden in mehreren Arten von Elektrolyten, einschließlich neutralen Lösungen, zyklisch betrieben werden können. Dadurch wird die nachteilige hohe Korrosion von Zink in den alkalischen Elektrolyten vermieden. Das Potenzial von Zn in neutralen Elektrolyten ist jedoch im Vergleich zu alkalischen Lösungen relativ gering. Um das Entladepotential von Zn zu erhöhen, wird die Legierung mit elektronenärmeren Materialien wie Zn–Al–Legierungen vorgeschlagen. Die getesteten Zn–10 Gew.% Al–Elektroden erfordern jedoch einen initialen kathodischen Impuls, um das negativere Potenzial zu enthüllen, dessen Einfluss auch zeitlich begrenzt ist.

Diese Studie zeigt, dass die Potenzialverbesserung durch die Einführung des Chelatbildners Ethylendiamintetraessigsäure (EDTA) weiter verbessert und verlängert werden kann. Ein solcher positiver Effekt ist auch unter Entladungsbedingungen vorhanden, selbst nach Anwendung von relativ hohen anodischen Stromdichten auf Zn–Elektroden. Das Zyklusverhalten der ZABs war in beiden Elektrolytformulierungen

möglich, konnte jedoch in Gegenwart von EDTA leicht verlängert werden, was auch zu höheren Entladespannungen im Vergleich zu reinem 2M NaCl führt.

Preface

This doctoral thesis summarizes the following publications and are referred within the text.

[1] **S. S. Montiel Guerrero**, Y. E. Durmus, Hermann Tempel, Stefan van Waasen, Hans Kungl, and Rüdiger–A. Eichel, "Unveiling the Potential of Silicon‐Air Batteries for Low‐Power Transient Electronics: Electrochemical Insights and Practical Application", *Batteries & Supercaps,* 7 (2024), n/a, doi.org/10.1002/batt.202300573.

[2] Y. E. Durmus, **S. S. Montiel Guerrero**, Hermann Tempel, Florian Hausen, Hans Kungl, and Rüdiger–A. Eichel, "Influence of Al Alloying on the Electrochemical Behavior of Zn Electrodes for Zn–Air Batteries with Neutral Sodium Chloride Electrolyte", *Frontiers in Chemistry*, 7 (2019), 1–13, doi.org/10.3389/fchem.2019.00800.

[3] **S. S. Montiel Guerrero**, Y. E. Durmus, Krzysztof Dzieciol, Shibabrata Basak, Hermann Tempel, Stefan van Waasen, Hans Kungl, and Rüdiger–A. Eichel, "Improved Electrochemical Performance of Zinc Anodes by EDTA in Near–Neutral Zinc–Air Batteries", *Batteries & Supercaps*, 4 (2021), 1–14, doi.org/10.1002/batt.202100116.

Contents

Chapter 1: Introduction

The ever–growing global energy demands observed since the 1850's reached the 173,340 TWh mark in 2019 [1]. The recent worldwide COVID pandemic in 2020 highly contributed to a slight dip of −4% on the global energy needs in comparison to the previous year, with also similar reductions on both global CO_2 emissions and GDP of 6% and ca. 4%, respectively [2]. The trend, however, is taking a turn around and increasing again as the world economy reactivates and so the need for energy, where the largest share of the energy sources still comes from fossil fuels [1,2]. As a consequence, 33 Gt of CO_2 were emitted in 2021, quite close to the highest historical value registered at 33.5 Gt in 2018 [3]. Still, as a compromise of "The Paris Agreement" [4] and trying to limit the global warming under the 1.5°C in comparison to the levels before the industrial revolution, renewable energies start to gain more momentum [5]. Namely, the accumulated share of renewables has reached the 7,444 TWh as of 2020 [6]. Still, some renewable energy technologies innately cannot store the energy excess in underuse periods, creating a possible lack when the energy demand increases, as estimated for the solar PV demand in 2050 for example [7].

In this regard, lithium–ion batteries have offered a solution for flexible energy storage in renewable energies, while its continuous intense research has extended its application from mobile devices to electrical vehicles [8,9]. The cumulative demand for Li–ion batteries is projected to reach the 9,300 GWh or equivalent 2.114×10^{6} metric tons of lithium carbonate in 2030 [10,11]. In addition to a high demand, Li is relatively scarce and geographically uneven distributed, which directly impacts the ongoing increasing price of the raw material (ca. 19.7k USD $\mathrm{tonne}_{\mathrm{Li}}^{-1}$ in May, 2017 versus over 86k USD $\mathrm{tonne}_{\mathrm{Li}}^{-1}$ in November, 2022) [12–14]. In addition, the performance of Li–ion batteries has seen significant increases over the course of the last decades, which started at around 100 $\mathrm{Wh\,kg^{-1}}$ in 1991 and has doubled to 260–270 $\mathrm{Wh\,kg^{-1}}$ for the commercially available batteries nowadays [15,16]. Nevertheless, the scientific community estimates a limited increase of 30% extra to the current energy density for Li–ion batteries, meaning a maximum performance at around 330 $\mathrm{Wh\,kg^{-1}}$ [15].

A possible stress alleviator in the energy storage sector are the metal–air batteries, which are becoming popular due to the high abundance of anode materials such as Zn, Fe, Al and

Si [17]. The current section aims to be a general introduction in the field of metal–air batteries.

1.1. Metal–Air Batteries: Motivation

Firstly developed in 1878 and commercialized since the 1930's [18], metal–air batteries or "metal–oxygen" batteries are in principle simple devices comprised of three main components: a metal anode, an electrolyte, and an air cathode. This kind of batteries use a so called "open cell structure", in which the cathode is "open" for the readily access of oxygen from the atmosphere into the battery [19]. Figure 1.1 shows a scheme of a typical metal–air battery and a simplified graphical explanation of the working principle.

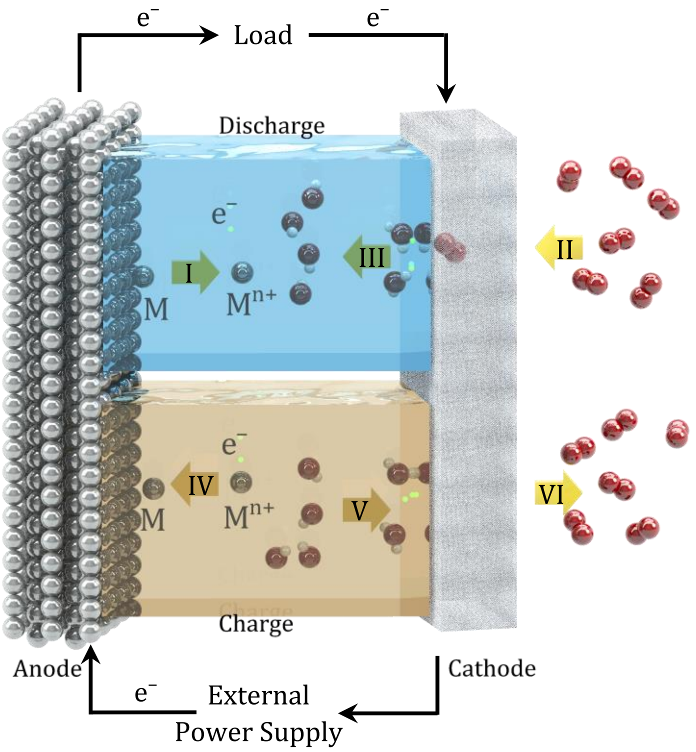

Figure 1.1: General description of a typical metal–air battery and its working principle.

Metal–air batteries use the electrons (green spheres in Figure 1.1) from the oxidation of metals (gray spheres in Figure 1.1) at the anode side to produce electricity, as indicated by the yellow arrow Figure 1.1–I. After the oxidation, the metal ions may further react to form soluble or insoluble species which is dependent on the electrolyte nature and its interaction with the metal ions [20]. An electrolyte in contact with the anode can create the conditions for the oxidation of the metal and allows the movement of the ions from anode to cathode and vice versa. The third main element of a metal–air battery is the air cathode (gray mesh on the right side of Figure 1.1) which allows the access of oxygen (red spheres in Figure 1.1–II) and consumes the electrons produced at the anode resulting in the reduction of oxygen to hydroxyl ion, as depicted in Figure 1.1–III. The air electrodes typically employ carbon powder mixed with a catalyst (e.g., MnO_2), which enhances the oxygen reduction reaction. The mixture carbon/catalyst is then pressed on a metal mesh and one of the sides is sealed with a membrane in order to avoid electrolyte leakage. Analogously, some metal–air batteries are electrically rechargeable, for which the described discharge process is reversed by inverting the current flow with an external power supply. The latter induces a higher potential on the anode, resulting in the redeposition of metallic species dissolved in the electrolyte or reduction of oxides on the anode surface as neat metal, indicated as charging in Figure 1.1–IV. Simultaneously at the air cathode, hydroxyl ions are oxidized (Figure 1.1–V) resulting in oxygen evolution (Figure 1.1–VI) under charging conditions

Metal–air batteries (MABs) can be divided into primary (discarded after a single discharge), secondary (rechargeable), and reserve (the battery is kept dry and electrolyte/water is added only when the battery is needed) [18]. Conditional on their design, MABs can also be mechanically “rechargeable” by replacing the exhausted anode material for a new one [18]. In addition, metal–air batteries can be subcategorized depending on the electrolyte employed: 1) aqueous, 2) non–aqueous, 3) hybrid (aqueous/non–aqueous), and 4) all–solid–state electrolyte [19,21,22]. For the purpose of this work, only aqueous and non–aqueous electrolytes are described and presented in Figure 1.2.

Aqueous electrolytes: The most commonly employed electrolytes in MABs are the alkaline solutions (e.g. KOH, NaOH, LiOH, etc.) due to their low price, easiness of preparation, moderate disposal requirement, and high ionic conductivities [23]. The high solubility of reaction products can reduce the clogging of the air electrode, whereas the moisture uptake is practically negligible in aqueous systems [22,24,25]. Yet, the evaporation of the electrolyte can be an issue for aqueous–based electrolytes at relatively high temperatures. Figure 1.2 also shows the possible precipitation of reaction products at the anode surface.

Non–aqueous electrolytes: The non–aqueous electrolytes include the ionic liquids (ILs), room temperature ionic liquids (RTILs) and water–free organic and inorganic solvents. RTILs are electrolytes composed of salts in liquid state without any additional solvent at temperatures below 373 K. RTILs also offer a wide electrochemical window, are chemically and thermally stable, besides offering tunable viscosity and ionic conductivity [26–28]. In addition, RTILs can reduce the parasitic corrosion reactions, which can effectively increase the practical specific energies of MABs. Water–free in/organic solvents can also decrease the limitations of typical water–based electrolytes, offering a larger electrochemical stability window. Some of the associated drawbacks of non–aqueous electrolytes are the possible ignition and decomposition of the electrolyte at elevated temperatures, whereas precipitation of reaction product can occur at the air cathode resulting in blockage of the gas channels (Figure 1.2).

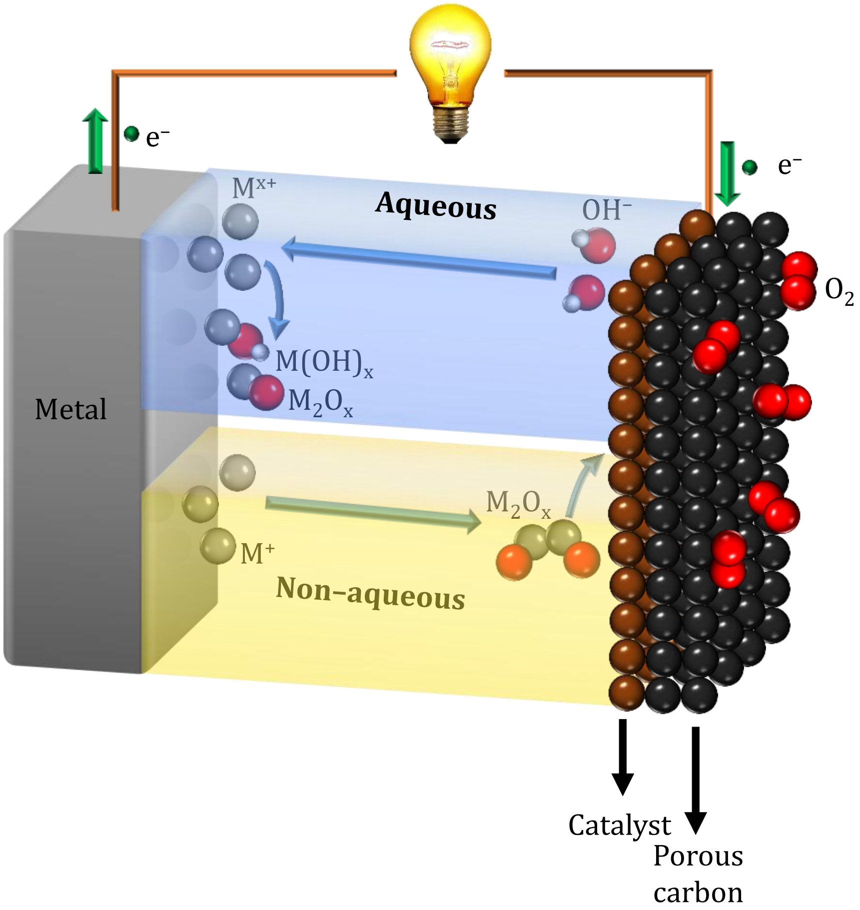

Figure 1.2: General scheme of aqueous and non–aqueous metal–air batteries.

One of the main advantages of the metal-air batteries is the relative high abundance of the anode active materials. Figure 1.3 graphically depicts the annual production versus the crust abundance of the elements, among which Si, Al, Fe and Zn coincide to be widely used in the industry and thus possess an elevated annual production in the orders of 10^{10}–10^{12} kg year^{-1} [17,29]. Accordingly, the elements found in the green, light green and nearby region are good candidates as anode materials for the metal–air batteries.

Elements found in the orange and red region with an annual production lower than 10^8 kg year^{-1} and abundance of less than 10^2 ppm may become bottlenecks for the fabrication of anode, cathode and additive materials [17,29].

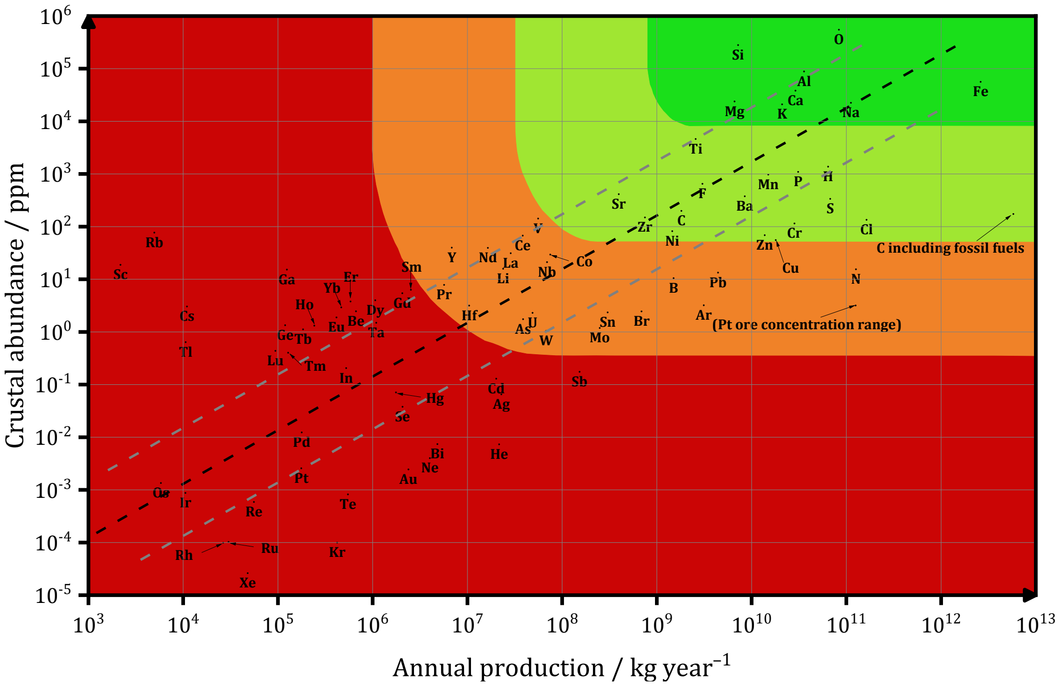

Figure 1.3: Annual production versus crustal abundance of elements. Notice that the scale is logarithmic on both axes. Figure reproduced after Weinrich et. al. [17].

Not only the abundance of materials is important in the contribution to climate–neutrality of the metal–air batteries, but also the remarkable high specific and volumetric energy densities as depicted in Figure 1.4. The specific energies of Mg (6,824 Wh $\mathrm{kg}_{\mathrm{Mg}}^{-1}$), Al (8,091 Wh $\mathrm{kg}_{\mathrm{Al}}^{-1}$), Si (8,461 Wh $\mathrm{kg}_{\mathrm{Si}}^{-1}$) and Li (11,431 Wh $\mathrm{kg}_{\mathrm{Li}}^{-1}$) are comparable to those of gasoline (13,000 Wh kg^{-1}) and higher than for Li–ion (800 Wh kg^{-1}).

The volumetric energy densities of Fe (9,677 Wh $\mathrm{L}_{\mathrm{Fe}}^{-1}$), Zn (9,653 Wh $\mathrm{L}_{\mathrm{Zn}}^{-1}$), Mg (11,860 Wh $\mathrm{L}_{\mathrm{Mg}}^{-1}$), Al (21,837 Wh $\mathrm{L}_{\mathrm{Al}}^{-1}$) and Si (19,748 Wh $\mathrm{L}_{\mathrm{Si}}^{-1}$) are significantly superior to gasoline (8,560 Wh L^{-1}) and Li–ion (4,050 Wh L^{-1}) [17]. Moreover, the specific energy is of special importance for certain applications where the weight of the fuel and/or battery becomes significant in the overall weight of e.g. a vehicle and might diminish its performance. The materials with still high volumetric energy densities can be of interest for stationary applications, where the space and not the weight is more important [17].

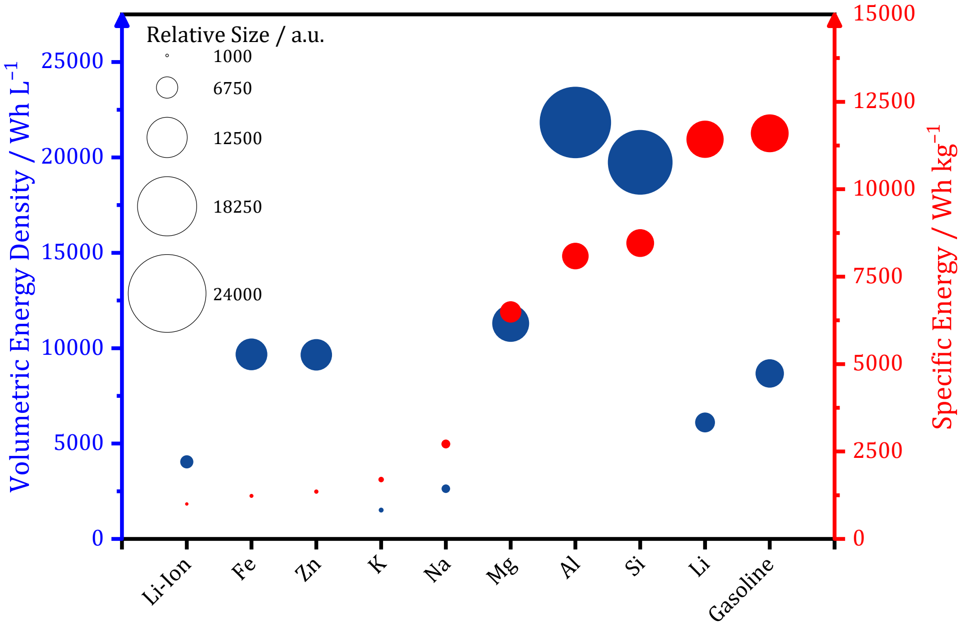

Figure 1.4: Specific and volumetric energy densities of typical metal–air batteries. Li–ion and gasoline are added for comparison purposes. Blue circles correspond to the left axis, red circles correspond to the right axis, and the size of the circles serves as a comparison among the same circle color and their relative values. Readapted after Weinrich et. al. [30].

The theoretical specific capacity describes the hypothetical total amount of energy produced by the electrochemical oxidation of an element per mass unit, which can be calculated as follows [31]:

$$Q_{\text{theoretical}} = \frac{nF}{3600\ M_w} \tag{1.1}$$

where $Q_{\text{theoretical}}$ is the theoretical specific capacity (in mAh g^{-1}), n is the number of electrons involved in the oxidation reaction, F is the Faraday's constant (96485.4 C mol^{-1}), and M_W is the molecular weight of the element being oxidized.

The $Q_{\text{theoretical}}$ for selected MABs is presented in Table 1-1 including the primary discharge product, cell voltage and practical proven reversibility. The most remarkable elements possessing a combination of both, high theoretical cell voltage and specific capacities, are Li, Mg, Al, and Si, whereas Fe and Zn are the best performing systems in terms of cyclability.

Table 1-1: Summary of some metal–air batteries systems and some of their main characteristics, including the reversibility.

.	Discharge Product	Theoretical		Reversibility / Cycles	Ref.
		Cell Voltage / V	Specific capacity /mAh g_{metal}^{-1}		
Li–O_2	Li_2O	2.91	3862	>250	[32]
	Li_2O_2	2.96	3862		[33]
Mg–O_2	MgO	2.95	2201	<10	[34]
Na–O_2	NaO_2	2.27	1166	>20	[35]
	Na_2O_2	2.33	1166		
K–O_2	KO_2	2.48	685	>200	[36]
Zn–air	ZnO	1.68	820	>75	[37]
Fe–air	$Fe(OH)_2$	1.28	960	3500	[38]
Al–air	Al_2O_3	~2.10	2996	Limited	[39]
Si–air	SiO_2	2.21	3828	No	[40,41]

As previously analyzed in Figure 1.3 and Figure 1.4, some elements are more abundant and geographically well distributed, such as Al, Zn and Si, with possessing highly attractive theoretical values. The present thesis focusses on these three elements and explores some of their advantages, limitations, challenges to overcome and possible solutions. The following section presents an overview of some commonly used techniques for the analysis and study of the metal–air batteries.

1.2. Current Status of Metal–Air Batteries: Overview

1.2.1. Silicon–Air Batteries: Current Status

Non–aqueous and aqueous electrolytes are the most commonly used electrolytes for Si–air batteries [41–49]. All–solid–state Si–air batteries have been also shown as feasible [50,51]. Within the framework of this thesis, only non–aqueous and aqueous Si–air batteries will be discussed.

1.2.1.1. Non–Aqueous Silicon–Air Batteries

First presented by Ein–Eli et. al. [42], the attractiveness of non–aqueous Si–air battery technology relies on the high crust abundance of the Si anode material (2nd place) [52], besides a high theoretical specific energy of 8,461 Wh $\mathrm{kg_{Si}^{-1}}$, energy density of 21,090 Wh $\mathrm{L_{Si}^{-1}}$, and a specific capacity of 3,828 mAh $\mathrm{g_{Si}^{-1}}$. Figure 1.5 shows the discharge profile of the first version of a non–aqueous Si–air battery using highly doped Si (100) wafers as anode material and $\mathrm{EMIm(HF)_{2.3}F}$ as electrolyte. The silicon anode requires doping to increase the conductivity and –depending on the element added– the silicon can become positively doped (p–type) or negatively–doped (n–type). Figure 1.5 displays steady cell voltages of 1.16 V under up to 0.1 mA $\mathrm{cm^{-2}}$ anodic current densities, while 0.3 mA $\mathrm{cm^{-2}}$ resulted in discharge voltages of ~0.92 V [42].

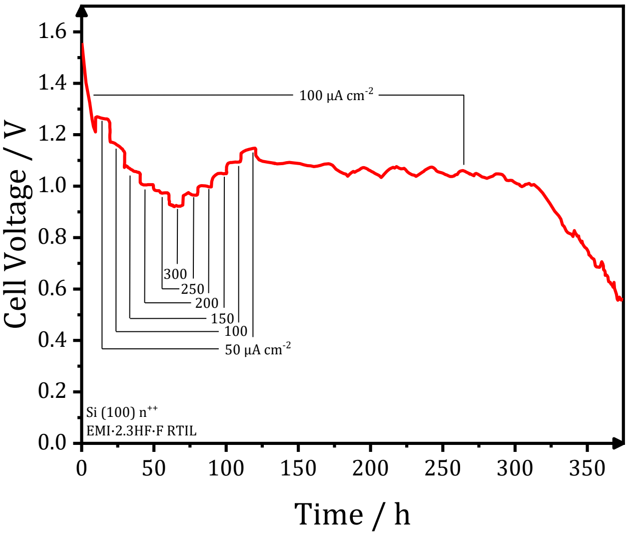

Figure 1.5: Discharge profile of heavily doped n–type Si in an $\mathrm{EMIm(HF)_{2.3}F}$–based Si–air battery under several current densities. Readapted after Cohn et. al. [42].

The employment of room temperature ionic liquids (RTIL) such as $\mathrm{EMIm(HF)_{2.3}F}$ provides a good electrochemical performance and relatively low corrosion [42,44,45,48,53,54]. Corrosion rates of the Si in presence of $\mathrm{EMIm(HF)_{2.3}F}$ as low as

<0.01–0.164 nm min^{-1} at OCP conditions are observed [42,44]. The governing reactions of the EMIm(HF)$_{2.3}$F–based Si–air batteries are the following:

Anode:	$Si + 12(HF)_2F^- \longrightarrow SiF_4 + 8(HF)_3F^- + 4e^-$	$E^0 = -1.8\ V_{SHE}$	**1.2**
Cathode:	$O_2 + 12(HF)_3F^- + 4e^- \longrightarrow 2H_2O + 16(HF)_2F^-$	$E^0 = 0.401\ V_{SHE}$	**1.3**
SiO_2 formation:	$SiF_4 + 2H_2O + 4(HF)_2F^- \longrightarrow SiO_2 + 4(HF)_3F^-$		**1.4**
Overall cell reaction:	$Si + O_2 \longrightarrow SiO_2$	$E = 2.201\ V$	**1.5**

Figure 1.6 shows the more recent evaluation of different dopants and crystal orientations of silicon on the electrochemical performance of non–aqueous Si–air batteries, showing the feasibility of discharging the cells under current densities as high as 0.5 mA cm^{-2} and displaying discharge voltages of 0.4–0.6 V [44]. The reported mass conversion efficiencies (the amount of Si effectively releasing its capacity during the discharge) were in the range of 40–50%, while the practical specific energy as high as 1,600 Wh kg$_{Si}^{-1}$ can be achieved [44]. Within the same study, the corrosion rates of B–doped <100> and <111> silicon wafers in EMIm(HF)$_{2.3}$F at OCP conditions were almost negligible, whereas As–doped <100> and <111> showed higher values [44].

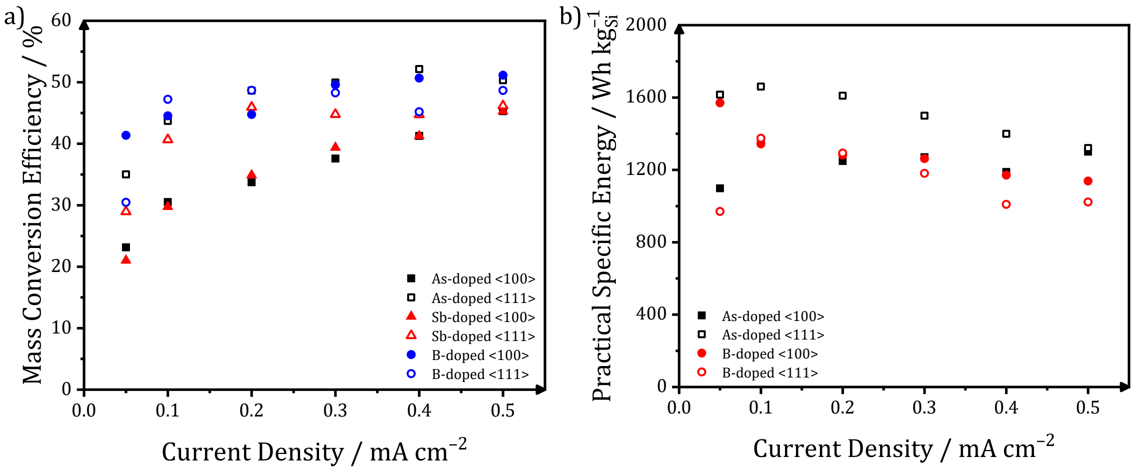

Figure 1.6: Performance parameters determined after discharge experiments under several current densities of non–aqueous Si–air batteries with different dopant and crystal orientations, a) mass conversion efficiency and b) practical specific energy [44].

Figure 1.7 shows a later evaluation of pulsed (interrupted) discharge over 200 h demonstrated the advantages of B<100> over As<100> silicon wafers, resulting in higher specific energies, specific capacities and anode mass conversion for the interrupted discharge of B<100> Si wafers [45]. Such benefits become less significant in the continuous discharge of the cells (p=1 of Figure 1.7a–c). SEM analysis of the As<100> Si surface displayed pits increasing in size for larger pulses (Figure 1.7d), while the micrographs of B<100> Si wafers presented a more homogeneous surface (Figure 1.7e) probably covered with nanopores [45].

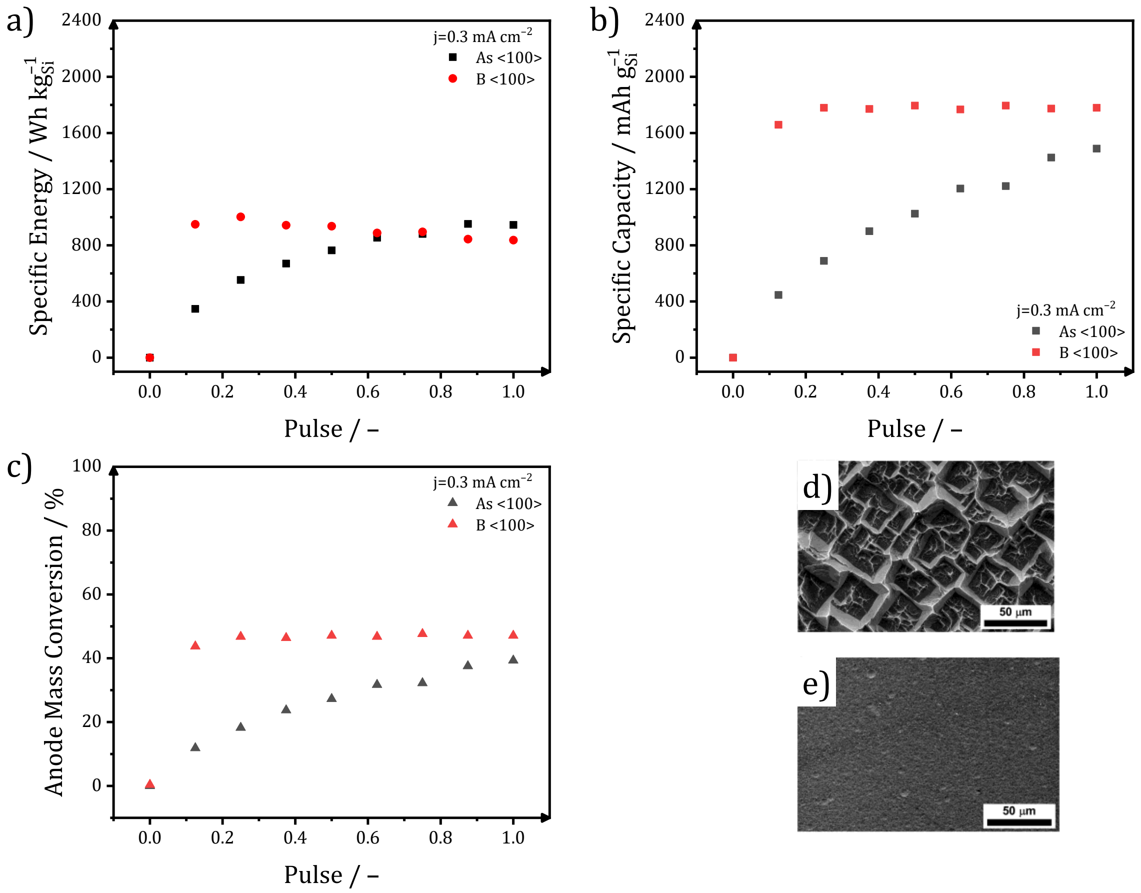

Figure 1.7: The practical values of Si–air batteries with As and B–dopants after discharging with 0.3 mA cm^{-2} current density, a) specific energy, b) specific capacity, and c) anode mass conversion after pulsed discharge of non–aqueous Si–air batteries, d) surface of As<100> and B<100> after continuous discharge (p=1). Reproduced after Durmus et. al. [45].

The application of RTILs in Si–air batteries still presents some challenges such as: (1) SiO_2 deposition on the air cathode, (2) capacity loss due to the limitations of the air electrode (transformation of MnO_2 catalyst to MnF_2 surface layer) and (3) anode related side reactions limiting the anode mass conversion efficiency [40,43,44]. Still, the non–aqueous Si–air batteries employing EMIm(HF)$_{2.3}$F possess the highest practical capacities (up to ~1800 mAh g_{Si}^{-1}), specific energies (up to 1600 Wh kg_{Si}^{-1}), and mass utilization efficiencies (over 50%) that have been reported for Si–air batteries so far.

1.2.1.2. Alkaline Silicon–Air Batteries

A cost–effective alternative to the RTILs is the KOH–based electrolytes, which is also a commonly employed electrolyte in other MABs. The main reactions governing the alkaline Si–air battery are as follows:

Anode: $$\mathrm{Si} + 4\mathrm{OH}^- \longrightarrow \mathrm{Si(OH)_4} + 4\mathrm{e}^- \qquad \mathrm{E}^0 = -1.697\ \mathrm{V_{SHE}} \tag{1.6}$$

Cathode: $$\mathrm{O_2} + 2\mathrm{H_2O} + 4\mathrm{e}^- \longleftrightarrow 4\mathrm{OH}^- \qquad \mathrm{E}^0 = 0.401\ \mathrm{V_{SHE}} \tag{1.7}$$

Silicate formation: $$\mathrm{Si(OH)_4} + 2\mathrm{OH}^- \longrightarrow \mathrm{SiO_2(OH)_2^{2-}} + 2\mathrm{H_2O} \tag{1.8}$$

Corrosion: $$\mathrm{Si} + 2\mathrm{OH}^- + 2\mathrm{H_2O} \longrightarrow \mathrm{SiO_2(OH)_2^{2-}} + 2\mathrm{H_2} \tag{1.9}$$

Passivation: $$\mathrm{Si(OH)_4} \longrightarrow \mathrm{SiO_{2(s)}} + 2\mathrm{H_2O} \tag{1.10}$$

Overall cell reaction: $$\mathrm{Si} + \mathrm{O_2} + 2\mathrm{OH}^- \longrightarrow \mathrm{SiO_2(OH)_2^{2-}} \qquad \mathrm{E}^0 = 2.098\ \mathrm{V} \tag{1.11}$$

Figure 1.8 shows the first experiments of alkaline Si–air batteries with highly doped n–type Si wafers (also denoted as n^{++} Si wafers). The reported discharge duration was in the order of hundreds of seconds for flat Si anodes, whereas the employment of nanostructured Si (nPSi) as anode material could extend the discharge over 30 h (Figure 1.8a) [46]. A following study approached the use of flat highly doped p–type (p^{++}) silicon anodes and the surface was apparently passivated within seconds leading to premature stop of the discharge, whereas further treatment of the surface to produce nanoporous silicon could extend the discharge to over 15 h (Figure 1.8a) [47].

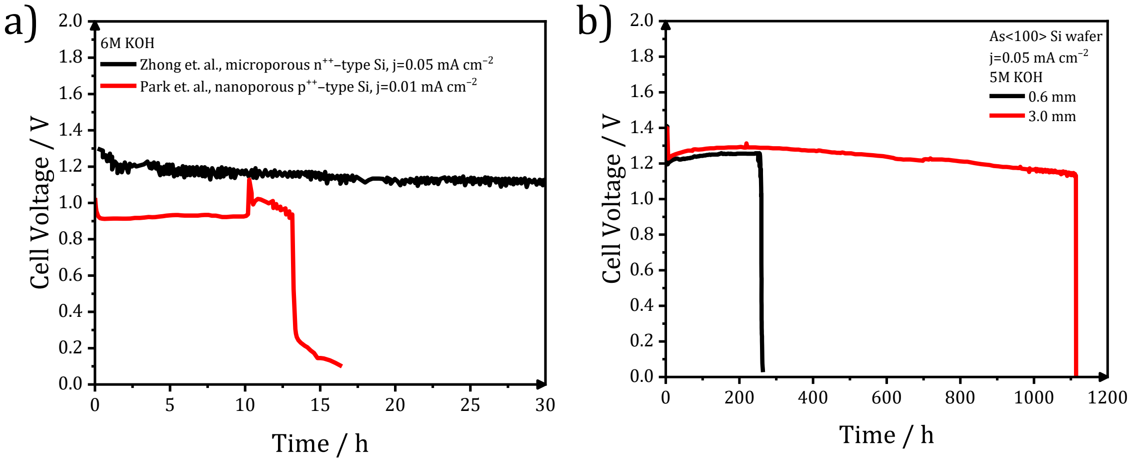

Figure 1.8: Discharge profile of a) microporous silicon wafers in 6M KOH under 0.05 mA cm^{-2} by Zhong et. al. [46] and nanoporous wafers in 6M KOH under 0.01 mA cm^{-2} by Park et. al. [47], and b) n^{++} As<100> flat Si wafers with 0.6 and 3.0 mm thickness in 5M KOH under 0.05 mA cm^{-2} by Durmus et. al. [41].

Durmus et. al., however, showed the possibility of longer discharge time of alkaline Si–air batteries with a refill type cell which replenished the electrolyte every 4 h [41]. Under such conditions, the alkaline Si–air battery could deliver up to 1.2 V under 50 µA cm^{-2} for more than 270 h with n^{++} As<100> flat Si wafers (thickness=0.6 mm, Figure 1.8b) [41]. The discharge of such cells could be further extended with the employment of thicker wafer (3.0 mm, Figure 1.8b), reaching up to 1100 h before the complete consumption of the highly doped n–type Si anode [41].

Figure 1.9 shows the results of the overall corrosion rates and cyclic voltammograms of n⁺⁺ As<100> Si wafers in alkaline media evaluated by Durmus et. al. [48]. The analysis revealed similar corrosion rate for KOH concentrations below 1M (Figure 1.9a), then a continuous increase in the range from 1–6M KOH, whereas higher concentrations (>6M KOH) displayed a plateau on the corrosion rates [48]. Such behavior could be directly related to the hydration model of Gemblocki et. al., stating that the corrosion of Si is initiated by free–water molecules catalyzed by the presence of KOH [55]. The free–water is understood as the H_2O molecules, which do not participate in the solvation of KOH.

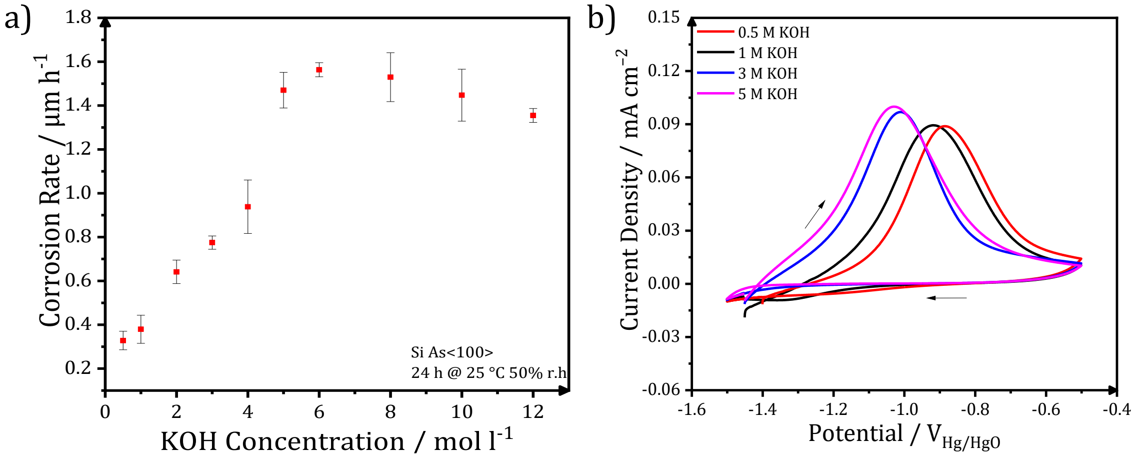

Figure 1.9: Characterization chemical and electrochemical behavior of the n⁺⁺ As<100> Si wafers by a) measurement of the corrosion rates after 24 h of exposure to different electrolyte concentrations ranging from 0.5 to 12M KOH and b) cyclic voltammetry of n⁺⁺ As<100> Si wafers in 0.5–5M KOH with a scan rate of 5 mV s^{-1} at 25°C.

The corrosion at low concentrations of KOH (<1M KOH) is initiated by the KOH itself, which explains the similar corrosion rates. 1–6M KOH solutions increasingly catalyze the free–water molecules, resulting in the steady increase of the corrosion with rising KOH concentration. Highly concentrated KOH (>6M), on the other hand, presents diffusion limitations as the saturation limits are approached, which is in agreement with the decreasing ionic conductivity observed for such elevated KOH concentrations [23,48]. Analysis of the chemical and electrochemical contribution to the overall corrosion by weight loss and potentiodynamic polarization revealed over 99% dominance of the chemical reaction during corrosion of Si at OCP conditions for 0.5–12M KOH [48]. Additional comparison of cyclic voltammograms of n⁺⁺ As<100> Si wafer in different KOH concentrations displayed almost identical electrochemical characteristics with a slight shift towards more negative potentials at higher KOH concentrations (Figure 1.9b). The electron transfer was, therefore, suggested as the rate determining step in the electrochemical behavior of Si since higher KOH concentrations barely change the anodic peak current density.

Some of the challenges associated to the alkaline Si–air batteries are: (1) high corrosion rates at OCV and discharge conditions, (2) anode mass conversion efficiency limited to ~3%, (3) reduced power output due to limited anodic current densities (maximum ~90 μA $\mathrm{cm^{-2}}$ on a flat Si), and (4) passivation of the Si surface upon higher discharge current densities [41,48]. In addition, Equation 1.6 suggests a potential of Si as high as −1.82 $V_{Hg/HgO}$ still to be unconstrained, which is around 400 mV more negative than the typical OCP values observed. Even under such constrains, practical specific capacities of 120 mAh $\mathrm{g_{Si}^{-1}}$, relative long discharge durations (>1100 h), and stable voltages (1.2 V under 50 μA $\mathrm{cm^{-2}}$) can be attained [41,48]. Additionally, Si–air batteries have shown as feasible with relatively low KOH concentrations (1M KOH) and still presenting stable discharge voltages (1.1 V under 50 μA $\mathrm{cm^{-2}}$) [41,48]. Major efforts for the further development of the alkaline Si–air batteries should focus on the understanding of the SiO_2 formation on the anode surface, prevention of corrosion and achievement of higher OCV and discharge voltages.

1.2.2. Zinc–Air Batteries

Zinc–air batteries (ZABs) are one of the most developed batteries as they have been present since 1878 [18,56,57]. ZABs are attractive not only because of their good theoretical specific and volumetric energy densities (1,352 Wh kg_{Zn}^{-1} and 9,653 Wh L_{Zn}^{-1}, respectively), but due to the cyclability of the metal anode which adds flexibility for energy storage [58,59]. Three main types of zinc–air batteries can be distinguished depending on the nature of the electrolyte: 1) aqueous, 2) non–aqueous, and 3) all–solid–state. Additionally, aqueous zinc–ion batteries using the intercalation of Zn^{2+} at the cathode are receiving more attention as a safe and cost–efficient energy storage alternative [59]. Focusing only on aqueous Zn–air batteries, they can be subdivided in three more categories: acid, near–neutral and alkaline. Table 1-2 summarizes some of the key characteristics and issues related to each kind of battery.

Table 1-2: Summary of some characteristics and limitations of the aqueous Zn–air batteries. Adapted after Mainar et. al. [60].

	Acidic	Neutral	Alkaline
CO_3^{-2} formation			X
Hydrogen evolution reaction	X	X	X
Dendrite formation	X		X
Ionic conductivity (mS cm^{-1})	500–600	200–300	500–700
Sensitive to impurities	No	No	No
Lower temperature range	X	X	X
Limited electrochemical window	X	X	X
Water evaporation or ambient moisture uptake	X	X	X
Corrosion	High	Low	High

The present discussion on ZABs will be limited to alkaline and near–neutral systems and the reader is referred to the literature for extended reviews on other Zn–air batteries configurations [21,58–62].

1.2.2.1. Alkaline Zinc–Air Batteries

The first commercially available alkaline ZAB was introduced in the market in 1932 by Heise and Schumacher, displaying an OCV of 1.4–1.45 V and discharge voltages of 1.1–1.2 V depending on the applied load [63]. The cell–level energy density was in the order of 87–106 Wh kg_{cell}^{-1} or 106–129 Wh L_{cell}^{-1}. Since then, different strategies have been attempted to improve the performance of ZABs and their cyclability by tuning the main components of a metal–air battery: 1) anode material, 2) electrolyte, 3) air cathode materials, and 4) separators (if employed). Table 1-3 present some of the possible approaches for improvements of ZABs focused on the effects over the Zn anode material summarized by Fu et. al. [58].

Additional to the strategies mentioned in Table 1-3, alloying of the Zn anode to materials with more negative standard electrode potential has demonstrated beneficial effects on the discharge performance of ZABs [64,65].

Table 1-3: Proposed strategies for the improvement of the zinc electrodes performance. Reproduced after Fu et. al. [58].

Strategy	Direct influence on			
	Dendritic growth	Shape change	Passivation and internal resistance	Hydrogen evolution
1. High surface area/3D electrode structure	Minimized (decreased charging overpotential)	Minimized (3D structure improves current distribution)	Minimized (High surface area minimizes ZnO film thickness)	(Higher surface area causes higher evolution rate)
2. Polymeric binders	–	Minimized (improves mechanical strength)	Increased (increases electrode resistance)	–
3. Carbon–based electrode additives	–	Minimized (improves current distribution)	Minimized (improves electrode conductivity)	–
4. Heavy–metal electrode additives	Minimized ("substrate effect" promotes denser deposits)	Minimized (improves current distribution)	Minimized (improves electrode conductivity)	Minimized (increases hydrogen overpotential)
5. Discharge–trapping electrode additives	Minimized ($Zn(OH)_4^{2-}$ concentration gradient is reduced)	Minimized (discharge product migration is reduced)	Possibly minimized (if trapped discharge product is more conductive than ZnO)	–
6. Electrolyte additives	Minimized (if additive adsorption onto active hydrogen evolution sites occurs)	Minimized (reduces $Zn(OH)_4^{2-}$ solubility)	Possibly increased (if early ZnO precipitation is induced)	Possibly minimized (if additive adsorption onto active hydrogen evolution sites occurs)
7. Electrode coatings	Minimized ($Zn(OH)_4^{2-}$ concentration gradient is reduced)	Minimized (discharge product migration is reduced)	–	–

Figure 1.10 shows relevant results of the work of Hosseini et. al., who recently showed the beneficial effects of DMSO added to 7M KOH for ZABs with ~0.8 mm–diameter granular Zn as anode material and MnO_2/carbon mixture as cathode material [66]. In a ratio of 20% v/v DMSO/KOH, this kind of electrolyte markedly increased not only the discharge capacity by 20%, but also the cyclability of Zn anodes in alkaline ZABs was significantly extended from 198 to over 600 cycles without noticeable performance loss [66].

Development and optimization of bifunctional air electrodes capable of oxygen reduction reaction (ORR) during discharge and oxygen evolution reaction(OER) during charging are of high interest in alkaline ZABs.

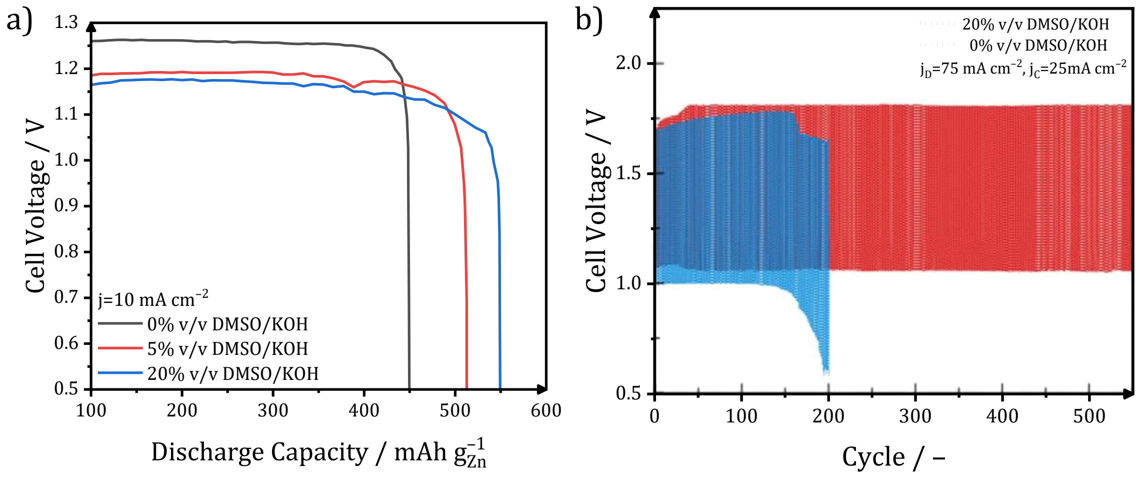

Figure 1.10: Electrochemical performance evaluation of alkaline Zn–air batteries with and without the addition of different amounts of DMSO, a) discharge capacity vs. cell voltage of a Zn–air battery with 7M KOH and different ratios of DMSO/KOH. Reproduced after Hosseini et. al. [66].

Figure 1.11 shows the results of recent studies on new configurations for the air electrodes and compare them to typical materials (IrO_2 for OER and Pt/C for ORR). The performance of the air cathodes depends on the capabilities for OER, represented by a higher positive current densities at lower potentials in Figure 1.11a, whereas the capabilities for ORR are displayed as larger negative current densities at more positive potentials in Figure 1.11b.

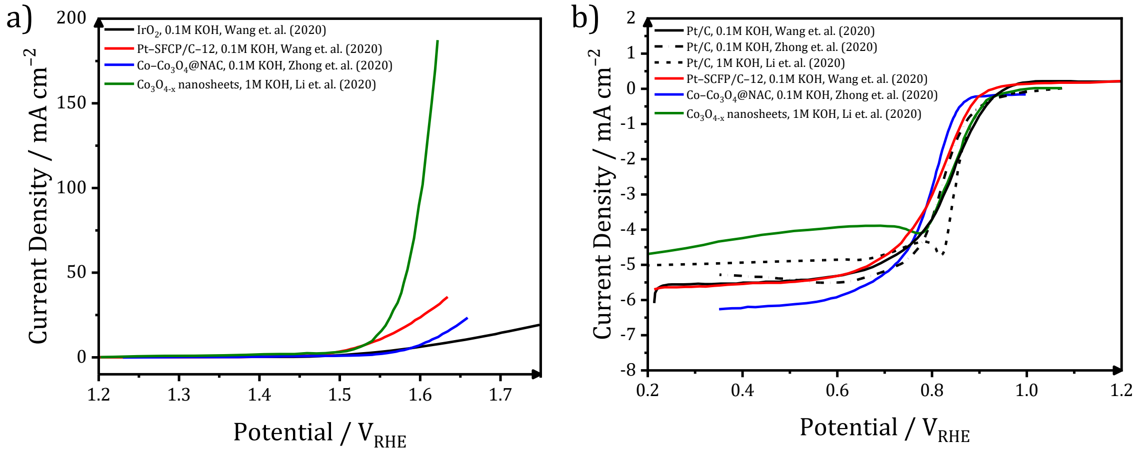

Figure 1.11: Linear sweep voltammetry evaluation for a) oxygen evolution reaction (OER) and b) oxygen reduction reaction (OER) of different air cathode materials for alkaline Zn–air batteries. Reproduced after [67–69].

In general, Figure 1.11 shows Co_3O_4 oxygen defficient (Co_3O_{4-x}) nanosheets as more beneficial for the OER and Co–Co_3O_4 with nitrogen–doped active carbon (Co–Co_3O_4@NAC) with higher ORR. $Sr(Co_{0.8}Fe_{0.2})_{0.95}P_{0.05}O_{3-\delta}$ with 12:1 ratio 20%

platinum/carbon (Pt–SCFP/C–12) cathode materials showed a more equilibrated behavior for OER and ORR.

Table 1-4 summarizes the performance of alkaline ZABs in recent works, which investigated different electrolyte formulations and air cathode compositions. The influence of the air cathode on the specific capacities during primary operation of the alkaline ZAB was clearly observed with values as high as 721–800 mAh g_{Zn}^{-1}, whilst the discharge/charge voltage difference could be effectively reduced from over 2.1 V to less than 1 V [67–69]. In addition, the electrolyte composition can successfully increase the cycling life for over 600 cycles [66].

Table 1-4: Summary of the recent progress on alkaline Zn–air batteries. Reproduced after Chen et. al. [70].

Electrolyte composition	Electrode materials	Specific capacity*	Durability	Ref.
6M KOH + 0.2M Zn acetate	Zn plate// Co–Co_3O_4@NAC[a]	721 mAh g_{Zn}^{-1} @ 10 mA cm^{-2}	35 h @10 mA cm^{-2} for 20 min $cycle^{-1}$	[68]
6M KOH + 0.2M Zn acetate	Zn foil// Co_3O_{4-x}[b]	800 mAh g_{Zn}^{-1} @ 5 mA cm^{-2}	150 h @10 mA cm^{-2} for 20 min $cycle^{-1}$	[69]
6M KOH + 0.2M $ZnCl_2$	Zn plate// Pt–SCFP[c]	781 mAh g_{Zn}^{-1} @ 10 mA cm^{-2}	80 h @5 mA cm^{-2} for 20 min $cycle^{-1}$	[67]
7M KOH + 5–20% v/v DMSO	Zn granules// MnO_2[a]	550 mAh g_{Zn}^{-1} @ 10 mA cm^{-2}	600 cycles @ discharge@75 mA cm^{-2} and charge@25 mA cm^{-2}	[66]
8M KOH + 0–50% v/v ethanol	Zn granules// MnO_2[a]	470 mAh g_{Zn}^{-1} @ 25 mA cm^{-2}	N/A	[71]
100 ml 1M KOH + 0.1 g water–suspended graphene	Zn strip// Co–Sn–CNP[d]	212.6 mAh g_{Zn}^{-1} @ 1 mA cm^{-2}	Discharge 15 h @1 mA cm^{-2}	[72]

* under primary cell operation

[a] Ni–foam, [b] carbon paper, [c] carbon cloth, [d] stainless steel

1.2.2.2. Near–Neutral Zinc–Air Batteries

The (near)–neutral Zn batteries can be tracked back to 1860s with the Leclanché and zinc–carbon batteries [18,56]. Leclanché batteries typically used 1M $ZnCl_2$ + 2M NH_4Cl as electrolyte in the pH range of 4–9, Zn sheet metal as anode and a carbon–MnO_2 mixture as cathode [56]. Later in the 1930's, Heise and Schumacher introduced a near–neutral ZABs in the market, where such early version used ammonium chloride paste as electrolyte, delivering up to 0.8–1.2 V under 1 A over 20 h before reaching a cutoff potential at 0.75 V [73]. The reactions describing this type of battery are the following:

Anode: $$\mathrm{Zn} \longrightarrow \mathrm{Zn}^{2+} + 2\mathrm{e}^{-} \qquad \mathrm{E}^0 = -0.761\ \mathrm{V_{SHE}} \tag{1.12}$$

Anode side reaction: $$\mathrm{Zn}^{2+} + 4\mathrm{Cl}^{-} \longrightarrow \mathrm{ZnCl}_4^{2-} \tag{1.13}$$

Cathode: $$\mathrm{MnO_2} + \mathrm{NH}_4^{+} + \mathrm{e}^{-} \longrightarrow \mathrm{MnOOH} + \mathrm{NH_3} \qquad \mathrm{E}^0 = 0.869\ \mathrm{V_{SHE}} \tag{1.14}$$

Cathode side reaction: $$\mathrm{ZnCl}_4^{2-} + \mathrm{NH_3} \longrightarrow \mathrm{Zn(NH_3)_2Cl_2} + 2\mathrm{Cl}^{-} \tag{1.15}$$

Overall cell reaction: $$\mathrm{Zn} + 2\mathrm{MnO_2} + 2\mathrm{NH_4Cl} \longrightarrow \mathrm{Zn(NH_3)_2Cl_2} + \mathrm{MnOOH} \qquad \mathrm{E}^0 = 1.63\ \mathrm{V_{SHE}} \tag{1.16}$$

The $ZnCl_2$–based and Zn alkaline cell are some variations of the Leclanché battery with similar construction materials but different electrolytes and cell configurations [56]. The zinc chloride battery resulted in high OCVs (1.75 V) and large drain capabilities, whereas the Zn alkaline cell presented slightly lower OCV (1.55 V) but higher discharge currents and longer storage life than the Leclanché and $ZnCl_2$–based batteries [56].

The later introduction of the zinc–air batteries (ZABs) could increase the energy density by using O_2 from the atmosphere as reactant at the cathode. Moreover, one of the main advantages of the (near) neutral systems over the alkaline and acid systems is the prevention of carbonate and dendrite formation, while some other characteristics such as a relatively high ionic conductivity and low sensitivity to impurities remain (Table 1-2). The common problems among the acid, neutral and alkaline systems arise from their aqueous nature. The reaction governing the discharge of aqueous near–neutral Zn–air batteries are as follows:

Anode:	$Zn \longrightarrow Zn^{2+} + 2e^-$	$E^0 = -0.761\ V_{SHE}$	**1.17**
Possible reactions in chloride–based systems:	$Zn^{2+}_{(aq)} + 2OH^- \rightarrow Zn(OH)_2$		**1.18**
	$5Zn^{2+} + 8OH^- + 2Cl^- + H_2O \rightarrow Zn_5(OH)_8Cl_2 \cdot H_2O$		**1.19**
	$Zn(OH)_2 \rightarrow ZnO + H_2O$		**1.20**
	$Zn(OH)_2 + 2OH^- \rightarrow Zn(OH)_4^{2-}$		**1.21**
	$5Zn(OH)_2 + 2Cl^- + H_2O \rightarrow Zn_5(OH)_8Cl_2 \cdot H_2O + 2OH^-$		**1.22**
	$Zn^{2+}_{(aq)} + 2Cl^- \rightarrow ZnCl_2$		**1.23**
Cathode:	$2H^+ + 0.5O_2 + 2e^- \longrightarrow H_2O$	$E^0 = 0.816\ V_{SHE}$ @pH 7	**1.24**
Overall cell reaction:	$2Zn + 4H^+ + O_2 \longrightarrow 2Zn^{2+} + 2H_2O$	$E = 1.577\ V$	**1.25**

It was until 1973 when Jindra et. al. [74] proposed the first primary Zn–air battery by using 5M NH_4Cl as electrolyte, porous Zn anodes, and carbon electrodes “open” to the atmosphere. Such cell configuration resulted in low corrosion of the Zn anode and cell voltages of 0.9–0.95 V under 10 mA cm^{-2} in ambient conditions as shown in Figure 1.12a [74]. Decades later, Amendola expanded the concept to rechargeable ZABs in 2012, reaching 200–500 cycles and displaying voltages of 0.9 and 2.1 V under discharge and charge conditions, respectively (Figure 1.12b) [75]. Amendola et. al. proposed current densities between 1 to 200 mA cm^{-2} in order to avoid Cl_2 formation and to favor the O_2 evolution upon charging [75].

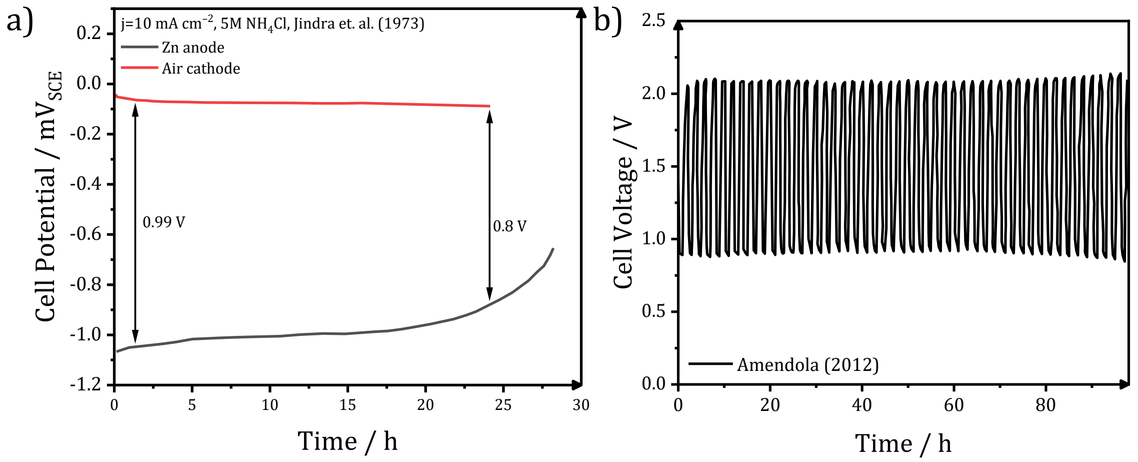

Figure 1.12: Early development and progress of ZABs, a) Zn and air cathode potentials in 5M NH_4Cl under 10 mA cm^{-2} galvanostatic discharge of the first neutral Zn–air battery by Jindra et. al. [74] and b) discharge/charge cycling of a neutral ZAB by Amendola et. al. [75].

More recently, Goh et. al. evaluated the effect of pH value, NH_4Cl–concentration, additives (thiourea and PEG) on neutral ZABs and were able to reach over 120 cycles/1,400 h of continuous cycling under ~0.5 mA cm^{-2} discharge and ~0.25 mA cm^{-2} current densities (Figure 1.13a) [76]. The employed electrolyte consisted of 2.34M NH_4Cl, 0.51M $ZnCl_2$, 1000 ppm PEG, 1000 ppm thiourea at pH 6 and achieved discharge/charge capacities in the range of 20 to 120 mAh [76]. Sumboja et. al. developed air cathodes for neutral ZABs consisting of directly grown MnO2 on carbon paper and achieved continuous cycling for over 2,160 h/540 cycles under 1 mA cm^{-2} in 5M NH_4Cl, 35 g L^{-1} $ZnCl_2$, and 1000 ppm thiourea at pH 7 (Figure 1.13b) [77,78].

Later simulation studies of neutral ZABs by Clark et. al. proposed an electrolyte composed of 1.6M NH_4Cl and 0.5M $ZnCl_2$ at pH 8 for a favorable operation and to deliver energy densities as high as 151 Wh L^{-1} [79]. In a following study, Clark et. al. simulated and studied the importance of pH changes and its influence on 1) the final discharge products, 2) catalyst degradation, and 3) material corrosion, which finally can limit the operation of neutral ZABs [80]. Additionally, ZABs containing NH_4Cl concentrations in the range of 1.6–2.34M, $ZnCl_2$ from 0.26–0.51M and at pH values from 4–8 could sustain over 150 cycles and 600 h under 1 mA cm^{-2} (Figure 1.13c) [80].

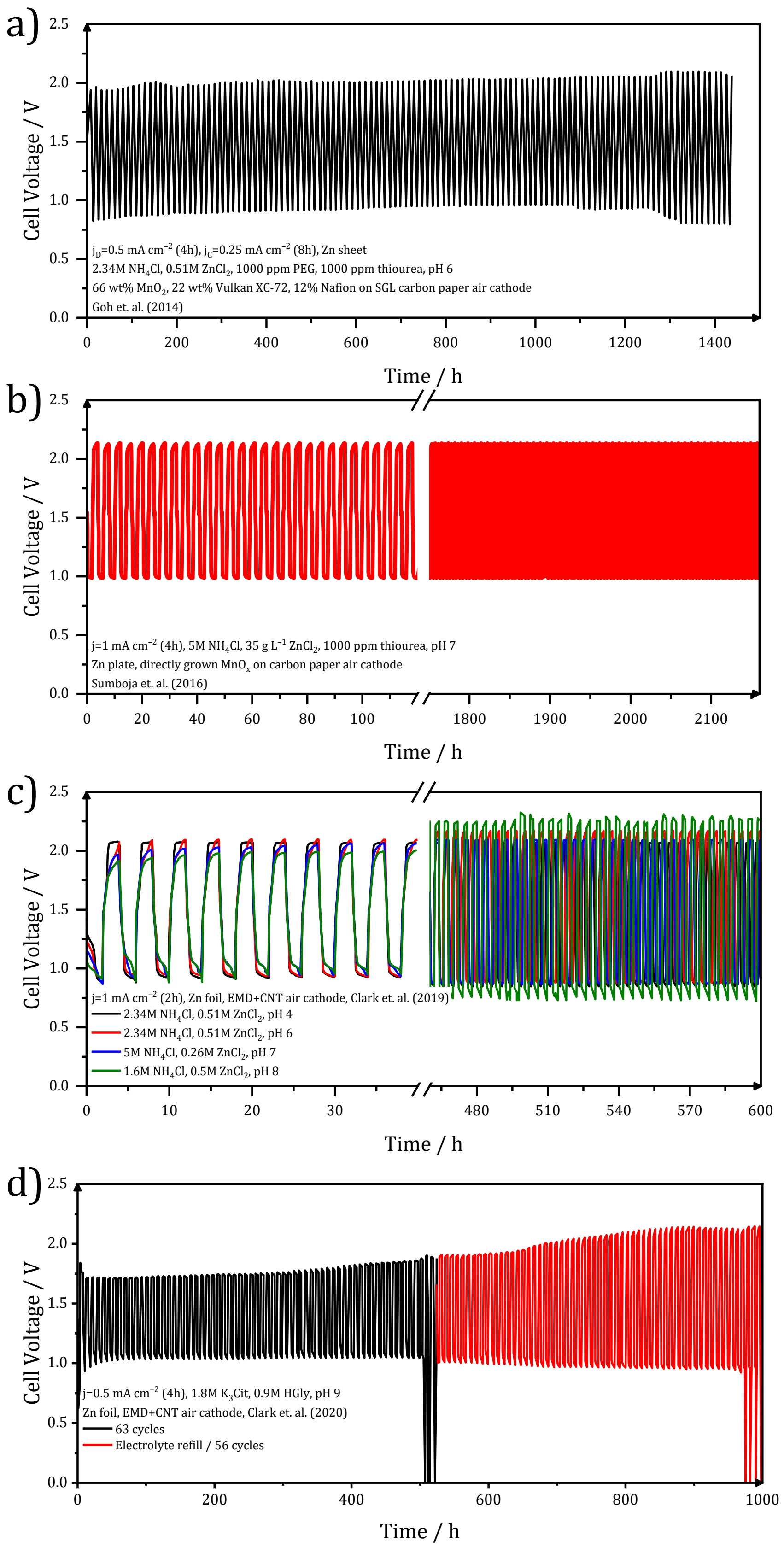

Figure 1.13: Cycling performance comparison of ZABs in (near) neutral electrolytes, a) NH_4Cl–$ZnCl_2$–based electrolyte, MnO_2–Vulkan–Nafion on SGL carbon paper air cathode, b) NH_4Cl–$ZnCl_2$-based electrolyte, directly grown MnO_x on carbon paper air cathode , c) NH_4Cl–$ZnCl_2$-based electrolyte, EMD+CNT air cathode, d) chloride–free organic electrolyte, EMD+CNT air cathode. Reproduced after [76,78,80,81].

The latest progress also from the group of Clark and Mainar proposed a chloride–free electrolyte composed of 1.8M Cit^{3-}, 0.9M HGly and saturated with ZnO at pH 9 to improve the cyclability of near–neutral Zn–air batteries [81]. Additionally, air cathodes composed of electrocatalytic MnO_2 (EMD), carbon nanotubes (CNT) and a combination of both materials (EMD+CNT) were evaluated and displayed better performance in the order of EMD<CNT<EMD+CNT. A total of 119 cycles and almost 1000 h were attained with the aqueous organic electrolyte and EMD+CNT air cathode under 0.5 $\mathrm{mA\,cm^{-2}}$ (Figure 1.13d).

As near–neutral Zn–air battery systems typically use chloride–based solutions, several reactions may occur simultaneously while they also depend on the pH and concentration of the Zn and Zn reaction products in the solution. The employment of chloride–free electrolytes proposed by Clark et. al. could decrease the risk of Cl_2 evolution upon recharge and lower pitting corrosion under discharge conditions [81]. In addition, substituting halide–based electrolytes by other organic salts capable of buffering the pH may display more stable and longer cycling of the ZABs, which is still a challenge to overcome in the near–neutral system [81]. The current results are, however, promising and considerations for future developments—including alternative electrolyte formulations—should be attaining high anode–based mass conversion efficiencies, specific capacities, and specific energies during primary and secondary operation of near–neutral ZABs.

1.2.3. Aluminum–Air Batteries

Aluminum possesses one of the highest specific energies among the metal–air batteries, while having a high abundance and annual production (see Section 1.1). Moreover, Al has high theoretical specific capacities ($2{,}996\ \mathrm{mAh\,g_{Al}^{-1}}$, just below silicon and lithium), nominal cell voltages of 2.1 V, and the largest volumetric energy density among several metal–air batteries ($21{,}837\ \mathrm{Wh\,L_{Al}^{-1}}$). Additionally, aluminum is recyclable and can reach high purity degrees with relative low costs [21]. The practical specific energies are usually limited due to losses at the Al anode of the cell, one of which is the parasitic corrosion reaction which consumes Al and water while H_2 is being evolved during OCV and discharge [18,82]. Due to this issue, Al–air batteries (AABs) are mainly considered as possible reserve systems and kept in dry condition until usage. The discharge of aluminum electrodes has been shown as feasible in alkaline or neutral electrolytes

[18,82–84]. Additionally, aqueous Al–air batteries cannot be electrically recharged due to the high stability of the reaction products that require high overpotentials, which would result in the water hydrolysis and degradation of the electrolyte. Therefore, aqueous Al–air batteries are considered as primary batteries (single use) only, with a possibility of being mechanically rechargeable (replenishment of the anode material). In addition, non–aqueous, semi–solid and solid electrolytes for primary Al–air batteries are also under development [39,40,82], and cycling of aluminum can be achieved in combination with adequate air cathodes [85–87]. The following section focuses only on the primary (near) neutral Al–air batteries.

1.2.3.1. Near–Neutral Al–Air Batteries

Similarly, as for the Zn–air batteries, Al–air with (near)–neutral electrolytes may reduce the corrosion issues and carbonation of the electrolyte, while keeping good ionic conductivities. The main reactions of Al in the near–neutral systems are depicted as follows:

Anode:	$2Al + 3H_2O \longrightarrow Al_2O_3 + 6H^+ + 6e^-$	$E_0 = -1.96\ V_{SHE}$ @pH 7	**1.26**
Possible reactions in chloride–based systems:	$2Al + 6H_2O \longrightarrow 2Al(OH)_3 + 3H_2$		**1.27**
	$2Al + 3H_2O \longrightarrow Al_2O_3 + 3H_2$		**1.28**
	$Al^{3+} + 3Cl^- \longrightarrow AlCl_3$		**1.29**
Cathode:	$2H^+ + 0.5O_2 + 2e^- \longrightarrow H_2O$	$E_0 = 0.861$ V @pH 7	**1.30**
Overall cell reaction:	$4Al + 3O_2 + 6H_2O \longrightarrow 4Al(OH)_3$	$E^0 = 2.82V$	**1.31**

Figure 1.14 shows the anodic polarization of Al alloys in 3% NaCl (~0.5M) and the current–voltage curve of the first neutral Al–air battery done by Despić et. al. back in 1976 [88]. The polarization curve of pure aluminum revealed current densities of 0.1 mA cm^{-2} at −0.8 V_{SCE}, whereas the same current densities were observed at −1.2 V_{SCE} for Al–0.19%In, −1.53 V_{SCE} for Al–0.12%Ga, and −1.6 V_{SCE} for an Al–In–Ga–Tl alloy. The same polarization curve displayed 100 mA cm^{-2} at −0.58 V_{SCE} for the pure Al sample, whereas the same current densities were observed at significant higher potentials for Al–0.19%In at −1.15 V_{SCE}, −1.24 V_{SCE} for Al–0.12%Ga, and −1.22 V_{SCE} for the Al–In–Ga–Tl alloy. Additionally, Despić also carried out tests with the Al–0.19%In samples, in which a cathodic polarization at −1.74 V_{SCE} was applied preceding the anodic polarization scan, represented as the blue dashed line in Figure 1.14a.

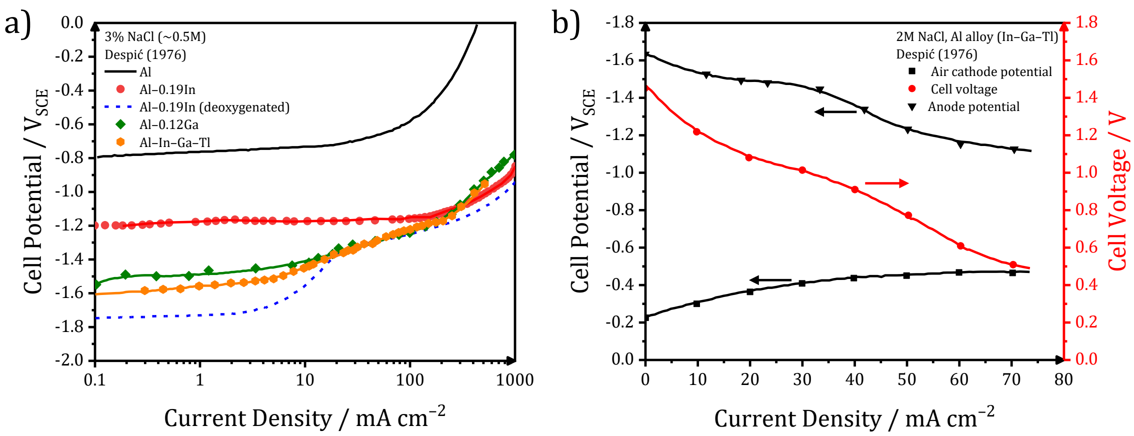

Figure 1.14: a) Anodic polarization of Al alloys in 3% NaCl solutions, after Despić et. al. [88], and b) current–voltage curve of the first neutral Al–air battery by Drazić [89,90].

Such prior cathodic polarization noticeable increased the anodic current densities with also significant lower potential drops than the "non–activated" Al–0.19%In samples (0.1 mA cm^{-2} at −1.74 V$_{SCE}$, 1 mA cm^{-2} at −1.73 V$_{SCE}$, and 10 mA cm^{-2} at −1.56 V$_{SCE}$). Such effect could be explained by the cathodic dissolution of Al already explored by Caldwell and Albano back in 1939, who postulated the decrease of H^{+} ion concentration and increase of the OH^{-} ions due to the cathodic polarization in neutral solutions [91]. The positive polarization could be able to locally alkalize the electrode and corrode the metal even under bulk neutral pH. Later studies further investigated such phenomenon and was designated as "cathodic activation" of the Al [92–94]. All the alloys evaluated by Despić could, at least in principle, deliver up to 1 A at potentials in the range of −0.78 to −0.95 V$_{SCE}$ [88]. Eventually, the same group of Dražić and Despić presented a neutral Al–air battery (Figure 1.14b), which brought economic advantages over the Zn–air and Mg–air (~3 times cheaper) at that time [89]. Al–air batteries with 2M NaCl as electrolyte and Al alloys with <2 ppt In–Ga–Tl displayed cell voltages of 1 V under 30 mA cm^{-2} and 0.6 V under 60 mA cm^{-2} [89,95]. Yet, some of the general issues with the neutral AAB was the gelation of the electrolyte, which could be overcome with addition of NaF to the electrolyte and by crystallization with aluminum oxide powder [89]. Studies on seawater activated Al–air batteries with excess of electrolyte demonstrated cell discharge voltages of up to 1.0 V under 10 mA cm^{-2} resulting in a practical specific energy of 2,000 Wh kg$_{\mathrm{Al}}^{-1}$ and anode mass conversion efficiencies of 60–70% [96]. Later reintroduction of the neutral AABs in 2006 by Han et. al. showed a stable discharge voltage of ~1.1 V under ~1.8 mA cm^{-2} over 140 h, resulting in anode mass conversion efficiencies of 95.7% and specific energies of 1,540 Wh kg$_{\mathrm{Al}}^{-1}$ [97]. The work of Smoljko et. al. found the Al–0.1%In alloy as a good anode material candidate with coulombic efficiencies as high as 92–95.4% under anodic current densities in the range of 20–100 mA cm^{-2} and delivering −1.0 to −1.24 V_{SCE} [98]. Some of the most recent and relevant progress were done by Ma et. al. [99] and Wu et. al. [100], where Al–Mg–Ga–Sn–Mn and Al–Mg–Ga–Sn–In were used respectively. The work of Ma et al. showed cell discharge voltages of around 1.24 V under 20 mA cm^{-2}, $\eta_{\text{Al based}}$ of 85.3%, and specific energies of around 3,152 Wh kg_{Al}^{-1} [99], whereas the modified alloy of Wu et. al. could increase the cell discharge voltage to 1.3 V under 20 mA cm^{-2}, $\eta_{\text{Al based}}$ to 90.6% and the specific energy to 3,385 Wh kg_{Al}^{-1} [100]. Table 1-5 shows a summary of the progress on (near) neutral Al–air batteries with some of the most relevant parameters.

The current challenges of (near) neutral Al–air batteries involve the limited discharge voltage, mainly due to the high polarization and pitting of the anode. Further development of AABs is focusing on different alloys mixtures to improve the anodic behavior of Al and open circuit corrosion behavior [98–103], the impact of different microstructures of the aluminum electrodes [83,104], electrolyte additives for corrosion inhibition [105], or electrolyte additives for the “activation” of the Al [106].

Table 1-5: Summary on the progress of neutral Al–air batteries.

Cell Description	Current Density / mA cm^{-2}	Nominal Voltage / V	Specific Energy / Wh kg_{Al}^{-1}	$\eta_{Al\ based}$ / %	Ref.
Anode: Al alloy (In–Ga–Tl) Cathode: not specified Electrolyte: 2M NaCl	30 60	1 0.6	- -	- -	[89] [89]
Anode: Al 99.999% Cathode: Carbon based Electrolyte: Seawater (excess of electrolyte)	10	1.0	2,000	60–70	[96]
Anode: Al 99.999% Cathode: Carbon based Electrolyte: 3%NaCl (~0.5M)	10	0.4	1,000	-	[96]
Anode: Al alloy (Ga–In–Sn–Bi–Pb–Mn) Cathode: catalyst (not specified) on Ni–mesh Electrolyte: 3.5% NaCl (~0.5M)	~1.8	1.15	1,540	95.7	[97]
Anode: Al 5N (99.999%) Counter electrode: Pt (half–cell) Electrolyte: 2M NaCl	100	−0.61 (V_{SCE})	1,568^{a}	86.3	[98]
Anode: Al (99.8%) Counter electrode: Pt (half–cell) Electrolyte: 2M NaCl	100	−0.62 (V_{SCE})	1,564^{a}	84.7	[98]
Anode: Al–0.1 wt.% In Counter electrode: Pt (half–cell) Electrolyte: 2M NaCl	100	−1.0 (V_{SCE})	2,712^{a}	91.0	[98]
Anode: Al–0.2 wt.% Sn Counter electrode: Pt (half–cell) Electrolyte: 2M NaCl	100	−1.24 (V_{SCE})	2,830^{a}	76.6	[98]
Anode: Al–0.1 wt.% In–0.2 wt.% Sn Counter electrode: Pt (half–cell) Electrolyte: 2M NaCl	100	−1.2 (V_{SCE})	2943^{a}	82.3	[98]
Anode: pure Al Cathode: MnO_2/C Electrolyte: 2M NaCl	20	0.56	~1,370^{b}	81.4	[107]
Anode: Al–0.5 wt.% Mg–0.02 wt.% Ga–0.1 wt.% Sn–0.5 wt.% Mn Cathode: MnO_2/C Electrolyte: 2M NaCl	20	1.24	~3,152^{b}	85.3	[107]
Anode: Coarse–grained Al (several mm) Cathode: Ag powder/Ni mesh Electrolyte: 2M NaCl	10	0.40	~1,096^{b}	13.5	[83]
Anode: Al 1085 Cathode: MnO_2/C on Ni–mesh Electrolyte: 2M NaCl	1	0.7	441	21.1^{d}	[108]
Anode: Al 7475 Cathode: MnO_2/C on Ni–mesh Electrolyte: 2M NaCl	10	0.4	484	40.6^{d}	[108]
Anode: Al foil Cathode: MnO_2/CNT on C paper Electrolyte: 4M NaCl	1	0.6	1480	82.7^{d}	[109]
Anode: Al ink Cathode: MnO_2/CNT on paper Electrolyte: 4M NaCl	1	0.6–0.2	-	-	[109]
Anode: Al foil 98.2% (kitchen foil) Cathode: Carbon paper Electrolyte: 4M NaCl	1	0.5	~1445^{c}	97^{c}	[110]
Anode: Al foil Cathode: Pd/C on graphite foil Electrolyte: 2M NaCl	20	0.46	1010	73.7	[110]
Anode: Al–0.5 wt.% Mg–0.1 wt.% Sn–0.05 wt.% Ga–0.05 wt.% In Cathode: MnO_2/C catalyst Electrolyte: 2M NaCl	20 160	1.3 0.55	3,385.4 ~1625	90.6^{b} ~99.9	[100] [100]
Anode: Al–6.1 wt.% Mg–0.93 wt.% Zn–0.54 wt. %In–0.17 wt.% Mn (avg. grain size=4.87 µm) Counter electrode: Pt sheet (half–cell) Electrolyte: Artificial seawater (0.45M NaCl)	10 50	−1.53 (V_{SCE}) −1.28 (V_{SCE})	~2,516^{a} ~2,219^{a}	55.2 58.2	[104]

[a] assuming 0 V_{SCE} for the air electrode, [b] estimated from the practical specific capacity or $\eta_{Al\ based}$
[c] stack efficiency, [d] estimated form practical specific energy

1.3. Scope of the Thesis

Realizing the promising prospective of the MABs, the current thesis presents some possible applications under the current status of development of the MABs and diverse strategies to improve their performance are attempted. Alkaline Si–air batteries and (near)–neutral Zn–air batteries are considered within the framework of these studies.

In Chapter 2, a possible practical application of alkaline Si–air batteries for low–power electronics is explored. The development of a printed circuit board (PCB) coupled to the current performance of the alkaline silicon–air battery is presented, and additionally the concept for self–destructing devices is proposed. A custom–made cell casing for the evaluation of integrated PCB/Si–air battery is also introduced.

Considering the general issues such as corrosion, passivation, and limited potentials of the anodes in metal–air batteries, hereby a Zn–Al alloy is proposed as an anode material to improve such aspects. The understanding of the metal galvanic coupling of an alloy and the resulting mixed potential can lead to new approaches on how to improve the electrochemical performance of metal–air batteries. Therefore, a comprehensive and systematic electrochemical and morphological evaluation of Zn–Al alloys in neutral NaCl solutions is presented.

A further possibility is the modification of the electrolyte and addition of chemical compounds to prevent the passivation of the metals, thus possibly enabling higher discharge potentials. In this regard, the addition of the chelating agent EDTA, which could successfully prevent the formation of the passivation film, was investigated in the near–neutral Zn–air battery (at pH 10). Additional chelating additives for near–neutral ZABs are also proposed.

Chapter 3 presents the practical application of alkaline Si–air batteries and coupling to a personalized PCB in a custom–made cell casing. The characterization and evaluation of Zn–Al alloys in neutral solutions are explored in chapter 4. Chapter 5 further explores the addition of chelating additives in the near–neutral electrolyte and its effects on the potential of Zn anodes, including the discharge and cycling evaluation of Zn–air cells.

Chapter 2: Common Analysis and Characterization Techniques in Metal–Air Battery Research

The processes occurring in the metal–air batteries arise from several physical and chemical conditions; thus, the analysis and characterization of batteries often involves a multidisciplinary approach to complement the limitations of some techniques with the help of more specific ones. The current section aims to be a general introduction on some basics of electrochemistry, characterization, and analysis techniques, as well as basics of chelation are presented in the Appendix 6 "Visualization of solvation, complexation, and precipitation". Within the present work, most of the aqueous solution concentrations will be referred as mol L^{-1}, or M for simplicity.

2.1. Gravimetric Techniques

One simple but still helpful technique is the gravimetric, which basically consists in measuring the mass of the electrode before and after a certain experiment [20]. By controlling the area and time of exposure, weight change rates (Δw) can be determined, as dictated by the following formula:

$$\Delta w = \frac{w_i - w_f}{t \times A} \qquad \textbf{2.1}$$

where w_i is the initial weight, w_f is the final weight, t is the time of the experiment and A is the exposed area. Depending on the conditions of the experiment, weight loss (positive Δw values) or weight gain (negative Δw values) may occur, which directly deliver information on the nature of the system. Weight loss can indicate dissolution of the sample (or corrosion), while weight gain can hint the adsorption or redeposition of the reaction species. If the density of the corroded material is known (or the approximated composition and density of adsorbed layers), the weight change rate can be converted into penetration rate (or growth rate), as expressed by the following formula:

$$R = \frac{\Delta w \cdot k}{t \cdot \rho_M \cdot A} \qquad \textbf{2.2}$$

where R is the penetration rate in μm h^{-1}, Δw is the weight change rate in mg h^{-1}, k is a conversion factor (10^4 μm cm^{-1}), ρ_M is the density of the material (in mg cm^{-3}) and A is the geometrical exposed area of the sample (in cm^2).

2.1.1. Electrochemical Characterization: Techniques and Terminology

Despite its usefulness, gravimetric techniques include the chemical and electrochemical processes, making difficult the differentiation of the electrochemical characteristics. Hence, potential polarization or galvanostatic techniques (among others) are commonly used. With the intention to understand these techniques, some basic concepts and principles will be hereby presented.

Standard electrode potential

Upon immersion of a metal in an electrolyte, a double layer is consequently formed. According to Helmholtz [111], the double layer is composed of positive ions from the metal and negative ions from the electrolyte. The formation of the double layer produces a "tension", properly defined as the electromotive force by Nernst in 1889 [112]. The electromotive force drives the reaction in the spontaneous direction, meaning from a high energy to a low energy state. This process is described by the half–cell reaction and its corresponding "tension", which is referenced by convention to the standard reaction of the reversible hydrogen evolution:

$$2H^{+}_{(aq)} + 2e^{-} \longrightarrow H_{2(g)} \qquad \textbf{2.3}$$

with a standard electrode potential value of $E^{\circ} = 0$ V at 25°C and 1 atm [20]. The "tension" of the half–cell reaction of the metal is referred as a potential. Extensive lists of the standard electrode potentials can be easily found in the literature and provide of useful information about the "reactivity" of a metal in an aqueous system [20,113]. Elements with more negative E^0 values are therefore more reactive (less noble) than those with more positive E^0 values (more noble). In the practice, the half–cell reactions are measured with a reference electrode. The reference electrodes are in principle also half–cells typically composed of a reversible metal, a salt of the metal and an electrolyte in equilibrium, meaning that its potential is constant since the reaction is reversible [20]. The reference electrodes used in this dissertation are silver/silver chloride (Ag/AgCl, expressed in units $V_{Ag/AgCl}$) and mercury/mercury oxide (Hg/HgO, expressed in units $V_{Hg/HgO}$). A table with the standard potentials for selected materials can be found in Table A–1.

A "three–electrode setup" composed by a metal to be analyzed (working electrode), a reference electrode, and a counter electrode like Pt is commonly employed for the study of the metal anodes in metal–air batteries, since it helps to differentiate the anodic and cathodic reactions and their contribution. If the reference electrode is removed and the counter electrode is replaced by a material allowing spontaneous cathodic reactions, a galvanic cell (also called full–cell) is formed. The voltage of a full–cell is derived from the absolute difference of half–cell reactions of the anode and the cathode as follows [114,115]:

$$E^0_{cell} = E^0_{cathode} - E^0_{anode} \tag{2.4}$$

Thus, the theoretical voltages of the metal–air batteries can be calculated according to Equation 2.4 and the values given by Table A–1.

Open Circuit Potential/Voltage

The condition where no current flows in the system is called open circuit potential (OCP) for the half–cells and open circuit voltage (OCV) for full–cells. The OCP/OCV is originated from the equilibrium of the oxidation and reduction reactions taking place at the surface of the electrodes. The OCP/OCV may or may not correspond to the theoretical standard potential or theoretical voltage depending on side reactions occurring at the electrodes/electrolyte interface. Hereafter the description of the electrochemical techniques focusses more on the half–cell setup.

Potentiodynamic Polarization

The potentiodynamic polarization (PoP) technique consist of a continuous change on the potential and measurement of the current response, which can be correlated to the cathodic and anodic electrochemical reactions of the half–cell. A typical potentiodynamic polarization typically starts scanning the potential with a constant rate at cathodic potentials to the OCP and continues towards more anodic potentials than the OCP. By starting at cathodic potentials, the potentiodynamic avoids excessive alteration of the working electrode by its oxidation (and possible corrosion) which could occur if the potential scan were started at anodic potentials. The potential and current of the investigated half–cell are usually controlled and monitored with a potentiostat. The whole setup of a typical electrochemical experiment is shown in Figure 2.1.

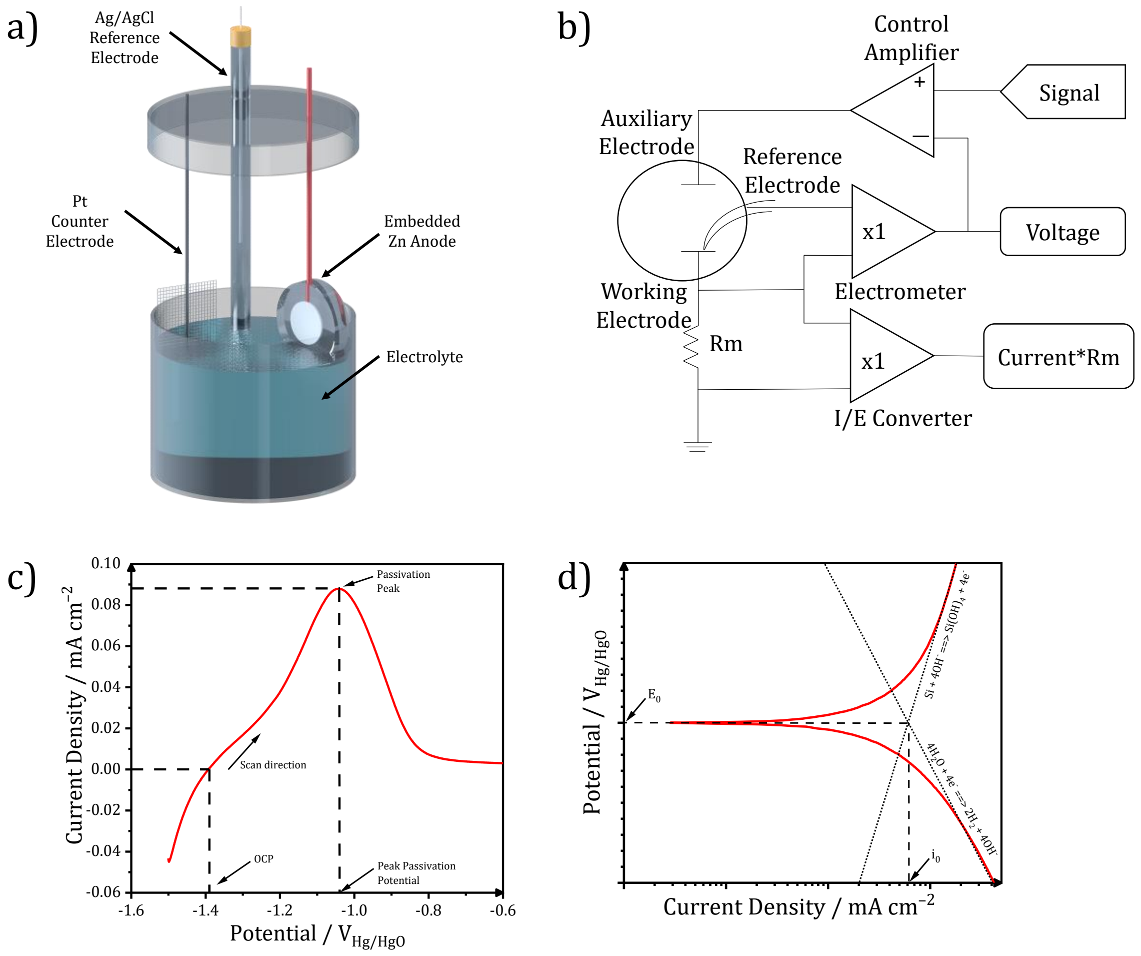

Figure 2.1 a) Typical “three–electrode setup” or half–cell used in electrochemical experiments, b) schematic of the operation of a potentiostat, c) typical voltage/current curve resulting after a potentiodynamic polarization of Si in 5M KOH, and d) Tafel arrangement of the potentiodynamic polarization of c). Diagram from b) reproduced after [116].

Figure 2.1a shows the typical three–electrode setup used in this work. Figure 2.1b shows the diagram of the operation of a potentiostat, where a signal (set of conditions given by the operator) is sent to the control amplifier unit and controls the potential of the auxiliary electrode [116]. Consequently, the working electrode responses to the change in the system induced by the auxiliary electrode, which is sensed by the reference electrode as a potential change and compared to the control amplifier and the working electrode signal at the electrometer. The latter loop delivers a voltage which is then continuously stored by a computer. Additionally, a series of adaptable resistances (represented as Rm in Figure 2.1b) can calculate the electrical current response by the current–to–voltage (I/E) converter and the signal is also sent to the electrometer for necessary adjustments at the auxiliary electrode. Figure 2.1c shows an example of the voltage/current curve resulting from a potentiodynamic polarization and some of the main characteristics, namely the OCP and the peak passivation current/potential of a Si As(100) sample in 5M KOH. The negative currents belong to the cathodic reactions and the positive currents are assigned to the anodic reactions at the working electrode surface. Figure 2.1d depicts the area close to the OCP (also called "Tafel region") of Figure 2.1c in the Tafel plot format ($\log|j_0|$ vs. E), where some linearity can be observed. The PoP curve of Figure 2.1d presents a cathodic and anodic slope, which can assist in the calculation of the corrosion current (j_0) and corrosion potential (E_0). The E_0 might have similar values as the OCP, but it can also be affected by the initial cathodic polarization, because of local changes in the pH value, reduction or removal of oxide layers, among other factors.

The interpretation of the potentiodynamic, potentiostatic and galvanostatic techniques relies on assessing the reactions taking place at the electrode surface under a set of conditions, which is also known as electrode reaction kinetics [20]. A further description of the working principle of the potentiodynamic polarization and the governing equations also used for the fitting of the PoP curve is included in the section "Polarization Principles and Analysis of Potentiodynamic Polarization Curves". Focusing on the anodic currents of a potentiodynamic polarization curve, several shapes and behaviors may be observed depending on the working electrode material, morphology, type of electrolyte, temperature, pH, stir conditions, etc.. For example, the anodic behavior of Figure 2.1c presents the typical shape of the passivation of Si in 5M KOH, revealed by the decrease if the current density at more anodic potentials than $-1.05\ V_{Hg/HgO}$ (ohmic polarization by the formation of SiO_2 at the electrode surface). This dissertation will concentrate only on three types of characteristics in PoP curves: active dissolution, passivation, and pitting.

Figure 2.2 illustrates in a simplified form the active dissolution, passivation, and pitting, as well as a possible path how the three phenomena are interconnected. Figure 2.2a shows a metal entering in contact with an electrolyte (t_0), whereas Figure 2.2b depicts the moment when the metal starts spontaneously dissolving into the electrolyte (t_{0+1}). Figure 2.2c depicts the metal forming oxide or hydroxide salts due to the aqueous nature of the electrolyte (t_{0+2}), while some of them may stay as adsorbed species at the metal surface (molecules I, III, IV and VII in Figure 2.2c), or as dissolved species (II and VII in Figure 2.2c). Moreover, some of the adsorbed species may undergo deprotonation and lose their hydrogen atoms if some current is locally exchanged (molecules I and III in Figure 2.2c), resulting in hydrogen evolution (molecule V in Figure 2.2c). The molecules VII in Figure 2.2c present a special case, where a single oxygen atom may bind to two superficial atoms of the metal matrix, thus becoming thermodynamically very stable and difficult to dissolve.

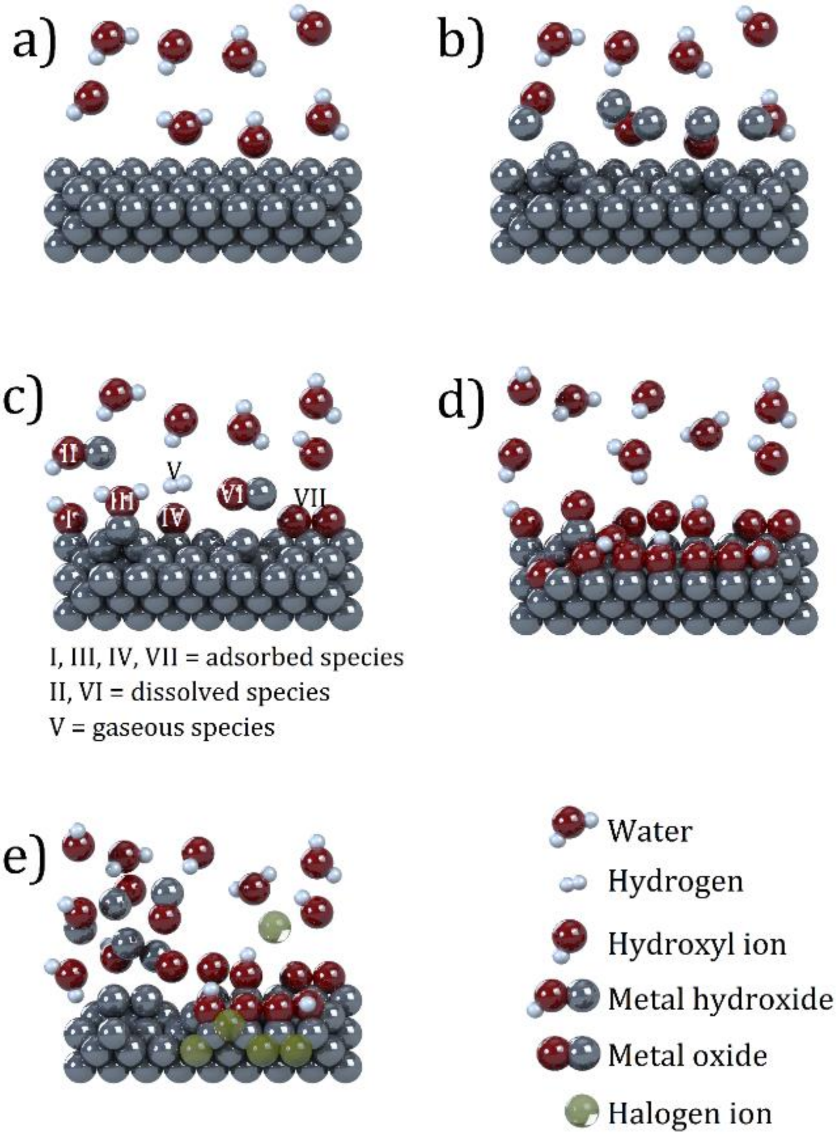

Figure 2.2 Scheme of the general passivation process of a metal. a) Initial state of the metal surface before oxidation. b) The metal starts reacting, dissolving, and oxidizing (spontaneously or induced). c) Depending on local conditions of the aqueous electrolyte, adsorbed, dissolved or gaseous species may form. d) The surface of the metal starts passivating due to the formation of an oxide/hydroxide layer coming from precipitated or adsorbed species. e) The metal surface may become reactive again if the passive layer (partially) dissolves or if halogen species are present (pitting).

Independently of the specie formed, if the solubility saturation is reached (t_{0+3}), the oxide/hydroxide molecules start precipitating and block the electrode surface (Figure 2.2d). In addition, the previously adsorbed oxide/hydroxide species at the electrode surface can boost the blockage of the electrode, resulting in an eventual mono– or multi–layer with passivating characteristics. Effects of such a passivation layer can be observed during the ohmic polarization of Figure 2.1c (described in this case as a passivation peak.), limiting the increase on the current density as the potential becomes more anodic. Depending on the nature of the electrolyte and its interaction with the electrode, the passivation layer may increase in thickness and manifest as an even sharper decrease of the current density at more anodic potentials. Nevertheless, if the passivation layer breaks down or by some means dissolves, a new layer of neat metal is exposed to the electrolyte (t_{0+4}), where active dissolution and/or re–passivation may restart (Figure 2.2e). Moreover, certain ions are able to penetrate and/or break down passive films and continue with the oxidation of the metals by the so–called pitting mechanism, as in the case of the halogens (yellow spheres in Figure 2.2e). The pitting effect on a potentiodynamic polarization curve are revealed by a sharp increase in the anodic current densities and the potential where it starts is called pitting potential [20,56]. The rapid increase on the current densities is due to the harsh reaction promoted by the halogen ions and the passivation layer is continuously formed and broken down.

Cyclic Voltammetry

The PoP and cyclic voltammetry (CV) are similar since the potential is shifted at a specific scan rate for both techniques. The difference relies on the starting potential of the CV, which typically is at OCP conditions and scans towards anodic potentials until a defined potential (vertex) and the scan is then reversed towards a second vertex at cathodic potentials. The scan can be cycled many times in order to observe the development of redox reactions. Some of the applications of the cyclic voltammetry in the electrochemical assessment of metals include: (1) the different oxidation peaks of polyvalent elements, (2) passivation currents and potentials, (3) the reduction characteristics of the oxidized species during the anodic scan, (4) the reduction/oxidation characteristics of the additives in the electrolyte and/or electrodes, (5) hydrogen evolution, (6) electrode kinetics and estimation of the symmetry coefficient α, among several more. CVs are typically depicted in the form potential versus current density (E vs. j), as in Figure 2.1c.

Potentiostatic and galvanostatic techniques

Having explored the effects of the polarization on the electrode in the dynamic state as for the PoP and CV techniques, the potentiostatic and galvanostatic techniques look at the "mid– and long–term" effects of the polarization. More explicitly, the potentiostatic polarization increases the selectivity for a specific reaction by applying a constant potential and the current response is simultaneously recorded. The galvanostatic polarization is more commonly employed for the investigation of the discharge, charge or cycling behavior since it emulates practical DC conditions. Hence, an anodic current is applied during the discharge and a cathodic current is used during the charge of a cell. If the electrochemical characteristics of the galvanostatic discharge (potential/voltage and current) are combined with the measurement of mass loss of the samples, useful information such as mass conversion efficiency, practical specific capacity and practical specific energy can be estimated.

2.1.2. Surface characterization

The surface characterization techniques and their working principles are an extensive and complicated topic on itself. For the purpose of this dissertation, only a brief and simple description of the techniques is presented.

The Laser Scanning Microscope (LSM) delivers a 3D reconstruction of the surface, allowing the non–destructive measurement of surface morphologies with an accuracy resolution of up to 10 nm [117]. A laser emitting diode irradiates the surface at a given distance, and an intensity image is captured by a sensor on the microscope. The latter process is repeated several times within a given range, creating a multilayer image, which is integrated into a single 3D picture. The intensity images can be converted into height units within the operating software. Characteristics such as the surface roughness or metal phases are qualitatively and quantitatively easy and quick to estimate.

The X–Ray Diffractometry (XRD) technique consist on the irradiation of a sample surface with an X–Ray beam at different angles [118]. The interaction of the different crystal orientations of the sample with the beam result in different intensities of the diffraction measured with a detector, which results in a series of intensity peaks at different angles. Every (powder) chemical compound and/or solid material (including metals) produce a distinctive spectrogram, which assist in the characterization of materials. The XRD is limited only to the surface of the materials since the X–ray beam cannot penetrate deep into the sample.

The Scanning Electron Microscopy (SEM) technique can overcome the limitations of conventional optical microscopes since the SEM uses focused electron beams instead of light waves to produce images, which results in an increase of the resolution as high as 1–2 nm in high–vacuum conditions [119]. In combination with the SEM, the energy–dispersive X–ray spectroscopy (EDS) can provide information about the chemical composition of the sample surface correlated to the SEM image [119]. The principle for the detection and identification of the elements by EDS is as follows:

1. One of the outer shell electrons (at the "surface") of an atom is excited by the electron beam, designated as e_1.
2. The transition of e_1 to a higher energy level and consequently relaxation produces an X–ray with a defined energy (or wavelength). This wavelength represents the difference between the excited and relaxed state.
3. The wavelengths are specific for each element, which allows its identification.

In comparison to the XRD, the EDS is more accurate on characterizing the local composition of a sample.

The Atomic Force Microscopy (AFM) is an imaging technique with accuracies as high as fractions of nm. In simpler terms, it allows to measure a sample by "touching" the surface with a very fine tip of a cantilever [120]. The displacement of the cantilever can be measured by several methods, one of which is the deflection of a photodiode beam irradiated at the cantilever. The latter is then measured by a detector and the signal is recorded by a computer, delivering topographical and mechanical information at the atomistic level. Additionally, the conductive AFM (c–AFM) allows the mapping of the conductivity of the sample surface.

2.1.3. Electrolyte characterization techniques

The conductivity and the pH of a solution can reveal discrete changes of the electrolyte, resulting in or from larger alterations of the metal/electrolyte interfaces. The conductivity of a solution is also known as ionic conductivity (usually expressed in $\mathrm{mS\,cm^{-1}}$) and describes the mobility degree of the ions in a solution. Generally speaking, electrolytes with high ionic conductivity ease the movement of the ions and thus such solutions are preferred for metal–air batteries [23,48]. Changes on the conductivity of an electrolyte during or after an experiment may be affected by several factors, such as higher concentration of dissolved species and evaporation. Conversely, the pH of a solution indicates the acidity, neutrality or alkalinity, which is defined by the concentrations of free H^+ or OH^- ions in the solution [115]. The pH of a solution can have a high impact on the behavior of a metal, such as its solubility and potential [20,121]. Thus, monitoring or adjusting the pH of the electrolytes critically influences the performance evaluation and application of metal–air batteries.

Another useful technique used in the analysis of the electrolytes is the inductively coupled plasma optical emission spectrometry (ICP–OES), which can detect the presence and concentration of metals in a solution [122]. For the analysis, a gas is ionized by induction to form a plasma and the nebulized electrolyte is fed into the plasma. The electrolyte is also ionized and emits light in certain wavelengths, which are quantified and qualified by a detector. The spectra generated by the excited electrolyte plasma can be analyzed and the concentration of the present metals can be determined.

Chapter 3: Practical Application of Alkaline Silicon–Air Batteries

The present chapter describes the concept idea of a Si–air battery with circuit elements powering a low–consumption LED directly mounted on the back side. Different substrates and conductive routing materials are proposed. The proposed configuration is compared to conventional printed circuit boards. The content of this section will be submitted for publication.

3.1. Motivation

Since the invention by the group led by Ein–Eli [43], silicon–air batteries are gaining more attention in the research field due to its relatively high theoretical specific capacity of 3,820 mAh g_{Si}^{-1} and high specific energy of 8,461 Wh kg_{Si}^{-1} [17,45,48,123]. Moreover, silicon is the second most abundant element on earth's crust, whilst its low cost and non–toxicity make it an appealing active material for MABs [41,42].

Specifically, alkaline Si–air batteries typically use KOH solutions as electrolytes and produce energy by the oxidation of the silicon anode and reduction of O_2 at the air cathode, as described by the equations 1.6, 1.7, and 1.11 [41]. Moreover, alkaline Si–air batteries present two major challenges: the high corrosion rate even under no load (OCV conditions) and the passivation of the surface under discharge current densities larger than ~90 µA cm^{-2}. The so called passivation peak in alkaline solutions is also observed in half–cell experiments at around −1.05 $V_{Hg/HgO}$ [41,48]. The corresponding corrosion and passivation reactions are described by equations 1.9 and 1.10. In addition, Si–air batteries with $EMIm(HF)_{2.3}F$ as electrolyte have shown better performances than their alkaline counterparts, where discharge current densities as high as 500 µA cm^{-2} can be applied resulting in stable discharge profiles [44,45]. The mass conversion efficiencies can be as high as >50% and over 1600 Wh kg_{Si}^{-1} specific energies [44,45]. The main reactions governing the non–aqueous Si–air batteries are presented in equations 1.2, 1.3, 1.4, and 1.5. The downsides of ionic liquid electrolytes are, however, their relative high toxicity and production price.

Even with the above mentioned limitations, the current performance of Si–air batteries in 5M KOH is of over 1100 h of discharge under 50 µA cm^{-2} and with a stable continuous voltage of 1.2 V [41]. On the other hand, non–aqueous Si–air batteries have shown voltages around 1.0 V under 100 μA cm^{-2} after 200 h of continuous discharge [45].

Yet, state of the art silicon–air batteries may be applied to low–power consumption devices and as a proof of concept, a dedicated circuit design can be coupled to the characteristics of the Si–air battery and directly mounted on the back side of the silicon anode. Moreover, there is no such practical integration of the Si–air batteries publicly reported up–to–date, but the idea has been presented by the Vanishing Programmable Resources Program (VPR) of the Defense Advanced Research Projects Agency (DARPA) of the USA Government as a self–disappearing device by utilizing room temperature ionic liquid $EMIm(HF)_{2.3}F$ [124].

For the illustration purposes of this idea, low power consumption, high efficiency Light Emission Diodes (LED) and simple data storage elements (EEPROM) can be integrated in the circuit. Furthermore, a custom–made case for the battery is required to contain the electrolyte and allow the complete dissolution of the silicon anode and destruction of the circuit. The current section presents, therefore, the proof of concept of a circuit coupled and mounted on a Si–air battery and its performance is evaluated.

3.2. Experimental Section

Materials and chemicals: Wafers of single crystalline Si doped with As <100> (0.001–0.007 Ωcm) were acquired from University Wafer and cut into 24 x 24 mm^2 square pieces. The Si wafers were treated by a two–step plasma process (PICO, Diener) prior to the experiments. The first step consisted of removal of organic contamination by Ar/O_2 plasma while the second step involved Ar/SF_6 to remove any oxide layer on the Si wafers. The freshly treated wafers were kept in an Ar atmosphere and directly used for the assembling of the battery. KOH pellets (≥85% KOH basis, Sigma–Aldrich) and deionized water (PURELAB Elga, conductivity ≥0.1μS/cm) were used for the preparation of 5M KOH electrolyte. The KOH solutions were purged with argon to reduce the dissolved oxygen. The $EMIm(HF)_{2.3}F$ ionic liquid was acquired from Morita Chemical Industries and was directly employed as electrolyte. The mass of the silicon anodes was measured by an analytical balance with an accuracy of ±0.01 mg (XA205, Mettler Toledo). The carbon–based air cathodes with manganese oxide catalyst (E4 type) were purchased from Electric Fuel Ltd.

Battery casing design: The cell consisted of 3 pieces of Poly(methyl methacrylate) (PMMA) and a 3D–rendered picture is displayed in Figure 3.1. The cell anode side was conceived to provide space to the circuit elements and the silicon anode. The extra space could safely retain the electrolyte once the silicon anode was depleted, allowing the complete dissolution of the silicon anode and the circuit itself. Additionally, a window on the cell anode side was installed to monitor the state of the circuit and the LED. The middle part provides containment for 3 mL of electrolyte and a surface area of 2.8 cm^2 for both, anode and cathode. Custom–cut EPDM flat gasket was used to seal the anode/circuit and the cathode. The cell cathode side provides support and an opening for the air cathode with a diameter of 19 mm.

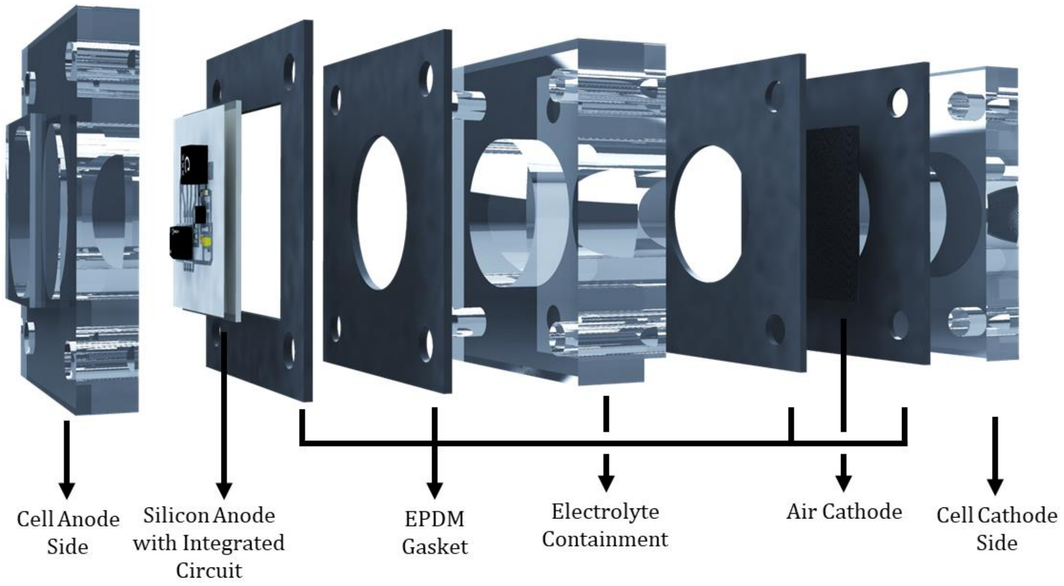

Figure 3.1: Assembly of the PCB/Si–air battery with the casing.

Circuit design: The circuit development was performed with a close collaboration to Christian Roth from the Central Institute of Engineering, Electronics and Analytics – Electronic Systems (ZEA–2) at Forschungszentrum Jülich. The detailed diagram of the circuit is depicted in Figure 3.2a and the description of the components is presented in Table 3-1. The selected LED was a 2–pin SMD (0603) low power consumption TLMS1000–GS08 (minimum 40 mW and 1.8 V, Mouser Electronics). Since the Si–air battery delivers 1.2 V under $50\ \mu A\ cm^{-2}$ discharge current density [48], a DC–DC converter MAX17220ELT+T (400 mV to 5.5 V input range, 1.8 to 5 V output voltage range, Mouser Electronics) was selected to increase the voltage to V_{OUT}=2.18 V.

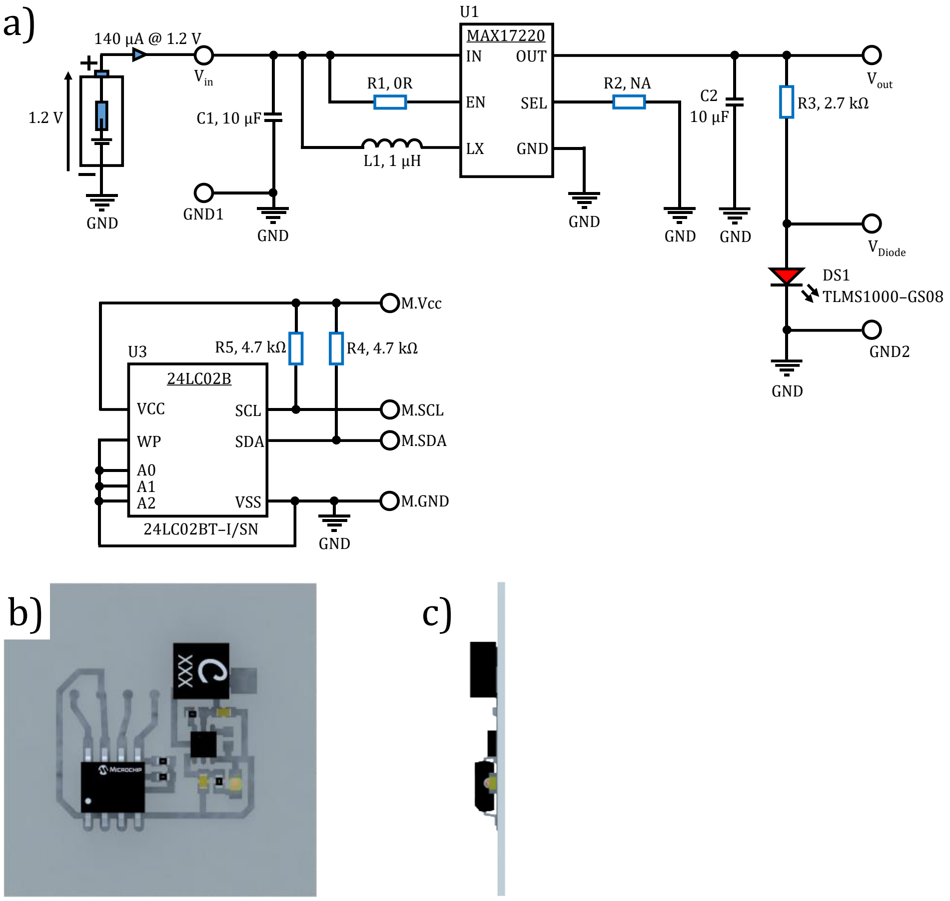

Figure 3.2: Design of the circuit: a) detailed diagram of the connection of the DC–DC converter for powering an LED with the supply characteristics of the Si–air battery (140 µA@1.2 V), also including the EEPROM, b) 3D representation of the mounted circuit on the back side of the silicon anode, and c) side view of b).

The quiescent and leak currents were calculated according to the following equation found in the data sheet of the DC–DC converter [125]:

$$I_{\mathrm{Q\,TOTAL\,SYSTEM}} = I_{\mathrm{Q\,IN\,TOTAL}} + \frac{I_{\mathrm{Q\,OUT}}}{\eta \times \frac{V_{\mathrm{IN}}}{V_{\mathrm{OUT}}}} \qquad \mathbf{3.1}$$

Assuming the default values given by the data sheet of $I_{\mathrm{Q\,IN\,TOTAL}}$=0.5 nA, $I_{\mathrm{Q\,OUT}}$=300 nA, and η=0.85 according to the efficiency vs. load current graph of the voltage booster's data sheet read at V_{IN}=1.2 V and 140 µA. The resulting $I_{\mathrm{Q\,TOTAL\,SYSTEM}}$=641.67 nA and the absolute current output (I_{OUT}) is calculated to be around 139.35 µA. Accordingly, R3 of Figure 3.2a is calculated as:

$$R_3 = \frac{V_{\mathrm{OUT}} - V_{\mathrm{LOAD}}}{I_{\mathrm{OUT}}} = \frac{2.18\ \mathrm{V} - 1.8\ \mathrm{V}}{139.35\ \mu\mathrm{A}} = 2.7\ \mathrm{k\Omega} \qquad \mathbf{3.2}$$

Commercially available printed circuit boards (PCBs) were initially employed as substrate for the evaluation of the circuit. The assembly of the PCB was kindly conducted by Christian Roth. In addition, different insulating substrate materials were assessed, which also could allow the complete dissolution in both of the electrolytes, KOH and EMIm(HF)$_{2.3}$F. The selected substrates included polyvinyl alcohol (PVA), cellulose acetate (CA), and grown SiO_2 (ca. 330 nm in thickness). The PVA and CA were directly applied by drop casting solutions of the polymers on the back side of the anode and left to dry until a thin film formed. The Si wafers with grown SiO_2 were kindly provided by Dr. Jürgen Moers from the Helmholtz Nano Facility (HNF) of Forschungszentrum Jülich.

Silver ink was evaluated as the material for the conducting path of the circuit, while a stencil was used as a mask to apply the conductive routing on the different insulating substrates. The circuit elements were mounted and fixed with the conductive ink as illustrated in Figure 3.2b–c.

Table 3-1 List of components for the PCB coupled to the Si–air battery.

Designator	Comment	Quantity	Description
C1	10 µF	2	Capacitor SMD 1005 0402 2–10 µF
C2			Capacitor SMD 1005 0402 2–10 µF
DS1	TLMS1000–GS08	1	Low Current LED, 40 mW, 1.8 V, −40 to 100°C, 2–Pin SMD (0603), RoHS, Tape and Reel
L1	1 µH	1	XFL4020–102MEC Shielded Power Inductor, 1 µH, 64 MHz, −40 to 125°C, 2–Pin SMD, RoHS, Tape and Reel
R1	1 kΩ	5	Resistor SMD 1005 0402 1/16 W
R2	N/A		NA = 1.8 V
R3	2.7 kΩ		Resistor SMD 1005 0402 1/16 W
R4	4.7 kΩ		Resistor SMD 1005 0402 1/16 W
R5	4.7 kΩ		Resistor SMD 1005 0402 1/16 W
U1	MAX17220ELT+T	1	IC REG BOOST ADJ 225MA 6UDFN
U3	EEPROM	1	24LC02B–I/SN 256x8–1.8 V

An EEPROM (24LC02B–I/SN, 256x8 – 1.8 V, Mouser Electronics) was included to program and store data programmed by Matlab via the test points M.Vcc, M.GND, M.SCL, and M.SDA. The only data stored in the EEPROM “Hello world!” was coded as follows

```
clear all; close all; clc;
i2cInfo=instrhwinfo (‘i2c’, ‘ni845x’);
disp(i2cInfo);
eeprom=i2c (‘ni845x’, 0, ‘50h’);
fopen (eeprom);


fwrite (eeprom, [‘Hello Wo’]);
pause (0.1);
fwrite (eeprom, [‘rld! ’]);

pause(0.1);
fwrite (eeprom, 0)
```

Subsequent to the flooding of the PCB with the electrolyte, the status of the EEPROM was tested via the test points M.Vcc, M.GND, M.SCL, and M.SDA with the following code lines:

```
char (fread(eeprom, 256));

fclose (eeprom)
clear (eeprom)
```

Since the integrated circuits (IC) of an EEPROM are encapsulated in a chemical resistant epoxy, decapsulation of the IC needed to be done according to procedures found on the web [126]. In this way, the silicon–based die of the IC could be easily reachable to the electrolytes once the silicon anode was consumed, also allowing the dissolution of the IC.

Characterization methods: The experiments were carried out in a climate chamber (Binder KMF115) to ensure controlled conditions of 25°C and 50% relative humidity. The condition of the silicon anodes with mounted circuit prior and after the experiments was analyzed by using a confocal laser scanning microscope (OLS4100, Olympus Corp., Japan). The voltage of the cell was continuously monitored by a potentiostat (Biologic VMP3), whilst the current was measured via a zero–resistance ammeter (ZRA) mode of the potentiostat with a parallel channel.

3.3. Experimental Results and Discussion

To confirm the compatibility of the designed circuit and characteristics provided by the customized cell casing, the amperometry of the circuit is presented in Figure 3.3.

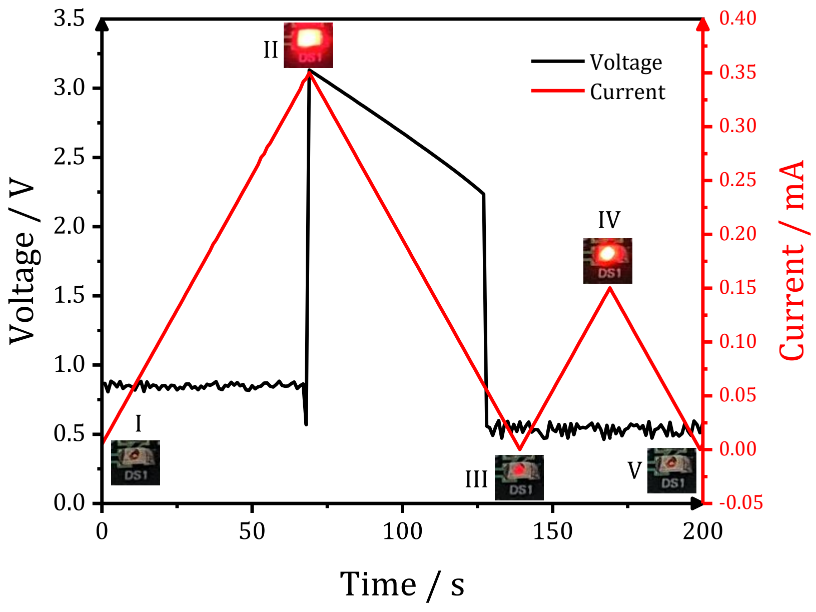

Figure 3.3: I–V curves of the customized PCB by amperometry with a scan rate of 5 μA s^{-1} (the insets depict the illumination status of the LED).

The amperometry of the circuit revealed that an input of around 350 μA and ~3.25 V are necessary at least for a short time to activate the DC/DC converter and light up the LED (inset II in Figure 3.3). Upon the reverse scan and even after reaching currents close to 0 μA, the LED was still emitting dimmed light (inset III in Figure 3.3). The circuit was also activated during the second forward scan as demonstrated by the illuminated LED (inset IV in Figure 3.3), requiring relatively low currents and voltages (150 μA and 0.5 V, respectively).

Figure 3.4 shows the cyclic voltammetry of the Si–air battery with KOH and EMIm(HF)$_{2.3}$F. The CV of the alkaline Si–air battery in Figure 3.4a displays currents around 100 μA at 1.15 V, 130 μA at 1.1 V, and 175 μA at 1.05 V without showing any passivation characteristics after two consecutive cycles. Similarly, the CV of the non–aqueous Si–air battery in Figure 3.4b shows currents as high as 1.01 mA at 1.15 V, 1.22 mA at 1.1 V, and 1.79 mA at 1.05 V during the first cycle, whilst the second cycle presents 0.87 mA at 1.15 V, 1.05 mA at 1.1 V, and 1.52 mA at 1.05 V. The provided currents by both, the alkaline and non–aqueous Si–air batteries, are high enough to activate the DC/DC converter and ignite the LED without passivation of the silicon anode. The electrochemical behavior of both types of Si–air batteries is in good agreement with previous reports [41,44]. The slight decrease on the observed currents delivered by the non–aqueous Si–air battery are practically negligible, as the power consumption of the LED is consistently very low.

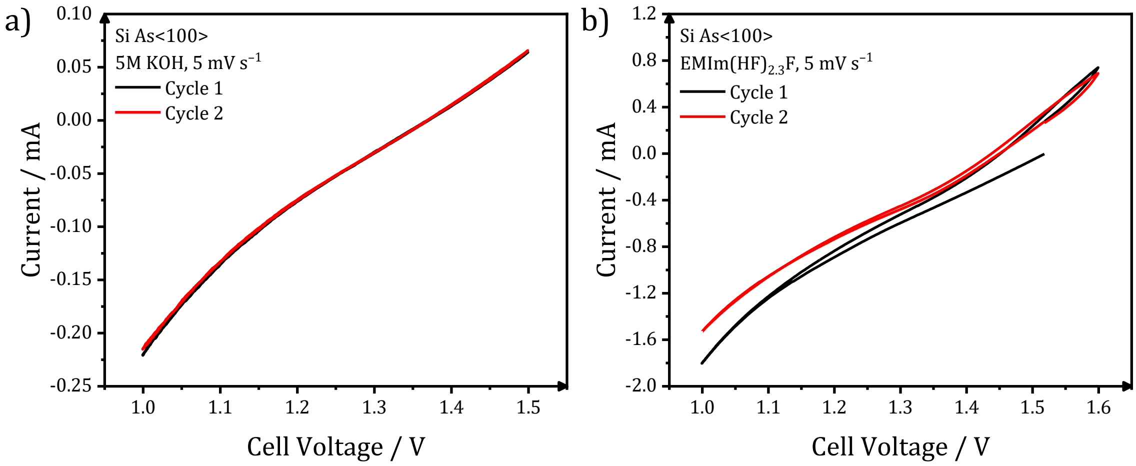

Figure 3.4: Cyclic voltammetry curves of the Si–air battery with a) 5M KOH and b) EMIm(HF)$_{2.3}$F, displaying the absolute current.

Figure 3.5 shows the Si–air battery with the mounted circuit assembly during operation and the voltage/current profiles of the alkaline and non–aqueous Si–air batteries. Figure

3.5b shows the average cell voltage of the alkaline Si–air battery relatively stable at around 1.1 V, whilst the lightning of the LED lasted for around 220 h. The absolute current was around 139 µA which corresponds to a current density of approximately 49.6 µA cm^{-2}. The passivation of the silicon anode in alkaline media can successfully be avoided if the voltage is above 1 V and current densities smaller than 100 µA cm^{-2} are applied [41,48]. The present cell setup prevents the passivation while the full consumption of the active area of the silicon anode is achieved by providing sufficient surface area of the anode and enough electrolyte volume. The observed voltage of ~0.6 V after the consumption of the active area of the silicon anode corresponds to the interaction between the few remaining Si parts still inside of the cell getting in contact with the KOH.

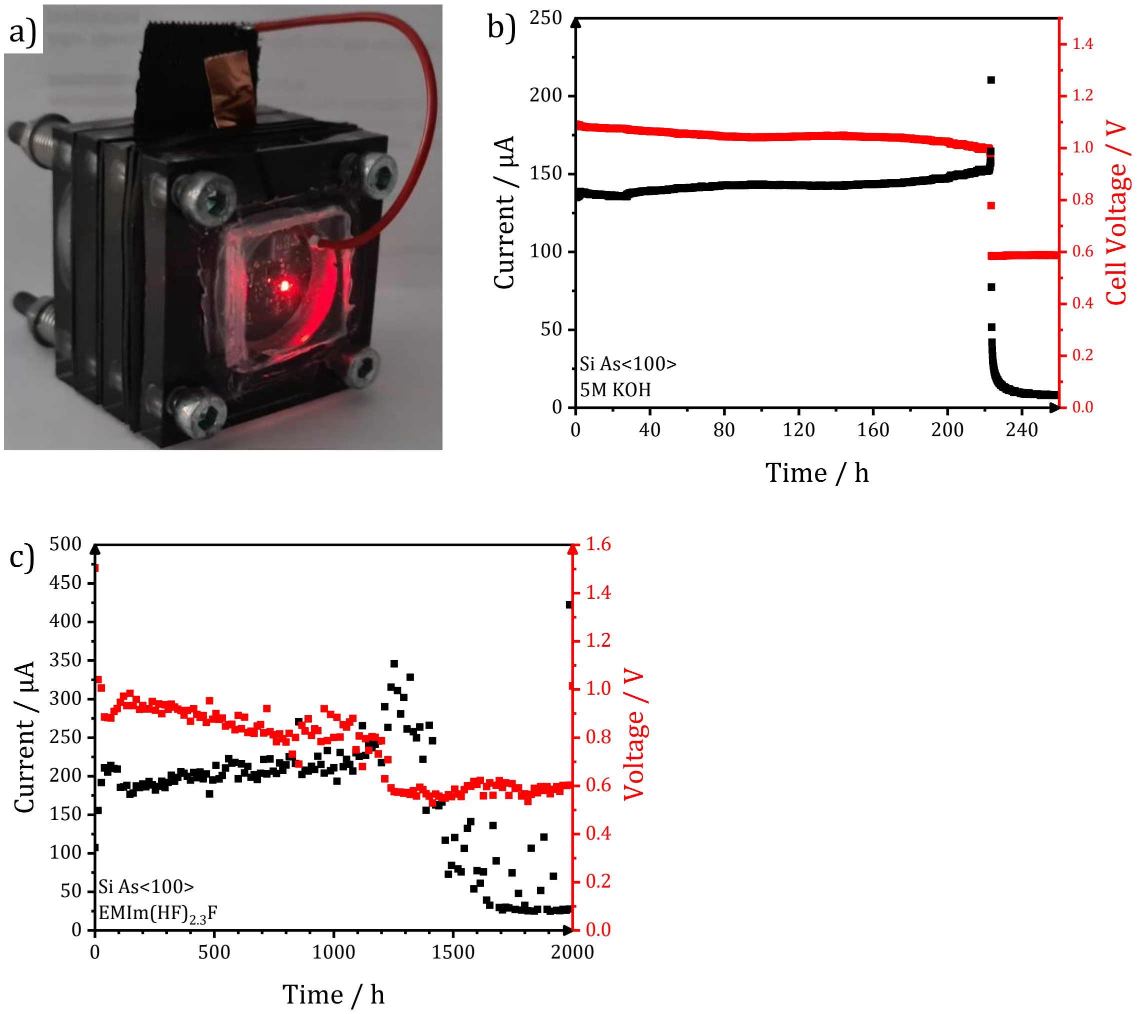

Figure 3.5: a) Running Si–air battery coupled to a PCB to power an LED, discharge and current profile of the Si–air battery with b) 5M KOH and c) EMIm(HF)$_{2.3}$F.

Figure 3.5c displays the open circuit voltage of the non–aqueous Si–air battery starting at around 1.54 V, which constantly decreases to 1 V over the first 17 h. The voltage drop continues less abruptly to values around 0.8 V over the 1200 h of discharge, after which a sharper decrease to approximately 0.6 V is again observed. Still, the discharge achieved a total of over 1982 h before full consumption of the Si wafer. Similar as for the alkaline Si–air battery, the 1 V observed after the stop of the cell discharge results from the contact of the remaining Si anode and the electrolyte. Analogously, the initial current drain of the non–aqueous Si–air battery starts at 100 μA, but continuously increases to over 200 μA during the first 30 h. As a consequence of the mentioned decreasing voltage, the current increases to values between 160 and 300 μA to keep a constant power output over the first 1200 h of discharge. Due the notorious decrease of the voltage after 1200 h, the current also increases again to a maximum of 350 μA, after which the current constantly declines to values close to 25 μA until the end of the discharge. The decreasing voltage observed for the non–aqueous Si–air battery is consistent with previous studies, where similar discharge current densities also resulted in constant declining voltages [44,45]. Moreover, the sharp changes on voltage and current after 1200 h could be attributed to the increased concentration of silicon in the electrolyte, which could result in a more sluggish electrochemical reaction. The collected electrolyte after the end of the experiment was notoriously more viscous than the fresh $EMIm(HF)_{2.3}F$, also suggesting a high content of silicon dissolved in the electrolyte.

A summary of the cell performance is presented in Table 3-2. The practical specific capacity of the alkaline Si–air battery is around 80.28–83.88 mAh g_{Si}^{-1} whilst the specific energy is approximately 88.31–100.65 Wh kg_{Si}^{-1}. The anode mass conversion according to the mass loss is around 2.5%, which is in agreement with previous works [41,48]. Conversely, the non–aqueous Si–air battery presented a practical capacity of 1072.43 mAh g_{Si}^{-1} and an energy density of around 841.48 Wh kg_{Si}^{-1}. The anode mass conversion was around 28.07%, significantly higher than the alkaline cell and similar to previously reported values [44].

Table 3-2 Performance parameters of the alkaline and non–aqueous Si–air battery.

	Anode Mass Conversion /%	Corrosion rate /mg day^{-1} cm^{-2}	Practical capacity /mAh g_{Si}^{-1}	Energy density /Wh kg_{Si}^{-1}
KOH	2.5	13.02	80.28–83.88	88.31–100.65
$EMIm_{2.3}HF$	28.07	0.99	1072.43	841.48

Figure 3.6 shows the status of a conventional printed circuit board (PCB) before and after the discharge experiment, controlled by the light microscopy mode of an LSM.

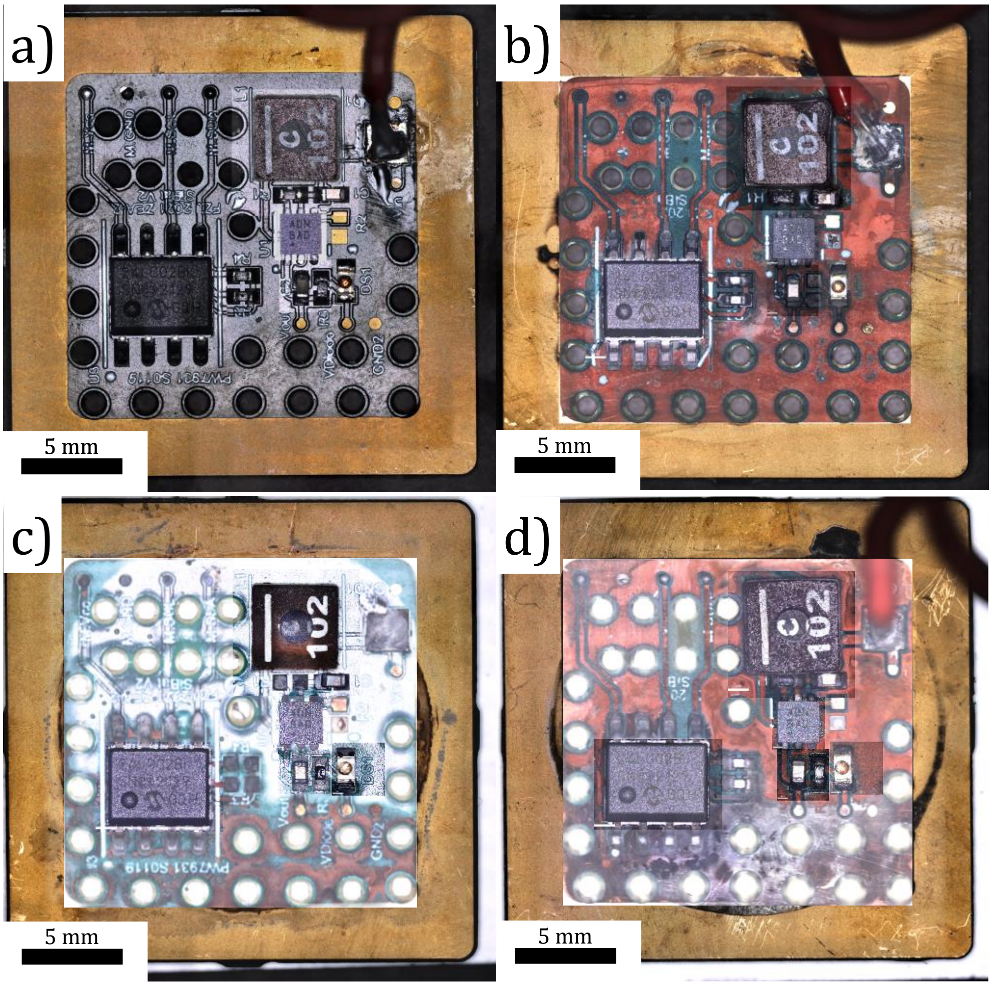

Figure 3.6: Light microscopy mode LSM pictures of the circuit a) before exposure to the electrolytes, after exposure to b) 5M KOH, c) $EMIm(HF)_{2.3}F$, and d) 5M KOH/0.6M KF.

Figure 3.6a shows the neat state of the PCB before exposure to the different electrolytes. Figure 3.6b displays the PCB after being in contact with the 5M KOH, where most of the insulator was removed by the KOH and some components detached form the PCB. However, most of the components remained still attached to the PCB. The weight loss of the PCB was practically negligible. Subsequent test with an external power source could not ignite the LED, probably due to the loss of some components and other possible damages. Figure 3.6c exhibits the PCB after consumption of the Si anode and exposure to the $EMIm(HF)_{2.3}F$, displaying partial damage on the lower side and detachment of some components. In order to improve the damaging of the circuit components, an additional attempt was made by incorporating dry KF powder into the same compartment where the PCB is located and its status could be monitored. The equivalent amount of KF resulted in 0.6M once the Si anode was depleted and the aqueous electrolyte dissolved the potassium fluoride salt. Figure 3.6d shows the PCB after exposure to the combination of 5M KOH/0.6M KF, displaying damage to the Cu substrate, although the components were still attached to the PCB. The LEDs on the PCBs from Figure 3.6c–d also could not be lit due to detached parts or damaged components. The information in the EEPROM was revised after the complete discharge of the Si–air battery and damaging of the circuit, revealing that the information was still accessible after several hours of immersion in each of the three different electrolytes employed. The casing of the EEPROM and some of the PCB components are made of or covered with FR–4, a glass–reinforced material based on epoxy laminates, whereas the contacting of the PCB is plated with gold. Both materials are chemically resistant and therefore difficult to dissolve.

In consequence, different possible substrates were investigated as degradable insulators, which could still fulfill the purpose of the PCB. As a preliminary test, a circuit was mounted on selected materials and directly immersed in 5M KOH, including drop–casted films of polyvinyl alcohol (PVA) and cellulose acetate (CA) solutions. PVA is a water–soluble polymer, which transitions from a semi–crystalline polymer to amorphous in presence of KOH [127]. The circuit mounted on PVA lost its rigidity, jellified, and eventually the circuit components detached. The cellulose acetate also losses its firmness, and turns into a soft gel after getting in contact with the KOH solution, leading to the detachment of the circuit elements. According to Dehaut et. al., CA is a KOH–soluble polymer, but its disintegration requires temperatures of at least 60°C for at least 24 h [128].

An additional solution are Si wafers with a coating of SiO_2 as insulator. The 5M KOH is capable to dissolve SiO_2 at an approximate rate of 2.24 nm h^{-1}, according to calculations based on the studies of Seidel et. al. [129]. Empirical evidence of the author corroborates this observation. Moreover, the destruction of the insulating SiO_2 substrate can be modulated by simply modifying its thickness. Regarding to the materials for the conducting path of the circuit, the silver ink is initially resistant to the KOH, but ultimately the silver nanoparticles oxidize and detach from each other. Based on the previous observations, a rather fast dissolving circuit substrate and routing materials were selected, namely the Si wafers with grown SiO_2 and silver ink. The assembly of the integrated circuit and the Si wafer is shown in Figure 3.7a.

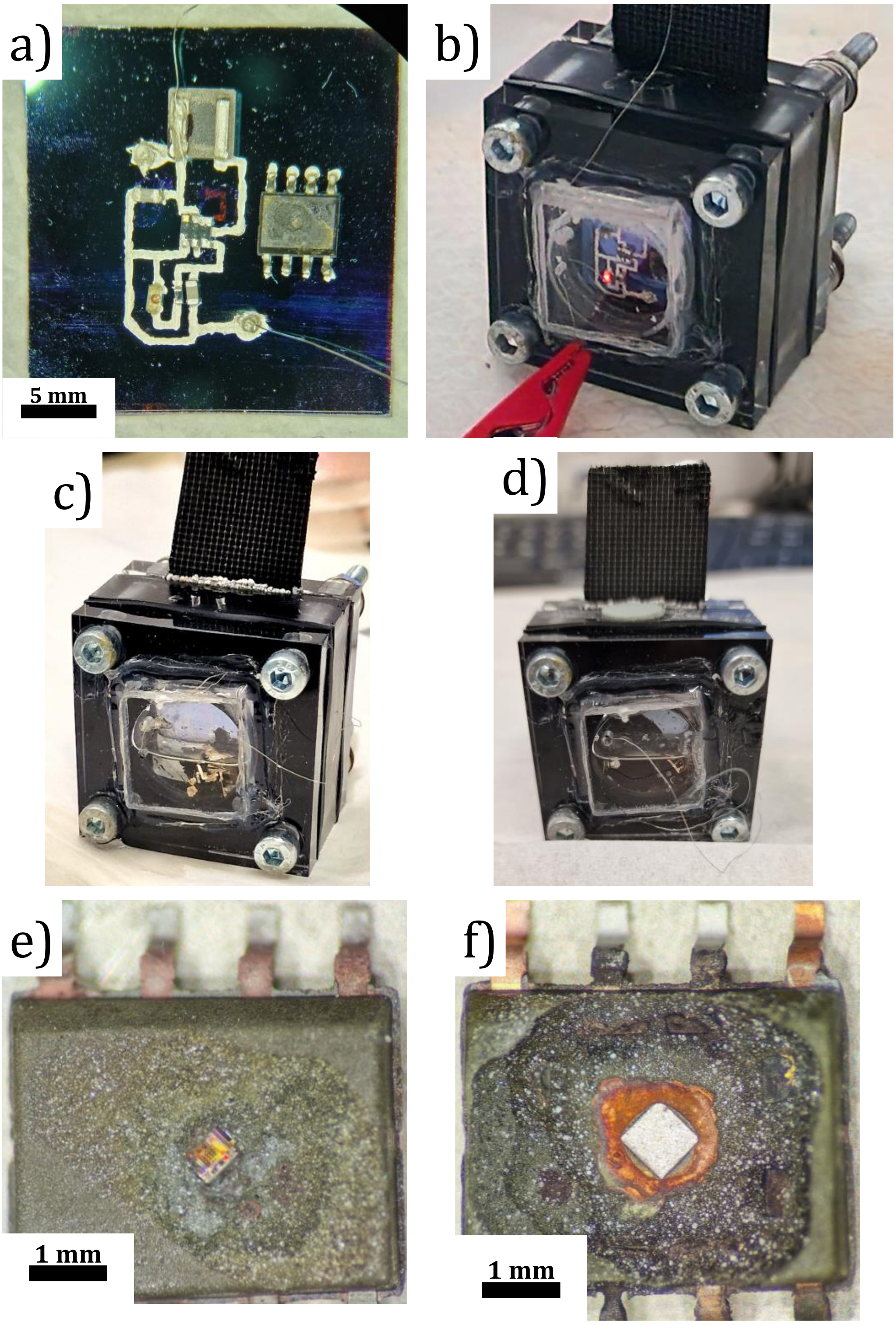

Figure 3.7: a) Assembly of the Si wafer with grown SiO_2 and circuit to power an LED and decapped EEPROM, b) operating Si–air battery with the circuit assembly of a), c) status of the assembly after penetration of the Si anode and degradation of the insulating SiO_2 by the 5M KOH, d) status of the self–destructive battery after longer immersion of the IC in the electrolyte, e) LSM picture of the decapped EEPROM prior to the contact with the 5M KOH, and f) LSM image of the EEPROM after long immersion in the alkaline electrolyte and dissolution of the Si die.

Figure 3.7b shows the operating prototype of a self–destructive circuit directly attached on a Si wafer. Figure 3.7c displays the prototype of the Si/IC assembly after the penetration of the Si anode and dissolution of the grown SiO_2 after exposure to the 5M KOH electrolyte of the battery. Figure 3.7d exhibits the progression of the dissolution of the IC after longer immersion in the electrolyte. Figure 3.7e shows in more detail the decapped EEPROM prior to contact with the electrolyte, where the Si die can be partially observed. Figure 3.7f shows the EEPROM after long immersion in the electrolyte, detachment from the Si anode of the battery, and dissolution of the Si die. The previous results show the feasibility of producing self–destructing devices which can be directly powered by the Si–air battery. In future attempts to improve the electrochemical behavior of Si in KOH, several strategies can be approached such as: i) the modification or exchange of electrolyte, ii) addition of corrosion additives, and iii) alloying and modification of the Si anode.

As a demonstration of the benefits of the alloying, a short evaluation of some proposed Si–Al alloys is included in the Appendix 4 "Electrochemical Evaluation of Si–Al alloys as anode materials for Si–air batteries in 5M KOH". The possible improvement of the electrochemical behavior is demonstrated by the possible higher current densities achievable by such samples, as shown in Figure A–3. Particularly, the cyclic voltammetry in Figure A–3a of Si–5%Al can display up to 5 mA cm^{-2} (50 times higher than a flat Si <100> As–doped wafer), whereas the galvanostatic discharge of the same sample shown in Figure A–3d was possible up to 250 μA cm^{-2} (over 3 times higher than any report so far). The preparation of the alloy by arc melting, however, possibly presented a major contribution on the higher corrosion rates observed for the alloys in comparison to single crystal Si <100> As–doped wafers (Table A–2 and Figure A–4). Future research work should focus on the improvement on the quality of the samples, but Si–Al alloys are still an interesting anode material to be investigated for Si–air batteries.

3.4. Summary and Remarks

The present section has shown the feasibility of incorporating a self–destructing circuit on the back side of the anode of a Si–air battery, also demonstrating the possible applications of Si–air batteries for low–power electronics. As a proof of concept, an LED was lid during the battery operation, which could be powered for at least 220 h in 5M KOH and over 1982 h in $EMIm(HF)_{2.3}F$. The tests were carried out until the complete consumption of the active area of the Si anode, and the Si–air battery delivered around

139 µA at 1.1 V for the cell with 5M KOH and 125–350 µA at 0.6–1 V for the cell with the ionic liquid. A conventional PCB was employed for the initial test, which showed some damage on some parts and components after exposure to the 5M KOH, EMIm$(HF)_{2.3}F$, and 5M KOH+0.6M KF. However, the complete dissolution of the PCB was not possible due to its high chemical resistance.

As a first approach for a self–destructing device, different materials as substrates for the circuit were proposed and the EEPROM was decapped to allow the complete dissolution of the integrated circuit. Since the circuit was mounted on a thin insulating SiO_2 layer with silver ink as routing material, complete dissolution of the circuit and silicon die of the EEPROM could be achieved. Upcoming approaches of a self–destructing device approach a more direct integration of the Si anode on the IC or other devices such as MEMS. The present study shows not only a practical application of Si–air batteries, but also proposes alternative materials to facilitate the recycling of integrated circuits. In this regard, polymers such as PVA, CA are relatively biodegradable, whereas natural materials like edible rice paper are more ecological. Thus, technological waste could be reduced in certain areas and applications. Furthermore, directly coupling of batteries and devices are demonstrated, also directing the attention to technology miniaturization.

Yet, some of the main challenges of alkaline Si–air batteries are related to the passivation upon relatively high anodic currents and the detrimental corrosion suffered upon discharge. Among the different strategies to improve the Si–air batteries, the use of corrosion inhibitors has been previously proposed in the literature as electrolyte additive in the metal–air batteries [130]. Another possibility is exchanging the highly corrosive KOH electrolyte in the Si–air battery for alternative electrolytes able to promote the electrochemical dissolution of Si with decreased corrosion. Some hints are given in previous studies, where the Si displays higher electrochemical discharge performance in presence of HF or EMIm$(HF)_{2.3}F$ electrolytes, suggesting that F^- ions are necessary to increase the discharge efficiency [31,42–45,131]. Accordingly, the performance of Si–air batteries with EMIm$(HF)_{2.3}F$ could be improved by alloying with Al, as proved by Özgür et. al [123]. The brief investigation of Si–Al alloys as anode material for alkaline Si–air batteries within the present thesis demonstrated possible benefits in terms of higher discharge current densities, while there is still a vast field for improvement on the preparation and tunning of the alloys.

Chapter 4: Effect of the Alloying on the Electrochemical Behavior of Zn Electrodes in Neutral Electrolytes

The present chapter is based on a published research paper with some modifications. The paper is available as “Influence of Al Alloying on the Electrochemical Behavior of Zn Electrodes for Zn–Air Batteries with Neutral Sodium Chloride Electrolyte” in *Frontiers in Chemistry*, 2019, 7, 1–13 [132]. The ICP–OES results were kindly provided by Nadine Wettengl from the Central Institute for Engineering, Electronics, –Analytics (ZEA–3), Forschungszentrum Jülich. The AFM results were generously supplied by Prof. Florian Hausen from the Institute for Energy and Climate Research – Fundamental Electrochemistry (IEK–9). The performing of the electrochemical measurements, LSM characterization, and analysis of results were performed by the PhD candidate and author of this thesis, Saúl Said Montiel Guerrero.

4.1. Motivation

As presented in Figure 1.3 and Figure 1.4 of the Section Metal–Air Batteries: Motivation, some elements are promising candidates as anode materials. Their electrochemical and corrosion behavior can further be improved by alloying to a suitable element in the fabrication of electrodes for metal–air batteries. The standard electrode potential of the element can serve as a reference for the selection of materials based on their electronegativity. In other words, alloying with elements possessing a more electronegative potential can increase the power output and the practical specific energy of the cell. Additional factors—like the inter–solubility of such materials and stability in the electrolyte employed—must be taken into consideration to produce homogeneous and/or stable active anode materials. The resulting synergistic effects of the alloy could hypothetically reduce the original drawbacks of the single elements used separately in the same operating conditions of the cells.

As a first possible approach in the selection of the alloying elements, phase diagrams are useful since these provide information about the melting points of alloys, the solubilities, possible phase transitions and the approximate microstructure of the alloys. Such diagrams can be binary (only two elements), ternary (three elements), or multielement. In the frame of this dissertation, only binary phase diagrams will be shortly discussed.

Depending on the desired properties of the electrode, specific alloying compositions can be selected accordingly. For example, a eutectic alloy may be preferred to obtain a finer microstructure. Nevertheless, the phase diagrams can give some hints of possible alloys and the limitations during the preparation, but further theoretical tools can assist on the decision over an appropriate alloy composition.

In addition, materials possessing different standard electrode potentials can be alloyed and benefit from the resulting galvanic coupling once employed in a cell. The mixed potential theory of Wagner and Traud can be expanded from single electrode/electrolyte interfaces to alloy/electrolyte interfaces [133]. Accordingly, all the electrochemical reactions have an anodic and cathodic component, whereas two metals in electrical (galvanic) contact can influence and polarize each other due to the corresponding electrochemical reactions occurring at each metal. Figure 4.1 graphically illustrates the resulting mixed potential of the hypothetical metal M_1 and M_2.

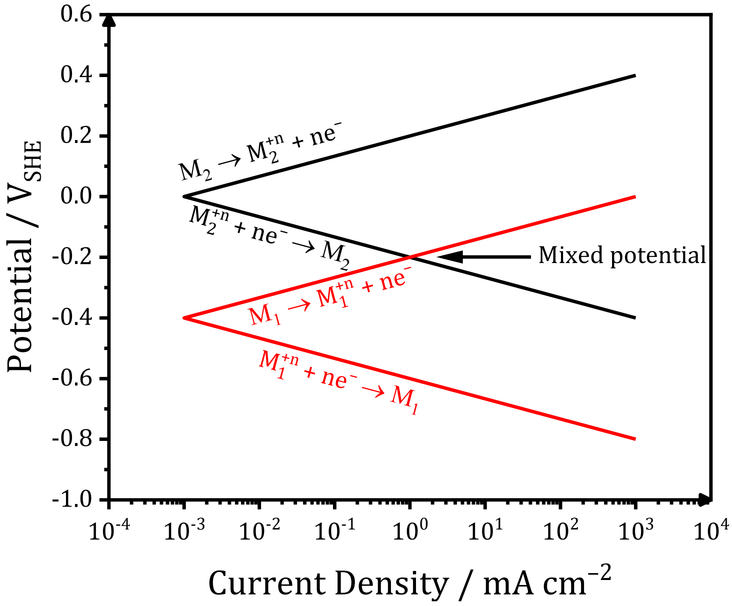

Figure 4.1: General scheme of the mixed potential theory, where two metals are in galvanic contact and influence on the electrochemical behavior of each other.

In the ideal case, the intersection of the extrapolation of the cathodic and anodic branches of M_1 and M_2 should result in a combined potential between the original potential of M_1 and M_2 [133]. The similarity of the potential of the alloy to one of the electrode potentials conforming the alloy depends on a series of factors such as the alloy composition, homogeneity, electrolyte, pH, selectivity for H_2 evolution, etc.. Experimental evidence of the mixed potential theory can be found in the literature [123].

A complementary tool in the selection of possible materials for metal–air batteries is the potential–pH diagram (E–pH), also named after Marcel Pourbaix [121]. Pourbaix diagrams provide a graphical overview of the possible potentials of a metal at a given pH value, but they are limited by the assumption of static thermodynamic equilibrium conditions of the metal with only water. In consequence, other anionic species possibly present in the electrolyte (e.g., F^-, Cl^-, etc.) and the possible reactions with the metal are ignored by the Pourbaix diagrams. Similarly, the constantly changing state and new equilibrium upon operation of the metal–air batteries can directly influence on the stable species formed, which is not included in the E–pH diagrams. The following section shows a brief overview of the Pourbaix diagram of Zn–H_2O and Al–H_2O system. A complete description of the construction process and information necessary for the calculation can be found in the literature or in online tools [20,121,134–136].

Figure 4.2 shows the Pourbaix diagrams of Zn and Al with a concentration of 10^{-6}M in water, where the solid lines represent the domain of the different species. Moreover, the blue– and red–dashed lines represent the oxygen and hydrogen evolution reaction, respectively. The species with the subindex (aq) indicate the solvated species (dissolved). The solid compounds such as oxides, hydroxides and oxyhydroxides are usually considered as passive compounds. The solid species $Zn_{(s)}$ and $Al_{(s)}$ denote the basal state of the metals and the corresponding area represent the immunity (non–reactivity) region of the elements. Furthermore, the solid line delimiting the immunity and the passivation/corrosion corresponds to the standard electrode potential. Figure 4.2 shows for all the materials a clear trend of an increasing potential at higher pH values. However, a passive surface may hinder such higher potentials, as described in Figure 2.2.

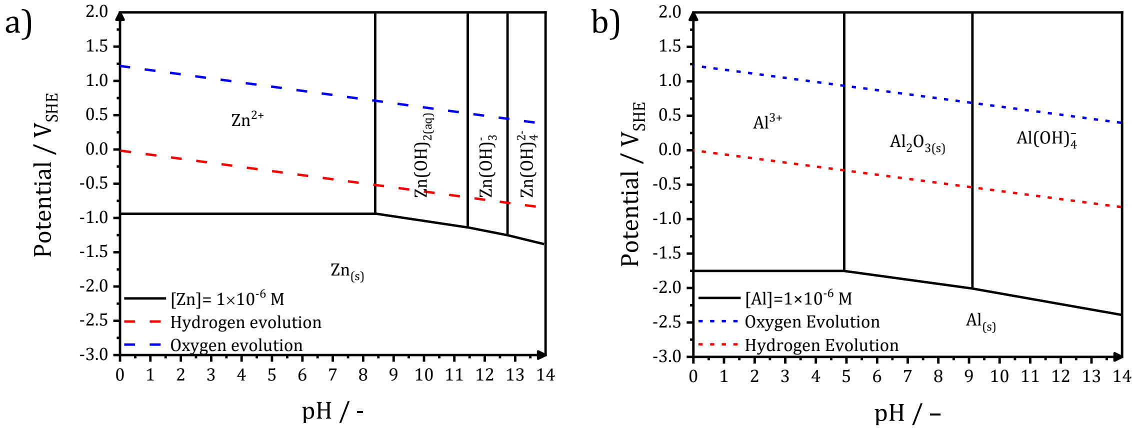

Figure 4.2*:* Pourbaix diagram of a) Zn and b) Al with a concentration of 10^{-6} M in water. Reproduced after [134–136].

Additional information on the possible changes of the potential and predominant species in the Pourbaix diagrams after changes in the concentration of the initial M^+ species is presented in the Appendix 3 “Pourbaix Diagrams” and in Figure A–1. The information provided by the Pourbaix diagrams can be assumed as a rough estimation of the changes occurring at the anode in an aqueous electrolyte. Moreover, it gives graphical information of the solubility limits of some species and their possible effects on the electrode surface. Nonetheless, the presence of other ions in the solution, some other characteristics of the electrolyte or alloyed electrodes can result in drastic changes. Focusing on the alloyed materials, the effect of an element mixed with another one can be advantageously used to benefit the overall electrochemical behavior of an electrode.

A highly desired characteristic of a battery is its cyclability, while the convenient and practical options among the metal–air batteries are limited. Zn–air batteries (ZABs) are, in this case, a potential alternative not only as a possible alternative for Li–ion technologies, but for effectively upscaling energy storage, as proposed by Amendola [75]. ZABs possess both good theoretical specific energy and high volumetric energy density, with values of 1,352 Wh $\mathrm{kg_{Zn}^{-1}}$ and 9,653 Wh $\mathrm{L_{Zn}^{-1}}$, respectively.

Due to such advantageous characteristics, the popularity of alkaline Zinc–air batteries has increased but with some drawbacks such as: i) high corrosion, ii) dendrite formation, iii) carbonation of the electrolyte, and iv) relatively low anode mass conversion efficiencies [60]. As an alternative, ZABs with neutral electrolyte were proposed to minimize the undesirable effects of the alkaline electrolytes, as presented by Jindra in 1973 [74]. Although the idea was left for several years, recent studies have successfully shown the cycling of ZAB with stable performances with over 5100 h and 540 cycles [76–81].

However, the discharge voltages displayed by the neutral ZABs are lower in comparison to the alkaline ZABs under similar conditions (1.04 V vs 1.32 V, respectively) [78]. Derived from the advantages of the neutral electrolytes and to compensate the relatively low potential of Zn under such conditions, alloying the Zn with an anode material possessing higher potentials could effectively counteract the mentioned limitations of Zn in neutral solutions. One possible candidate is Al due to its more negative standard electrode potential (Table A–1), high specific energy (8,091 Wh $\mathrm{kg_{Al}^{-1}}$), and outstanding volumetric energy density (21,837 Wh $\mathrm{L_{Al}^{-1}}$), while the Al–solubility in Zn is relatively high upon alloying [137–139]. Furthermore, the neutral Al–air battery has been previously shown as a feasible technology with discharge voltages of 1.1 V under ~1.9 mA cm^{-2} in a 3.5% NaCl solution [85,97,98].

Thus, a complete electrochemical characterization of a Zn–Al alloy in neutral solutions is required for possible applications in a neutral electrolyte Zn–Al alloy–air battery. Moreover, the results of such evaluation could be a valuable scientific contribution as an experimental verification of the mixed potential theory applied for alloys.

4.2. Experimental Section

Materials Preparation and Chemicals: Zinc–Aluminum alloy (Zn–10Al) was prepared from cold drawn tempered zinc rods (4N, Alfa Aesar) and aluminum rods (Puratronic grade, 5N, Alfa Aesar) with a composition of 90 wt.% Zn and 10 wt.% Al. The pure Zn and Al electrodes were prepared directly from the rods. The materials were melted in a tube furnace (Gero REST–E 400/6, Germany) at 700°C for 3 h and subsequently cooled down to room temperature under continuous flow of argon gas. Composition analysis of the alloy was obtained by inductively coupled plasma optical emission spectrometry (ICP–OES) as shown in Table 4-1.

Table 4-1 ICP–OES analysis of the as–cast Zn–10Al alloy.

Alloy	Si wt. %	Mg wt. %	Fe wt. %	Pb wt. %	Cu wt. %	Al wt. %	Zn wt. %
Zn–10Al	<0.001	<0.001	0.001	<0.005	0.001	9.93	Balance

The samples were cut into discs, the pieces were embedded in cold mount epoxy (EpoFix, Struers) and the surfaces were ground with 800 SiC paper. The corresponding areas for the Zn, Zn–10Al alloy and Al electrodes are 1.32, 1.32, and 0.77 cm^2, respectively. 2M NaCl solutions were prepared by dissolving NaCl crystals (≥99.5%, Merck–Millipore) in deionized water (conductivity <0.1 μS/cm, PURELAB Elga). The solutions were degassed by flowing argon for several minutes (>10min) in order to remove dissolved oxygen. Adjustment of the pH was done by adding small amounts of 0.1M NaOH solution until reaching pH 7. The pH of the NaCl solutions was measured by a pH meter (Duo S213, Mettler Toledo).

Electrochemical Methods and Corrosion: A three electrode setup with Zn, Al, and Zn–10Al as working, Pt mesh as counter, and silver/silver chloride (Ag/AgCl) as reference electrodes was employed in the experiments (Figure 2.1a). The cell volume was 20 mL. Electrochemical cyclic voltammetry, galvanostatic, and potentiodynamic polarization experiments were carried out with a Biologic VMP3 potentiostat. Cyclic voltammetry (CV) and potentiodynamic polarization were conducted with a scan rate of 5 mV s^{-1}. The galvanostatic discharge was performed by applying 0.005, 0.01, 0.05, 0.1, 0.25, 0.5, and 1 mA cm^{-2} discharge current densities. For the Al activation experiments, a potentiostatic cathodic pulse at $-1.6V_{Ag/AgCl}$ was applied for 60 min prior to discharge. All the experiments were carried out in a climate chamber (Binder KMF115) to ensure constant controlled ambient conditions.

The gravimetric corrosion experiments were measured over 7 days in 2M NaCl with pH 7. After exposure, the samples were cleaned with saturated glycine solution according to ISO 8407 standard [140]. The weight losses were determined by using an analytical balance with an accuracy of 0.01 mg (XA205, Mettler Toledo).

Microstructure and Elemental Analysis: The previously embedded samples were ground and polished using a Tegramin system (Struers, Germany) for microstructural analysis. The final polishing steps consisted of 3 μm (DiaPro Mol B) and 1 μm (DiaPro Nap B) water–based diamond suspensions with lubricating liquid. The microstructures were characterized by a confocal laser scanning microscope (LSM, OLS4100, Olympus Corp., Japan) and by scanning electron microscopy (Quanta 650, FEI, USA) using the concentric backscatter electron (CBS) detector and energy–dispersive X–ray spectroscopy (EDS) (Octane Super Detector, EDAX, USA). Applied acceleration voltages in the SEM measurements were 20 kV. Atomic force microscopy (AFM) images of the polished samples have been obtained with a Bruker Dimension ICON (St. Barbara, CA, USA) inside a glove box (O_2<1 ppm, H_2O<1 ppm) in conductive–AFM mode. As cantilevers SCM–PIT–V2 (Bruker, St. Barbara, CA, USA) with a Platinum–Iridium coating and a nominal spring constant of 3 N m^{-1} as well as a tip radius of 25 nm have been used as received and calibrated individually. For conductivity experiments, the sample was contacted from underneath. Inductively coupled plasma optical emission spectrometry (ICP–OES) was conducted with ThermoFischer scientific iCAP 7600 spectrometer with Echelle–optic and CID–semiconductor detector. For the analysis, 50 mg of alloy sample was dissolved in 3 mL HNO3/3mL HCl solution with a total volume of 50 mL. Two independent parallel digestion solutions of this sample were analyzed by ICP–OES.

4.3. Experimental Results and Discussion

As–Cast Microstructure of the Alloy: The microstructure of the Zn–10Al alloy undergoes several transformations when cooled down from the melt, as displayed in Figure 4.3.

According to the phase diagram (Figure 4.3) for the Zn–10wt.%Al alloy the liquidus temperature is at ~419.5°C at which primary γ–ZnAl starts to nucleate from the melt. γ–ZnAl denotes a face centered cube (fcc) phase containing 70–76 wt.% Zn with possibly ordered structure [137–139]. Under equilibrium conditions solidification is completed at the eutectic temperature (382°C), where the alloy consists of primary phase γ–ZnAl and eutectic phase fromβ–Zn and γ–ZnAl. On further cooling to 275°C, the material undergoes a eutectoid transformation, in which—depending on the cooling conditions—α–Al and β–Zn form from the γ–ZnAl. While the equilibrium phases of α–Al and β–Zn are quite low in content of the respective other component, microstructure constituents with deviating composition might be remaining under non–equilibrium conditions.

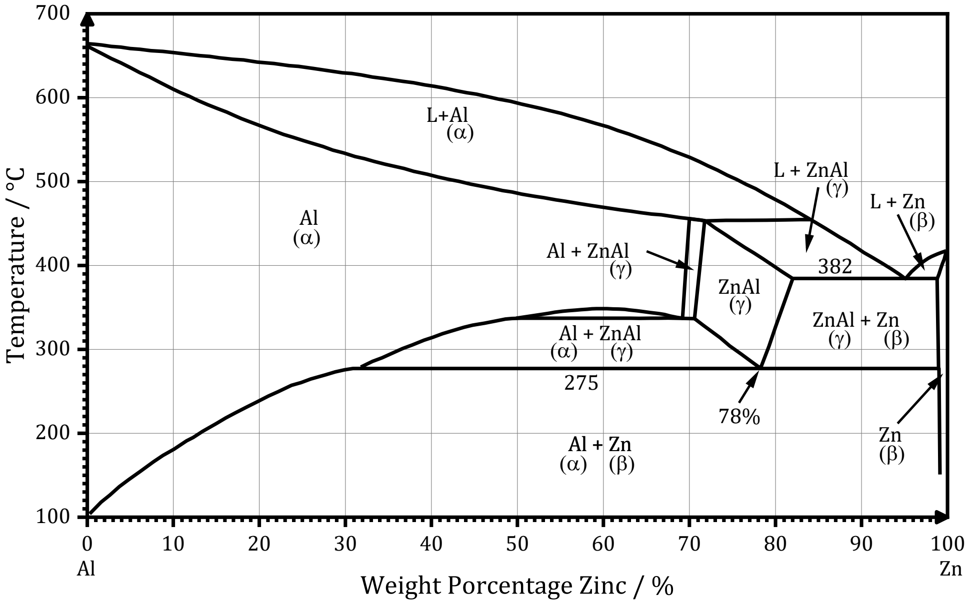

Figure 4.3: Phase diagram of Zn–Al alloy. Reconstructed after [138,139,141].

At low magnification (Figure 4.4a), the SEM image of the alloy shows large dark areas, small dark lamellas, and islands surrounded by light areas covering the rest of the surface. The light areas are the β–Zn phase. The shape and the size of the dark areas varies with typical size of up to 50 μm. They are surrounded by Zn–rich halos with a width of <10 μm, characteristic for hypereutectic Zn–Al alloys (>5 wt.% Al) at low cooling rates [142,143].

At higher magnifications more distinct features in the region toward a 2–5 μm wide rim of the large dark areas as well as in their inner part (Figure 4.4c) can be identified. In the near rim regions, the material splits into two phases on a 100–500 nm scale, with one of them forming round shaped grains [141]. Lamellar structures, with spacings in the range from 50 to 100 nm can be distinguished in some regions of the inner part of the large dark areas [144]. The nanostructures are attributed to formation of the eutectoid [141,144]. While for the large area bright regions the EDS detects a Zn–content of almost 100 wt.%, the eutectoid in the inner part contains 80 wt.% Zn and 20 wt.% Al on average (Figure 4.4c,e). Resolution within these nanostructures of the eutectoid is not possible due to the limitation of the EDS spot size. The somewhat larger structures of the eutectoid in the rim area allow for a better resolution indicating the Al content in the dark areas thereof is higher.

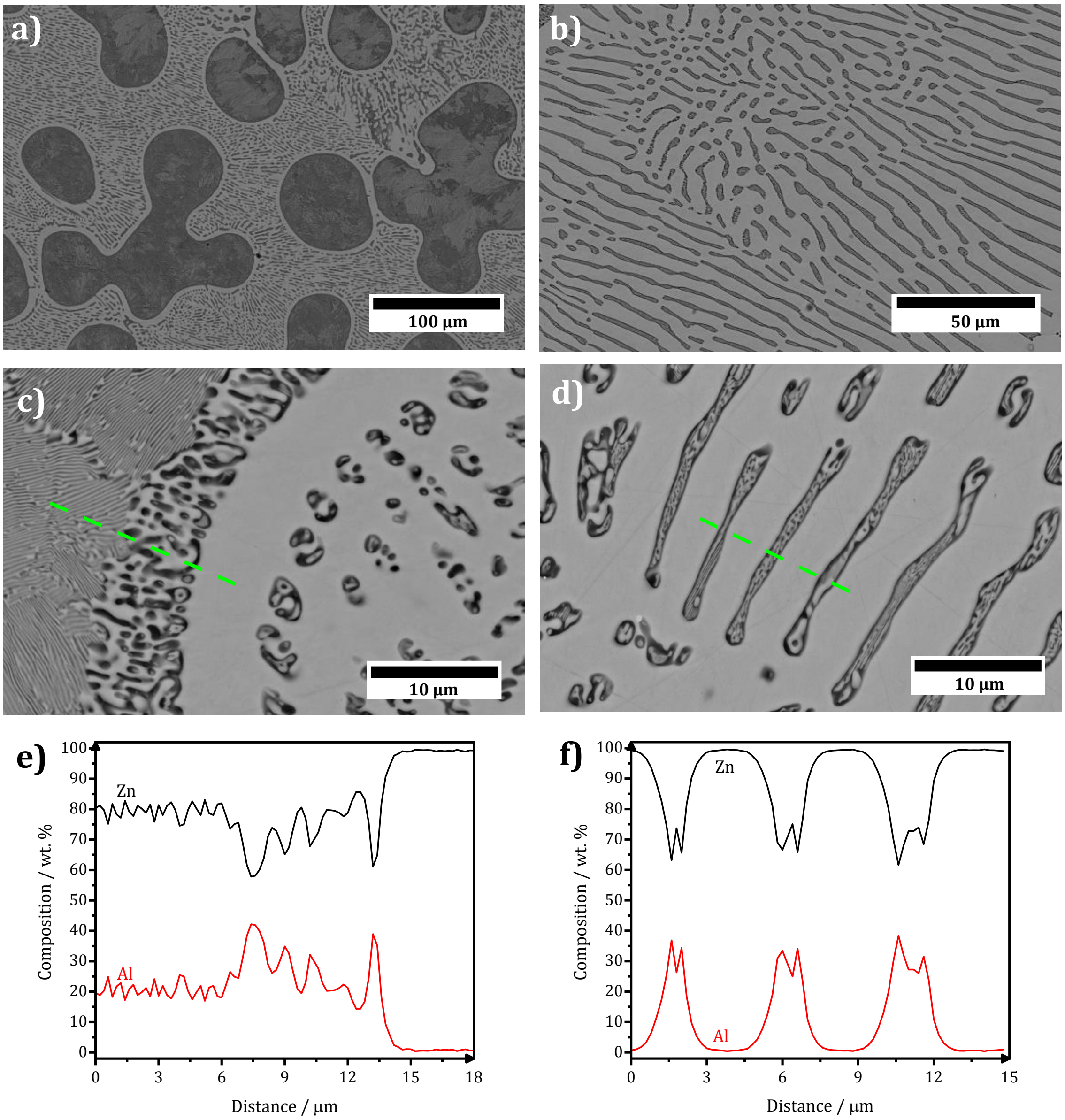

Figure 4.4: SEM images recorded with backscatter electron detector of as–cast Zn–10Al alloy, a) 500× magnification overview of microstructure constituents, b) 1,100× magnification of the lamellas and islands, c) 5,000× magnification of the boundary region between the dark and bright zone, d) 5,000× magnification of the lamellas and islands, e) and f) are the results from EDS analysis for line scans indicated in c) and d), respectively.

The dark regions appearing on low magnification as lamellae (Figure 4.4b) and islands are originally formed during the eutectic reaction. In the regions with predominantly lamellar structures the interlamellar spacing λ is 3 µm approximately. However, these structures are not perfectly laminar, but contain substantial rod shaped constituents appearing as islands, which is typical for Zn–Al alloys with Al contents higher than 7 wt.% [142]. Therefore, although the value for lamellar interspacing roughly matches the results for this type of alloys at relatively low cooling rates, it cannot be considered a precise result for establishing correlations [142]. SEM images at higher magnifications reveal, that within both—lamellae and islands—a nanostructured framework is formed (Figure 4.4d), which most likely corresponds to α–Al/β–Zn– eutectoid. For the average content of the eutectoid lamellae regions the EDS indicates 70 wt.% Zn and 30 wt.% Al (Figure 4.4d,f).

Electrochemical Behavior of the Alloy

Cyclic Voltammetry: The electrochemical activities of the prepared alloy, pure Al, and pure Zn electrodes were investigated with cyclic voltammetry (CV) experiments. Figure 4.5 demonstrates the CVs of Al, Zn, and Zn−10Al alloy starting at open circuit potential (OCP) conditions towards more positive values within a potential range of −1.4 to $-0.8\ V_{Ag/AgCl}$ in 2M NaCl with pH value of 7. The voltammogram for Al does not show any significant electrochemical activity during both forward and reverse scans since no significant current density was measured. The Zn electrode, on the other hand, shows onset of oxidation starting at $-1.08\ V_{Ag/AgCl}$ with constantly increasing current. The reverse scan reveals a reduction peak for Zn around $-1.08\ V_{Ag/AgCl}$ of the reverse reaction depicted in Equation 1.17. Concomitant to Zn reduction, originating from the nature of the aqueous electrolyte, there is also a hydrogen evolution at such relatively high potentials according to the Pourbaix diagram of Zn in Figure 4.2a. However, at a much slower rate in comparison to the Zn reduction/deposition reaction. The CV for the Zn−10Al alloy is almost identical to pure Zn with similar characteristics regarding to the redeposition of Zn and H_2 evolution.

According to the CV experiments, alloying of Zn with Al does not impede any pronounced influence on the electrochemical behavior. Considering the similar CV results of Zn and Zn−10Al in combination with the apparent no electrochemical activity of Al, Zn is suggested to be the only active component in the alloy in presence of the neutral electrolyte. Aluminum, for which the theoretical electrochemical potential is more negative (see Table A–1), is very likely present as passivated in the pure Al as well as in the alloy electrodes.

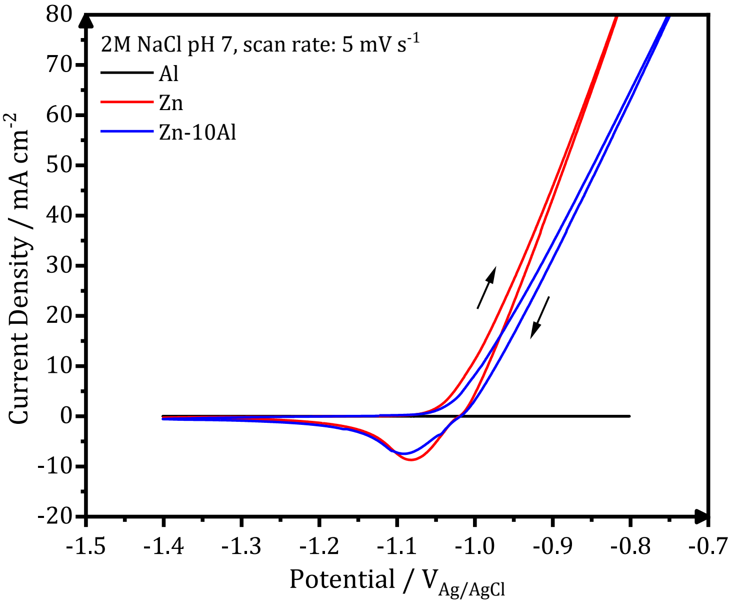

Figure 4.5: Cyclic voltammograms of pure Al and Zn, and Zn–10Al alloy electrodes in 2M NaCl at pH value of 7. The scan was initiated toward anodic potentials as shown with the arrows. The scan rate was 5 mV s^{-1}.

It is also noteworthy to mention that both Zn and Zn–10Al electrodes exhibit a steady increase of the oxidation current during the anodic scans without any visible oxidation peak over the complete anodic potential range. Generally, typical cyclic voltammograms show a single or multiple oxidation peaks after which the currents start to decrease due to depletion of active species or formation of passivation layer. Remaining within the electrochemical stability window of the electrolyte, a continuous increase of the oxidation current as shown in Figure 4.5 indicates that the oxidation reaction of Zn continues at relatively high anodic overpotentials via pitting mechanism. Pitting is known as localized accelerated dissolution of a metal as a result of localized breakdown of passive film [56,145]. A graphical description of this process is shown in Figure 2.2e. The presence of aggressive anionic species, such as chloride (Cl^-), is mainly the cause for pitting mechanism [56,145,146].

Galvanostatic Discharge: Figure 4.6 presents the galvanostatic discharge experiments (or stripping experiments due to half–cell setup) of Al, Zn, and Zn–10Al alloy in 2M NaCl with pH value of 7 under various current densities. To examine the possible influence of Al alloying on the electrochemistry and to prevent significant pitting formations, current densities only up to 1 mA cm^{-2} were employed. Discharging the Al electrode in the neutral electrolyte results in relatively low anodic potentials. As shown in Figure 4.6a, even at very low current densities (0.1 mA cm^{-2}), the Al could anodically be utilized only at about -0.76 $V_{Ag/AgCl}$. In case of Zn and Zn–10Al, both electrodes provided discharge potentials around -1.03 $V_{Ag/AgCl}$. There was no pronounced difference on the discharge potentials for current densities up to 1 mA cm^{-2} and the potentials of the three electrodes were stable over 24 h. Overall, the alloy showed very similar discharge profiles to Zn electrode during the galvanostatic studies. The elemental steps of the reactions governing the dissolution of Zn and Al upon discharge are described in Equation 1.17 and 1.26, respectively.

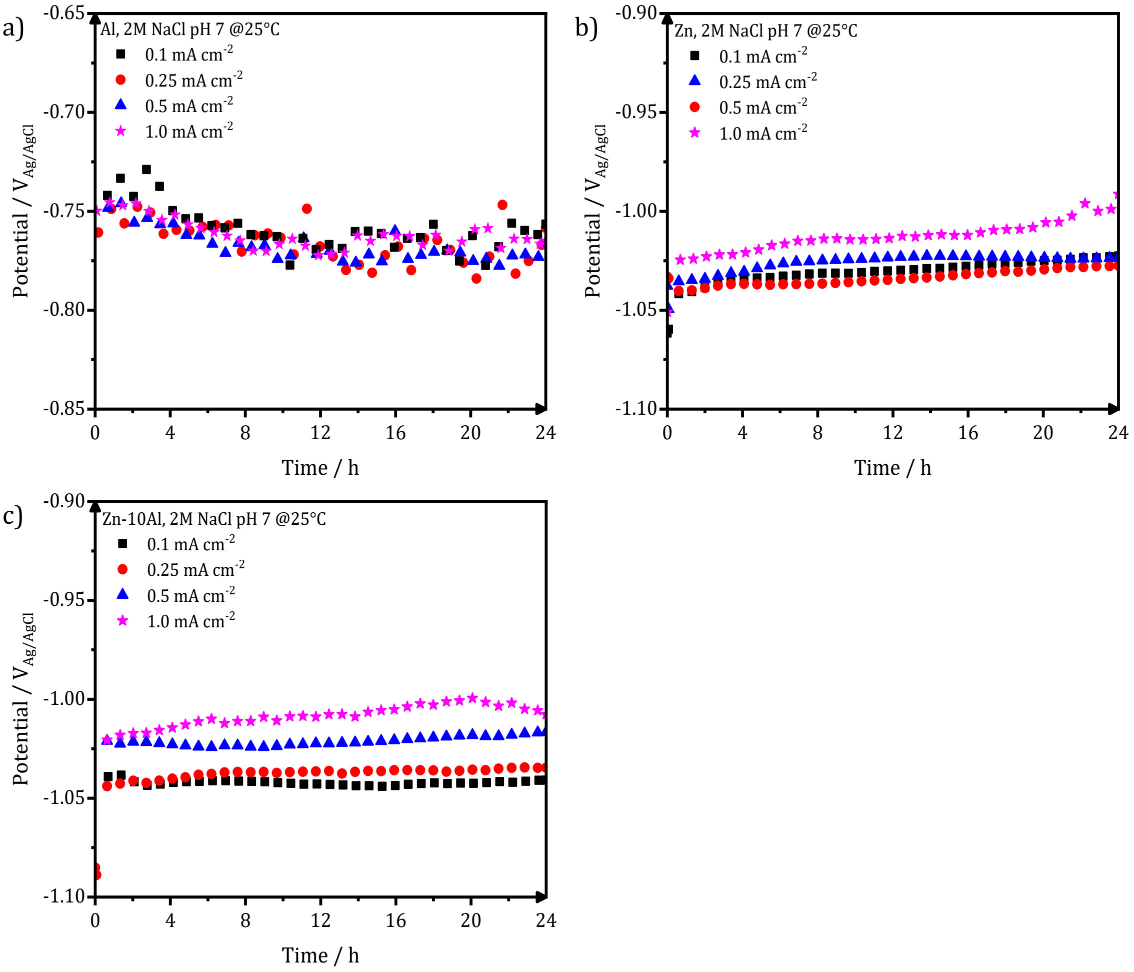

Figure 4.6: Galvanostatic discharge (or stripping) experiments of (a) pure Al, (b) pure Zn, and (c) Zn–10Al alloy electrodes. The discharge current densities were 0.1, 0.25, 0.5, and 1.0 mA cm^{-2} over 24 h.

The formed aqueous ions, Zn^{2+} and Al^{3+}, would further complex with other species in the electrolyte. In the presence of NaCl, when the solubility limits are exceeded, zinc hydroxide chloride, or Simonkolleite [$Zn_5(OH)_8Cl_2{\cdot}H_2O$], as well as zinc oxide (ZnO), can be formed in case of zinc [147,148], while for Al, aluminum hydroxide [$Al(OH)_3$], aluminum oxide (Al_2O_3) and even aluminum chloride ($AlCl_3$) species may be formed [149,150]. A more detailed explanation on the mechanism behind the formation of insoluble/passive species can be found in the Appendix 6 “Visualization of solvation, complexation, and precipitation”. Moreover, if both metals are present on the electrode surface, as for Zn–10Al, layered double zinc–aluminum hydroxides can also be produced in neutral and near neutral aqueous solutions [151,152]. The existence of the end products is highly dependent on the pH value of the solution (see Figure A–13) [146,151].

According to the Pourbaix diagrams in Figure 4.2, Al and Zn are thermodynamically not stable in aqueous solutions over the complete pH range since their immunity regions are below the stability window of water [121]. Thereby, these metals react with aqueous electrolyte instantly to produce stable species which are in the form of dissolved ions (corrosion region) or solid oxide/hydroxides (passivated region). In the pH range of interest for our study (pH value of 7) Al remains in the “passivated region” while Zn is in the “corrosion region.” Under these conditions, galvanostatic discharge of Al through the passive layer is only possible if the passive layer is dissolved or attacked by the adsorbed Cl^- ions to initiate pits (Figure 2.2e). Once the Al is exposed to electrolyte, discharge (active dissolution) continues via pitting at a stable potential at least over 24 h as shown in Figure 4.6a. Dissolution kinetics and the conductivity of electrolyte are high enough resulting in similar steady state potentials of $-0.76\ V_{Ag/AgCl}$ in the range of 0.1 to 1 mA cm^{-2} current densities. Smolijko et al. also reported discharge potentials of Al around $-0.75\ V_{Ag/AgCl}$ even under an anodic current density of 20 mA cm^{-2} in 2M NaCl electrolyte [98]. Moreover, the steady state potentials linearly increase for anodic currents between 20 and 100 mA cm^{-2}; while the discharge potential under 100 mA cm^{-2} was around $-0.6\ V_{Ag/AgCl}$ [98]. Specially such high current densities may result in severe pit formations which could be detrimental for the stability of the discharge experiments in a battery application.

On the contrary, The Zn and Zn–10Al electrodes exhibit discharge potentials of about 0.28 V more negative than that of Al under the same current densities. Since Zn is in the corrosion regime, there is apparently no compact passive layer on the surface. Consequently, the electrochemical reactions on the Zn and alloy electrodes occur at much lower electrode polarizations (see the polarization principle in Appendix 2 “Polarization Principles and Analysis of Potentiodynamic Polarization Curves”); thus, more negative steady state potentials are obtained as shown in Figure 4.6b,c. Almost identical discharge profiles of Zn and Zn–10Al alloy electrodes together with the CV results suggest that Al does not contribute or influence the electrochemistry of the electrode and Zn is the only active component. Since the discharge potential is not close to Al discharge (or pitting) potential (Figure 4.6a), the Al in the alloy probably remains passive.

Surface Analysis of the Alloy

LSM: Further investigations have been conducted by laser scanning microscopy (LSM) in order to obtain better insight into the dissolution behavior of the alloy during the galvanostatic discharge experiments. Figure 4.7 illustrates the LSM images of the Zn–10Al alloy which was discharged with 1 mA cm^{-2} current density for 3 h. Figure 4.7a,b represent an area on the surface prior to the experiment while Figure 4.7c,d represent the same area subsequent to 3 h of discharge.

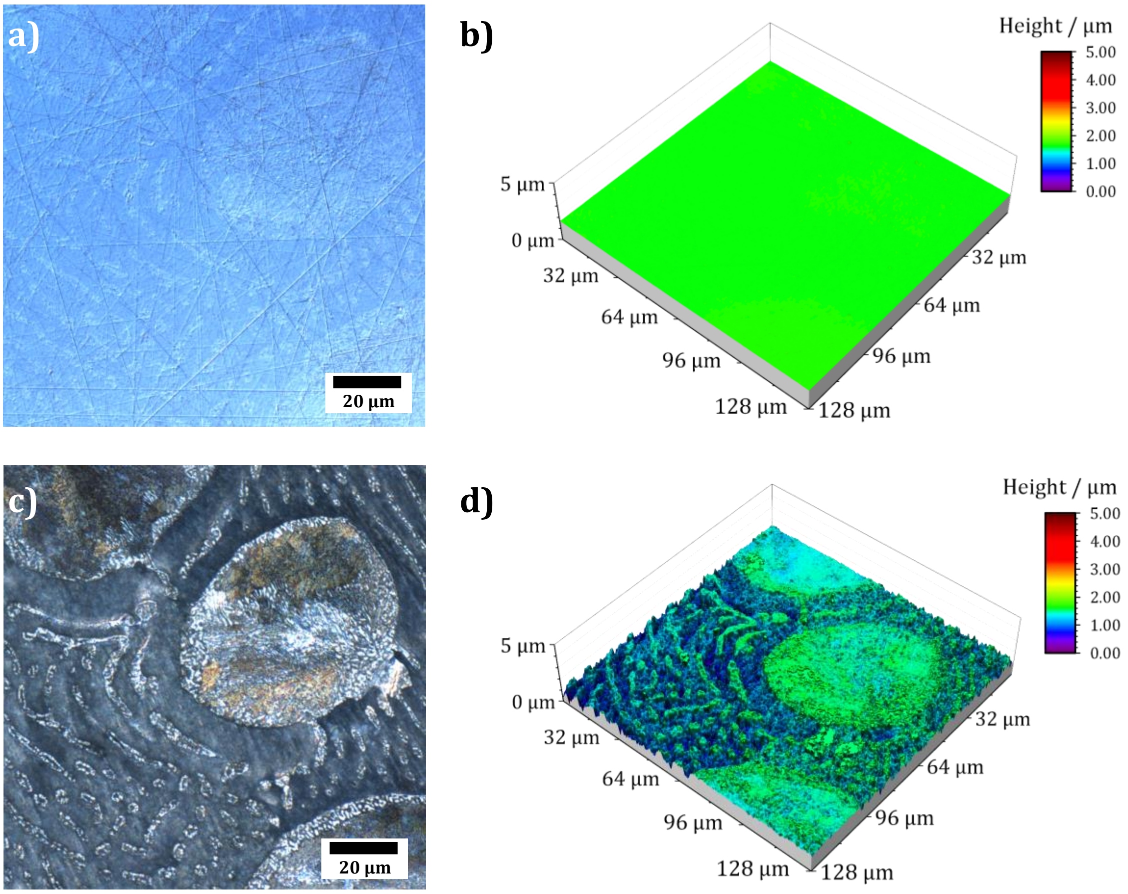

Figure 4.7: Laser scanning micrographs of Zn–10Al alloy electrodes: (a) 2D image of the surface prior to galvanostatic discharge, (b) 3D image of the same area shown in (a), (c) 2D image of the same area after 3 h of galvanostatic discharge with 1 mA cm^{-2} in 2M NaCl electrolyte with pH 7, (d) 3D image of the same area shown in (c).

From the comparison of the Figure 4.7a,c, the contrast difference between the microstructures is clearly enhanced upon discharge. The larger grains containing eutectoid Zn–Al became more visible. Also, the γ–ZnAl phase lamellas and islands in the eutectic can be distinguished. Moreover, the β–Zn phase filling the areas between the other phases seems partially etched away. A comparison of the height profiles is shown by the Figure 4.7b,d where a 3D image of the same area is provided. According to Figure 4.7d, there is a height difference of almost 3 μm between the β–Zn phase and the other phases which contain some Al.

The LSM images support the findings of the electrochemical experiments, showing that the Zn is the most active component in the alloy since the β–Zn phase is preferentially dissolved from the alloy surface as shown in Figure 4.7. Otherwise, a more homogeneous dissolution would be expected on the surface. However, basing only on the LSM images, it is unclear if the other phases remain completely inactive because a certain fraction of Zn is present also in the Al containing constituents. Accordingly, Zn dissolution on the other phases might also be occurring but at a much lower rate.

AFM: The surface of the prepared Zn–10Al alloy electrode was further investigated by conductive atomic force microscopy (c–AFM). While LSM is not sensitive to chemical or mechanical differences of the surfaces under investigation, c–AFM is measuring electrical properties simultaneously next to topographical features as well as the lateral force. The surface topography of as–cast Zn–10Al alloy is depicted in Figure 4.8. The morphology shows several bumps and depressions on an overall rather smooth surface. Additionally, it exhibits several scratches in various directions due to the polishing process of the surface. The observed surface morphology is similar to the very flat surface in LSM (Figure 4.7b). The typical microstructural composition of the Zn–10Al alloy as found in SEM experiments (Figure 4.4) cannot be distinguished from topography. This can be expected since the topography mode does not provide any material–specific contrast and thus, cannot differentiate between Zn and Al rich constituents.

Lateral forces between the AFM tip and the alloy have been probed simultaneously to the surface morphology. Such lateral forces are very sensitive even to subtle materials changes, as expected to be present in the system under study. Figure 4.8b shows the recorded lateral force image (trace). A quadratic part of lower lateral forces (darker appearance) is recognizable as indicated by the highlighted edges. The size of this structure is 35×35 μm^2, corresponding to the scan size of the beforehand image. Two different materials can be differentiated in the lateral force image: Several regions of higher lateral force (brighter appearance) are recognizable in form of isolated areas with a few μm in size especially in the top half of the image as well as in form of a larger sized quadrant in the bottom right corner. These regions are surrounded by a darker matrix. These structures do not have a counterpart in the topography image and can therefore be attributed to different materials, such as β–Zn and Al containing (probably eutectic γ–ZnAl) parts of the alloy. A closer inspection reveals that the brighter grains exhibit a similar lateral force inside and outside the square while the surrounding area shows reduced lateral forces inside the quadratic feature. It can be concluded that the surrounding is stronger affected by previous mechanical load than the isolated areas.

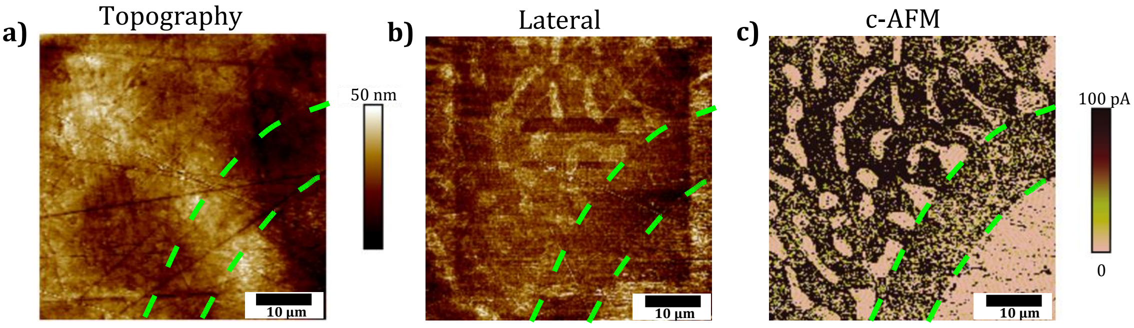

Figure 4.8: Atomic force microscopy images of as–cast Zn–10Al alloy electrodes. (a) The surface topography, (b) Lateral force, (c) conductive–AFM (c–AFM). All the images were recorded simultaneously. In (b), the green highlighted edges of the quadratic area indicate the previous scan. In all the images, as a guide to the eye dashed lines are shown corresponding to part of the halo structure separating the large Al–rich grain from the eutectic lamellas and islands.

Figure 4.8c demonstrates the local conductivity of the surface area and was recorded simultaneously to the images shown in Figure 4.8a,b. Here, a very strong material contrast of the surface is observed. Interestingly, these properties are not reflected in the topography image but in the lateral force image and can be therefore directly related to β–Zn and Al containing parts in accordance with the previously discussed findings from SEM and LSM. While the isolated Al containing areas possess only marginal conductance (bright color), the β–Zn surrounding (darker appearance) demonstrates a significantly higher conductance. The scratches originated in the polishing process do not contribute to the overall conductivity. As a guide to the eye green dashed lines are shown in Figure 4.8a–c for direct comparison and separate the bottom right Al containing quadrant grain from the smaller isolated Al containing areas embedded in the β–Zn phase. Interestingly, a clear halo feature of β–Zn phase is encompassing the quadrant–like Al containing structure. This halo can also be noticed in the SEM as well as LSM images shown in Figure 4.4 and Figure 4.7 and is between 7.5 and 10 μm in width, exhibiting a rather conductive region. According to the c–AFM experiment, the β–Zn regions exhibit high conductivity, indicating the metallic character of the surface, whereas a passivating layer which limits the conductance is present on the surface of the Al containing areas.

Corrosion Behavior of the Alloy

The potentiodynamic polarization curves of pure Al and Zn, and Zn–10Al alloy in 2M NaCl solution are shown in Figure 4.9. The corrosion potential (E_{corr}) of Al was about −1.5 $V_{Ag/AgCl}$; thus, being more negative than for the Zn and the alloy while the cathodic and anodic currents were shifted to lower values. The shape of the anodic curve reveals a broad passive region down to −0.76 $V_{Ag/AgCl}$ with a passive current of about 7 μA cm^{-2}. The abrupt increase of the current at the end of the passive region is attributed to the breakdown of the passive film followed by an onset of the pitting mechanism [102,153,154].

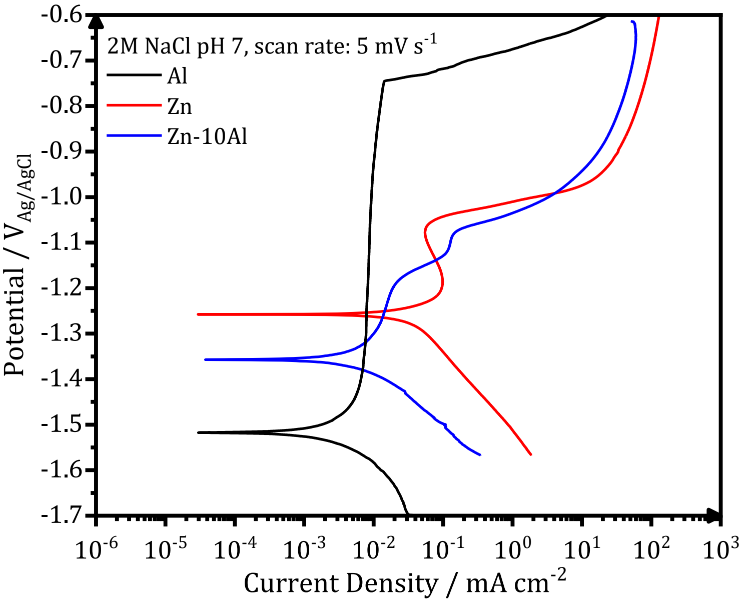

Figure 4.9: Potentiodynamic polarization curves of pure Al and Zn, and Zn–10Al alloy electrodes in 2M NaCl solutions with pH 7. The scans for each electrode were initiated at cathodic potentials toward the anodic direction with a scan rate of 5 mV s^{-1}.

The polarization curve of Zn represents a different behavior from that of Al. The curve in general was shifted toward higher currents while the E_{corr} of Zn was at more positive value (−1.24 $V_{Ag/AgCl}$). During the anodic polarization, a peak was observed which represents the anodic oxidation of Zn. The anodic current starts to increase around −1.0 $V_{Ag/AgCl}$ due to initiation of pitting. The Zn–10Al alloy exhibits a polarization curve which differs from pure Zn. The E_{corr} was enhanced toward negative direction by almost 100 mV in comparison to pure Zn. The anodic scan reveals two peaks that could be assigned for Al and Zn oxidation. Similar to Zn, there is pitting initiation around −1.0 $V_{Ag/AgCl}$.

The corrosion parameters extracted from the polarization curves are shown in Table 4-2. The corrosion current densities, which represents the rate of material dissolution, were obtained by Tafel fits in the range of ±50 mV relative to OCP. Among the three investigated electrodes, Zn exhibits the highest corrosion current density (16.2 μA cm^{-2}) while Al is the least susceptible electrode to corrosion with 1.5 μA cm^{-2}. The effect of Al alloying is visible on the corrosion current density that is lowered by almost 5 times (3.4 μA cm^{-2}) in comparison to Zn electrode. The corrosion rates calculated from gravimetric weight loss experiments are also included in Table 4-2. The intermediate term stability of the electrodes was investigated in 2M NaCl at pH value of 7 over 7 days of exposure. The Al electrode did not show any measurable weight loss owing to its passive behavior under steady state conditions. As expected, the highest corrosion rate was found for the Zn while the Zn–10Al alloy revealed more stable behavior in such immersion conditions. The results of the gravimetric weight loss experiments also confirm that Al alloying is advantageous in terms of reduced corrosion rates.

Considering the results from CV and galvanostatic discharge experiments, a different behavior of the alloy was observed in the potentiodynamic polarization curves. The essential difference originates from the fundamentals of the polarization experiment; the scan starts from the cathodic potentials toward anodic direction. During the cathodic range, the current is produced from either dissolved oxygen reduction or water reduction reactions [56]. The solutions were always degassed with Ar prior to experiments; hence, water reduction reaction is more likely to take place. Nevertheless, the common product of both reactions are hydroxyl ions (OH^-). Continuous cathodic polarization gives a rise to alkalinity at the local spots on the alloy surface due to the generation of OH^-. Accordingly, local alkalization results in hydration and/or dissolution of aluminum oxide and eventually, revealing the bare Al surface. This phenomenon is known as “cathodic corrosion of Al” or “activation of Al by cathodic polarization” [92–94]. The cathodic scan for the potentiodynamic polarization experiment was initiated at −1.7 $V_{Ag/AgCl}$ which is different in comparison to CV and galvanostatic discharge studies, thus enabling the activation of Al. Consequently, as shown in the polarization curves (Figure 4.9), the corrosion potential of pure Al is located at more negative potentials. The activity of Al cannot be kept at anodic potentials due to the very low solubility and limited generation of OH^- leading to formation of passive oxide film.

The activation of Al on the Zn−10Al surface influences the electrochemical behavior of the alloy. According to the mixed potential theory of Wagner and Traud [133], due to the electrochemical galvanic coupling reactions between the two metals in a binary alloy, the corrosion potential and corrosion current would be altered. The mixed potential theory suggests that the corrosion potential of an alloy should lie between the potentials of uncoupled two metals (Figure 4.1). When Al is activated, the potential of Zn−10Al alloy is found to be between Zn and Al potentials as shown in Figure 4.9. Moreover, the corrosion current density is also affected by alloying in line with the mixed potential theory.

Table 4-2 Corrosion parameters obtained from potentiodynamic polarization curves and gravimetric weight loss experiments.

	Polarization curves		Weight loss
	E_{corr} [$mV_{Ag/AgCl}$]	J_{corr} [µA cm^{-2}]	M_{corr} [µg cm^{-2} h^{-1}]
Zn	−1,242	16.2	4.43 ± 0.89
Zn−10Al	−1,350	3.4	2.61 ± 0.92
Al	−1,517	1.5	0

Discharge Behavior of the Alloy

After Al Activation in the potentiodynamic polarization studies, the effect of alloying was seen in terms of enhanced electrode potential with reduced corrosion current densities. For a battery application, however, the behavior of the electrode under galvanostatic polarization is of more interest. Therefore, different from the previous galvanostatic discharge experiments, an activation step was applied to enable the effect of alloying on the electrochemistry. Prior to discharge step, a cathodic potentiostatic pulse (−1.6 $V_{Ag/AgCl}$) was applied for 60 min.

Figure 4.10 represents the potential−time profiles of the Al, Zn, and Zn−10Al alloy electrodes in 2M NaCl at pH 7 over 24 h. The first period of 60 min corresponds to the cathodic pulse. The discharge profiles of the Al, Zn, and Zn−10Al alloy electrodes are depicted in Figure 4.10a,b, where a current density of 1 mA cm^{-2} was applied directly after the cathodic pulse. Initiation of the galvanostatic discharge resulted in a sudden drop of the potential of Zn to −1.02 $V_{Ag/AgCl}$ which is then stabilized around −1.00 $V_{Ag/AgCl}$. The potential of the Zn−10Al alloy first drops to −1.09 $V_{Ag/AgCl}$ within few seconds, and then remains at very close to Zn potential for the rest of the time. The Al electrode also exhibits a rapid drop to −0.80 $V_{Ag/AgCl}$ as soon as the current was applied. The potential plateau of Al was around −0.76 $V_{Ag/AgCl}$ over 24 h.

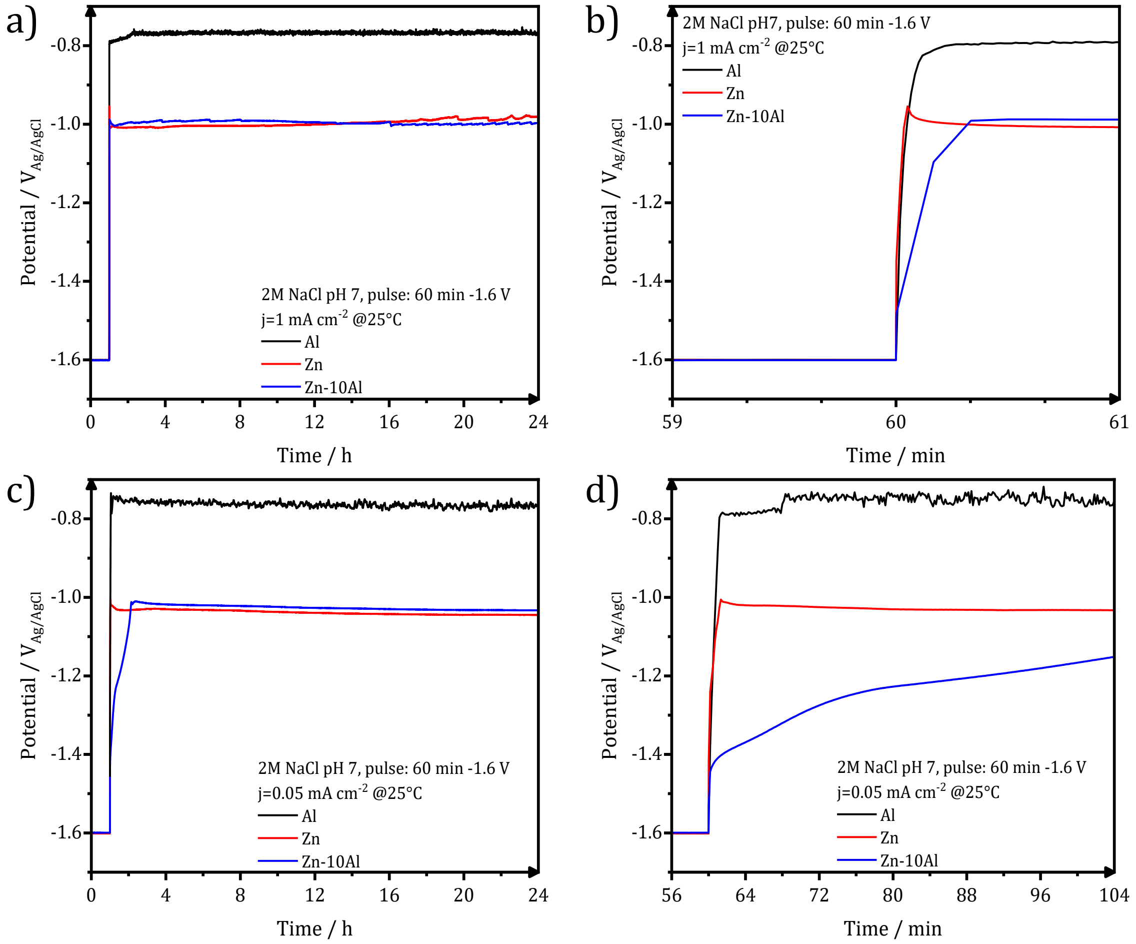

Figure 4.10: Galvanostatic discharge (stripping) experiments of pure Al and Zn, and Zn−10Al alloy electrodes: (a) Potential−time profile of electrodes under 1 mA cm^{-2} current density over 24 h, (b) Potential response upon initiation of the discharge with 1 mA cm^{-2}, (c) Potential−time profile of electrodes under 0.05 mA cm^{-2} current density over 24 h, (d) Potential response upon initiation of the discharge with 0.05 mA cm^{-2}. Initial 60 min of (a,c) correspond to the potentiostatic pulse of −1.6$V_{Ag/AgCl}$ which was applied to activate the Al constituents.

The discharge profiles in Figure 4.10a,b show that imposing a 1 mA cm^{-2} discharge current density on the electrodes vanishes all the effects of activation step. After application of a cathodic pulse for 60 min, the Al on the Zn−10Al alloy as well as pure Al electrodes are expected to be activated and thus, higher discharge potentials should be observed. On the contrary, the sudden drop of the electrode potentials to the values observed in Figure 4.6 suggests that the passive film was formed instantaneously on the Al compounds once the discharge was initiated. Most probably, the 1 mA cm^{-2} discharge current density was too high for the electrodes to sustain the active state. This can also be seen on the polarization curves (Figure 4.9), which illustrates that under 1 mA cm^{-2} current density the Al is already in the pitting stage.

In order to reveal the activation effect on the discharge profiles, significantly reduced current densities (0.005, 0.01, 0.05, 0.1 mA cm^{-2}) were employed subsequent to the cathodic pulse. As an example, the potential–time profiles of the electrodes under 0.05 mA cm^{-2} are depicted in Figure 4.10c,d. The lower current density applied showed no significant difference on the potential profiles of Zn and surprisingly of Al electrodes comparing to discharge profile with 1 mA cm^{-2}. The discharge plateau of Zn was slightly shifted to more negative values (around −1.03 $V_{Ag/AgCl}$) while for the Al there was only few mV difference. A marked difference was observed for the potential profile of Zn–10Al alloy. Instead of a sudden drop, the potential decreased only gradually over time. Within the first few minutes of discharge, there was a potential difference of more than 400 mV between the Zn and alloy electrodes. Even after 50 min of anodic polarization, the potential was still in favor of the alloy by 100 mV. The effect of the enhanced negative potential of the alloy lasted for over ~70 min until the potential plateau of Zn was reached. A summary of the time period analysis of the potential differences between Zn and Zn–10Al alloy under various current densities is depicted in Figure 4.11.

Figure 4.11 clearly shows that reduced current densities (<0.1 mA cm^{-2}) lead to significantly longer periods in which the discharge of Zn–10Al alloy can occur under stronger negative potentials than that of Zn. By discharging at 0.005 or 0.01 mA cm^{-2}, enhanced potentials (by 100 mV) of alloy are maintained for almost 1 h. The re-establishment of the passive film on the surfaces takes place much more slowly in the alloy in comparison to pure Al which passivated almost immediately. The fact that the activation effect during discharge was observed only for the Zn 10Al alloy can be explained by the presence of Al and Zn constituents together on the surface. In the case of pure Al electrode, the compact passive oxide film is established immediately on the activated Al surface due to the very little solubility limits of the discharge products. Thereby, even under 0.05 mA cm^{-2}, the surface instantly passivates, and the discharge continues by the adsorption of Cl$^-$ ions leading to initiation of pitting. For the alloy electrode, on the other hand, the Al is present with Zn in the alloy constituents which, most likely, prevents the formation of compact passive film on the Al. It is also known that Zn promotes the specific adsorption of Cl$^-$ ions on it, which may retard the instant Al passivation [155,156]. Consequently, originating from the mixed potential theory, the alloy electrode exhibits a higher discharge potential until the Al compounds are partially exhausted or eventually passivated. Further investigations are required in order to understand the dissolution mechanism, whether it is a co–discharge of Zn and Al or only Al, during the enhanced potential periods.

Under different conditions, Zhang et al. investigated the selective dissolution of Zn and/or Al from a Zn–Al alloy by using online atomic emission spectroelectrochemistry (AESEC) method [157]. Studies on the release rate of Zn and Al from Galvalume (55 wt.% Al, 43.4 wt.% Zn, 1.6 wt.% Si) in synthetic sea water (0.56M NaCl with pH 8.1) during ~40 min immersion and OCP experiments resulted in significantly higher zinc release rates in comparison to aluminum. Under an anodic potential of −400mV$_{NHE}$, mostly Zn was dissolved from the surface during the initial period. Over time, the release rate of Zn was lowered gradually, while for Al it was increasing slowly before reaching a plateau. After 40 min of anodic polarization, 56% of the total amount of dissolved metals was aluminum under such high anodic potentials. Thereby, it was shown that co–dissolution of both metals during anodic polarization is possible.

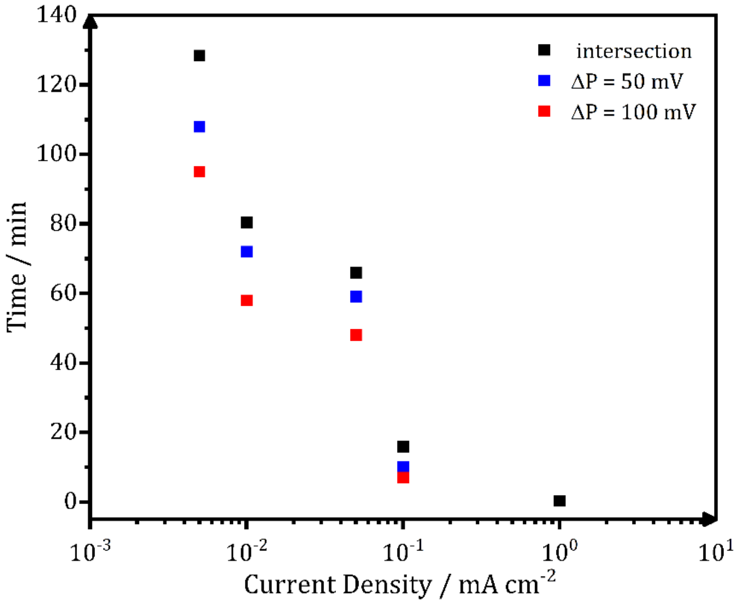

Figure 4.11: The time period analysis of the potential differences between Zn and Zn–10Al alloy electrodes during galvanostatic discharge experiments (see Figure 4.10) under various current densities.

All in all, the results obtained in this study clearly show that the electrochemical and corrosion behavior of zinc electrode can be influenced by alloying with aluminum under certain conditions. At low discharge currents, Al–alloying of the Zn provides enhanced discharge potentials for a limited time span after applying cathodic pulses to the cells. To be applicable as an anode material in a Zn–air battery, the stability of the discharge potentials with respect to discharge currents and time has to be considerably improved.

Summary and Remarks

Alloys containing 90wt.% Zn and 10wt.% Al were prepared, and the chemical composition was corroborated by ICP–OES, while the microstructure was validated by SEM and EDS. The electrochemical behavior of the Zn–Al alloys was initially evaluated by cyclic voltammetry and galvanostatic discharge (half–cell stripping). Both techniques revealed electrochemical inactivity of the Al in the potential range scanned during the CVS and no significant improvement on the observed discharge potentials of the alloy. The Zn and Zn–10Al electrodes displayed potentials around −1.0 to −1.05 $V_{Ag/AgCl}$, whereas the potential of the Al electrodes was around −0.76 $V_{Ag/AgCl}$ under the applied anodic current densities. The Al is assumed to be in a passive state, while the Zn is possibly the only active specie in the alloy. Further support was provided by LSM measurements, revealing the preferential consumption of Zn–rich constituents. Similarly, AFM analysis showed also lower conductivity of the Al–rich areas.

However, potentiodynamic polarization experiments of Zn, Zn–10Al and Al electrodes revealed corrosion potentials higher than the open circuit potentials, probably influenced by the initial cathodic potentials applied during the technique. Accordingly, the cathodic activation of the electrodes occurs through “local alkalization” upon water hydrolysis and OH^- ions formation, which can remove the possible passive layer on the electrodes surface. Based on this assumption, 60 min of cathodic polarization at −1.6 $V_{Ag/AgCl}$ were applied prior to the discharge experiments, revealing enhanced potentials of the Zn–10Al alloy over 120 min under low current densities (0.005 mA cm^{-2}). The “activation” effect was more limited under higher anodic current densities with practically no enhancement under 1 mA cm^{-2}.

Although the results of Zn–10Al are promising, the constant use of a cathodic pulse to activate the battery is not feasible in practical applications. Therefore, an alternative to reach the theoretical higher potentials of Al is needed. Moreover, the results of the potentiodynamic polarization also indicate to a possibly higher potential of Zn. One of the possible options to achieve higher potentials could be by the use of electrolyte additives capable of “activate” the surface of the metal electrodes.

Chapter 5: Effect of EDTA as Electrolyte Additive in Near–Neutral Zinc–Air Batteries

The present chapter presents the results published in the article "Improved Electrochemical Performance of Zinc Anodes by EDTA in Near–Neutral Zinc–Air Batteries" available in *Batteries and Supercaps*, 2021, 4, 1–14 [158]. The publication was also included as "Cover Feature" in the issue *Batteries and Supercaps, 12/2021* and can be found in the Figure A–5 [159].

5.1. Motivation

As discussed in the previous chapter, Zn, Zn–10Al and Al electrodes can be discharged in the neutral electrolyte, while the potential enhancement was only revealed after a cathodic activation pulse and were limited to several minutes under low discharge conditions. The latter was caused by the formation of passive film on the surface upon discharge conditions, blocking the active material underneath as explained in Figure 2.2, Figure A–6. In this regard, an alternative to prevent the formation of passive films could be the addition of chelating agents.

Figure 5.1 presents the ethylenediaminetetraacetic acid (EDTA) as an example of the chelating agents. This type of additive presents different functional groups (like $-COOH$, $-NH_3$, among others, as shown in Figure 5.1a) also called ligands, which are capable of binding to several of the active sites of a metal cation (Figure 5.1b,c). The resulting compound is soluble under a relatively wide range of pH values due to the overall (mostly) negative charged structure (see Figure A–6d).

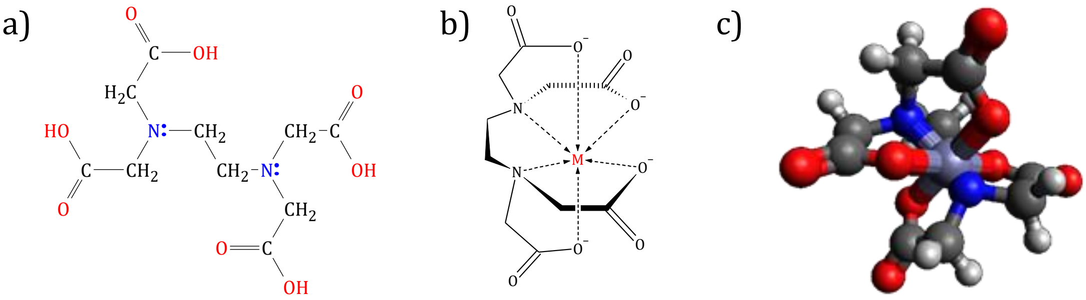

Figure 5.1: a) Molecular formula of EDTA, b) 2D and c) 3D general structure of EDTA–Metal complex (atom colors: black=carbon, white=hydrogen, red=oxygen, blue=nitrogen, and pale blue=zinc).

The word chelation derives from the Greek word "claw", which is an appropriate analogy to the phenomenon occurring between the metal and the chelation agent. The "claws" of such additives are formed by the functional groups, “isolate” the metal ion in the middle of the structure and the resulting metal–complex molecule is highly soluble. Moreover the “claws” (ligands or functional groups) mostly present one or several H atoms which can be dissociated, meaning that they can be ionized and “separated” from the complexing molecule. Such transition can be observed by the comparison of Figure 5.1a and Figure 5.1b, where the H atoms on the –OH group are absent after deprotonation and the resulting O^- group can bond to the metal ion.

The number of “free” ligands of a complexing molecule is also described by the *acid dissociation constants* K_a, which is similar to the equilibrium constants K_n. However, K_a represents the acid strength and the degree of dissociation and easiness to donate its protons (H^+ ions). The following equation applies for monoprotic acids (acids with a single H^+ ion):

$$HA \xleftrightarrow{K_a} H^+ + A^- \qquad K_a = \frac{[H^+][A^-]}{[HA]} \tag{5.1}$$

where HA is the acid, H^+ is the dissociated proton, A^- is the conjugate base (in this case the dissociated complexing agent) and K_a is the acid dissociation constant determined by the ratio of the H^+ and A^- concentration over the initial concentration of the acid HA. The *acid dissociation constant* is more commonly represented by its negative logarithmic value, according to the following equation:

$$pK_a = -\log(K_a) \tag{5.2}$$

Polyprotic acids like EDTA possess several hydrogen atoms which can be dissociated; thus, it presents 6 different pK_a values. Furthermore, the dissociation of a molecule is pH dependent and calculated based on its pK_a values. A list of pK_a and the corresponding fractional composition diagrams for several complexing agents and pH buffering additives can be found in the Appendix 7 “Chelating Agents and pH Buffering additives: Structure and Properties” in Table A–3, Figure A–11, Figure A–10, and Figure A–12. A larger number of “free” ligands (pK_a) is preferred for a more stable metal–complex molecule, meaning that the fully dissociated molecule will have an optimum chelation ability. The strength of the bonding between the metal and the chelating agent is numerically defined by the *stability constant of complexation* β and is described for the fully dissociated acid, hereby represented as Y^{4-} for EDTA:

$$M^{n+} + Y^{4-} \xleftrightarrow{\beta} MY^{n-4} \qquad \beta = \frac{[MY^{n-4}]}{[M^{n+}][Y^{4-}]} \qquad \textbf{5.3}$$

Where M^{n+} is the metal ion, Y^{4-} is the fully dissociated EDTA, and β is the stability constant of complexation, which is analogously similar to the formation constants in the Equations A–6, A–7, and A–8. Similarly, larger values of β indicate higher reaction probabilities and higher stability of the molecule formed. Accordingly, the reaction products will depend on the magnitude of β and the K_n of the typical reaction products without the chelating agents, whereas the metal–complex will more likely form if β is higher than the K_n. A list with β–values for different complexing agents can be found in the Table A–4.

Based on the formation constants and the stability constants of complexation, predominance diagrams can be generated in order to predict or gain better understanding on the behavior of a metal after dissolution. Figure A–13 presents the specie predominance of Zn and Al depending on their respective concentrations versus pH assuming a 2M Cl^- concentration. Additional specie formation of Zn and Al depending on their respective concentrations versus the EDTA concentration at pH value of 7 (black lines) and pH value of 10 (red lines) is also included in Figure A–13. The diagrams were created using the Make Equilibrium Diagrams Using Sophisticated Algorithms (MEDUSA) software [160]. Although thermodynamic and chemical equilibria information is currently available in the literature, there is limited knowledge on the electrochemical performance of the chelating agents such as EDTA in the near–neutral media. Therefore, the electrochemical evaluation and correlation to the thermodynamic predictions of the chelating agents is scientifically relevant and could allow better performances of near–neutral Zn–air batteries. Previous studies have shown a more electrochemically active electrode in presence of EDTA for both metals (Al and Zn, separately) since higher open circuit potentials and corrosion potentials are attained [106,161]. Nevertheless, no publication up–to–date has widely explored the electrochemical activity of both electrodes after addition of EDTA in the near–neutral electrolytes.

In order to corroborate the observations of the earlier publications, mid–term OCP measurements of the Zn, Zn–10Al and Al in absence and presence of 0.1M EDTA were conducted as an initial study. Figure 5.2a shows the OCP profiles of the three different electrodes in 2M NaCl pH 7 as a reference, displaying potentials between −1.15 and

−1.0 $V_{Ag/AgCl}$. Upon addition of 0.1M EDTA in Figure 5.2b, the potentials of Zn and Zn−10Al are initially slightly increased to almost −1.2 $V_{Ag/AgCl}$ but decrease along the 24 h to −1.1 $V_{Ag/AgCl}$, whereas the Al shows a significant increase to around −1.35 $V_{Ag/AgCl}$. Various advantages can be achieved by increasing the pH from 7 to 10, namely i) higher potentials for the Zn and Al (see Figure 4.2), ii) a higher dissociation of EDTA (see Figure A−11), and iii) higher solubility limits of the Zn−EDTA and Al−EDTA complexes before precipitation (see Figure A−13).

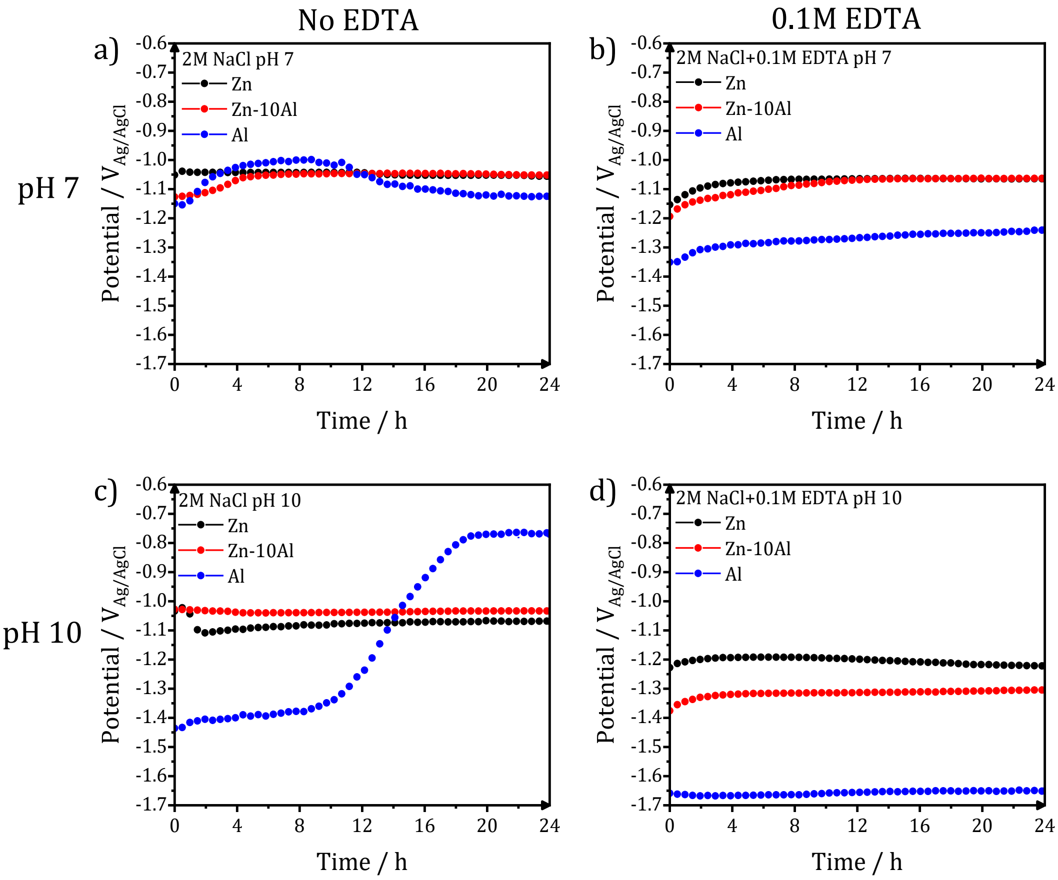

Figure 5.2: OCP profiles of Zn (black circles), Zn−10Al (red circles), and Al (blue circles) in 2M NaCl at a) pH 7 without EDTA, b) pH 7 with EDTA, c) pH 10 without EDTA and d) pH 10 with EDTA.

As a reference of the changes induced by the increase of the pH value, OCP measurements of Zn, Zn−10Al and Al were carried out in 2M NaCl pH 10 without EDTA. Figure 5.2c reveals similar potentials for the Zn and Zn−10Al in the electrolyte without at pH 10 in comparison to pH 7 (Figure 5.2a). The Al electrodes, on the other hand, initially showed an increase on the potential to −1.45 $V_{Ag/AgCl}$ after immersion in the electrolyte at pH 10 (blue circles in Figure 5.2c), but continuously decrease with a sharp decline after 10 h and stabilize at −0.77 $V_{Ag/AgCl}$ after 19 h. The largest increase on the potential was observed in combination of pH 10 and the addition of 0.1M EDTA (Figure 5.2d), where the Al displayed stable OCP values of −1.65 $V_{Ag/AgCl}$ with over 650 mV increase in comparison to the OCP observed at pH 7 without EDTA. Moreover, Zn and Zn−10Al presented potentials of −1.22 and −1.3 $V_{Ag/AgCl}$, respectively. Accordingly, the potential for Zn and Al is larger at higher pH (see Figure 4.2), while the fully dissociation of EDTA also increases (see Figure A−11). It is noteworthy to mention that the OCP values of Zn and Al in Figure 5.2d are close to the theoretical potentials presented by the Pourbaix diagrams, whilst the potential displayed by the Zn−10Al alloy immersed in the electrolyte with EDTA at pH value of 10 is higher in comparison to the potential of Zn without requiring a "cathodic" activation.

Although the previous results are encouraging for the three electrodes, the present study focuses on the further electrochemical evaluations basing only on the Zn electrodes due to their cyclability features [76–81]. Therefore, this section of the current work will focus on the effects of EDTA on zinc anodes only, whereas the electrolyte with 0.1M EDTA at pH value of 10 will be selected due to the better chelating abilities of the EDTA which enhances the Zn electrode potential more pronouncedly. In addition, the predicted reaction products are only $Zn(EDTA)^{2-}$, $Zn(OH)_2$, and ZnO (black lines in Figure A−13), while Zn−Cl reaction products typically produced at pH 7 are avoided (red lines in Figure A−13). The formation of Zn−Cl species could consume the chloride−based electrolyte, leading to premature termination of the cell discharge. The outcome of this study could give some insights on the addition of chelating additives in the electrolyte to achieve better performances of near−neutral Zn−air batteries.

5.2. Experimental Section

Material preparation and chemicals: Zinc rod (4N) was acquired from Alfa Aesar. The electrodes were prepared by cutting sections of the Zn rod into 1.25 mm thickness discs. For the half−cell experiments, the Zn discs were embedded in cold mount epoxy (EpoFix, Struers) and the surfaces of the electrodes were prepared by grinding with 800 SiC sandpaper. The exposed area of the electrodes for half−cell and full−cell experiments were 1.32 cm^2 and 0.44 cm^2, respectively. The 2M NaCl−based electrolyte solutions were prepared from NaCl crystals (≥99.5%, Merck−Millipore) and Ethylenediaminetetraaceticacid (EDTA) (99.3%, VWR Chemicals). Deionized water was obtained from a PURELAB Elga water purification system (conductivity<0.1 $\mu S\ cm^{-1}$). The electrolyte solutions were prepared by dissolving the NaCl and EDTA in deionized water, and then the pH of all solutions was initially adjusted to pH 10 with NaOH solutions by the help of a dual pH/conductivity meter (Duo S213, MettlerToledo).

Electrochemical half–cell setup: The half–cell used in this section was previously described in Figure 2.1. The potentiodynamic polarization tests were undertaken in the range from $-1.6\ V_{Ag/AgCl}$ to $-0.6\ V_{Ag/AgCl}$ starting from cathodic potentials. Half–cell stripping (or galvanostatic discharge) was performed under 0.1, 0.25, 0.5 and 1 mA cm^{-2} current densities with a cut–off potential of $-0.5\ V_{Ag/AgCl}$.

Electrochemical full–cell setup: The full–cell setup consisted of freshly ground Zn discs as anode, porous carbon–based commercial air electrodes (E4 type, ElectricFuel Ltd), and 2M NaCl with pH value of 10 with and without addition of EDTA (0.1M). The full–cell is made of three poly(methyl methacrylate) (PMMA) discs with an inner volume of 0.6 mL. The details of the cell setup can be found in a previous study [41]. The symmetrical exposed area of the anode and air cathode to the electrolyte was 0.44 cm^2. The cell was connected to a pump (Reglo Analog MS–4/112, Ismatec) and to a reservoir with capillary tubes ($ø_{in}$=0.75 mm. PEEK, BOLA). The electrolyte was circulating in bottom–top direction. Both ends of the full–cell were connected to the same reservoir which contained 20 mL of the electrolyte. Following the discharge experiments, the weight loss of the Zn electrodes was calculated after cleaning with saturated Glycine solution according to DIN EN ISO 8407 [162]. A continuous recirculation of the electrolyte from a reservoir was performed for the full–cell discharge experiments. The electrolyte of the full–cell cycling experiments was circulated by pumping every 25 min for 5 min with a flow rate of 0.1 mL min^{-1} for each cell in order to provide enough dissolved Zn. The intermittent operation of the pump was controlled by a TTL pulse via the analogue connection of the Biologic VMP3 potentiostat.

All the experiments were conducted in a climate chamber (Binder KMF115) to keep constant conditions of 25°C and 50% r.h. and electrochemical experiments were controlled with a Biologic VMP3 potentiostat.

Sample analysis and microscopy: Characterization of the microstructures of the Zn anodes after discharge was done by confocal laser scanning microscopy (OLS4100, Olympus Corp., Japan) and scanning electron microscopy (Quanta 650, FEI, USA) using the Everhart–Thornley Detector (ETD). The elemental analysis was performed by energy–

dispersive X–ray spectroscopy (EDX) (Octane Super Detector, EDAX, USA) and the corresponding phase maps were obtained by using TEAM EDAX software. The SEM measurements were performed with 20 kV of applied acceleration voltages. Crystallographic characterization of the Zn anode surfaces was performed by X–ray diffraction (XRD) (Cu–source Empyrean, Malvern Panalytical, Germany).

5.3. Experimental Results and Discussion

Open circuit potential and potentiodynamic polarization

Figure 5.3 shows the OCP profiles of Zn in 2M NaCl at pH 10, in absence (black curve) and presence (red curve) of EDTA. The potential of Zn in neat 2M NaCl starts at initial values of around −1.05 $V_{Ag/AgCl}$, slightly increasing to −1.11 $V_{Ag/AgCl}$ after 2 h and then slowly decays to −1.06 $V_{Ag/AgCl}$ after 24 h, while the potential of Zn in 2M NaCl with 0.1M EDTA is stable at around −1.22 $V_{Ag/AgCl}$ during the 24 h of OCP experiment. Thus, the addition of EDTA to the 2M NaCl results in an increase of the potential of about 170 mV.

The increase of the initial potential towards more negative values along the first 2 h of the Zn in the 2M NaCl could be attributed to the slow adsorption of OH^- ions present in the electrolyte. Subsequently, slight decay of the potential results from the drop on the pH value due to the lack of buffering capabilities of NaCl solutions [163]. According to the Pourbaix diagram of Zn (Figure 4.2a), the cell potential slightly decreases (around 160 mV) when the pH value changes between 11 and 8.5 [121,134]. Measurement of the pH value of the electrolyte after the 24 h of OCP supports this observation, since the pH value drops from 10 to around 8 while there is also 50 mV decrease on the electrode potential. The limited decay of the electrode potential can be due to the quasi–passive state of the Zn surface since it is not completely active. In line with the Pourbaix diagram [121,134], the potential of Zn at pH 10 should be around −1.25 $V_{Ag/AgCl}$ (−1.03 V_{SHE}). However, the experimental results indicate that the surface of Zn is in a quasi–passive state since the potential of the Zn in the neat 2M NaCl is lower than the expected value. On the other hand, addition of EDTA to the 2M NaCl results in an enhanced potential to −1.22 $V_{Ag/AgCl}$, which is similar to the potential given by the Pourbaix diagram.

The enhancement of the potential in presence of EDTA can be attributed to two main factors: (1) the chelating properties of EDTA, and (2) an increase of the pH stability of the NaCl electrolyte. The chelation process (or complexation) prevents the formation of insoluble species of Zn, resulting in highly soluble Zn–EDTA complexes. However, EDTA can be present as several dissociated species (6 possible deprotonated species) depending on the pH value, where the completely deprotonated species are more effective for complexation (30% EDTA is fully dissociated at pH 10 [115]). The addition of EDTA to the 2M NaCl solution increases the pH stability of the electrolyte, as observed from the almost unaffected pH of the electrolyte after the 24 h of OCP experiments in presence of EDTA. Also, the higher potentials with EDTA in comparison to neat NaCl solution corroborates the absence of a passive film on the Zn surface.

Possible mechanisms of the interaction between the Zn and EDTA can be found in the literature, among which Ryczkowski[164] demonstrated via (PA) FT–IR (Photoacoustic Fourier transform infrared spectroscopy) that EDTA could be adsorbed on some inorganic oxides and hydroxides. Different adsorption mechanisms were proposed depending on the pH of the solution and the nature of the metal surface involved in the chelation, namely if it consisted of oxides, hydrous oxides, hydroxides, oxyhydroxides, hydrous or superficially hydrated oxides [164,165]. Moreover, previous studies have shown that EDTA is capable of leaching metal ions from oxides or hydroxides [166–168]. Hence, similar mechanisms could also be the origin of the EDTA influence on the Zn potentials shown in this study.

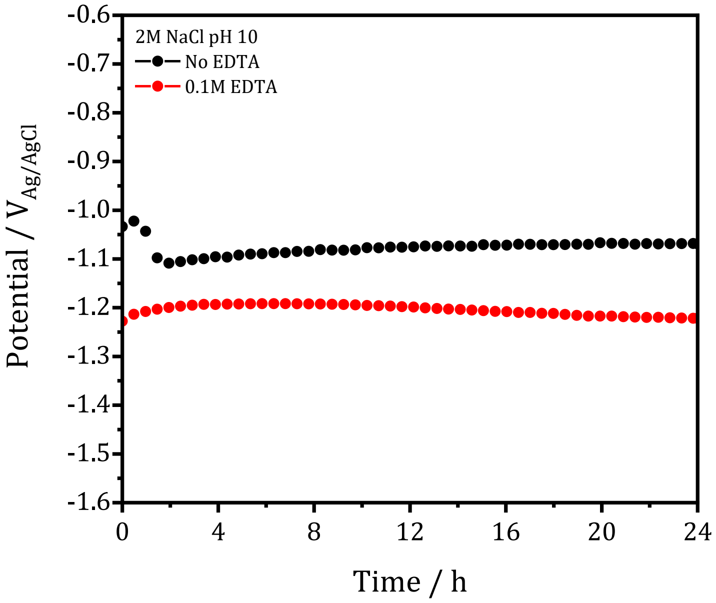

Figure 5.3: OCP profiles of Zn in 2M NaCl at pH 10 in absence (black curve) and presence of 0.1M EDTA (red curve).

Further experiments were performed by potentiodynamic polarization method to get more insights on the possible influence of EDTA on the electrochemical behavior of Zn in NaCl electrolytes. Figure 5.4 shows the potentiodynamic polarization of Zn in neat

2M NaCl (black curve) and in presence of 0.1M EDTA (red curve). The corrosion parameters were obtained by Tafel fit in the range of ±50 mV of the corrosion potential (E_{corr}) and are summarized in Table 5-1.

Table 5-1: OCP values and corrosion parameters derived from potentiodynamic polarization of Zn in 2M NaCl at pH 10.

	OCP after 24 h / mV	Potentiodynamic polarization	
		E_{corr} / mV	J_{corr} / µA cm^{-2}
No EDTA	−1070	−1255.5±4.7	4.8±0.9
0.1M EDTA	−1220	−1323.0±6.9	5.4±0.8

The E_{corr} of Zn in neat 2M NaCl is around −1.25 $V_{Ag/AgCl}$, while addition of EDTA shifted the E_{corr} to −1.32 $V_{Ag/AgCl}$. The corrosion current densities are obtained as 4.75 and 5.39 µA cm^{-2} in absence and presence of EDTA, respectively. Both curves show a shoulder at around −1.08 V without EDTA and −1.0 V in presence of EDTA. These shoulders resemble a passivation peak, where the current slightly decreases as the anodic scan continues. However, the current densities continue increasing at potentials more anodic than the semi–passivation peak, indicating that the Zn could still readily react. The rapid increase on the current densities originate from pitting caused by the chloride ions, which starts at around −1.05 $V_{Ag/AgCl}$ ($E_{pitting}$) [56].

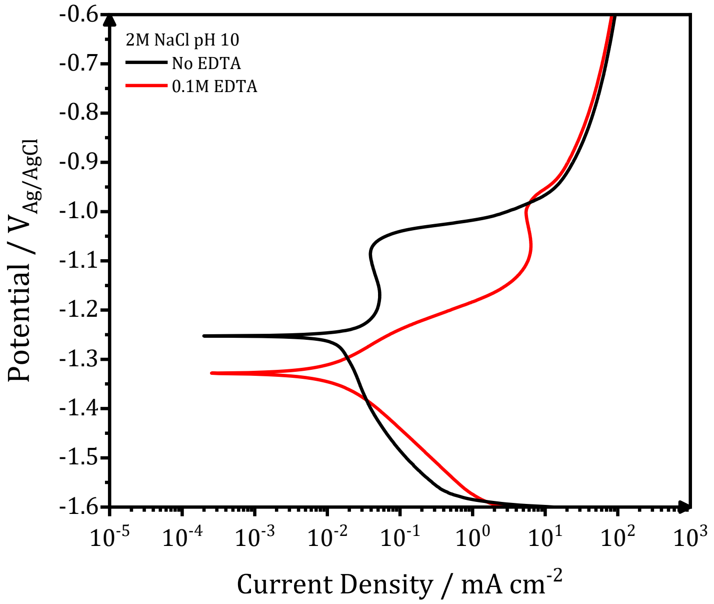

Figure 5.4: Potentiodynamic polarization of Zn in 2 M NaCl at pH 10 in absence (black curve) and presence of 0.1 M EDTA (red curve) with a scan rate of 5 mV s^{-1}.

The slight decrease on the current densities between E_{corr} (−1.25 $V_{Ag/AgCl}$) and $E_{pitting}$ (−1.05 $V_{Ag/AgCl}$) during the potentiodynamic polarization of Zn in neat 2M NaCl confirms the existence of a passive film. On the contrary, the potentiodynamic polarization of the

Zn in presence of 0.1M EDTA shows less significant passivation peak, but a higher E_{corr} and larger current densities in the range from E_{corr} (−1.32 $V_{Ag/AgCl}$) to $E_{pitting}$ (−1.05 $V_{Ag/AgCl}$) in comparison to the solutions not containing EDTA. Under high anodic polarizations (>−1.0 $V_{Ag/AgCl}$), the current response of the Zn for both solutions show almost identical behavior; hence, it suggests that there might be a limiting current for the effectivity of EDTA on the enhanced potentials but no visible adverse effect in comparison to neat electrolyte.

The fact that the OCP is more positive than the E_{corr} for the solutions with and without EDTA can be explained through the cathodic corrosion of Zn in chloride solution [169]. As proposed by Baugh [155], water reduction occurs at potentials more cathodic than −1.37 $V_{Ag/AgCl}$ on Zn in chloride based solutions according to the following reaction:

$$2H_2O + 2e^- \rightarrow 2OH^- \tag{5.4}$$

Since the present polarization experiments start at −1.6 $V_{Ag/AgCl}$, OH^- ions from hydrolysis could be produced in relatively high amounts. Upon the local concentration increase of the produced OH^- ions, "local alkalization" can occur on Zn resulting in cathodic corrosion [169,170]. Although the Zn is immersed in near–neutral electrolyte, local dissolution of a possible passive layer could also be expected similarly as in the alkaline electrolytes [56]. Furthermore, Prestat et al. studied the reaction products of Zn under prolonged cathodic potentials in near–neutral NaCl media, where Raman microscopy and X–ray diffraction revealed the presence of metallic Zn after holding a cathodic potential of −1.27 $V_{Ag/AgCl}$ for at least 17 h. It was reported that ZnO is mainly present in the range from −1.04 to −1.26 $V_{Ag/AgCl}$, while Simonkolleite mainly appears at potentials anodic to −1.01 $V_{Ag/AgCl}$ [169]. Thus, the reaction products on Zn electrodes show differences depending on the potentials that were applied and most likely, also on the polarization durations.

According to the potentiodynamic polarization curves, the observed E_{corr} of Zn in 2M NaCl without EDTA (Figure 5.4) corresponds to the potential of neat Zn, which is activated by the cathodic polarization. Further evidence for the cathodic activation of Zn can be found in previous studies which report the polarization curves of Zn electrodes in NaCl solutions and are summarized in Table A–5 and Table A–6. If the initial scan potential for the potentiodynamic polarization is more cathodic than the water reduction potential (<−1.37 $V_{Ag/AgCl}$), the resulting E_{corr} is also more negative than the commonly reported open circuit potentials (<−1.05 $V_{Ag/AgCl}$), which is in good agreement with the present work [170–172]. Contrariwise, the corrosion potential of Zn near −1.05 $V_{Ag/AgCl}$ is usually obtained when the initial scans start at more positive values than the water reduction potential [173,174]. Therefore, it can be stated that neither the NaCl concentration, pH, scan rate, electrode area, immersion time nor counter electrode have no influence on the resulting E_{corr} derived from the potentiodynamic polarization. On the other hand, the reported E_{corr} is more dependent on the potential at which the potentiodynamic experiments were started.

In contrast to the neat 2M NaCl electrolyte, the resulting polarization curve of the electrolyte containing 0.1M EDTA is affected by the cathodic activation, only at a minor degree. More specifically, the difference between the OCP and E_{corr} in the electrolyte without EDTA is around 185 mV, while for the electrolyte containing 0.1M EDTA is around 102 mV. In the OCP profiles, however, the overall enhancement of the potential with the addition of EDTA to the electrolyte is around 150 mV, and the increased potential is stable without the necessity of a cathodic polarization. This effect can be attributed to the chelation properties of EDTA and the increased pH stability of the NaCl solutions containing 0.1M EDTA due to its buffering capabilities.

Galvanostatic discharge / Half–cell stripping

As previously examined by the OCP profiles and potentiodynamic polarization experiments, the Zn is in a quasi–passivated state in the 2M NaCl, while addition of EDTA allegedly hinders the formation of a passive film resulting in a more active metallic Zn surface. The semi–passivated (without EDTA) and activated (with EDTA) state of Zn was further investigated under several anodic current densities (galvanostatic discharge or half–cell stripping) as presented in Figure 5.5.

Figure 5.5a shows a stable discharge potential of Zn in neat 2M NaCl at around −1.03 $V_{Ag/AgCl}$ under 0.1 to 1 mA cm^{-2} anodic currents, while the discharge potential of Zn in EDTA containing electrolyte (Figure 5.5b) is around −1.25 $V_{Ag/AgCl}$ under 0.1 and 0.25 mA cm^{-2}. The resulting potential of Zn in presence of EDTA is initially lower at −1.14 $V_{Ag/AgCl}$ under 0.5 mA cm^{-2} and at −1.1 $V_{Ag/AgCl}$ under 1 mA cm^{-2}, but in both cases the potential increases to −1.25 $V_{Ag/AgCl}$ within 12 hours. The reason for this gradual shift to more negative discharge potentials upon 0.5 and 1 mA cm^{-2} in presence of EDTA is still unknown and needs further investigation. Overall, the average discharge potentials are

220 mV more negative for all the applied currents on Zn in presence of 0.1M EDTA and directly increase the power output in comparison to the Zn discharged in neat 2M NaCl.

According to Pourbaix diagram [121,134], the immunity region of metallic Zn remains below the stability window of water in aqueous solutions and therefore Zn dissolves while producing H_2. Zn is in the "passive" regime at pH 10 and should not display potentials at around −1.25 $V_{Ag/AgCl}$. The discharge potential of Zn in the neat electrolyte at pH 10 is not significantly different in comparison to discharge behavior in 2M NaCl with pH 7 [132]. The lack of enhanced potential at pH value of 10 could be partially explained by the poor pH stability of neat NaCl solutions, since the pH value of such solutions is dependent on the salt concentration and the resulting effect on the activities of H^+ and OH^- [115]. Experimentally, the poor pH stability of neat NaCl is confirmed by the drop of the pH value from 10 to around 8 after the galvanostatic discharge (the pH value of the solutions was measured before and after the experiments by the pH electrode). Thus, lower pH values also contribute to lower potentials of Zn in accordance with Pourbaix. The almost unaffected discharge potential under different current densities (Figure 5.5a) in the neat electrolyte suggests the discharge of Zn continues through pitting mechanism, which agrees with the results from the potentiodynamic polarization experiments. Moreover, the possible presence of a passive film seems to reduce the potential of Zn but does not inhibit the dissolution.

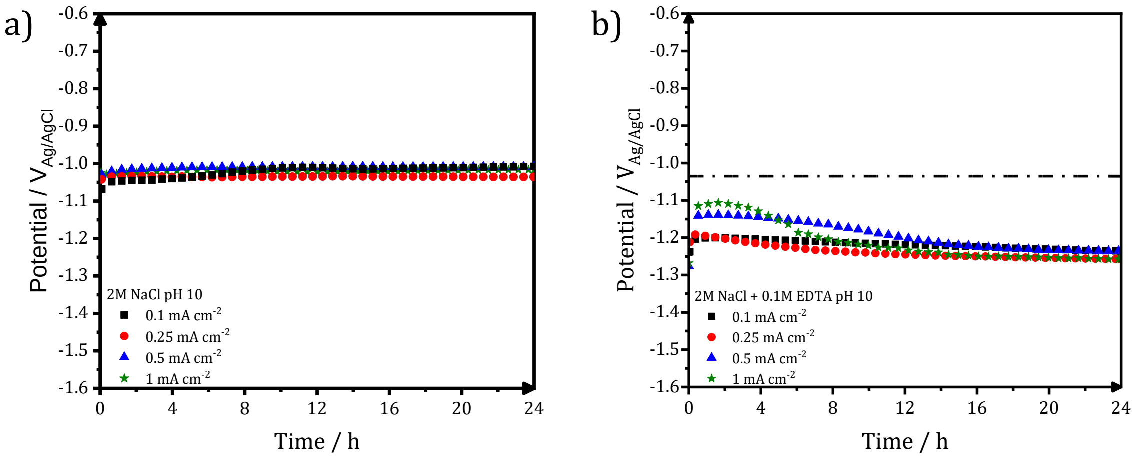

Figure 5.5: Galvanostatic half–cell discharge of Zn in 2M NaCl at pH 10 under 0.1, 0.25, 0.5 and 1 mA cm^{-2} in a) absence of EDTA and in b) presence of 0.1M EDTA. The abscissa in (b) illustrates the average discharge potential of the Zn electrodes in the neat electrolyte (obtained from (a)).

In order to understand the possible origin of such passive film in presence of neat NaCl, a reaction mechanism of Zn during discharge is hereby provided. As previously discussed, Zn spontaneously reacts in aqueous solutions as described by Equation 1.17.

According to McMahon et. al. [163], the Zn^{2+} ion is quite abundant at low Cl^- concentrations (0.06M), while its ion fraction is almost zero at high Cl^- concentrations (5.45M). Accordingly, Zn^{2+} is not stable in 2M NaCl and will tend to further react as described in the equation 1.18 and 1.19.

For simplicity, the $Zn_5(OH)_8Cl_2 \cdot H_2O$ reaction product will be referred hereafter as Simonkolleite, which is a white and low water–soluble powder. Upon saturation, the continuously produced $Zn(OH)_2$ from Equation 1.18 can further react depending on the local pH and Cl^- concentration as expressed by Equation 1.20, 1.21 and 1.22.

The formation of ZnO requires a dehydration of a stable layer of $Zn(OH)_2$ upon local saturation, as described by Equation 1.20 [121]. Under anodic conditions, the production of $Zn(OH)_2$ increases, and the saturation is faster reached, which possibly promotes the production of ZnO. Given the bulk conditions of the neat 2M NaCl, production of zincates ($Zn(OH)_4^{2-}$) can occur only at a minor degree in near–neutral electrolytes since it requires high pH conditions. Prestat et. al. could mainly identify Simonkolleite at potentials close to −1.02 $V_{Ag/AgCl}$ while ZnO is mainly found at −1.12 $V_{Ag/AgCl}$ in 0.6M NaCl solutions [169]. In accordance with the potentials observed in the discharge experiments (−1.03 $V_{Ag/AgCl}$), a mixture of reaction products Simonkolleite, ZnO and $Zn(OH)_2$ could be expected, where a thin but still present layer $Zn(OH)_2$ is the intermediate compound before the formation of ZnO and Simonkolleite [155,169]. These products are the proposed compounds of the passive film.

Furthermore, depending on the applied currents, white flake–like precipitates were present in the electrolyte at the end of the experiments. For instance, after 24 h discharge at 1 mA cm^{-2} there are appreciable precipitates, while the electrolyte is relatively clear after 24 h at 0.1 mA cm^{-2}. Table A–7 shows a summary of the physical properties of the possible reaction products of Zn in NaCl electrolytes. $Zn(OH)_2$, ZnO and Simonkolleite are all white precipitates and are between 127 and 234% larger in volume than the metallic Zn. The volume increase of the reaction products and the subsequent mechanical stress produced could partially explain the presence of such precipitates.

A possible way to decrease or even completely prevent the formation of a passive film on the Zn surface could be achieved by using complexing agents in the electrolyte, which are widely used in chemistry due to their chelation properties with metallic ions. The resulting complex species are highly soluble in water [115]. In the chelation process, the metallic ion is surrounded by the complexing agent and the reaction between the metallic ion and the surrounding media is reduced. The bonding strength between the metallic ion and the complexing agent is indicated by the magnitude of the chelation stability constants, where higher values result in more stable complexes. The increase on the discharge potential of Zn upon addition of EDTA to the 2M NaCl could be therefore attributed to the relatively high chelation stability constant of EDTA with the Zn^{2+} ions (16.5) and the continuous solvation of the resulting Zn–EDTA complex in the electrolyte [115]. Thus, the formation of passive species adsorbed on the Zn surface is most likely hindered.

With respect to the pH value stability of the NaCl solutions, formation of zinc hydroxide or Simonkolleite according to the Equation 1.18 and 1.19 lead to consumption of hydroxyl ions; thus the pH value tends to decrease as confirmed by the discharge experiments. Contrariwise, the presence of EDTA in the solutions stabilizes the pH value of NaCl solutions during the discharge, as confirmed by the pH value still close to 10 after the 24 h discharge experiments, due to complexing Zn^{2+} ions before the other possible reactions that would consume OH^- ions can take place. Furthermore, in accordance to previous studies [166–168], EDTA can be adsorbed on the surface of ZnO or even leach the ions from the respective oxide or hydroxide, which adds up to the synergetic effects of addition of EDTA to the 2M NaCl on discharge performance.

Characterization of the Zn surfaces

Laser Scanning Microscopy (LSM) investigations have been performed to gain better insights into the surface morphologies of the Zn after galvanostatic discharge experiments. Figure 5.6 shows the 3D LSM images of the Zn samples after 1 and 24 h discharge with 1 mA cm^{-2} in presence and absence of EDTA. The surface of Zn after 1 h of discharge for both electrolytes show a similar roughness of less than 10 µm, as shown in Figure 5.6a,c. However, Zn shows a thin film with some areas exposing a metallic surface underneath after discharge in neat 2M NaCl (Figure A–14) while the Zn discharged in presence of EDTA shows a more homogeneous surface and no film or other particulates on the surface.

More remarkable differences appear after 24 h of discharge, where the surface of the Zn in neat 2M NaCl has height differences up to 100 µm, as seen in Figure 5.6b. Within the large pits, a metallic Zn surface was visible (blue regions), suggesting that some areas of the metallic anode were continuously exposed during the 24 h of discharge upon partial breakage of the passive film (yellow and orange regions). Conversely, the Zn discharged in the solutions containing 0.1M EDTA shows a surface roughness of around 40 µm (Figure 5.6d) and no apparent layer or particulates were observed. Thus, these findings confirm that the presence of EDTA effectively suppresses the formation of a passive film. The absence of any solids on the Zn surface after discharge also indicates that all the discharged Zn is dissolved in the electrolyte.

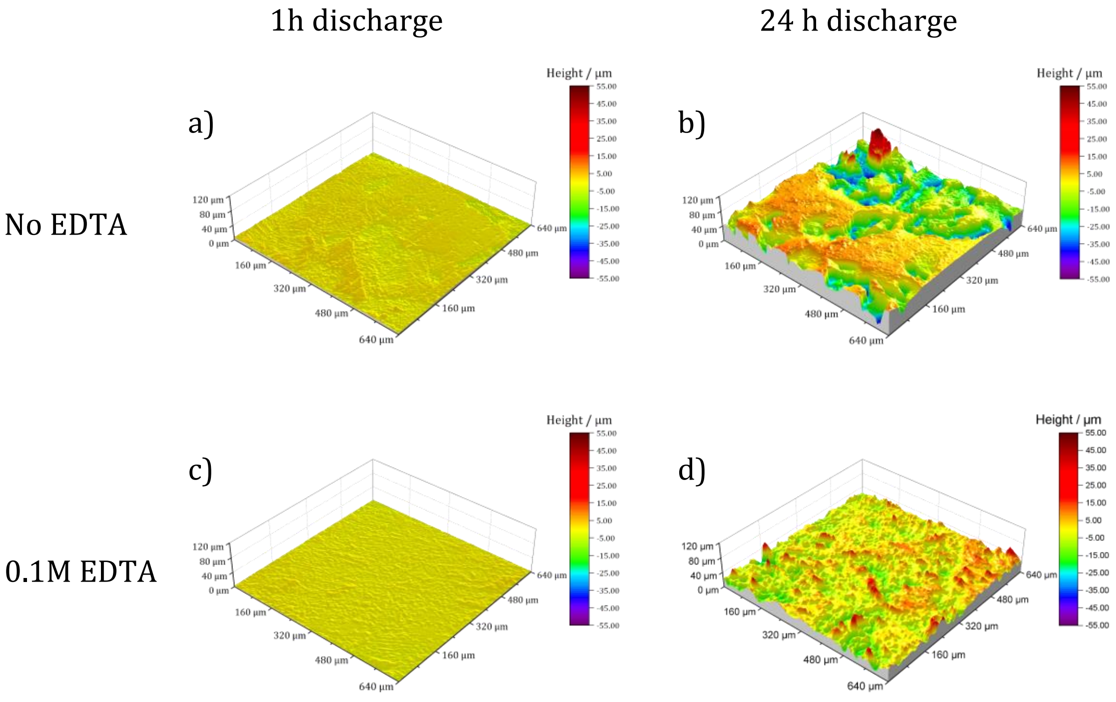

Figure 5.6: Laser scanning microscopy images of Zn discharged in 2M NaCl pH 10 in absence (a, b) and presence of EDTA (c, d) after 1 h (a, c) and 24 h (b, d) with 1 mA cm^{-2}. Yellow/orange areas in (b) represent the passive layer formed after 24 h of discharge in neat 2M NaCl pH 10.

In addition to the characterization of the surface morphologies by LSM, the chemical nature of the surfaces of the Zn electrodes after discharge was analyzed by X–Ray Diffraction (XRD). Figure 5.7 shows the XRD patterns of the Zn samples that were discharged under 1 mA cm^{-2} for 24 h in 2M NaCl with and without EDTA.

In Figure 5.7a both patterns (purple and yellow) show that the Zn surface is mostly in metallic state while the Zn surface discharged in neat electrolyte also reveals some extra peaks which indicate the presence of Simonkolleite (Figure 5.7b,c). However, on both electrodes neither ZnO nor $Zn(OH)_2$ could be detected, as shown in the enlarged area in Figure 5.7c. Furthermore, the white precipitates in the neat 2M NaCl electrolyte were collected, dried, and analyzed by XRD (orange line) revealing the presence of Simonkolleite, ZnO and Zn.

Until now, it could be concluded that Simonkolleite and possibly ZnO are the main components of the passive film when Zn is discharged in the neat 2M NaCl. But as shown in Equations 1.19, 1.20 and 1.22, the production of Simonkolleite and ZnO requires $Zn(OH)_2$ as an intermediate step. Thus, the passive layer on the Zn discharged in neat electrolyte should also show the presence of $Zn(OH)_2$, but the amount might be too small to be identified by XRD or it may be amorphous. Similarly, if a thin $Zn(OH)_2$ passive layer is also present on the Zn after discharge in presence of 0.1M EDTA, it might not be possible to be detected by XRD.

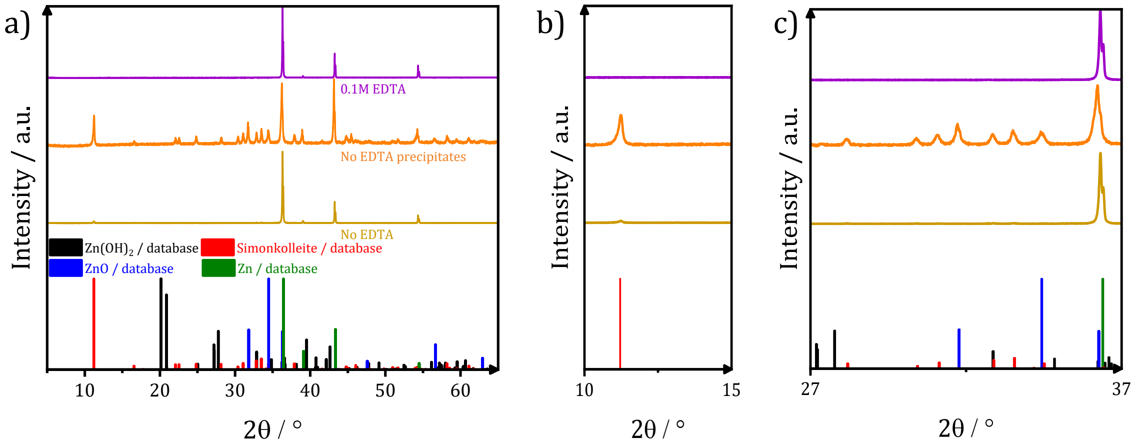

Figure 5.7: a) XRD patterns of Zn discharged in 2M NaCl at pH 10 with and without EDTA under 1 mA cm^{-2} after 24 h, b) enlarged region of the peaks between 10 and 15° and c) enlarged region of the peaks between 27 and 37°.

In order to gain further insights into the surface products of the Zn electrodes, Scanning Electron Microscopy (SEM) imaging coupled to Energy Dispersive Spectroscopy element analysis (EDX) was carried out. Figure 5.8 shows the SEM images and EDX maps of Zn after 24 h of discharge at 1 mA cm^{-2} in 2M NaCl without and with 0.1M EDTA. The Zn surface in Figure 5.8a (no EDTA) shows the microstructure of the region where the passive film partially extends over the metallic Zn. The EDX map in Figure 5.8c depicts a better contrast between the film and the metallic Zn. The SEM image in Figure 5.8b (0.1M EDTA) illustrates a surface without any apparent layer on top of the Zn surface, while the EDX map in Figure 5.8d shows two regions containing mostly Zn. The elemental distribution is provided in Table 5-2. The individual elemental maps of Figure 5.8c,d are provided in Figure A–16. Also, the SEM images and elemental maps for 1 h discharged surfaces can be found in the supporting info (Figure A–14, Figure A–15 and Table A–8).

Table 5-2: Theoretical element weight distribution of Zn corrosion products and EDX elemental analysis of Zn after 24 h discharge at 1 mA cm^{-2} in 2M NaCl pH 10 with and without 0.1M EDTA

		Zn wt%	O wt%	Cl wt%	C wt%
Theoretical	ZnO	80.34	19.66		
	$Zn(OH)_2$[a]	67.14	32.86		
	$Zn_5(OH)_8Cl_2 \cdot H_2O$[a] (Simonkolleite)	60.33	26.58	13.09	
Zn in 2M NaCl	Zn/O phase (red)	96.08	2.37	1.54	
	Zn/Cl/O phase (yellow)	67.92	21.89	10.19	
	Zn/O phase (blue)	83.15	12.32	4.53	
	Zn/O phase (green)	59.39	32.61	8.00	
Zn in 2M NaCl with 0.1M EDTA	Zn phase (red)	98.16	0.18	0.19	1.46
	Zn/O/Cl/C phase (cyan)	86.18	3.30	0.95	9.58

The sample discharged in neat 2M NaCl under 1 mA cm^{-2} in Figure 5.8c shows four different regions. The red region corresponds to metallic Zn. The yellow region has an elemental composition that is close to Simonkolleite. The blue and green regions are attributed to ZnO and $Zn(OH)_2$ respectively while neglecting the Cl content. Figure 5.8d shows two regions on the Zn surface that was discharged in 2M NaCl containing 0.1M EDTA. The red region corresponds to pure Zn with probably some EDTA still adsorbed. The cyan region has a composition that is also very close to metallic Zn with additional ~10 wt% C. The difference between the red and the cyan region can be attributed to the possibly different amount of remaining adsorbed EDTA on the Zn surface.

Considering equations 1.18, 1.19, 1.20, 1.21 and 1.22 in addition to the results provided by XRD, SEM and EDX analysis are important to determine the nature of the passive film forming on Zn upon discharge in 2M NaCl without EDTA. Equation 1.18 shows that $Zn(OH)_2$ can be formed following the oxidation of Zn to Zn^{2+}. Upon local saturation of $Zn(OH)_2$, ZnO or Simonkolleite can be formed. However, as revealed by the XRD and EDX results, Simonkolleite can be clearly detected only after long discharge time (at least 24 h). Thus, ZnO could be assumed as a second component of the passive film, besides the $Zn(OH)_2$. However, it is noteworthy to mention that the surface of the Zn electrodes could possibly be changing while cleaning and transferring into other characterization tools after the electrochemical investigations. Hence, for example, ZnO might mainly be detected instead of $Zn(OH)_2$ although the latter may be the main product during the electrochemical studies, as previously described by equation 1.20. Once the ZnO/$Zn(OH)_2$ passive film is formed over the neat Zn, the reaction continues as dictated by equation 1.22 and Simonkolleite is formed. Moreover, this passive film grows until forming scales, which breaks upon the mechanical stress of the volume increase (see Table A–7) and some pieces might precipitate. Support for this idea can be observed in the SEM images (surface films in Figure 5.8a and Figure A–15), besides the flakes found in the sediments after 24 h of discharge. Additionally, the XRD results after 24 h of discharge (Figure 5.7) show a high presence of Simonkolleite in the sediments collected, while the intensity peaks of Simonkolleite on the Zn electrode after discharge were not significant. However, some amount of Simonkolleite was detected by EDX (Figure 5.8c and Table 5-2). Thus, it could be concluded that the thin passive film on Zn upon discharge in 2M NaCl without EDTA consists of a combination of ZnO/Zn(OH)$_2$ and Simonkolleite.

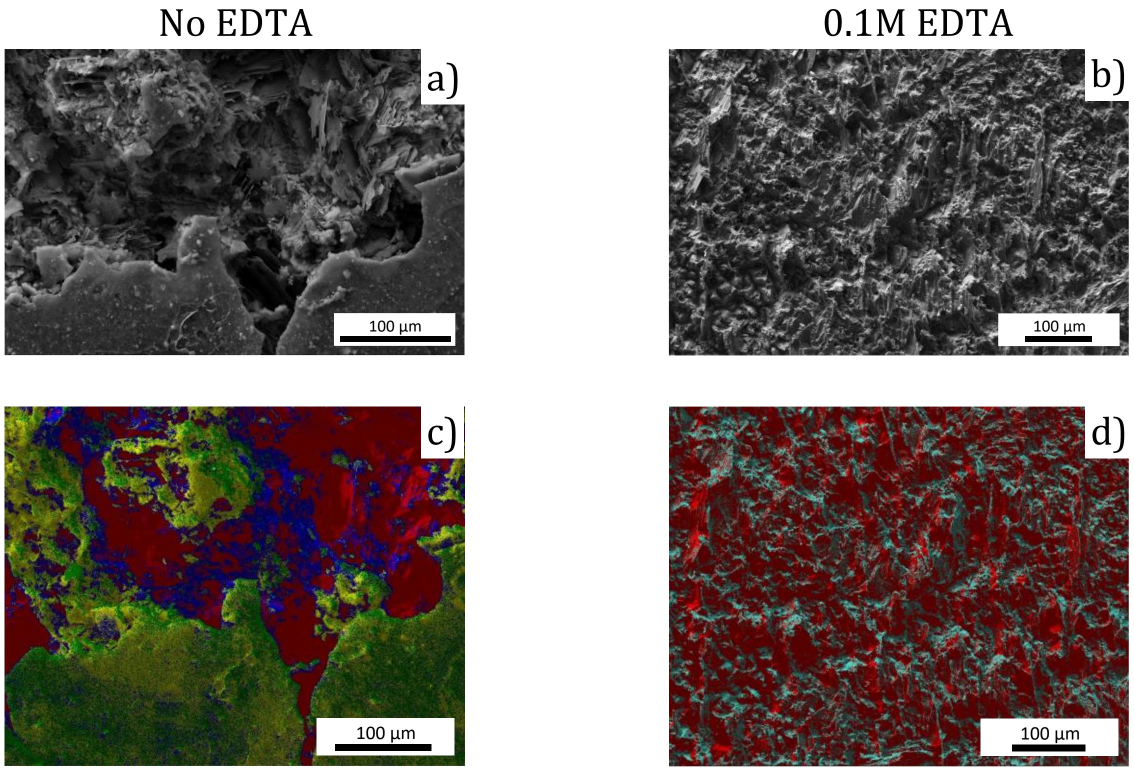

	Zn wt.%	O wt.%	Cl wt.%
🟥	96.08	2.37	1.54
🟨	67.92	21.89	10.19
🟦	83.15	12.32	4.53
🟩	59.39	32.61	8.00

	Zn wt.%	O wt.%	Cl wt.%	C wt.%
🟥	98.16	0.18	0.19	1.46
🟦	86.18	3.30	0.95	9.58

Figure 5.8: SEM images (a, b) and EDX maps (c, d) of Zn discharged for 24 h at 1 mA cm^{-2} in 2M NaCl pH 10 without (a, c) and with 0.1M EDTA (b, d). The weight distribution of the EDX maps is provided below the figure.

Conversely, the addition of EDTA to the 2M NaCl interferes with the formation of a passive film by complexing the Zn directly after its oxidation (Equation 1.20), as evidenced by the SEM, EDX and LSM results. Furthermore, the electrolyte has no precipitates and remains clear after discharging the Zn in presence of EDTA, implying that the Zn–EDTA complex remains solvated.

Accordingly, the following mechanism can be proposed for the OCP and discharge experiments of Zn in 2M NaCl pH 10 with 0.1M EDTA. The EDTA is directly adsorbed on the Zn surface upon immersion of the electrode by possibly interacting with the metallic surface [164,165]. After the spontaneous (OCP conditions) reaction or anodic oxidation (discharge conditions) of Zn to Zn^{2+}, the adsorbed EDTA chelates and captures the Zn^{2+} limiting the formation of ZnO, $Zn(OH)_2$ or Simonkolleite as schematically shown in Figure 5.9. The Zinc–EDTA complex remains as an aqueous specie, thus avoiding the formation of a passive film. The inhibition of passive film formation leaves the next layer of metallic Zn available to continue with the reaction and no potential drop is expected with enough EDTA to continue the chelation process. Such limitation is therefore of interest in a full–cell experiments over extended periods of discharge.

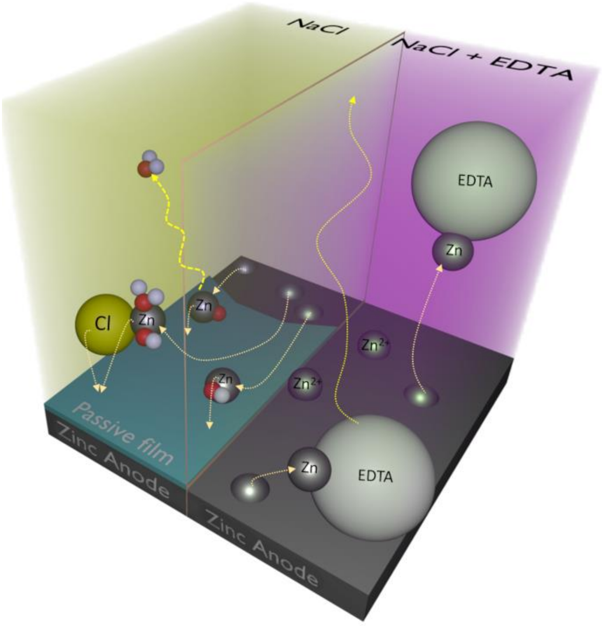

Figure 5.9: Schematic representation of the complexation process and possible differences on Zn surfaces that are in contact with the neat NaCl and NaCl+EDTA solutions. For simplicity, the ions and the molecules are shown in spherical shapes.

Full–cell galvanostatic discharge experiments

Figure 5.10 shows the full–cell galvanostatic discharge profiles of Zn in 2M NaCl pH 10 electrolytes under 0.25, 0.5 and 1 mA cm^{-2} in absence (black curves) and presence of 0.1M EDTA (red curve). The Open Circuit Voltage (OCV) of Zn in the neat 2M NaCl is around 1.1 V, while the discharge voltages are similar among all the applied currents at around 0.9 V during the first hours. However, the Zn discharged in neat electrolyte under 0.25 mA cm^{-2} shows a fluctuating voltage after 291 h and reached a total of 931 h, whereas it could be discharged under 0.5 and 1 mA cm^{-2} for a total of 255 and 110 h, respectively.

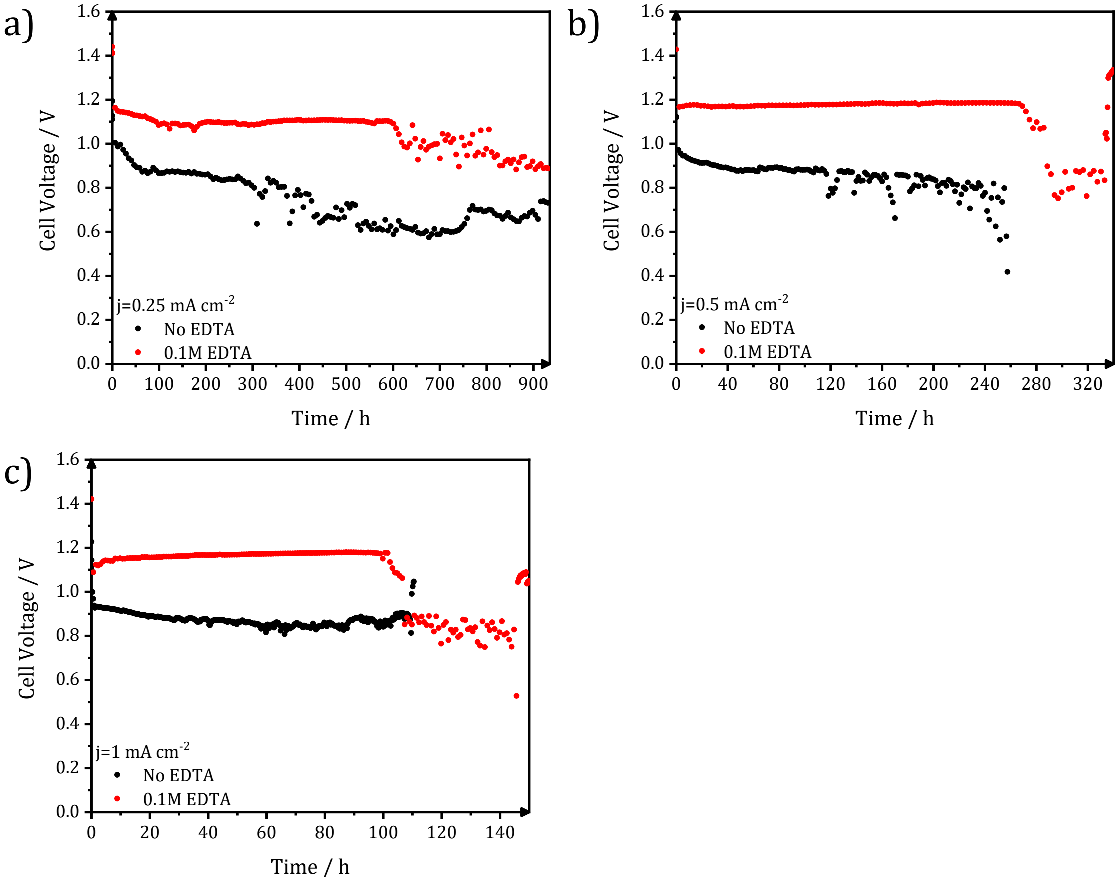

Figure 5.10: Full–cell galvanostatic discharge profiles of Zn in 2M NaCl at pH 10 in absence (black curves) and presence (red curves) of 0.1M EDTA under a) 0.25 mA cm^{-2}, b) 0.5 mA cm^{-2}, c) 1 mA cm^{-2}.

The OCV of Zn in 2M NaCl with 0.1M EDTA is at around 1.4 V, while the discharge voltage under the applied currents is similar at around 1.1 to 1.15 V. The overall discharge voltage enhancement provided by the addition of EDTA to the electrolyte is around 270 to 320 mV higher in comparison to the neat electrolyte. Nevertheless, the discharge voltage of Zn in presence of EDTA noticeably decreases after 600 h under 0.25 mA cm^{-2}, after 270 h under 0.5 mA cm^{-2} and after 101 h under 1 mA cm^{-2}. The resulting values after the voltage drop are then similar to the respective cell voltages without EDTA. It is noteworthy to mention that there were strong fluctuations on the cell voltages most likely due to discharge via pitting mechanism after the effect of EDTA was lost. The cells containing EDTA could be operated in total up to 931 h under 0.25 mA cm^{-2}, 330 h under 0.5 mA cm^{-2} and 146 h under 1 mA cm^{-2}.

In order to determine the limiting factor on the enhanced discharge voltage, further experiments under 1 mA cm^{-2} with a 40 mL electrolyte reservoir (vs. 20 mL from Figure 5.10) were performed (see Figure A–17), showing a significant increase of the discharge time with similar discharge voltages to those presented in Figure 5.10c. Thus, the total amount of EDTA available in the electrolyte for the discharge plays an important role for extending the improved discharge energies of Zn–air batteries.

In comparison to similar near–neutral battery systems under the same discharge current densities [76,78,81], the addition of EDTA to the electrolyte shows noteworthy higher discharge voltages (1 V vs 1.15 V, respectively), which are also fairly comparable to the voltages observed in alkaline systems (1.25 V_{KOH} vs 1.15 V_{NaCl} at 1 mA cm^{-2}) [78,175]. Besides the cell voltage enhancement, all the full–cell discharge experiments performed with the electrolyte containing EDTA exhibited no deposits on the electrode surfaces, while the electrolyte was also almost free of precipitates. Conversely, the cell discharged with neat 2M NaCl electrolyte showed a thick white layer covering the air electrode, which probably led to clogging and stopped the discharge. Similarly, large amounts of precipitates could be found in the used 2M NaCl without EDTA and the Zn anode was also covered with a thick white layer.

As discussed in the half–cell stripping section, a passive film forming upon contact of Zn with the neat 2M NaCl could also explain the relatively low OCV and discharge voltage of the full–cell, besides the poor pH stability of NaCl and formation of insoluble reaction products (such as Simonkolleite). In contrast, the enhanced voltage observed for the cells containing EDTA could be attributed to the absence of film formation resulting from the chelating properties of EDTA. Therefore, the surface of the discharged samples in the full–cell setup was further analyzed by XRD in order to detect possible reaction products which could explain the observed discharge voltages.

Figure 5.11 presents the XRD patterns of the samples after the long–run full–cell discharge experiment from Figure 5.10. The XRD results show the presence of Simonkolleite on the Zn electrodes discharged under 1 mA cm^{-2} in neat 2M NaCl (purple line), while the XRD patterns after discharged in 2M NaCl with 0.1M EDTA electrolyte illustrate almost exclusively the peaks for metallic Zn (yellow line). Furthermore, the XRD analysis of Zn discharged with a larger reservoir volume show Simonkolleite in absence of EDTA and only the Zn peaks in presence of EDTA (see Figure A–17b). Based on the present results, it could be argued that the Simonkolleite is the main component of the passive film of Zn in presence of neat 2M NaCl, but the presence of ZnO and $Zn(OH)_2$ underneath the Simonkolleite layer cannot be conclusively discarded as shown by the previous EDX analysis. In the case of the Zn discharged with EDTA, there are no indications for a film formation from the XRD results.

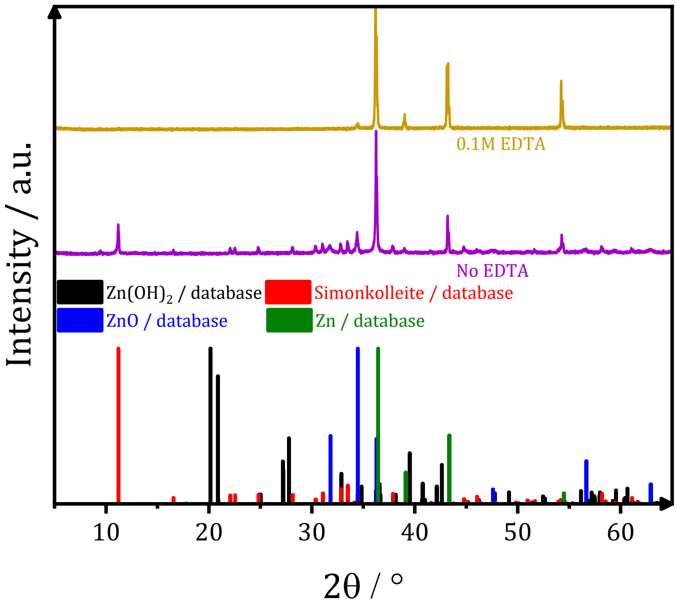

Figure 5.11: XRD pattern of Zn samples discharged in full–cells under 1 mA cm^{-2} in 2M NaCl pH 10 in absence (purple) and presence (yellow) of 0.1M EDTA.

Table 5-3 presents a summary of the practical capacity, practical specific energy and mass utilization efficiency calculated after the discharge of Zn in 2M NaCl in absence and presence of 0.1M EDTA under several current densities. The calculation of the values was based on the total mass loss of the discharged Zn anodes. The practical capacity of Zn discharged in neat 2M NaCl is in average 744 mAh g_{Zn}^{-1}, while the average practical specific energy is 573 Wh kg_{Zn}^{-1}. The overall utilization efficiency is around 90%. Contrariwise, the cells discharged in presence of 0.1M EDTA showed an increase in the practical capacity with an average of 779 mAh g_{Zn}^{-1}. The practical specific energy shows a significant increase with an average of 833 Wh kg_{Zn}^{-1}, which is around 45% higher than for the cells discharged in neat 2M NaCl. The overall average mass utilization efficiency for the cells discharged in presence of 0.1M EDTA is 95%, which is slightly higher than the cells discharged in absence of EDTA.

The enhanced practical specific energy of the cells discharged in presence of EDTA is explained by the higher discharge voltage in comparison to the cells discharged in absence of EDTA. The data in Table 5-3 shows that the most efficient cells are those discharged in 2M NaCl with 0.1M EDTA under 0.25 mA cm^{-2}, where the enhanced voltage lasts almost until the end of the experiment. The latter suggests that even higher practical specific energies and mass utilization efficiencies could be achieved with non–interrupted enhanced voltages, specifically if enough EDTA is provided to achieve longer runs. All in all, the discharge of Zn in a full–cell is possible with 2M NaCl in absence and in presence of 0.1M EDTA, while the latter depicts better performances.

Table 5-3: Practical capacity, practical specific energy and mass utilization efficiency calculated after the discharge of Zn in 2M NaCl pH 10 in absence and presence of 0.1M EDTA under several currents.

Electrolyte	Current density / mA cm^{-2}	Practical capacity / mAh g_{Zn}^{-1}	Practical specific energy / Wh kg_{Zn}^{-1}	Mass utilization efficiency / %	Discharge time	
					Enhanced / h	Total / h
2M NaCl	0.25	751.1 ± 3.5	535.8 ± 17.4	91.6 ± 0.4	-	931
	0.5	735.1 ± 17.3	574.9 ± 65.5	89.6 ± 2.1	-	255
	1	748.4 ± 18.7	611.0 ± 28.2	91.3 ± 2.3	-	110
2M NaCl + 0.1M EDTA	0.25	796.4 ± 5.0	829.5 ± 7.7	97.1 ± 0.6	600	931
	0.5	750.8 ± 35.6	842.3 ± 38.8	91.5 ± 4.3	270	330
	1	791.3 ± 8.6	829.4 ± 23.4	96.5 ± 1.1	101	146

Full–cell galvanostatic cycling

The possible beneficial effects of EDTA as additive for NaCl electrolytes should be further extended to not only primary Zn–air batteries, but also for secondary batteries, as suggested by earlier studies in alkaline media. Thus, the evaluation of the effects of EDTA on Zn upon charging in NaCl solutions is relevant to establish an initial framework since no previous works exist to the knowledge of the authors.

Figure 5.12 shows the galvanostatic full–cell cycling profiles (at low depth of discharge) under 0.5 mA cm^{-2} current densities for 4 h per step (charge and discharge). The cycling of Zn in neat 2M NaCl (black curve) shows an average discharge voltage at around 0.86 V and charging voltages at around 1.59 V, which results in a 0.73 V voltage difference. The cells cycled in presence of EDTA (red curve) showed an average discharge voltage around 1.15 V and an average charge voltage at around 1.62 V, although at the initial cycles (200 h) the cells with the EDTA additive exhibit slightly higher charging voltages in comparison to the cell with the neat electrolyte. The origin of such higher charging voltage, whether it is from the air cathode or from the initial Zn–EDTA complexes is not clear and requires further investigations. The average discharge voltage in presence of EDTA is 290 mV higher than without EDTA. The smaller discharge/charge voltage difference in presence of EDTA (0.47 V voltage difference) indicates less overpotentials, which is beneficial for battery applications

Considering the cycling stability, the discharge performance of Zn–air cell with neat 2M NaCl starts to decay from the 68th cycle after 550 h, eventually leading to termination of the cell operation due to reaching the 0.5 V cut–off voltage rapidly. Similar cycling life was also achieved by the full–cells with 0.1M EDTA additive while displaying enhanced performance for at least 51 cycles (416 h) with discharge voltages at around 1.25 V. However, the discharge voltage starts to decrease from the 52nd cycle (after 420 h) to around 0.95 V, which has a similar value to the cells without EDTA. Nevertheless, the discharge voltage of the subsequent cycles partially recovers to 1.2 V for a limited time, and eventually the positive influence of the EDTA additive was almost completely lost for the remaining cycles.

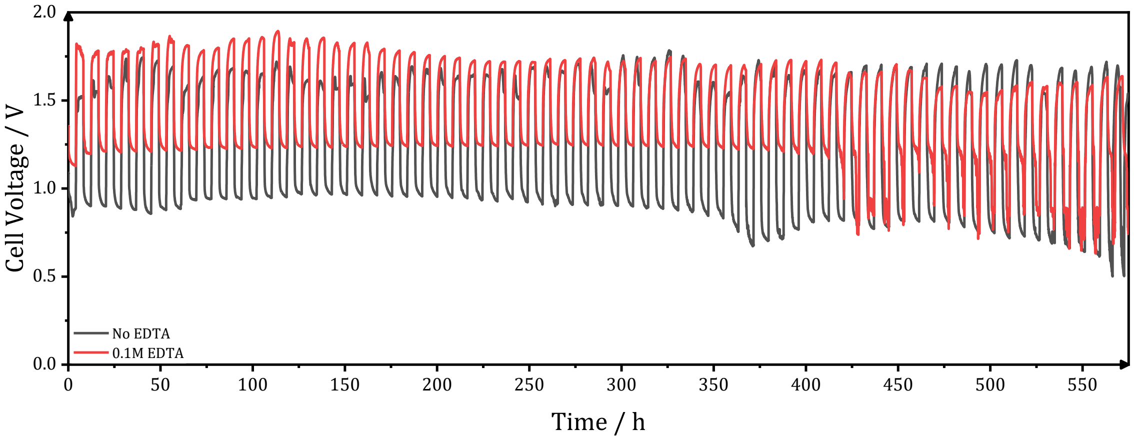

Figure 5.12: Full–cell galvanostatic cycling of Zn under 0.5 mA cm^{-2} for 4 h per step in 2M NaCl pH 10 in absence (black curve) and presence (red curve) of 0.1M EDTA.

All in all, the full–cell experiments demonstrate the feasibility of cycling of Zn in 2M NaCl pH value of 10 with and without 0.1M EDTA additive. Moreover, the cycling of Zn in the electrolyte containing 0.1M EDTA shows a better performance in terms of the higher discharge voltage, higher power output and discharge energies. However, further investigations are needed in order to achieve better regeneration of active EDTA, which would result in longer full–cell cycling with enhanced discharge and lower charging voltages. In comparison to other Zn–air batteries with near–neutral electrolytes which are mostly based on NH_4Cl electrolytes[76,78,80] for their high buffering capabilities, this study also provides a possible alternative electrolyte as NaCl–based solutions with additives that prevent passive film formation and also help to stabilize the pH while providing higher discharge voltages. The ability of EDTA to diminish or hinder the formation of passive films could be further extended to other anode materials which suffer from similar constrains in near–neutral electrolytes, while the only limitation is the ability of the EDTA to complex such materials.

5.4. Summary and Remarks

As revealed by the OCP, potentiodynamic polarization, and half–cell discharge experiments, the electrochemical activity of Zn electrodes is enhanced in presence of EDTA at pH value of 10. The potential is increased at least 150 mV at OCP conditions and 200 mV up to 1 mA cm^{-2} anodic current densities. The reason behind the potential enhancement is attributed to the inhibition of a passive film, which is normally formed upon immersion of the Zn in the chloride–based electrolyte. Furthermore, the Zn^{2+} ion is most likely chelated by the EDTA right after its formation, while the EDTA also increases the pH value stability in comparison to the neat electrolyte.

The LSM measurements gave further support to the existence of a passive film on the Zn electrode immersed in the neat electrolyte, whereas the Zn surface presented no observable deposits in presence of EDTA. The XRD diffractograms indicate the presence of Simonkolleite on the electrode surface and in the precipitates formed upon discharge, while only Zn peaks could be recognized for the Zn samples immersed in EDTA. However, according to the theoretical reactions of Zn, $Zn(OH)_2$ and ZnO should be present after discharge in the neat electrolyte but not all of them could be identified by XRD. Further measurements by SEM/EDS—with more localized detection—suggested the presence of Simonkolleite, ZnO and $Zn(OH)_2$ in the samples discharged in the neat 2M NaCl, while only Zn with minor traces of O and C could be found.

The study was extended to full–cell discharge experiments, depicting better electrochemical performance in presence of EDTA with remarkable higher specific energies than in the neat electrolyte (45% higher). The latter increase is due to the higher discharge voltages with the 0.1M EDTA (1.15–1.2 V vs. less than 0.9 V) and longer discharge, whereas the enhanced voltages were eventually lost probably due to depletion of the EDTA in the electrolyte. The XRD diffractograms of the samples *post–mortem* showed the presence of Simonkolleite for the electrolyte without additive, while some peaks of ZnO could be identified for the solution with EDTA. Further possible benefits of the EDTA on the electrochemical behavior of Zn were tested by full–cell cycling experiments. The results show higher discharge voltages of the Zn in presence of EDTA but also initial higher charge voltages, which continuously decreased to similar voltages as for the Zn cycled in the neat electrolyte. The cycling experiments in presence of EDTA lost the enhanced discharge voltages after 52 cycles and 420 h eventually leading to cell failure.

The chelating effects of EDTA were effectively observed for battery applications, but further improvements regarding to longer discharge times with enhanced voltages and better cyclability of the Zn electrodes is needed. Possible candidates for this task could belong to the aminopolycarboxylates, polycarboxylic acid or other inorganic acids with similar or better pH buffering and chelating abilities.

Chapter 6: Conclusion

Looking for energy storage alternatives, this thesis aimed to find possible applications for alkaline Si–air batteries under the current status of development, whereas anode and electrolyte modification of Zn–air batteries was done to improve their performance.

A feasible application of an alkaline and non–aqueous Si–air battery with a mounted circuit on the backside of the anode has been demonstrated, showing the possible usage of such Si–air batteries for low–power consumption devices. With the existing cell casing design, self–destructing devices are feasible with the incorporation of circuits on the back side of the anode. Under the current conditions, the alkaline Si–air battery could deliver up to 160 μA at 1.1 V for over 220 h, whereas the non–aqueous could deliver 125–350 μA at 0.6–1 V for over 1982 h. Both battery types could power an LED until complete depletion of the Si anode and destruction of the circuit. The estimated specific capacity according to the mass loss of the anode was around 83.88 mAh g_{Si}^{-1} for the alkaline battery and 1072.43 mAh g_{Si}^{-1} for the non–aqueous battery. The tests showed the complete dissolution of Si anode, insulating grown SiO_2, and the silicon die of the decapped EEPROM. Further improvement on the electrochemical characteristics of the Si in 5M KOH could be achieved by alloying it with Al. The galvanostatic discharge experiments with the Si–5%Al alloys in 5M KOH revealed a maximum attainable current density of 0.25 mA cm^{-2}, whereas the anode mass conversion could not be significantly increased in comparison to the Si <100> As–doped samples.

The approach of anode alloying to improve the electrochemical characteristics was implemented to Zn–10Al anode alloys in neutral 2M NaCl electrolyte (pH 7), since Al presents a more negative standard electrode potential than Zn. Initial half–cell experiments (CV and galvanostatic discharge) revealed no enhancement of the Zn–alloy anode in comparison to the pure Zn electrode. The discharge potentials of Zn and Zn–10Al were around −1.05 $V_{Ag/AgCl}$ under several current densities between 0.1–1 mA cm^{-2}, whilst the Al electrode displayed discharge potentials around −0.75 $V_{Ag/AgCl}$ under the same anodic currents. The observed discharge potentials indicated discharge via pitting mechanism for all the tested samples. LSM and AFM analysis of the samples before and after the discharge displayed the higher selective consumption of the Zn–rich areas, whilst the Al–rich areas were almost unaffected. Analysis by potentiodynamic polarization experiments showed a more negative corrosion potential than the corresponding open circuit potential for each sample (Zn, Zn–10Al and Al). The initial cathodic potential applied during the potentiodynamic polarization assisted in the so called "cathodic alkalization", which locally produced OH^- ions able to remove the oxide layer formed on the Zn and Al upon immersion in the NaCl–based electrolyte. By applying a 1 h cathodic polarization pulse and followed by a galvanostatic discharge under several currents, the enhanced potentials of the Zn–10Al alloy electrode could be observed and quantified. A maximum duration of 130 min enhanced potential starting at $-1.4\ \mathrm{V_{Ag/AgCl}}$ until the intersection with the potential of pure Zn was observed for current densities of 5 μA cm^{-2}, whilst the effect was practically lost when 1 mA cm^{-2} anodic currents were applied.

As the cathodic activation method is not completely practical for the operation of a battery, a different strategy to activate the surface of the Zn was attempted by using the chelating additive EDTA. The detailed electrochemical characterization of Zn electrodes in 2M NaCl pH 10 with and without 0.1M EDTA revealed the advantages of employing EDTA as an additive within the electrolyte. The discharge potentials observed in half–cell experiments were increased by around 200 mV under 0.1–1 mA cm^{-2} in presence of EDTA. LSM analysis of the surface revealed a more homogeneous consumption of the Zn electrodes discharged in presence of EDTA, whilst the neat electrolyte induced the formation of a passive film. A more comprehensive analysis of the Zn samples after discharge in the neat electrolyte by XRD and SEM revealed the presence of a film composed of Simonkolleite, ZnO and $Zn(OH)_2$, whereas the Zn electrodes discharged in presence of EDTA were free of any film and presented only traces of ZnO and adsorbed C. Hereby is proposed that the EDTA complexes with the Zn and forms soluble compounds, preventing the formation of a passive film. The study was extended to full–cell experiments and showed a significant increase of 45% in the practical specific energy in presence of EDTA (up to 842.3 $\mathrm{Wh\,kg_{Zn}^{-1}}$) due to the higher discharge voltages. The cyclability of the Zn in the 2M NaCl pH 10 with and without 0.1M EDTA was evaluated, displaying higher discharge voltages but also initial higher charging overvoltages. A total of 51 cycles with discharge voltages of 1.15 V and charging voltages of 1.62 V over 416 h could be achieved. Future experimenting with similar chelating and buffering additives may further improve the discharge and cyclability of Zn in near neutral electrolytes.

Further progress on alkaline Si–air batteries could be achieved by the employment of Si–alloys, including elements like Al or In, which could modify characteristics such as the passivation or corrosion of the Si in KOH. The development of new types of electrolytes capable to discharge the Si could be an alternative, as well as electrolyte additives to improve the performance of Si–air batteries. Similarly, chelating agents seem to be a good alternative to improve the performance of ZABs, but further characterization and studies are needed. The application of chelating agents as electrolyte additives or even as main component of the electrolyte for ZABs and other MABs is still a promising research field and needs further research to better understand the mechanisms behind the improvements observed.

List of Figures

List of Tables

Bibliography

[1] H. Ritchie, M. Roser, Energy, (2020). https://ourworldindata.org/energy-production-consumption (accessed March 4, 2022).

[2] IEA, Global Energy Review 2021 – Analysis, (2021). https://www.iea.org/reports/global-energy-review-2021 (accessed March 4, 2022).

[3] IEA, CO2 emissions – Global Energy Review 2021 – Analysis - IEA, (2021). https://www.iea.org/reports/global-energy-review-2021/co2-emissions (accessed March 5, 2022).

[4] United Nations - Climate Change, The Paris Agreement | UNFCCC, (2015). https://unfccc.int/process-and-meetings/the-paris-agreement/the-paris-agreement (accessed March 5, 2022).

[5] IEA, World Energy Balances: Overview, (2021). https://www.iea.org/reports/world-energy-balances-overview/world (accessed March 5, 2022).

[6] H. Ritchie, M. Roser, Renewable Energy, (2020). https://ourworldindata.org/renewable-energy (accessed March 5, 2022).

[7] IEA, Example of daily load profile for solar PV production relative to electricity demand in 2050, (n.d.). https://www.iea.org/data-and-statistics/charts/example-of-daily-load-profile-for-solar-pv-production-relative-to-electricity-demand-in-2050 (accessed March 17, 2022).

[8] T. Placke, R. Kloepsch, S. Dühnen, M. Winter, Lithium ion, lithium metal, and alternative rechargeable battery technologies: the odyssey for high energy density, J. Solid State Electrochem. 2017 217. 21 (2017) 1939–1964. https://doi.org/10.1007/S10008-017-3610-7.

[9] Statista, Global lithium-ion battery demand in EVs by region, (n.d.). https://www.statista.com/statistics/1103229/global-battery-demand-by-region-forecast/ (accessed March 17, 2022).

[10] Statista, Chart: High Demand for Lithium-Ion Batteries, (n.d.). https://www.statista.com/chart/23808/lithium-ion-battery-demand/ (accessed March 17, 2022).

[11] Statista, Projection total lithium demand globally 2030, (n.d.).

https://www.statista.com/statistics/452025/projected-total-demand-for-lithium-globally/ (accessed March 17, 2022).

[12] C. Grosjean, P. Herrera Miranda, M. Perrin, P. Poggi, Assessment of world lithium resources and consequences of their geographic distribution on the expected development of the electric vehicle industry, Renew. Sustain. Energy Rev. 16 (2012) 1735–1744. https://doi.org/10.1016/J.RSER.2011.11.023.

[13] Trading Economics, Lithium - 2022 Data - 2017-2021 Historical - 2023 Forecast - Price - Quote - Chart, (n.d.). https://tradingeconomics.com/commodity/lithium (accessed January 5, 2023).

[14] Statista, Lithium reserves worldwide top countries 2021, (n.d.). https://www.statista.com/statistics/268790/countries-with-the-largest-lithium-reserves-worldwide/ (accessed March 17, 2022).

[15] R. Van Noorden, The rechargeable revolution: A better battery, Nature. 507 (2014) 26–28. https://doi.org/10.1038/507026A.

[16] Why Does Energy Density Matter In Batteries? | Dragonfly Energy, (n.d.). https://dragonflyenergy.com/why-does-energy-density-matter-in-batteries/ (accessed January 5, 2023).

[17] H. Weinrich, Y.E. Durmus, H. Tempel, H. Kungl, R.-A. Eichel, Silicon and Iron as Resource-Efficient Anode Materials for Ambient-Temperature Metal-Air Batteries: A Review, Materials (Basel). 12 (2019) 2134. https://doi.org/10.3390/ma12132134.

[18] D. Linden, T.B. Reddy, HANDBOOK OF BATTERIES, 3rd. editi, McGraw-Hill, 2002.

[19] M.A. Rahman, X. Wang, C. Wen, High Energy Density Metal-Air Batteries: A Review, J. Electrochem. Soc. 160 (2013) A1759–A1771. https://doi.org/10.1149/2.062310jes.

[20] E. McCafferty, Introduction to Corrosion Science, Springer New York, New York, NY, 2010. https://doi.org/10.1007/978-1-4419-0455-3.

[21] J.S. Lee, S.T. Kim, R. Cao, N.S. Choi, M. Liu, K.T. Lee, J. Cho, Metal-air batteries with high energy density: Li-air versus Zn-air, Adv. Energy Mater. 1 (2011) 34–50. https://doi.org/10.1002/aenm.201000010.

[22] P.K. Shen, C.Y. Wang, S.P. Jiang, X. Sun, J. Zhang, Electrochemical Energy: Advanced Materials and Technologies, CRC Press, 2016.

[23] R.J. Gilliam, J.W. Graydon, D.W. Kirk, S.J. Thorpe, A review of specific conductivities of potassium hydroxide solutions for various concentrations and temperatures, Int. J.

Hydrogen Energy. 32 (2007) 359–364. https://doi.org/10.1016/j.ijhydene.2006.10.062.

[24] S.J. Visco, B.D. Katz, Y.S. Nimon, L.C. De Jonghe, Protected active metal electrode and battery cell structures with non-aqueous interlayer architecture US Patent 7,282,295, (2007).

[25] M.S. Whittingham, Metal-Air Batteries: A Reality Check, in PRiME, Honolulu, USA, Electrochem. Soc. (2012).

[26] H. Sakaebe, H. Matsumoto, K. Tatsumi, Application of room temperature ionic liquids to Li batteries, Electrochim. Acta. 53 (2007) 1048–1054. https://doi.org/10.1016/j.electacta.2007.02.054.

[27] M. Galiński, A. Lewandowski, I. Stepniak, Ionic liquids as electrolytes, Electrochim. Acta. 51 (2006) 5567–5580. https://doi.org/10.1016/j.electacta.2006.03.016.

[28] P. von Czarnecki, M. Ahrens, B. Iliev, T.J.S. Schubert, Ionic Liquid Based Electrolytes for Electrical Storage, ECS Trans. 77 (2017) 79–87. https://doi.org/10.1149/07701.0079ecst.

[29] P.C.K. Vesborg, T.F. Jaramillo, Addressing the terawatt challenge: Scalability in the supply of chemical elements for renewable energy, RSC Adv. 2 (2012) 7933–7947. https://doi.org/10.1039/c2ra20839c.

[30] H. Weinrich, Renaissance of the Iron–Air Battery, Forschungszentrum Press Releases. (2017). https://www.fz-juelich.de/SharedDocs/Meldungen/IEK/IEK-9/EN/Fe-air battery.html (accessed March 17, 2022).

[31] Y.E. Durmus, Investigation and Development of a Resource Efficient Metal – Air Battery – Silicon – Air, (2018).

[32] X. Liang, C. Hart, Q. Pang, A. Garsuch, T. Weiss, L.F. Nazar, A highly efficient polysulfide mediator for lithium–sulfur batteries, Nat. Commun. 2015 61. 6 (2015) 1–8. https://doi.org/10.1038/ncomms6682.

[33] A. Riaz, K.N. Jung, W. Chang, K.H. Shin, J.W. Lee, Carbon-, binder-, and precious metal-free cathodes for non-aqueous lithium-oxygen batteries: Nanoflake-decorated nanoneedle oxide arrays, ACS Appl. Mater. Interfaces. 6 (2014) 17815–17822. https://doi.org/10.1021/AM504463B/SUPPL_FILE/AM504463B_SI_001.PDF.

[34] T. Shiga, Y. Hase, Y. Kato, M. Inoue, K. Takechi, A rechargeable non-aqueous Mg–O2 battery, Chem. Commun. 49 (2013) 9152–9154. https://doi.org/10.1039/C3CC43477J.

[35] H. Yadegari, M.N. Banis, B. Xiao, Q. Sun, X. Li, A. Lushington, B. Wang, R. Li, T.K. Sham, X. Cui, X. Sun, Three-dimensional nanostructured air electrode for sodium-oxygen batteries: A mechanism study toward the cyclability of the cell, Chem. Mater. 27 (2015) 3040–3047.

https://doi.org/10.1021/ACS.CHEMMATER.5B00435/SUPPL_FILE/CM5B00435_SI_001.PDF.

[36] N. Xiao, X. Ren, M. He, W.D. McCulloch, Y. Wu, Probing Mechanisms for Inverse Correlation between Rate Performance and Capacity in K-O2 Batteries, ACS Appl. Mater. Interfaces. 9 (2017) 4301–4308. https://doi.org/10.1021/ACSAMI.6B06280/SUPPL_FILE/AM6B06280_SI_001.PDF.

[37] Z. Chen, A. Yu, D. Higgins, H. Li, H. Wang, Z. Chen, Highly active and durable core-corona structured bifunctional catalyst for rechargeable metal-air battery application, Nano Lett. 12 (2012) 1946–1952. https://doi.org/10.1021/NL2044327/SUPPL_FILE/NL2044327_SI_001.PDF.

[38] C. Yang, A.K. Manohar, S.R. Narayanan, A High-Performance Sintered Iron Electrode for Rechargeable Alkaline Batteries to Enable Large-Scale Energy Storage, J. Electrochem. Soc. 164 (2017) A418–A429. https://doi.org/10.1149/2.1161702JES/XML.

[39] D. Gelman, B. Shvartsev, Y. Ein-Eli, Aluminum–air battery based on an ionic liquid electrolyte, J. Mater. Chem. A. 2 (2014) 20237–20242. https://doi.org/10.1039/C4TA04721D.

[40] D. Gelman, B. Shvartsev, Y. Ein-eli, Challenges and Prospect of Non-aqueous Non-alkali (NANA) Metal – Air Batteries, Top. Curr. Chem. 374 (2016). https://doi.org/10.1007/s41061-016-0080-9.

[41] Y.E. Durmus, Ö. Aslanbas, S. Kayser, H. Tempel, F. Hausen, L.G.J. de Haart, J. Granwehr, Y. Ein-Eli, R.A. Eichel, H. Kungl, Long run discharge, performance and efficiency of primary Silicon–air cells with alkaline electrolyte, Electrochim. Acta. 225 (2017) 215–224. https://doi.org/10.1016/j.electacta.2016.12.120.

[42] G. Cohn, D. Starosvetsky, R. Hagiwara, D.D. Macdonald, Y. Ein-Eli, Silicon-air batteries, Electrochem. Commun. 11 (2009) 1916–1918. https://doi.org/10.1016/j.elecom.2009.08.015.

[43] G. Cohn, Y. Ein-Eli, Study and development of non-aqueous silicon-air battery, J. Power Sources. 195 (2010) 4963–4970. https://doi.org/10.1016/j.jpowsour.2010.02.070.

[44] Y.E. Durmus, S. Jakobi, T. Beuse, Ö. Aslanbas, H. Tempel, F. Hausen, L.G.J. de Haart, Y. Ein-Eli, R.-A. Eichel, H. Kungl, Influence of Dopant Type and Orientation of Silicon Anodes on Performance, Efficiency and Corrosion of Silicon–Air Cells with EMIm(HF) 2.3 F Electrolyte , J. Electrochem. Soc. 164 (2017) A2310–A2320. https://doi.org/10.1149/2.0301712jes.

[45] Y.E. Durmus, C. Roitzheim, H. Tempel, F. Hausen, Y. Ein-Eli, H. Kungl, R.A. Eichel, Analysis

on discharge behavior and performance of As- and B-doped silicon anodes in non-aqueous Si–air batteries under pulsed discharge operation, J. Appl. Electrochem. 50 (2020) 93–109. https://doi.org/10.1007/s10800-019-01372-5.

[46] X. Zhong, H. Zhang, Y. Liu, J. Bai, L. Liao, Y. Huang, X. Duan, High-capacity silicon-air battery in alkaline solution, ChemSusChem. 5 (2012) 177–180. https://doi.org/10.1002/cssc.201100426.

[47] D.W. Park, S. Kim, J.D. Ocon, G.H.A. Abrenica, J.K. Lee, J. Lee, Controlled electrochemical etching of nanoporous si anodes and its discharge behavior in alkaline si - Air batteries, ACS Appl. Mater. Interfaces. 7 (2015) 3126–3132. https://doi.org/10.1021/am507360e.

[48] Y.E. Durmus, S.S. Montiel Guerrero, Ö. Aslanbas, H. Tempel, F. Hausen, L.G.J. de Haart, Y. Ein-Eli, R.A. Eichel, H. Kungl, Investigation of the corrosion behavior of highly As-doped crystalline Si in alkaline Si–air batteries, Electrochim. Acta. 265 (2018) 292–302. https://doi.org/10.1016/j.electacta.2018.01.145.

[49] G. Cohn, D.D. MacDonald, Y. Ein-Eli, Remarkable Impact of Water on the Discharge Performance of a Silicon–Air Battery, ChemSusChem. 4 (2011) 1124–1129. https://doi.org/10.1002/CSSC.201100169.

[50] G. Cohn, A. Altberg, D.D. MacDonald, Y. Ein-Eli, A silicon–air battery utilizing a composite polymer electrolyte, Electrochim. Acta. 58 (2011) 161–164. https://doi.org/10.1016/J.ELECTACTA.2011.09.026.

[51] A. Inoishi, T. Sakai, Y.W. Ju, S. Ida, T. Ishihara, A rechargeable Si–air solid state oxygen shuttle battery incorporating an oxide ion conductor, J. Mater. Chem. A. 1 (2013) 15212–15215. https://doi.org/10.1039/C3TA14023G.

[52] Mineral Commodity Summaries 2010, U.S. Geol. Surv. (n.d.).

[53] P. Jakes, G. Cohn, Y. Ein-Eli, F. Scheiba, H. Ehrenberg, R.A. Eichel, Limitation of discharge capacity and mechanisms of air-electrode deactivation in silicon-air batteries, ChemSusChem. 5 (2012) 2278–2285. https://doi.org/10.1002/cssc.201200199.

[54] G. Cohn, R.-A. Eichel, Y. Ein-Eli, New insight into the discharge mechanism of silicon-air batteries using electrochemical impedance spectroscopy, Phys. Chem. Chem. Phys. 15 (2013) 3256–3263. https://doi.org/10.1039/c2cp43870d.

[55] O.J. Glembocki, E.D. Palik, G.R. Deguel, D.L. Kendall, Hydration model for the molarity dependence of the etch rate of Si in aqueous alkali hydroxides, J. Electrochem. Soc. 138 (1991) 1055–1063. https://doi.org/10.1149/1.2085715.

[56] X.G. Zhang, Corrosion and Electrochemistry of Zinc, Springer US, Boston, MA, 1996. https://doi.org/10.1007/978-1-4757-9877-7.

[57] L. Maiche, 127069, 127069, 1878.

[58] J. Fu, Z.P. Cano, M.G. Park, A. Yu, M. Fowler, Z. Chen, Electrically Rechargeable Zinc–Air Batteries: Progress, Challenges, and Perspectives, Adv. Mater. 29 (2017). https://doi.org/10.1002/adma.201604685.

[59] N. Borchers, S. Clark, B. Horstmann, K. Jayasayee, M. Juel, P. Stevens, Innovative zinc-based batteries, J. Power Sources. 484 (2021) 229309. https://doi.org/10.1016/j.jpowsour.2020.229309.

[60] A.R. Mainar, E. Iruin, L.C. Colmenares, A. Kvasha, I. De Meatza, M. Bengoechea, O. Leonet, I. Boyano, Z. Zhang, J.A. Blazquez, An overview of progress in electrolytes for secondary zinc-air batteries and other storage systems based on zinc, J. Energy Storage. 15 (2018) 304–328. https://doi.org/10.1016/j.est.2017.12.004.

[61] A.G. Olabi, E.T. Sayed, T. Wilberforce, A. Jamal, A.H. Alami, K. Elsaid, S.M.A. Rahman, S.K. Shah, M.A. Abdelkareem, Metal-Air Batteries—A Review, Energies. 14 (2021) 7373. https://doi.org/10.3390/en14217373.

[62] Y. Li, H. Dai, Recent advances in zinc–air batteries, Chem. Soc. Rev. 43 (2014) 5257–5275. https://doi.org/10.1039/C4CS00015C.

[63] G.W. Heise, E.A. Schumacher, An Air-Depolarized Primary Cell with Caustic Alkali Electrolyte, Trans. Electrochem. Soc. 62 (1932) 383. https://doi.org/10.1149/1.3493794.

[64] C.J. Lan, T.S. Chin, P.H. Lin, T.P. Perng, Zn-Al alloy as a new anode-metal of a zinc-air battery, J. OfNew Mater. Electrochem. Syst. 9 (2006) 27–32.

[65] A.D. Martin, J.H. Zhu, Effect of Microstructure on the Performance of a Zn-Al Alloy Anode for Zn-Air Battery Application, ECS Electrochem. Lett. 1 (2012) A13–A16. https://doi.org/10.1149/2.012201eel.

[66] S. Hosseini, A. Abbasi, L.O. Uginet, N. Haustraete, S. Praserthdam, T. Yonezawa, S. Kheawhom, The Influence of Dimethyl Sulfoxide as Electrolyte Additive on Anodic Dissolution of Alkaline Zinc-Air Flow Battery, Sci. Rep. 9 (2019) 1–12. https://doi.org/10.1038/s41598-019-51412-5.

[67] X. Wang, J. Sunarso, Q. Lu, Z. Zhou, J. Dai, D. Guan, W. Zhou, Z. Shao, High-Performance Platinum-Perovskite Composite Bifunctional Oxygen Electrocatalyst for Rechargeable Zn – Air Battery, Adv. Energy Mater. 1903271 (2020) 1–10.

https://doi.org/10.1002/aenm.201903271.

[68] X. Zhong, W. Yi, Y. Qu, L. Zhang, H. Bai, Y. Zhu, J. Wan, S. Chen, M. Yang, L. Huang, M. Gu, H. Pan, B. Xu, Co single-atom anchored on Co3O4 and nitrogen-doped active carbon toward bifunctional catalyst for zinc-air batteries, Appl. Catal. B Environ. 260 (2020) 118188. https://doi.org/10.1016/j.apcatb.2019.118188.

[69] M. Li, F. Luo, Q. Zhang, Z. Yang, Z. Xu, Atomic layer Co3O4-x nanosheets as efficient and stable electrocatalyst for rechargeable zinc-air batteries, J. Catal. 381 (2020) 395–401. https://doi.org/10.1016/j.jcat.2019.11.020.

[70] P. Chen, K. Zhang, D. Tang, W. Liu, F. Meng, Q. Huang, J. Liu, Recent Progress in Electrolytes for Zn–Air Batteries, Front. Chem. 8 (2020) 372. https://doi.org/10.3389/FCHEM.2020.00372/BIBTEX.

[71] S. Hosseini, S.J. Han, A. Arponwichanop, T. Yonezawa, Ethanol as an electrolyte additive for alkaline zinc-air flow batteries, Sci. Rep. (2018) 1–11. https://doi.org/10.1038/s41598-018-29630-0.

[72] K.K. Kumar, R. Brindha, M. Nandhini, M. Selvam, K. Saminathan, K. Sakthipandi, Water-suspended graphene as electrolyte additive in zinc-air alkaline battery system, Ionics (Kiel). 25 (2019) 1699–1706. https://doi.org/10.1007/s11581-019-02924-7.

[73] G.W. Heise, E.A. Schumacher, AIR DEPOLARIZED PRIMARY BATTERY, US1899615A, 1932. https://patents.google.com/patent/US1899615A/en (accessed March 18, 2022).

[74] J. Jindra, J. Mrha, M. Musilová, Zinc-air cell with neutral electrolyte, J. Appl. Electrochem. 3 (1973) 297–301. https://doi.org/10.1007/BF00613036.

[75] S. Amendola, M. Binder, P.J. Black, S. Sharp-Goldman, L. Johnson, M. Kunz, E. Al., Electrically Rechargeable, Metal-Air Battery Systems and Methods, U.S. Patent No US20120021303A1, 2012.

[76] F.W. Thomas Goh, Z. Liu, T.S.A. Hor, J. Zhang, X. Ge, Y. Zong, A. Yu, W. Khoo, A Near-Neutral Chloride Electrolyte for Electrically Rechargeable Zinc-Air Batteries, J. Electrochem. Soc. 161 (2014) A2080–A2086. https://doi.org/10.1149/2.0311414jes.

[77] A. Sumboja, X. Ge, F.W.T. Goh, B. Li, D. Geng, T.S.A. Hor, Y. Zong, Z. Liu, Manganese Oxide Catalyst Grown on Carbon Paper as an Air Cathode for High-Performance Rechargeable Zinc-Air Batteries, Chempluschem. 80 (2015) 1341–1346. https://doi.org/10.1002/cplu.201500183.

[78] A. Sumboja, X. Ge, G. Zheng, F.W.T. Goh, T.S.A. Hor, Y. Zong, Z. Liu, Durable rechargeable

zinc-air batteries with neutral electrolyte and manganese oxide catalyst, J. Power Sources. 332 (2016) 330–336. https://doi.org/10.1016/j.jpowsour.2016.09.142.

[79] S. Clark, A. Latz, B. Horstmann, Rational Development of Neutral Aqueous Electrolytes for Zinc-Air Batteries, ChemSusChem. 10 (2017) 4735–4747. https://doi.org/10.1002/cssc.201701468.

[80] S. Clark, A.R. Mainar, E. Iruin, L.C. Colmenares, J.A. Blázquez, J.R. Tolchard, A. Latz, B. Horstmann, Towards rechargeable zinc-air batteries with aqueous chloride electrolytes, J. Mater. Chem. A. 7 (2019) 11387–11399. https://doi.org/10.1039/c9ta01190k.

[81] S. Clark, A.R. Mainar, E. Iruin, L.C. Colmenares, J.A. Blázquez, J.R. Tolchard, Z. Jusys, B. Horstmann, Designing Aqueous Organic Electrolytes for Zinc–Air Batteries: Method, Simulation, and Validation, Adv. Energy Mater. 10 (2020) 1–16. https://doi.org/10.1002/aenm.201903470.

[82] D. Gelman, I. Lasman, S. Elfimchev, D. Starosvetsky, Y. Ein-Eli, Aluminum corrosion mitigation in alkaline electrolytes containing hybrid inorganic/organic inhibitor system for power sources applications, J. Power Sources. 285 (2015) 100–108. https://doi.org/10.1016/j.jpowsour.2015.03.048.

[83] L. Fan, H. Lu, J. Leng, Performance of fine structured aluminum anodes in neutral and alkaline electrolytes for Al-air batteries, Electrochim. Acta. 165 (2015) 22–28. https://doi.org/10.1016/j.electacta.2015.03.002.

[84] S. Zaromb, The Use and Behavior of Aluminum Anodes in Alkaline Primary Batteries, J. Electrochem. Soc. 109 (1962) 1125. https://doi.org/10.1149/1.2425257.

[85] R. Mori, Recent Developments for Aluminum – Air Batteries, Electrochem. Energy Rev. 3 (2020) 344–369. https://doi.org/10.1007/s41918-020-00065-4.

[86] R. Mori, Rechargeable Aluminum–Air Battery Using Various Air-Cathode Materials and Suppression of Byproduct Formation on Both Anode and Air Cathode, ECS Meet. Abstr. MA2017-02 (2017) 565–565. https://doi.org/10.1149/ma2017-02/5/565.

[87] Z.A. Zafar, S. Imtiaz, R. Razaq, S. Ji, T. Huang, Z. Zhang, Y. Huang, J.A. Anderson, Cathode materials for rechargeable aluminum batteries: current status and progress, J. Mater. Chem. A. 5 (2017) 5646–5660. https://doi.org/10.1039/c7ta00282c.

[88] A.R. Despic, D.M. Drazic, M.M. Purenovic, N. Cikovic, Electrochemical properties of aluminium alloys containing indium, gallium and thallium, J. Appl. Electrochem. 6 (1976) 527–542.

[89] D.M. Drazic, A.R. Despic, S. Zecevic, M. Atanackovic, I. Iliev, Neutral electrolyte aluminium-air battery, Power Sources 7 Res. Dev. Non-Mechanical Electr. Power Sources. (1979) 353–362. https://ui.adsabs.harvard.edu/abs/1979psrd.symp..353D/abstract.

[90] R.J. Brodd, Electrochemistry in Industry: New Directions, 1st editio, Springer, New York, 1982. https://books.google.com.mx/books?hl=en&lr=&id=4OPcBwAAQBAJ&oi=fnd&pg=PA181&dq=neutral+al-air+battery&ots=jLBkr5hR0F&sig=4yJt53S9Efd-Ygc0P_n8WIOr2so&redir_esc=y#v=onepage&q=neutral al-air battery&f=false (accessed April 2, 2022).

[91] B.P. Caldwell, V.J. Albano, Rate of Solution of Zinc and Aluminum while Cathodic, Trans. Electrochem. Soc. 76 (1939) 271. https://doi.org/10.1149/1.3500282.

[92] S.-M. Moon, S.-I. Pyun, The corrosion of pure aluminium during cathodic polarization in aqueous solutions, Corros. Sci. 39 (1997) 399–408. https://doi.org/10.1016/S0010-938X(97)83354-9.

[93] A.G. Muñoz, S.B. Saidman, J.B. Bessone, Corrosion mechanism of Al-Zn-In alloys in chloride solutions, Lat. Am. Appl. Res. 33 (2003) 275–280.

[94] S. Gudić, J. Radošević, I. Smoljko, M. Kliškić, Cathodic breakdown of anodic oxide film on Al and Al–Sn alloys in NaCl solution, Electrochim. Acta. 50 (2005) 5624–5632. https://doi.org/10.1016/j.electacta.2005.03.041.

[95] J.F. Cooper, High performance metal/air fuel cells. Part 1. General review. [Li, Al, Ca, Cd, Mg], (1977). https://doi.org/10.2172/7084912.

[96] M. Ritschel, W. Vielstich, Sea water activated aluminium-air cell, Electrochim. Acta. 24 (1979) 885–886. https://doi.org/10.1016/0013-4686(79)87012-7.

[97] B. HAN, G. LIANG, Neutral electrolyte aluminum air battery with open configuration, Rare Met. 25 (2006) 360–363. https://doi.org/10.1016/S1001-0521(07)60106-5.

[98] I. Smoljko, S. Gudić, N. Kuzmanić, M. Kliškić, Electrochemical properties of aluminium anodes for Al/air batteries with aqueous sodium chloride electrolyte, J. Appl. Electrochem. 42 (2012) 969–977. https://doi.org/10.1007/s10800-012-0465-6.

[99] J. Ma, J. Wen, J. Gao, Q. Li, Performance of Al–0.5 Mg–0.02 Ga–0.1 Sn–0.5 Mn as anode for Al–air battery in NaCl solutions, J. Power Sources. 253 (2014) 419–423. https://doi.org/10.1016/J.JPOWSOUR.2013.12.053.

[100] Z. Wu, H. Zhang, K. Qin, J. Zou, K. Qin, C. Ban, J. Cui, H. Nagaumi, The role of gallium and

indium in improving the electrochemical characteristics of Al–Mg–Sn-based alloy for Al–air battery anodes in 2 M NaCl solution, J. Mater. Sci. 55 (2020) 11545–11560. https://doi.org/10.1007/s10853-020-04755-8.

[101] H.. El Shayeb, F.. Abd El Wahab, S. Zein El Abedin, Electrochemical behaviour of Al, Al–Sn, Al–Zn and Al–Zn–Sn alloys in chloride solutions containing stannous ions, Corros. Sci. 43 (2001) 655–669. https://doi.org/10.1016/S0010-938X(00)00101-3.

[102] H.. El Shayeb, F.. Abd El Wahab, S. Zein El Abedin, Effect of gallium ions on the electrochemical behaviour of Al, Al–Sn, Al–Zn and Al–Zn–Sn alloys in chloride solutions, Corros. Sci. 43 (2001) 643–654. https://doi.org/10.1016/S0010-938X(00)00100-1.

[103] Y. Tang, L. Lu, H.W. Roesky, L. Wang, B. Huang, The effect of zinc on the aluminum anode of the aluminum–air battery, J. Power Sources. 138 (2004) 313–318. https://doi.org/10.1016/J.JPOWSOUR.2004.06.043.

[104] Y. Gu, J. Jiang, Q. Xie, A. Ma, Z. Gao, Improved discharge performance of equal-channel-angular-pressed AZ61-In alloys as anodes for seawater-activated batteries, J. Alloys Compd. 890 (2022) 161809. https://doi.org/10.1016/J.JALLCOM.2021.161809.

[105] K. Xhanari, M. Finšgar, Organic corrosion inhibitors for aluminum and its alloys in chloride and alkaline solutions: A review, Arab. J. Chem. 12 (2019) 4646–4663. https://doi.org/10.1016/J.ARABJC.2016.08.009.

[106] G. Treacy, A. Rudd, C. Breslin, Electrochemical behaviour of aluminium in the presence of EDTA-containing chloride solutions, J. Appl. Electrochem. 30 (2000) 675–683. https://doi.org/10.1023/A:1003945214539.

[107] J. Ma, J. Wen, J. Gao, Q. Li, Performance of Al-0.5 Mg-0.02 Ga-0.1 Sn-0.5 as anode for Al-air Battery, Electrochim. Acta. 161 (2014) A376–A380. https://doi.org/10.1016/j.electacta.2014.02.080.

[108] M. Pino, D. Herranz, J. Chacón, E. Fatás, P. Ocón, Carbon treated commercial aluminium alloys as anodes for aluminium-air batteries in sodium chloride electrolyte, J. Power Sources. 326 (2016) 296–302. https://doi.org/10.1016/J.JPOWSOUR.2016.06.118.

[109] Y. Wang, H. Kwok, W. Pan, H. Zhang, D.Y.C. Leung, Innovative paper-based Al-air batteries as a low-cost and green energy technology for the miniwatt market, J. Power Sources. 414 (2019) 278–282. https://doi.org/10.1016/J.JPOWSOUR.2019.01.018.

[110] Y. Wang, H.Y.H. Kwok, W. Pan, H. Zhang, X. Lu, D.Y.C. Leung, Parametric study and optimization of a low-cost paper-based Al-air battery with corrosion inhibition ability, Appl. Energy. 251 (2019). https://doi.org/10.1016/j.apenergy.2019.113342.

[111] H. v. Helmholtz, Studien über electrische Grenzschichten, Ann. Der Phys. Und Chemie. 7 (1879) 337–382. https://doi.org/10.1002/andp.18792430702.

[112] W. Nernst, Die elektromotorische Wirksamkeit der Jonen., Zeitschrift Für Phys. Chemie. IV (1889) 129–181.

[113] D.R. Lide, CRC Handbook of Chemistry and Physics, J. Am. Chem. Soc. 131 (2009) 12862–12862. https://doi.org/10.1021/ja906434c.

[114] D.A. Skoog, D.M. West, F.J. Holler, S.R. Crouch, Fundamentals of Analytical Chemistry, 9th Editio, Brooks/Cole, Cengage Learning, 2014.

[115] D.C. Harris, Quantitative chemical analysis, 7th. editi, W. H. Freeman and Company, New York, 2007.

[116] Potentiostat/Galvanostat Electrochemical Instrument Basics, (n.d.). https://www.gamry.com/application-notes/instrumentation/potentiostat-fundamentals/ (accessed November 26, 2021).

[117] LEXT OLS4100 Industrial Laser Confocal Microscopes - Olympus 3D Laser Measuring Solution, (n.d.). https://www.olympus-ims.com/en/metrology/ols4100/ (accessed November 30, 2021).

[118] M. Gonon, Case Studies in the X-ray Diffraction of Ceramics, Encycl. Mater. Tech. Ceram. Glas. (2021) 560–577. https://doi.org/10.1016/B978-0-12-818542-1.00005-9.

[119] D.J. Stokes, Principles and Practice of Variable Pressure/Environmental Scanning Electron Microscopy (VP-ESEM), Princ. Pract. Var. Press. Scanning Electron Microsc. (2008) 1–221. https://doi.org/10.1002/9780470758731.

[120] G. Binnig, C.F. Quate, C. Gerber, Atomic force microscope, Phys. Rev. Lett. 56 (1986) 930–933. https://doi.org/10.1103/PHYSREVLETT.56.930/FIGURE/1/THUMB.

[121] M. Pourbaix, Atlas of electrochemical equilibria in aqueous solutions, Second ed., NATIONAL ASSOCIATION of CORROSION ENGINEERS, Houston, Texas, USA, 1974.

[122] B. Meddings, G.M. Hieftje, H. Anderson, H. Kaiser, R. Rezaaiyaan, Design and Construction of a Low-Flow, Low-Power Torch for Inductively Coupled Plasma Spectrometry, Appl. Spectrosc. Vol. 36, Issue 6, Pp. 627-631. 36 (1982) 627–631. https://www.osapublishing.org/abstract.cfm?uri=as-36-6-627 (accessed November 30, 2021).

[123] Ö. Aslanbas, Y.E. Durmus, H. Tempel, F. Hausen, Y. Ein-Eli, R.A. Eichel, H. Kungl, Electrochemical analysis and mixed potentials theory of ionic liquid based Metal–Air

batteries with Al/Si alloy anodes, Electrochim. Acta. 276 (2018) 399–411. https://doi.org/10.1016/j.electacta.2018.04.176.

[124] Defense Advanced Research Projects Agency (DARPA), Vanishing Programmable Resources (VAPR) (Archived), (n.d.). https://www.darpa.mil/program/vanishing-programmable-resources (accessed October 8, 2021).

[125] I. Analog Devices, MAX17220–MAX17225, (n.d.). https://www.mouser.de/datasheet/2/256/MAX17220_MAX17225-1089911.pdf (accessed April 27, 2022).

[126] Learning to Decapsulate Integrated Circuits using Acid Deposition · Hack The World, (n.d.). https://jcjc-dev.com/2020/10/20/learning-to-decap-ics/ (accessed August 9, 2022).

[127] F. Santos, J.P. Tafur, J. Abad, A.J. Fernández Romero, Structural modifications and ionic transport of PVA-KOH hydrogels applied in Zn/Air batteries, J. Electroanal. Chem. 850 (2019) 113380. https://doi.org/10.1016/j.jelechem.2019.113380.

[128] A. Dehaut, A.L. Cassone, L. Frère, L. Hermabessiere, C. Himber, E. Rinnert, G. Rivière, C. Lambert, P. Soudant, A. Huvet, G. Duflos, I. Paul-Pont, Microplastics in seafood: Benchmark protocol for their extraction and characterization, Environ. Pollut. 215 (2016) 223–233. https://doi.org/10.1016/j.envpol.2016.05.018.

[129] H. Seidel, L. Csepregi, A. Heuberger, H. Baumgartel, Anisotropic Etching of Crystalline Silicon in Alkaline Solutions I . Orientation Dependence and Behavior of Passivation Layers, J. Electrochem. Soc. 137 (1990) 3612–3626. https://doi.org/10.1149/1.2086277.

[130] Y. Ein-Eli, Enhanced Corrosion Inhibition of Zn in Alkaline Solutions Containing Poly(ethylene glycol) Diacid, Electrochem. Solid-State Lett. 7 (2004) B5–B7. https://doi.org/10.1149/1.1626111.

[131] X.G. Zhang, Electrochemistry of Silicon and Its Oxide, Kluwe Academic Publishers, New York, 2004. https://doi.org/https://doi.org/10.1007/b10033.

[132] Y.E. Durmus, S.S. Montiel Guerrero, H. Tempel, F. Hausen, H. Kungl, R.A. Eichel, Influence of Al Alloying on the Electrochemical Behavior of Zn Electrodes for Zn–Air Batteries With Neutral Sodium Chloride Electrolyte, Front. Chem. 7 (2019) 1–13. https://doi.org/10.3389/fchem.2019.00800.

[133] C. Wagner, W. Traud, In the Interpretation of Corrosion Processes Through the Superposition of Electrochemical Partial Processes and on the Mixed Electrodes, Z. Elektrochem. 44 (1938) 391.

[134] B. Beverskog, I. Puigdomenech, Revised pourbaix diagrams for zinc at 25–300 °C, Corros. Sci. 39 (1997) 107–114. https://doi.org/10.1016/S0010-938X(97)89246-3.

[135] K.A.P. A. Jain*, S.P. Ong*, G. Hautier, W. Chen, W.D. Richards, S. Dacek, S. Cholia, D. Gunter, D. Skinner, G. Ceder, Materials Project, Mater. Proj. (2020). https://materialsproject.org/#apps/pourbaixdiagram (accessed November 27, 2020).

[136] A.M. Patel, J.K. Nørskov, K.A. Persson, J.H. Montoya, Efficient Pourbaix diagrams of many-element compounds, Phys. Chem. Chem. Phys. 21 (2019) 25323–25327. https://doi.org/10.1039/c9cp04799a.

[137] A.A. Presnyakov, Y.A. Gorban, V. V. Chervyakova, The aluminium-zinc phase diagram., Russ. J. Phys. Chem. 35 (1961) 632–633.

[138] G.R. Goldak, J.A. Gordon Parr, High-temperature x-raydiffractometer study of the zinc-aluminium system in the region 40-75 wt.% Zinc., J. Inst. Met. 95 (1964) 230–233.

[139] L.F. Mondolfo, Structure of the aluminium: magnesium: zinc alloys, Int. Mater. Rev. 16 (1971) 95–124. https://doi.org/10.1179/095066071790137865.

[140] DIN EN ISO 8407, Corrosion of metals and alloys – Removal of corrosion products from corrosion test specimens, 2014, (n.d.).

[141] X. Wei, L. Ren, X. Geng, Z. Sun, H. Hu, X. Nie, A. Banerji, Nano microstructure development and solidification of Zn-6 wt% Al hypereutectic alloy, Mater. Charact. 147 (2019) 295–302. https://doi.org/10.1016/j.matchar.2018.11.016.

[142] S.T. Bluni, M.R. Notis, A.R. Marder, Nucleation characteristics and microstructure in off-eutectic Al-Zn alloys, Acta Metall. Mater. 43 (1995) 1775–1782. https://doi.org/10.1016/0956-7151(94)00397-Z.

[143] W. Yang, H. Fredriksson, S. Ji, Halo formation of Zn-Al alloys under conventional solidification and intensive convection solidification, J. Alloys Compd. 696 (2017) 460–469. https://doi.org/10.1016/j.jallcom.2016.11.281.

[144] Y. hua Zhu, General Rule of Phase Decomposition in Zn-Al Based Alloys (II), Mater. Trans. 45 (2004) 3083–3097. https://doi.org/10.2320/matertrans.45.3083.

[145] G.S. Frankel, Pitting Corrosion of Metals: A Review of the Critical Factors, J. Electrochem. Soc. 145 (1998) 2186–2198. https://doi.org/10.1149/1.1838615.

[146] W. Miao, I.S. Cole, A.K. Neufeld, S. Furman, Pitting Corrosion of Zn and Zn-Al Coated Steels in pH 2 to 12 NaCl Solutions, J. Electrochem. Soc. 154 (2007) C7. https://doi.org/10.1149/1.2372691.

[147] Q. Qu, L. Li, W. Bai, C. Yan, C. Cao, Effects of NaCl and NH4Cl on the initial atmospheric corrosion of zinc, Corros. Sci. 47 (2005) 2832–2840. https://doi.org/10.1016/j.corsci.2004.11.010.

[148] M. Mouanga, P. Berçot, J.Y. Rauch, Comparison of corrosion behaviour of zinc in NaCl and in NaOH solutions. Part I: Corrosion layer characterization, Corros. Sci. 52 (2010) 3984–3992. https://doi.org/10.1016/j.corsci.2010.08.003.

[149] R.T. Foley, T.H. Nguyen, The Chemical Nature of Aluminum Corrosion: V . Energy Transfer in Aluminum Dissolution, J. Electrochem. Soc. 129 (1982) 464–467. https://doi.org/10.1149/1.2123881.

[150] C. Vargel, Corrosion of Alumunium, 1st. Editi, Elsevier Science and Technology, Amsterdam, 2004.

[151] T.N. Vu, P. Volovitch, K. Ogle, The effect of pH on the selective dissolution of Zn and Al from Zn–Al coatings on steel, Corros. Sci. 67 (2013) 42–49. https://doi.org/10.1016/j.corsci.2012.09.042.

[152] M. Salgueiro Azevedo, C. Allély, K. Ogle, P. Volovitch, Corrosion mechanisms of Zn(Mg, Al) coated steel in accelerated tests and natural exposure: 1. The role of electrolyte composition in the nature of corrosion products and relative corrosion rate, Corros. Sci. 90 (2015) 472–481. https://doi.org/10.1016/j.corsci.2014.05.014.

[153] C.B. Breslin, L.P. Friery, W.M. Carroll, Influence of Impurity Elements on Electrochemical Activity of Aluminum Activated by Indium, CORROSION. 49 (1993) 895–902. https://doi.org/10.5006/1.3316015.

[154] S.Z. El Abedin, F. Endres, Electrochemical Behaviour of Al, Al–In and Al–Ga–In Alloys in Chloride Solutions Containing Zinc Ions, J. Appl. Electrochem. 34 (2004) 1071–1080. https://doi.org/10.1023/B:JACH.0000042672.23588.df.

[155] L.M. Baugh, Corrosion and polarization characteristics of zinc in neutral-acid media - I. Pure zinc in solutions of various sodium salts, Electrochim. Acta. 24 (1979) 657–667. https://doi.org/10.1016/0013-4686(79)87048-6.

[156] S.B. Saidman, J.B. Bessone, Cathodic polarization characteristics and activation of aluminium in chloride solutions containing indium and zinc ions, J. Appl. Electrochem. 27 (1997) 731–737. https://doi.org/10.1023/A:1018400207300.

[157] X. Zhang, T.-N. Vu, P. Volovitch, C. Leygraf, K. Ogle, I.O. Wallinder, The initial release of zinc and aluminum from non-treated Galvalume and the formation of corrosion products in chloride containing media, Appl. Surf. Sci. 258 (2012) 4351–4359.

https://doi.org/10.1016/j.apsusc.2011.12.112.

[158] S.S. Montiel Guerrero, Improved Electrochemical Performance of Zinc Anodes by EDTA in Near-Neutral Zinc-Air Batteries, Batter. Suppercaps. 4 (2021) 1830–1842. https://doi.org/doi.org/10.1002/batt.202100116.

[159] S.S. Montiel Guerrero, Y.E. Durmus, K. Dzieciol, S. Basak, H. Tempel, S. Waasen, H. Kungl, R. Eichel, Cover Feature: Improved Electrochemical Performance of Zinc Anodes by EDTA in Near-Neutral Zinc−Air Batteries (Batteries & Supercaps 12/2021), Batter. Supercaps. 4 (2021) 1782–1782. https://doi.org/10.1002/batt.202100332.

[160] I. Puigdomenech, Making Equilibrium Diagrams Using Sophisticated Algorithms (MEDUSA), (2010). https://sites.google.com/site/chemdiagr/home?authuser=0.

[161] S. Stankovic, B. Grgur, N. Krstajic, M. Vojnovic, Kinetics of the zinc anodic dissolution reaction in near neutral EDTA solutions, J. Serbian Chem. Soc. 68 (2003) 207–218. https://doi.org/10.2298/JSC0303207S.

[162] DIN EN ISO 8407, 2014. https://doi.org/https://dx.doi.org/10.31030/2116692.

[163] M.E. McMahon, R.J. Santucci, J.R. Scully, Advanced chemical stability diagrams to predict the formation of complex zinc compounds in a chloride environment, RSC Adv. 9 (2019) 19905–19916. https://doi.org/10.1039/c9ra00228f.

[164] J. Ryczkowski, IR studies of EDTA alkaline salts interaction with the surface of inorganic oxides, Appl. Surf. Sci. 252 (2005) 813–822. https://doi.org/10.1016/j.apsusc.2005.02.056.

[165] G.A. Parks, The Isoelectric Points of Solid Oxides, Solid Hydroxides, and Aqueous Hydroxo Complex Systems, Chem. Rev. 65 (1965) 177–198. https://doi.org/10.1021/cr60234a002.

[166] J.A. Rumball, G.D. Richmond, Measurement of oxidation in a base metal flotation circuit by selective leaching with EDTA, Int. J. Miner. Process. 48 (1996) 1–20. https://doi.org/10.1016/S0301-7516(96)00010-5.

[167] H. Tamura, N. Ito, M. Kitano, S. Takasaki, A kinetic model of the dissolution of copper(II) oxide in EDTA solutions considering the coupling of metal and oxide ion transfer, Corros. Sci. 43 (2001) 1675–1691. https://doi.org/10.1016/S0010-938X(00)00171-2.

[168] M. Kuśmierz, S. Pasieczna-Patkowska, FT-IR/PAS Study of Surface EDTA-ZnO Interactions, Ann. UMCS, Chem. 68 (2014) 25–31. https://doi.org/10.2478/umcschem-2013-0003.

[169] M. Prestat, J. Soares Costa, B. Lescop, S. Rioual, L. Holzer, D. Thierry, Cathodic Corrosion of Zinc under Potentiostatic Conditions in NaCl Solutions, ChemElectroChem. 5 (2018) 1203–

1211. https://doi.org/10.1002/celc.201701325.

[170] H. Leidheiser, Y. Momose, R.D. Granata, Technical Note: Inhibition of the Cathodic Reaction on Zinc in Aerated 3% NaCl Solution, CORROSION. 38 (1982) 178–179. https://doi.org/10.5006/1.3579271.

[171] K. Bae, J. La, I. Lee, S. Lee, K. Nam, Effects of annealing heat treatment on the corrosion resistance of Zn/Mg/Zn multilayer coatings, Met. Mater. Int. 23 (2017) 481–487. https://doi.org/10.1007/s12540-017-6478-2.

[172] L. Hao, G. Lv, Y. Zhou, K. Zhu, M. Dong, Y. Liu, D. Yu, High performance anti-corrosion coatings of poly (Vinyl Butyral) composites with poly N-(vinyl)pyrrole and carbon black nanoparticles, Materials (Basel). 11 (2018). https://doi.org/10.3390/ma11112307.

[173] K. Aramaki, Effects of organic inhibitors on corrosion of zinc in an aerated 0.5 M NaCl solution, Corros. Sci. 43 (2001) 1985–2000. https://doi.org/10.1016/S0010-938X(00)00174-8.

[174] S. Thomas, N. Birbilis, M.S. Venkatraman, I.S. Cole, Corrosion of Zinc as a Function of pH, CORROSION. 68 (2012) 015009-1-015009–9. https://doi.org/10.5006/1.3676630.

[175] D. Schröder, N.N. Sinai Borker, M. König, U. Krewer, Performance of zinc air batteries with added K2CO3 in the alkaline electrolyte, J. Appl. Electrochem. 45 (2015) 427–437. https://doi.org/10.1007/s10800-015-0817-0.

[176] BioLogic, EC-Lab Documentation, (2014) 149–152.

[177] J.L. Murray, A.J. McAlister, The Al-Si (Aluminum-Silicon) system, Bull. Alloy Phase Diagrams 1984 51. 5 (1984) 74–84. https://doi.org/10.1007/BF02868729.

[178] ECHA, Glycine pKa, (n.d.). https://echa.europa.eu/de/registration-dossier/-/registered-dossier/14889/4/22 (accessed March 23, 2022).

[179] PubChem, Iminodiacetic acid, (n.d.). https://pubchem.ncbi.nlm.nih.gov/compound/Iminodiacetic-acid (accessed March 23, 2022).

[180] ECHA, Nitrilotriacetic Acid, (n.d.). https://echa.europa.eu/de/registration-dossier/-/registered-dossier/12171/4/22 (accessed March 23, 2022).

[181] ECHA, N-carboxymethyliminobis(ethylenenitrilo)tetra(acetic acid) (DTPA), (n.d.). https://echa.europa.eu/de/registration-dossier/-/registered-dossier/13561/4/22 (accessed March 23, 2022).

[182] ECHA, Tartaric acid, (n.d.). https://echa.europa.eu/de/registration-dossier/-/registered-dossier/15126/4/22 (accessed March 23, 2022).

[183] L. Dong, F. Jiao, W. Qin, Q. Wei, Utilization of iron ions to improve the depressive efficiency of tartaric acid on the flotation separation of scheelite from calcite, Miner. Eng. 168 (2021) 106925. https://doi.org/10.1016/j.mineng.2021.106925.

[184] M.M. Luckey, IMINODIACETIC ACID COMPLEXATION WITH LANTHANIDES UNDER ACIDIC CONDITIONS, Colorado School of Mines, 2017. https://mountainscholar.org/bitstream/handle/11124/171179/Luckey_mines_0052N_11304.pdf?sequence=1&isAllowed=y.

[185] Dojindo EU, Metal Chelates, (n.d.).

[186] A.E. Martell, R.M.S. Editors, Critical Stability Constants Volume 5, 1983. https://doi.org/10.1016/0307-4412(83)90054-7.

[187] R.M. Smith, A.E. Martell, Critical stability constants, enthalpies and entropies for the formation of metal complexes of aminopolycarboxylic acids and carboxylic acids, Sci. Total Environ. 64 (1987) 125–147. https://doi.org/10.1016/0048-9697(87)90127-6.

[188] B. Yang, P. Zhang, G. Wang, A. Wang, X. Chen, S. Wei, J. Xie, Effect of graphene oxide concentration in electrolyte on corrosion behavior of electrodeposited Zn-electrochemical reduction graphene composite coatings, Coatings. 9 (2019). https://doi.org/10.3390/coatings9110758.

[189] H. Yan, Q. Zhao, N. Du, Y. Hu, L. Wang, S. Wang, Formation process and corrosion resistance of trivalent chromium passivation film on Zn-plated Q235 steel, J. Chinese Soc. Corros. Prot. 37 (2017) 547–553. https://doi.org/10.11902/1005.4537.2016.138.

[190] K.T. Bae, J.H. la, I.G. Lee, S.Y. Lee, K.H. Nam, Effects of annealing heat treatment on the corrosion resistance of Zn/Mg/Zn multilayer coatings, Met. Mater. Int. 23 (2017) 1–7. https://doi.org/10.1007/s12540-017-6478-2.

[191] H. Nady, Tricine [N-(Tri(hydroxymethyl)methyl)glycine] – A novel green inhibitor for the corrosion inhibition of zinc in neutral aerated sodium chloride solution, Egypt. J. Pet. 26 (2017) 905–913. https://doi.org/10.1016/j.ejpe.2016.02.004.

[192] Z.A. Hamid, S.S.A. El Rehim, A.A. Shama, M. Ebrahim, Improvement the Corrosion Resistance for the Galvanized Steel by Adding Sn, J. Surf. Eng. Mater. Adv. Technol. 06 (2016) 58–71. https://doi.org/10.4236/jsemat.2016.62006.

[193] R. Li, J. Liang, Y. Hou, Q. Chu, Enhanced corrosion performance of Zn coating by

incorporating graphene oxide electrodeposited from deep eutectic solvent, RSC Adv. 5 (2015) 60698–60707. https://doi.org/10.1039/c5ra11577a.

[194] H.I. Ünal, S. Zor, H.M. Gökergil, Corrosion behavior of Zn and Ni coated carbon steels in 3% NaCl, Prot. Met. Phys. Chem. Surfaces. 49 (2013) 591–596. https://doi.org/10.1134/S2070205113050158.

[195] C. A. M. Dutra, E. N. Codaro, R. Z. Nakazato, Electrochemical Behavior and Corrosion Study of Electrodeposits of Zn and Zn-Fe-Co on Steel, Mater. Sci. Appl. 03 (2012) 348–354. https://doi.org/10.4236/msa.2012.36050.

[196] M.E.P. Souza, E. Ariza, M. Ballester, L.A. Rocha, C.M.A. Freire, Comparative behaviour in terms of wear and corrosion resistance of galvanized and zinc-iron coated steels, Matéria (Rio Janeiro). 12 (2007) 618–623. https://doi.org/10.1590/s1517-70762007000400011.

[197] Y.P. Zhao, R.H. Yin, W.M. Cao, A.B. Yuan, ELECTROPOLYMERIZATION OF ANILINE ON ZINCELECTROPLATED STEEL FROM NEUTRAL AQUEOUS MEDIUM BY SINGLE-STEP PROCESS, Acta Metall. Sin. (English Lett. 17 (2004) 849–855.

[198] F. Andreatta, J. Rodriguez, M. Mouanga, A. Lanzutti, L. Fedrizzi, M.G. Olivier, Corrosion protection by zinc-magnesium coatings on steel studied by electrochemical methods, Mater. Corros. 70 (2019) 793–801. https://doi.org/10.1002/maco.201810554.

[199] C. Hu, Y. Li, N. Zhang, J. Zhang, Preparation of Poly(o-ethylaniline)-SiC/Zinc Bilayer Coatings and Study of Its Corrosion Resistance Properties, J. Electrochem. Soc. 165 (2018) G56–G65. https://doi.org/10.1149/2.0871803jes.

[200] S. Anwar, Y. Zhang, F. Khan, Electrochemical behaviour and analysis of Zn and Zn-Ni alloy anti-corrosive coatings deposited from citrate baths, RSC Adv. 8 (2018) 28861–28873. https://doi.org/10.1039/c8ra04650f.

[201] N.K. Onkarappa, P.S. Adarakatti, P. Malingappa, A Study on the Effect of Additive Combination on Improving Anticorrosion Property of Zinc Electrodeposit from Acid Chloride Bath, Ind. Eng. Chem. Res. 56 (2017) 5284–5295. https://doi.org/10.1021/acs.iecr.7b00154.

[202] X. Shang, B. Zhang, W. Ke, Effect of Sb-Rich Intermetallic Phase on the Corrosion Resistance of Zn Alloy in Near-Neutral and Acidic Solutions, Jinshu Xuebao/Acta Metall. Sin. 53 (2017) 351–357. https://doi.org/10.11900/0412.1961.2016.00419.

[203] M.K. Punith Kumar, M.P. Singh, C. Srivastava, Electrochemical behavior of Zn-graphene composite coatings, RSC Adv. 5 (2015) 25603–25608. https://doi.org/10.1039/c5ra02898a.

[204] H.S. Lee, M.A. Ismail, H.B. Choe, Arc thermal metal spray for the protection of steel structures: An overview, Corros. Rev. 33 (2015) 31–61. https://doi.org/10.1515/corrrev-2014-0055.

[205] Y. Wang, J. Zeng, Effects of manganese addition on microstructures and corrosion behavior of hot-dip zinc coatings of hot-rolled steels, Surf. Coatings Technol. 245 (2014) 55–65. https://doi.org/10.1016/j.surfcoat.2014.02.040.

[206] X. Zhang, J. Liang, B. Liu, Z. Peng, Preparation of superhydrophobic zinc coating for corrosion protection, Colloids Surfaces A Physicochem. Eng. Asp. 454 (2014) 113–118. https://doi.org/10.1016/j.colsurfa.2014.04.029.

[207] V.D. Bachvarov, M.T. Peshova, S.D. Vitkova, N.S. Boshkov, Corrosion properties of Zn-Ni-P alloys in neutral model medium, Cent. Eur. J. Chem. 12 (2014) 1183–1193. https://doi.org/10.2478/s11532-014-0564-9.

[208] A.A. Daniyan, L.E. Umoru, A.P.I. Popoola, O.S.I. Fayomi, Comparative studies of microstructural, tribological and corrosion properties of Zn-TiO2 and Zn-TiO2-WO3 nano-composite coatings, Results Phys. 7 (2017) 3222–3229. https://doi.org/10.1016/j.rinp.2017.08.048.

[209] B.A. Abd-El-Naby, O.A. Abdullatef, A.M. Abd-El-Gabr, M.A. Shaker, G. Esmail, Effect of some natural extracts on the corrosion of zinc in 0.5 M NaCl, Int. J. Electrochem. Sci. 7 (2012) 5864–5879.

[210] H.B. Sherine, C.C. Rajakumari, S. Rajendran, Corrosion behaviour of stainless steel 304 electroplated with zinc followed by blue passivation, Port. Electrochim. Acta. 29 (2011) 295–305. https://doi.org/10.4152/pea.201104295.

[211] A.M. Simões, J. Torres, R. Picciochi, J.C.S. Fernandes, Corrosion inhibition at galvanized steel cut edges by phosphate pigments, Electrochim. Acta. 54 (2009) 3857–3865. https://doi.org/10.1016/j.electacta.2009.01.065.

[212] A.G. Muñoz, S.B. Saidman, J.B. Bessone, Corrosion of an Al-Zn-In alloy in chloride media, Corros. Sci. 44 (2002) 2171–2182. https://doi.org/10.1016/S0010-938X(02)00042-2.

[213] K. Aramaki, Treatment of zinc surface with cerium(III) nitrate to prevent zinc corrosion in aerated 0.5 M NaCl, Corros. Sci. 43 (2001) 2201–2215. https://doi.org/10.1016/S0010-938X(00)00189-X.

[214] American Elements, Zinc Chloride Hydroxide Monohydrate, (n.d.). https://www.americanelements.com/zinc-chloride-hydroxide-monohydrate-12167-79-2 (accessed March 30, 2020).

[215] European Chemical Agency, Zinc Oxide, (n.d.). https://echa.europa.eu/de/registration-dossier/-/registered-dossier/16139/4/9/?documentUUID=a167451b-af09-4950-9f3e-f5a9c631a445 (accessed March 30, 2020).

[216] European Chemical Agency, Zinc hydroxide, (n.d.). https://echa.europa.eu/de/registration-dossier/-/registered-dossier/10329/4/9/?documentUUID=9cd99045-fbf4-476a-8f2d-7741792a1f51 (accessed March 30, 2020).

Supervised Works of Students and Curriculum Vitae

The works of the students listed below were supervised during the research work for this PhD thesis:

- S. Bulut, *"Coating Development for Corrosion Inhibition and Optimization of Silicon–Air Batteries"*, Research Internships, Faculty of Mathematics, Computer Science and Natural Sciences of the RWTH Aachen University, 2020.
- V. Lewandowski, *"Electrochemical Characterization of Silicon–Aluminum Alloys for Silicon–Air Batteries"*, Research Internships, Faculty of Mathematics, Computer Science and Natural Sciences of the RWTH Aachen University, 2021.
- M. Heidler, *"Investigation of Electrolyte Additives on the Electrochemical Behavior of Zinc Electrodes in Near–Neutral Electrolyte"*, Master Thesis, Faculty of Chemical Engineering of the FH Münster, 2022.

Curriculum Vitae of Saúl Said Montiel Guerrero

Saúl Said Montiel Guerrero, born in Tepeji del Río de Ocampo, Hidalgo, Mexico concluded his high school in the Tepeji's Cultural Institute (Instituto Tepejano de Cultura). He completed his 1st bachelor's degree on Chemical Engineering at the Technological Mexican University (UNITEC, campus Atizapán de Zaragoza, Mexico State) on December 2012 and his second bachelor's degree on Environmental and Sustainability Engineering at the same university on December 2013. He worked as a professor's assistant from January to August 2014 at UNITEC. He moved to Germany on October 2014 for German courses and started his Master's degree on March 2015 at the Technological University of Aachen (Fachhochschule Aachen, campus Jülich). On August 2015 he started as a research assistant at the Institute for Energy and Climate Change–Basics of Electrochemistry (IEK–9) in the Forschungszentrum Jülich GmbH and completed his Master Thesis "Corrosion Studies and Inhibition in Silicon–air Batteries" on February 2018 under the supervision of Prof. Dr. rer. nat. Rüdiger–A. Eichel, Prof. Dr. W. J. Quadakkers, and Dr. Yasin Emre Durmus. He continued as a scientific assistant from March to December 2018 at the IEK–9 and started his PhD project "Performance Enhancement and Corrosion Studies of Metal–Air Batteries" on January 2019 under the supervision of Prof. Dr. rer. nat. Rüdiger–A. Eichel, Prof. Dr.–Ing. Stefan van Waasen, and Dr. Yasin Emre Durmus, focusing on Si–air and Zn–air batteries. From January 2022 till January 2023 he expanded his research on Zn–air and Fe–air batteries at the IEK–9 of the Forschungszentrum Jülich.

Appendix

1. Standard Electrode Potential

Table A–1: Standard electrode potentials at 25°C. Reproduced after McCafferty [20].

Reaction	E^0 / V_{SHE}
$O_2 + 4H^+ + 4e^- \longrightarrow 2H_2O$	+1.229
$Pt^{2+} + 2e^- \longrightarrow Pt$	+1.180
$Cu^+ + e^- \longrightarrow Cu$	+0.521
$O_2 + 2H_2O + 4e^- \longrightarrow 4OH^-$	+0.401
$Cu^{2+} + 2e^- \longrightarrow Cu$	+0.342
$AgCl + e^- \longrightarrow Ag^+ + Cl^-$	+0.222
$Hg_2O + H_2O + 2e^- \longrightarrow 2Hg + 2OH^-$	+0.123
$2H^+ + 2e^- \longrightarrow H_2$	0.000
$Ni^{2+} + 2e^- \longrightarrow Ni$	−0.257
$Fe^{2+} + 2e^- \longrightarrow Fe$	−0.447
$Zn^{2+} + 2e^- \longrightarrow Zn$	−0.762
$SiO + 2H^+ + 2e^- \longrightarrow Si + H_2O$	−0.800
$Al_2O_3 + 6H^+ + 6e^- \longrightarrow 2Al + 3H_2O$	−1.550
$Al^{3+} + 3e^- \longrightarrow Al$	−1.662
$SiO_3^{2-} + 3H_2O + 4e^- \longrightarrow Si + 6OH^-$	−1.697
$Li^+ + e^- \longrightarrow Li$	−3.040

2. Polarization Principles and Analysis of Potentiodynamic Polarization Curves

In order to understand the basics of the electrode reaction kinetics, a detailed explanation of the physicochemical changes of the electrode is attained by decomposing the PoP shown in Figure 2.1c. The electrodes with a different potential than its OCP are then in a "polarized" state. The working electrode (WE) in a half–cell can become negatively charged upon supply of electrons from an external source, resulting in a cathodic polarization of the WE. The excess of electrons promotes the cathodic reactions of the WE, which can result in water reduction and hydrogen evolution for aqueous electrolytes. Also, reducible species present in the electrolyte can be redeposited (plating in half–cell terminology), as in the case of $ZnCl_2$ dissolved in near–neutral electrolytes for example. Since the counter electrode (CE) usually consist of a non–reactive metal, water oxidation, oxygen evolution and/or other oxidation reactions may occur at the counter electrode. Inversely, when electrons are removed from the working electrode by an external load, the oxidation of the WE is promoted (stripping in half–cell terminology) and the electrode is under anodic polarization. Additionally, the electrons provided at the counter electrode can promote reduction reactions, such as water reduction, hydrogen evolution and plating of reducible soluble species present in the electrolyte. The latter can be also originated from the oxidized species of the working electrode.

In the practical situation when the potential is initially shifted from the OCP to more cathodic potentials, a current response with negative value coming from the cathodic electrochemical reactions at the working electrode surface is measured by the potentiostat, as seen in Figure 2.1c. Following the scan direction toward more negative potentials, the current eventually becomes zero and may have a similar value to the OCP. Since the PoP technique constantly changes the potential, the zero net current condition may arise from a different equilibrium than the observed under OCP conditions and the term corrosion potential (E_0) is employed. After the E_0 is reached and the potential continues in the more anodic direction, the current response with positive values coming from the anodic reactions at the working electrodes may start increasing again. Additionally, the total current measured by the potentiostat (represented as i) requires a correction to current density (j) and it is done by dividing the total current by the working electrode area (typically with units of mA cm^{-2}).

During the change in the electrode potential, mainly three different types of polarization can be differentiated [20]:

1. Activation polarization, characterized as a slow electrode reaction, meaning that electrons flow in or out of the electrode faster than they can react. Under cathodic polarization, the electrons accumulate at the surface of the electrode turning it more negative. If the electrons leave the metal matrix faster than the reacting atoms leave the matrix, the electrode surface becomes more positive and anodic polarized.
2. Concentration polarization, which occurs when the reactants or products change its concentration near to the electrode surface and the presence of such ions contributes to the overall polarization.
3. Ohmic polarization, caused by current/resistance (IR) drops in solution or across surface films, such as oxides or salts at the WE surface. The reason for an IR drop can be attributed to low conductivity of the electrolyte or misplacement of the reference electrode, which in such case should be placed as close as possible for electrolytes with low conductivity. Moreover, the ohmic polarization caused by the presence of a film in a system may be of interest in the characterization of electrode/film/electrolyte interfaces.

As proposed by the mixed electrode potential of Wagner and Traud [133] and the Tafel analysis [20], the cathodic and anodic reactions simultaneously contribute to the overall current measured during the PoP. The discrete contributions of each reaction are easier to distinguish during the activation polarization, where the influence of other effects (such as the concentration or ohmic polarization) is reduced. The so called Tafel extrapolation (or Tafel analysis) can be applied in the potential region where the activation polarization takes place, which also shows some linearity at around ±50 mV of the OCP. To facilitate the Tafel analysis, the polarization curve is rearranged as the logarithm of absolute current density versus the working electrode potential (log |j| vs. E), as seen in Figure 2.1d. In this new arrangement, the currents located at cathodic potentials of the E_0 correspond to the branch of the cathodic reactions and vice versa. Moreover, Figure 2.1d shows the Tafel extrapolation (linear region for each reaction), and the respective contributions to the global polarization curve become more evident. Technically speaking, the anodic reactions also take place along the cathodic side of the polarization (cathodic branch), but its contribution is meaningless in comparison as the current densities logarithmically decrease. The same analogy applies for the anodic branch, where the cathodic reactions still occur but in a trivial degree. The intersection of the cathodic and anodic branches extrapolation assists in the estimation of the corrosion current density (j_0) for corroding metals.

The mathematical description of the Figure 2.1d is given by the Tafel equation for non–corroding metals (derived after the Butler–Volmer equation) [20], and is as follows:

$$\log j = \log j_0 + (E - E_0)\frac{\alpha nF}{2.303\ RT} \qquad \textbf{A–1}$$

where j is the current density, j_0 is the corrosion current density, E is the applied potential, E_0 is the corrosion potential, α is the degree of symmetry of the free energy barrier resulting from E, n is the number of electrons involved in the reaction, F is the Faraday's constant (96,485.4 C), R is the gas constant and T is the temperature. The terms j_0 and E_0 for non–corroding metals in Equation A–1 can be substituted by j_{corr} and E_{corr} for corroding metals. The Equation A–1can be rewritten for the anodic reactions as

$$\eta_a = b_a \log\frac{j}{j_0} \qquad \textbf{A–2}$$

where η_a is the anodic overpotential $E - E_0$, and b_a is defined as

$$b_a = \frac{dE}{d\log j} = \frac{2.303\ RT}{\alpha nF} \qquad \textbf{A–3}$$

whereas the extrapolation for the cathodic reactions can be expressed as

$$\eta_c = b_c \log\frac{j}{j_0} \qquad \textbf{A–4}$$

where η_c is the cathodic overpotential $E - E_0$, and b_c is described as

$$b_c = \frac{dE}{d\log |j|} = -\frac{2.303\ RT}{(1-\alpha)nF} \qquad \textbf{A–5}$$

Software such as EC–Lab from Biologic™ already possess tools assisting the user to manually and visually fit the Tafel plot, making the extraction of the electrochemical data user–friendly and faster [176].

3. Pourbaix Diagrams

As described in the working principle of a metal–air battery (Figure 1.1), metal ions constantly dissolve into the electrolyte under discharge (or spontaneous corrosion) conditions and modify the equilibrium state of the system. In addition, the reaction products of the half–cell reactions may change the local or bulk pH value.

Assuming only the influence of the increase in the concentration of the metal ions, Figure A–1 shows the Pourbaix diagrams of Si, Zn and Al with a concentration of 10^{-2}M, reproduced after [135,136]. The first noticeable remark in Figure A–1a is the transition of the region with $H_4SiO_{4(aq)}^{\square}$ to $SiO_{2(s)}^{\square}$, which is a passive compound. Figure A–1b depicts a smaller area in the acidic pH for the $Zn_{(aq)}^{2+}$, whereas the passive $ZnO_{(s)}^{\square}$ substitutes the soluble $Zn(OH)_{2(aq)}^{\square}$, $Zn(OH)_{3(aq)}^{-}$ and $Zn(OH)_{4(aq)}^{2-}$. In the case of Al (Figure A–1c), the domain of $Al_{(aq)}^{3+}$ and $Al(OH)_{4(aq)}^{-}$ is shrunk and the passive $Al_2O_{3(s)}$ region grows.

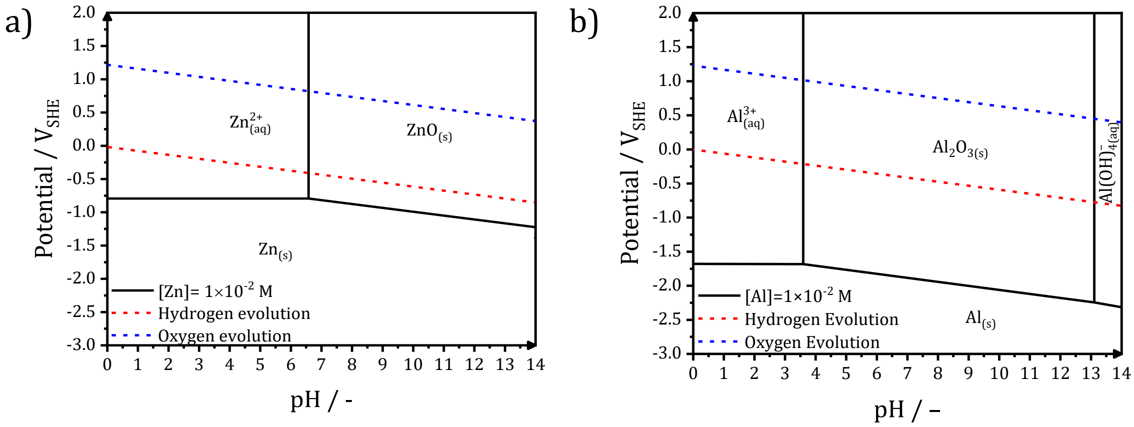

Figure A–1: Pourbaix diagram of a) zinc and b) aluminum with a concentration of 10^{-2}M. Reproduced after [134–136].

The change in the concentration of the metal also has an impact on the standard electrode potential as defined by the Nernst equation, and by the comparison of the transition lines of the immunity/corrosion/passivation in Figure 4.2 and Figure A–1.

4. Electrochemical Evaluation of Si–Al alloys as anode materials for Si–air batteries in 5M KOH

Figure A–2 shows the binary phase diagram of silicon and aluminum. The Si–Al alloy present a single eutectic point at around 12.6%Al/87.4%Si and 577°C. RM–Si, Si–1%Al, and Si–5%Al samples were produced by arc melting.

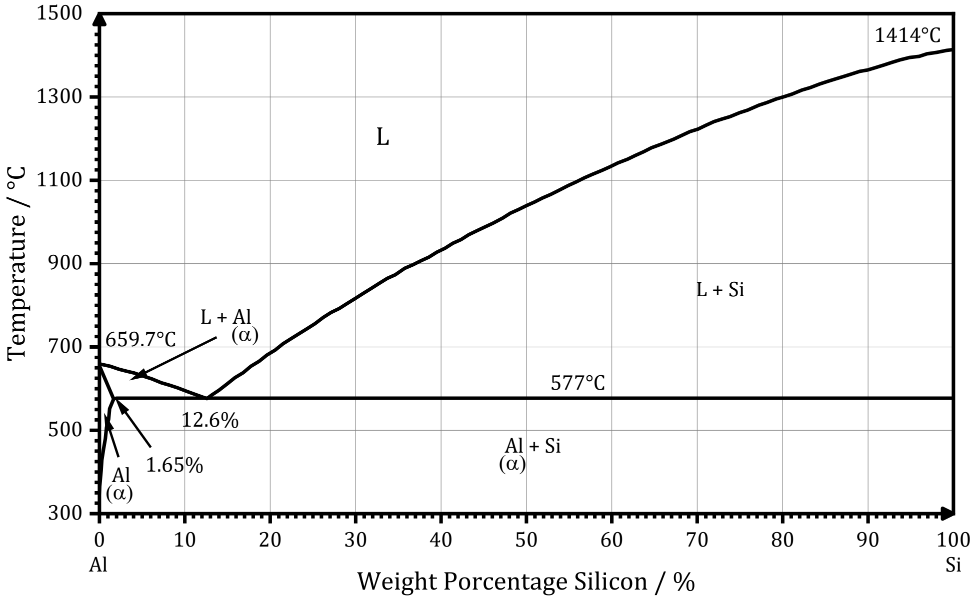

Figure A–2: Phase diagram of Si–Al alloys. Reconstructed from Murray et. al. [177].

Table A–2 presents the results of weight loss experiments and the equivalent corrosion rate for Si–Al alloys. The values for Si <100> As–doped are added for comparison. The RM–Si presents a 36% higher weight loss and corrosion rates, whereas the Si–1%Al and Si–5%Al shows a 71% and 143% higher weight loss and corrosion rates, respectively. The samples, however, presented some cracks and pores prior to the experiment due to the arc melting method employed. Such imperfections could partially explain the higher corrosion observed for the RM–Si and also for the Si–Al alloys.

Table A–2: Weight loss results and equivalent corrosion rate for Si <100> As–doped wafer, RM–Si, Si–1%Al, and Si–5%Al after 24 h of immersion in 5M KOH.

Alloy	Weight Loss Rate /mg day^{-1}cm^{-2}	Corrosion Rate /µm h^{-1}
Si <100> As–doped	8.22±0.45	1.47±0.81
RM–Si	11.20±1.12	4.59±0.46
Si–1%Al	14.07±2.93	5.77±1.20
Si–5%Al	20.05±1.70	8.22±0.69

The electrochemical evaluation of Si–Al alloys in 5M KOH are presented in Figure A–3. The half–cell cyclic voltammetry (CV) of the Si–Al alloys in KOH reveal possible higher anodic current densities with increasing content of Al of up to 5 mA cm^{-2} without apparent passivation, as observed for Si–5wt.%Al (blue curve) of Figure A–3a. In comparison, the remelted Si (RM–Si) displays the typical CV profile as the Si As(100) wafers(black curve of the inset of Figure A–3a), while the Si–1wt.%Al can slightly increase the maximum current densities from 0.09 to 0.47 mA cm^{-2} [41,48]. The discharge behavior of the Si–Al alloys was also characterized by full–cell discharge, showing stable voltages at around 1.0 to 1.2 V for the three alloys up to 100 µA cm^{-2} (Figure A–3b-d). However, only the Si–5wt.%Al alloy could be discharged under 250 µA cm^{-2} delivering up to 1.18 V, as shown in Figure A–3d.

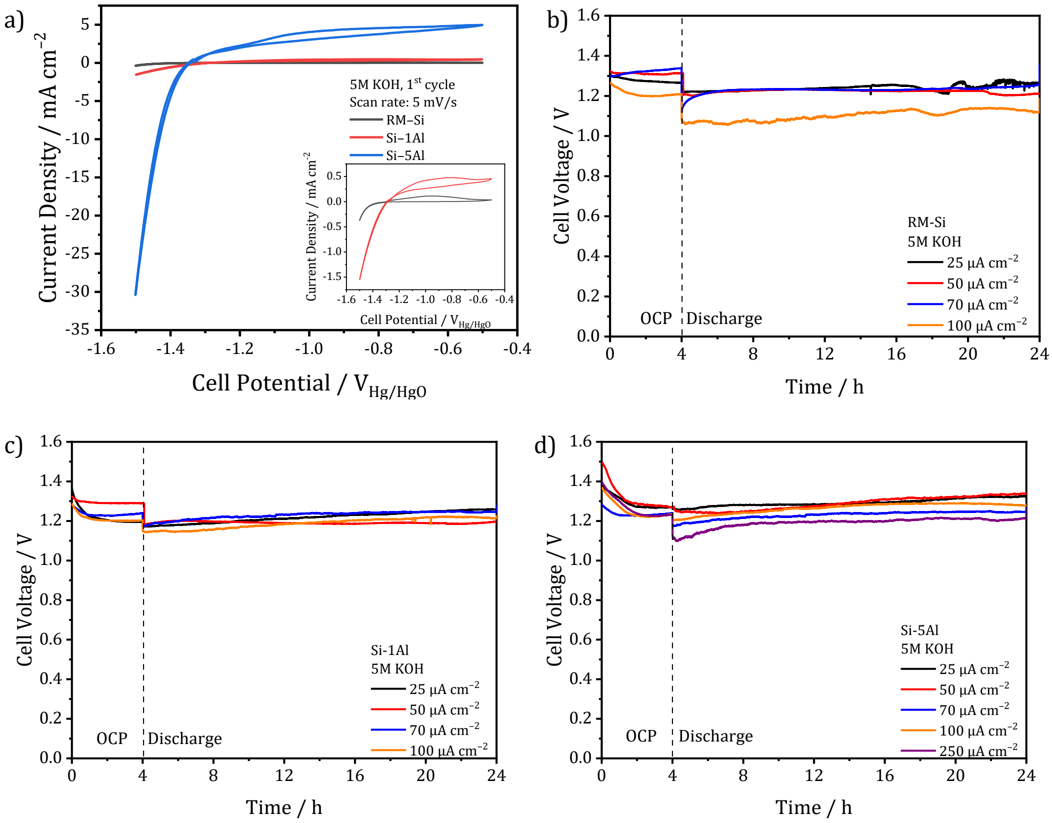

Figure A–3: Electrochemical evaluation of Si–Al alloys by a) cyclic voltammetry of RM–Si (black curve), Si–1wt.%Al (red curve), and Si–5wt.%Al in 5M KOH, and discharge profiles of b) RM–Si, c) Si–1wt.%Al, and d) Si–5wt.%Al in 5M KOH under several current densities.

The previous set of experiments partially reveal the effect of the mixed potential theory as only higher anodic current densities were observed but the potential/voltage showed no significant increase, which can be attributed to the relatively low content of Al. Further evaluation of the corrosion mass and anode mass conversion (based on the Si only) is presented in Figure A–4. Figure A–4a reveals corrosion masses of the RM–Si in the range of 7.5 to 12.5 mg, similar to the values observed for Si–1%Al in Figure A–4b. The Si–5%Al samples displayed the highest corrosion masses in the range of 17.5 to 27.5 mg (Figure A–4c). In general, all the anode mass conversion was under 3% for RM–Si, below 1.5% for the Si–1%Al, and under 2.25% for the Si–5%Al (Figure A–4a-c). The relatively high corrosion masses and low anode mass conversion can be partially attributed to the low quality of the samples due to the preparation method by arc melting, similar as the weight loss and corrosion rates presented in Table A–2. An imperfection–free sample could possibly increase the anode mass conversion and reduce the corrosion currently observed for Si–Al alloys.

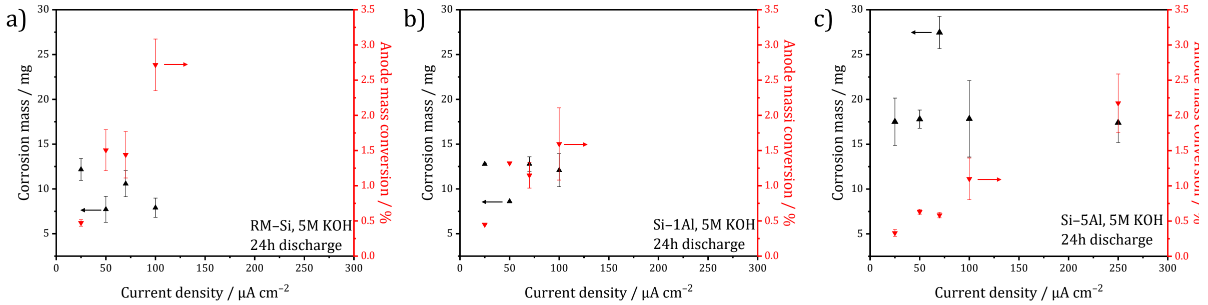

Figure A–4: Corrosion mass and anode mass conversion of a) RM–Si, b) Si–1wt.%Al, and c) Si–5wt.%Al after discharge under several current densities in 5M KOH.

5. Cover Feature: Improved Electrochemical Performance of Zinc Anodes by EDTA in Near-Neutral Zinc–Air Batteries (Batteries & Supercaps 12/2021)

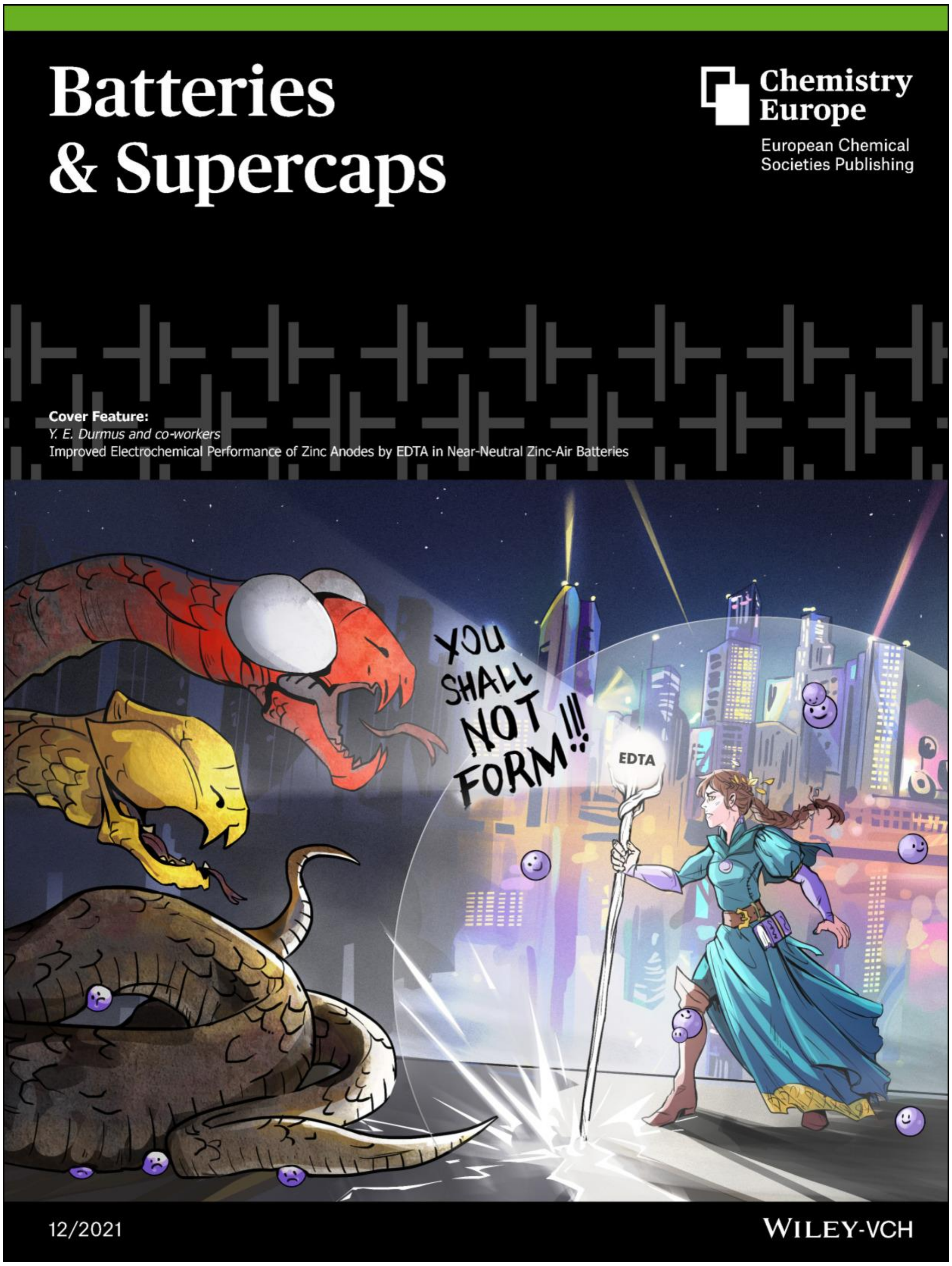

Figure A–5: The Cover Feature illustrates how the EDTA "spell" prevents the hydra from corrupting the "place of power", which otherwise would not be able to efficiently power the city. Hydra′s heads are representing H2O and Cl−, which result in formation of quasi-passive films by blocking the purple Zn2+ ions at the surface. The presence of EDTA, on the other hand, prevents the formation of such passivating films due to its remarkable Zn2+-chelation ability and directly leads to improved electrochemical performance of the Zn electrodes in resource-efficient Zn-air batteries [159].

6. Visualization of solvation, complexation, and precipitation

In essentially any oxidation process of a metal in aqueous media, the formation of complex molecules is consequence as the oxidized metal losses its outermost shell electrons and becomes positively charged. The positive sites of the metal cation are then exposed and prone to further interactions with the aqueous electrolyte, which can result in its solvation, complexing, or precipitation. The term solvation refers to the interaction of a solvent with a dissolved specie and applies to any solvent, while hydration is specifically applied for water–solute interactions. Taking the water molecule as an example, the oxygen atom has a larger electronegativity than the hydrogen atoms, meaning that the O atom "pulls" the electrons of the H atoms. Derived from this phenomenon there is a resulting partial negative charge localized around the oxygen atom commonly represented as δ^{-}, while the hydrogen atoms become partially positive charged (denoted as δ^{+}) [115]. Additionally, the negative partial charges of the water are attracted to positively charged species and vice versa, which results in the solvation of the solute due to the interaction of the charges. The solvation effect becomes stronger for molecules with larger differences on the partial charges, while a more homogeneous distribution of the partial charges within a molecule result on poorer solvents.

Figure A–6 shows a simplified visualization of the oxidation and solvation or reaction of the resulting metal cation under different pH conditions. Figure A–6a shows the metal in the basal state with the outermost shell of electrons filled, which after oxidation and release of the electrons becomes positively charged (Figure A–6b). The metal cation can then undergo different reactions depending on the pH conditions of the aqueous electrolyte. The high abundance of H^{+} ions (red spheres in Figure A–6c) at low pH conditions has a deficit of electrons and keeps the metal cations solvated, whereas the excess OH^{-} ions (blue/red spheres in Figure A–6e) also solvate the positive metal ion and negatively charge the metal in alkaline environments. Nevertheless, if the conditions of the electrolyte are close to neutrality, the charge contribution of H^{+} or OH^{-} ions is counterbalanced and the formation of solid species without charge is likely to occur, as depicted by the formation of a metal oxide in Figure A–6d.

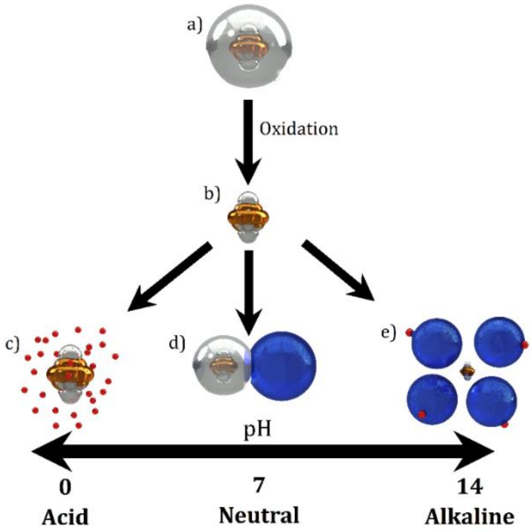

Figure A–6: Visualization of the solvation of an oxidized metal under different pH conditions, where a) is the basal state of the metal, b) the oxidized metal without the electrons of the outermost orbital shell, c) the metal cation solvated by H^+ ions (red spheres) in acidic media, d) the metal ion sharing the electrons of the oxygen (blue sphere) resulting in a solid specie in neutral media and e) the metal ion solvated by OH^- ions (blue/red spheres) in alkaline conditions. See text for an extended explanation.

The previous description can be applied to several Pourbaix diagrams of anodic–type metals under the condition of low concentration of the metal cation in a water–based media [121]. However, other conditions may affect the formation of insoluble/uncharged species, such as the concentration of the metal cation, effects of the metal cation over the pH, electrolyte composition, temperature, additives in the solution, etc. The production of the solid, complex, or solvated species is described by the *formation constants* or *equilibrium constants* K_n, according to the following equations:

$$\mathrm{M} + \mathrm{X} \xleftrightarrow{\mathrm{K_1}} \mathrm{MX} \qquad \mathrm{K_1} = \frac{[\mathrm{MX}]}{[\mathrm{M}][\mathrm{X}]} \tag{A–6}$$

$$\mathrm{MX} + \mathrm{X} \xleftrightarrow{\mathrm{K_2}} \mathrm{MX_2} \qquad \mathrm{K_2} = \frac{[\mathrm{MX_2}]}{[\mathrm{MX}][\mathrm{X}]} \tag{A–7}$$

$$\mathrm{MX_{n-1}} + \mathrm{X} \xleftrightarrow{\mathrm{K_n}} \mathrm{MX_n} \qquad \mathrm{K_n} = \frac{[\mathrm{MX_n}]}{[\mathrm{MX_{n-1}}][\mathrm{X}]} \tag{A–8}$$

where M is the metal ion, X is the complexing agent, MX_n is the resulting complex molecule and K_n is the stepwise formation constants derived from the relation of the products over the reactants. The magnitude of K_n indicates the stability of the product of the reaction also indicating the formation likeliness of such molecule. A way to interfere with the formation of “unwished” products is by introducing chelating agents, which can keep the metal ions solvated.

7. Chelating Agents and pH Buffering additives: Structure and Properties

Different organic and inorganic molecules can be employed to stabilize the pH and/or complex with metal ions. Figure A–7 presents the structure of aminopolycarboxylic acids, which present amino and carboxylic ligands.

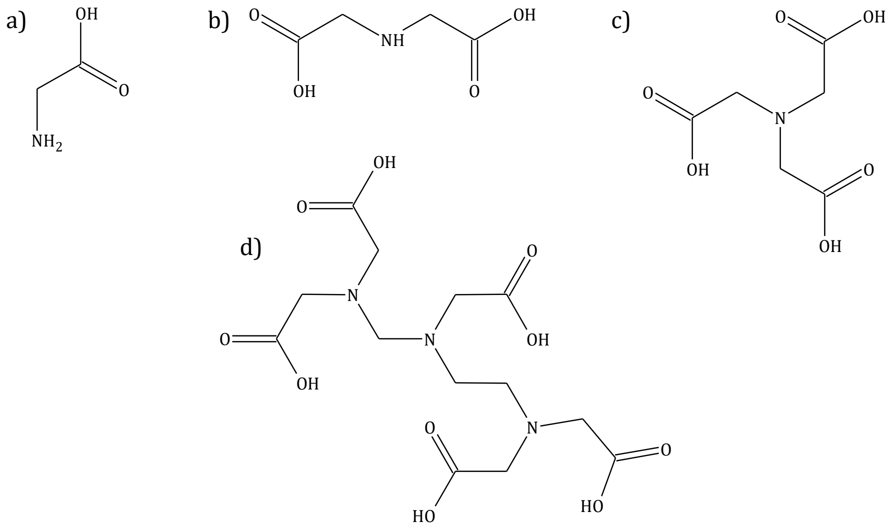

Figure A–7: Group of aminopolycarboxylic acid: a) glycine (Gly), b) iminodiacetic acid (IDA), c) nitrilotriacetic, acid (NTA), d) diethylenetriaminepentaacetic acid (DTPA).

Figure A–8 present the structure of the polycarboxylic acids, which only present COOH groups.

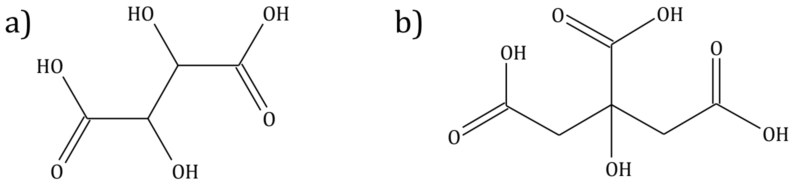

Figure A–8: Group of polycarboxylic acids: a) citric acid (CA), and b) tartaric acid (TA).

Figure A–9 displays the structure of some buffering additives.

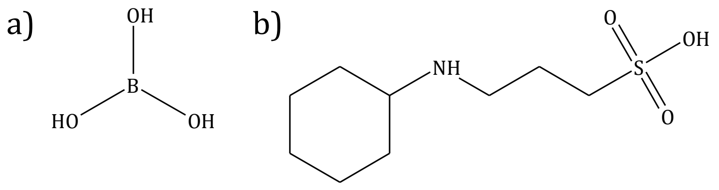

Figure A–9: Buffering additives: a) boric acid (BA), and b) N–cyclohexyl–3–amino–propanesulfonic acid (CAPS).

Table A–3 summarizes the pK$_a$–values and buffer range of some complexing agents and pH buffering additives. The buffer range was estimated base on pK$_a$±1 [115].

Table A–3: pK_a–values and buffer range of some selected complexing agents and pH buffering additives

	pK_a–values						Buffer range	Ref.
Gly	2.4	9.80					8.8–10.8	[178]
IDA	2.6	9.90					8.9–10.9	[179]
NTA	1.8	2.50	9.60				8.6–10.6	[180]
EDTA	0.0	1.50	2.00	2.69	6.13	10.37	9.37-11.37	[115]
DTPA	1.8	2.60	4.40	8.8	10.40		7.8–11.4	[181]
TA	2.9	4.30					1.9–5.3	[182]
CA	3.1	4.80	6.40				2.1–7.4	[115]
BA	9.2	12.74					8.2–10.2	[115]
CAPS	10.50						9.5–11.5	[115]

The fractional composition diagrams of the complexing agents and pH buffering additives listed in Table A–3 are presented in Figure A–10, Figure A–11, and Figure A–12. The species with the most positive charge represent the fully protonated complexing agent (with all its H atoms), the intermediate species lose stepwise one H^+ ion as the pH increases becoming more negative, and the more negative specie represents the fully dissociated/deprotonated molecule.

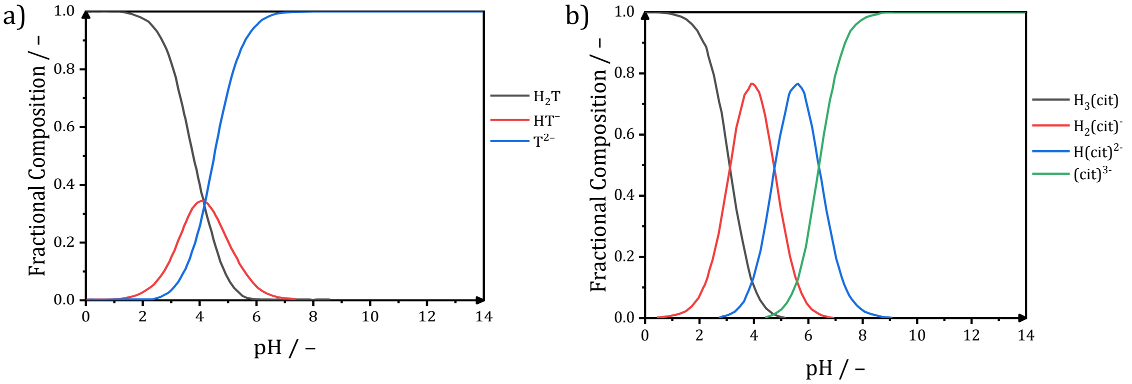

Figure A–10: Fractional composition of dissociated species versus pH of polycarboxylic acids: a) TA, and b) CA. Reproduced after [160,183]

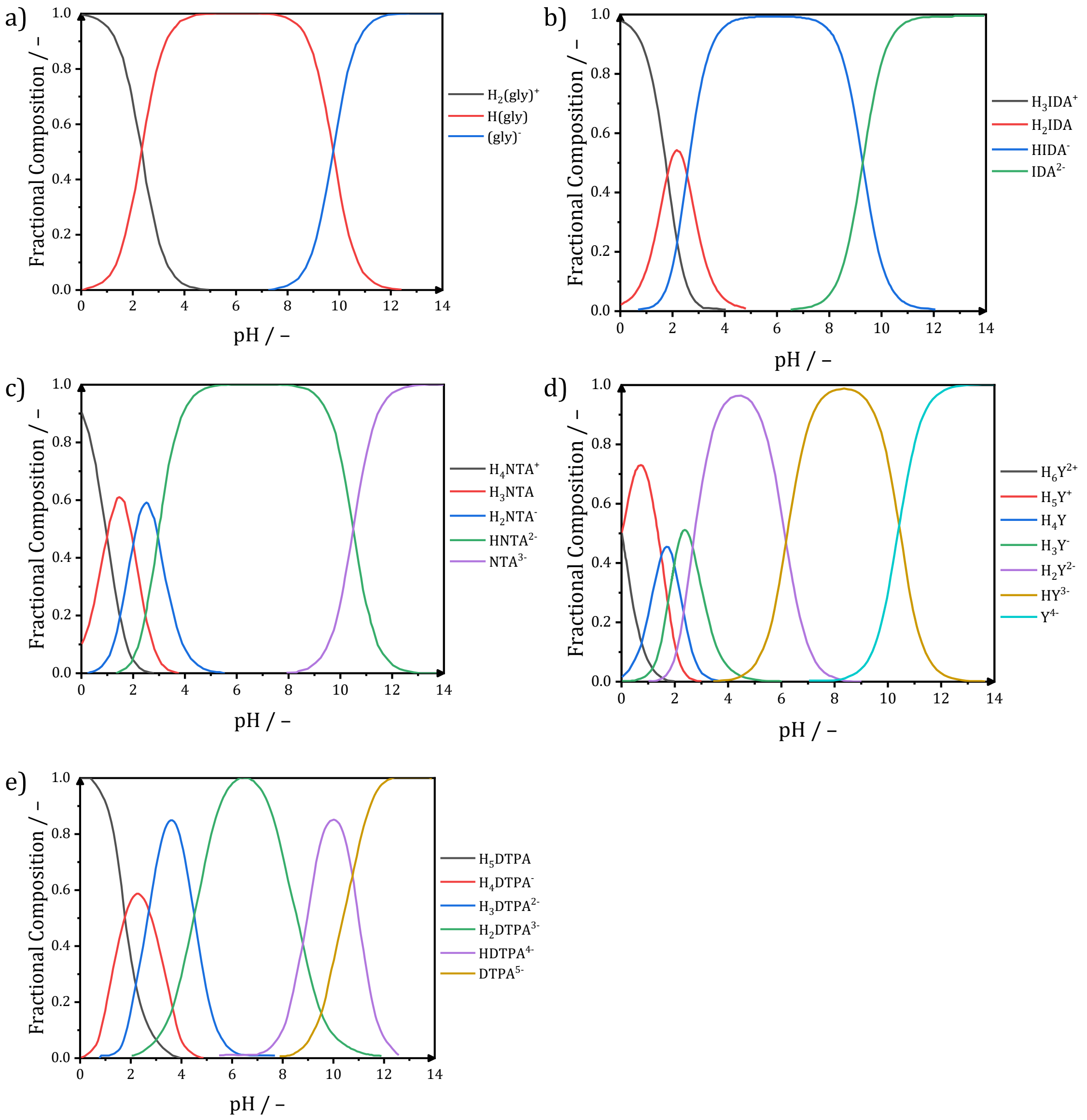

Figure A–11: Fractional composition of dissociated species versus pH of aminopolycarboxylic acids: a) Gly, b) IDA, c) NTA, d) EDTA, and e) DTPA. Reproduced after [115,160,184]

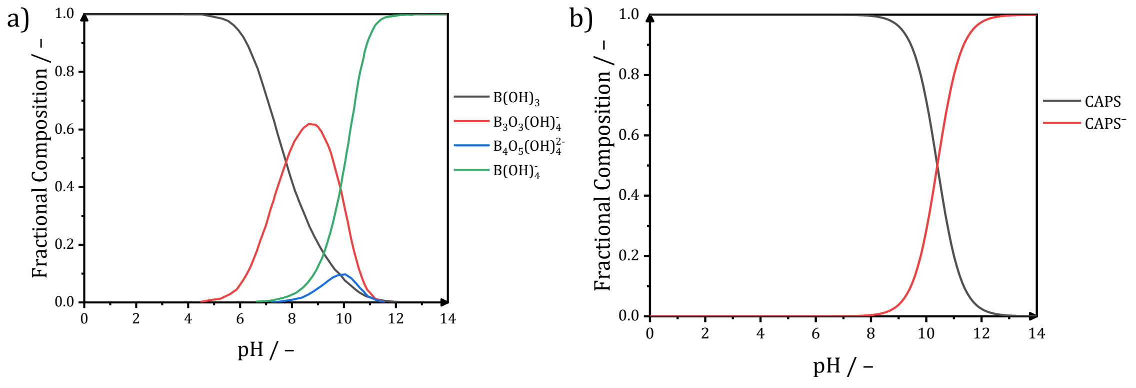

Figure A–12: Fractional composition of dissociated species versus pH of buffering additives: a) BA and b) CAPS. Reproduced after [160]

Table A–4 summarizes the stability constants of complexation of several chelating agents and metals. Taking the EDTA as an example, it shows relative high stability formation constants with all the displayed metals, making it a possible candidate as electrolyte additive in metal–air batteries and the inhibition of certain passive species. Similarly, iminodiacetic acid (IDA), glycine (Gly), nitrilotriacetic acid (NTA), diethylenetriamine–pentaacetic acid (DTPA) and citric acid (CA) display promising values for e.g., Al and Zn.

Table A–4: Stability constants of complexation of several chelating agents and metals. Summarized from [185–187].

Metal	Complexing agent						
	Gly	IDA	NTA	EDTA	DTPA	TA	CA
Al^{3+}	4.94	8.16	9.50	16.13	18.40	1.18	7.98
Ca^{2+}	N/A	2.59	6.41	10.96	10.74	1.95	3.45
Cu^{2+}	8.12	10.63	12.96	18.80	21.53	2.5	3.61
Fe^{2+}	4.13	5.80	8.84	14.33	16.55	2.24	4.8
Fe^{3+}	6.34	10.42	15.87	25.10	28.05	N/A	N/A
In^{3+}	N/A	9.54	16.90	24.95	29.00	N/A	N/A
Mg^{2+}	1.34	2.94	5.46	8.69	9.30	1.44	3.45
Mn^{2+}	N/A	N/A	7.44	14.04	15.60	2.49	N/A
Mn^{3+}	N/A	N/A	20.9	24.80	32.6	N/A	N/A
Na^{+}	0.00	0.4	2.15	1.66	2.00	0.50	0.71
Ni^{2+}	5.78	8.90	11.54	18.62	19.40	2.60	5.17
Sn^{2+}	N/A	N/A	N/A	18.30	N/A	N/A	N/A
Ti^{3+}	N/A	N/A	N/A	17.30	N/A	N/A	N/A
Zn^{2+}	4.96	7.27	10.66	16.50	18.75	2.66	4.76

Figure A–13 presents the specie predominance of Zn and Al depending on their respective concentrations versus pH assuming a 2M Cl^- and the specie formation of Zn and Al depending on their respective concentrations versus the EDTA concentration at pH 7 (black lines) and pH 10 (red lines). The diagrams were created using the Make Equilibrium Diagrams Using Sophisticated Algorithms (MEDUSA) software [160].

Figure A–13a,b are in partial agreement with the explanation of Figure A–6, since soluble species are present almost independent of the Zn and Al concentration at extreme acidic and alkaline pH but specially at low pH values for the Zn. Contrariwise, very insoluble species tend to form in the near–neutral pH range (pH 5 to 10) for both metals, denoted with the subindex (s) for solid species. In the case of Zn, $Zn(OH)_2$, $Zn_5(OH)_8Cl_2$ (Simonkolleite) and ZnO at saturation points of Zn concentrations as low as 10^{-5}M, whereas the solubility limits for Al are lower at 10^{-8}M resulting in $Al(OH)_3$. Figure A–13a,b also show some correlation with the Pourbaix diagrams of Figure 4.2b,c and Figure A–1b,c but differ in the elements considered for its construction. Namely, the Pourbaix considers only Zn–H_2O and Al–H_2O while the MEDUSA diagram can include Zn–H_2O–Cl and Al–H_2O–Cl. The latter can better assist in the estimation of possible reaction products of Zn in the near–neutral chloride–based electrolytes. In contrast, Figure A–13c,d display a significant solubility increase in presence of EDTA for both Zn and Al, resulting in $Zn(EDTA)^{2-}$ and $Al(EDTA)OH^{2-}$ at pH 7 and 10. Of the pH is increased from 7 to 10, there is a remarkable increase on the amount of fully dissociated EDTA more capable for complexation, as seen in Figure A–11d. A further possible advantage upon addition of EDTA would be the inhibition of Simonkolleite and chloride–compounds formation, which otherwise consume the chloride–based electrolyte. Yet, the formation of the soluble Zn–EDTA and Al–EDTA complex could take advantage of the higher potentials displayed at higher pH values (Figure 4.2b,c and Figure A–1b,c). In accordance, higher concentrations of EDTA can complex with more Zn and Al, preventing the formation of insoluble species, as observed in Figure A–13c,d.

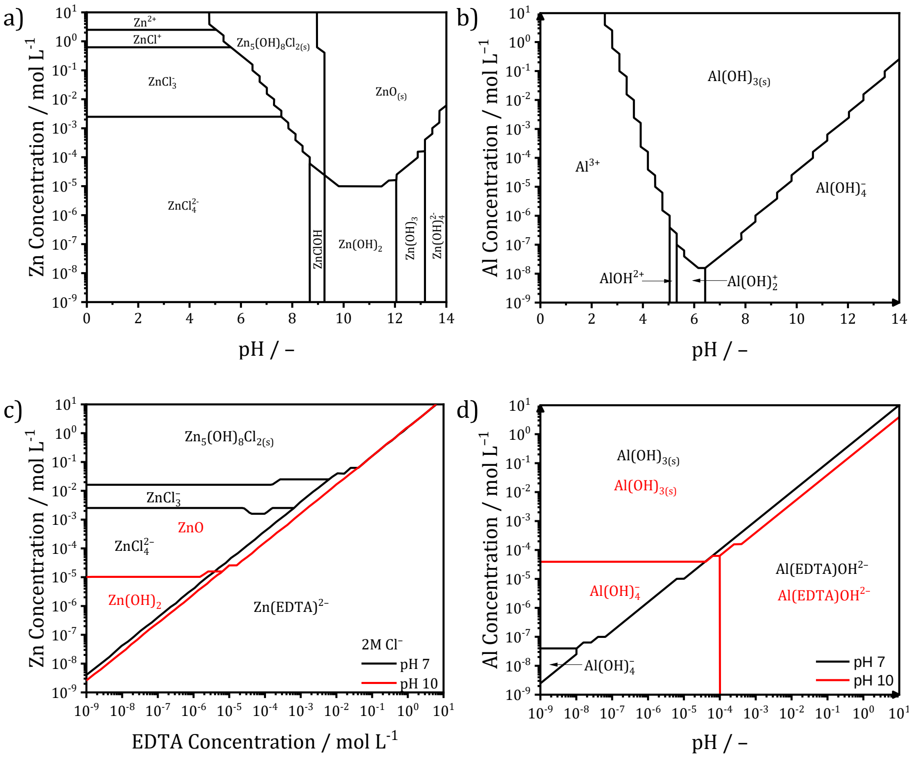

Figure A–13: Species predominance of a) Zn and b) Al concentration versus pH assuming a 2M Cl^- concentration. c) Zn and d) Al concentration versus EDTA concentration assuming 2M Cl^- at pH 7 (black lines) and pH 10 (red lines).

8. Supporting information of the Chapter 5

Table A–5 Comparison of electrochemical parameters obtained from potentiodynamic polarization with initial scan potential more negative than the water reduction potential (−1.37 $V_{Ag/AgCl}$).

Material	Initial scan potential ($V_{Ag/AgCl}$)	E_{corr} ($V_{Ag/AgCl}$)	NaCl concentration (M)	pH	T (°C)	Scan rate (mV/s)	Electrode area (cm^2)	OCP time (min)[a]	Counter electrode	Autor
Zn, 4N	−1.6	−1.242	2.00	7	25	5	1.32	5	Pt	Durmus [132]
Zn, 99.97% pure	−1.7	−1.143	0.60	-	25	1	1	60	Graphite flake	Yang [188]
Pure zinc sheets 1 mm thick	−1.585*	−1.285*	0.60	-	25	1	2	36.6	Pt plate	Hao [172]
Zinc Plating	−1.465*	−1.22*	0.60	7	28	5	1	15	Pt	Yan [189]
Pure Zn	−1.965*	−1.263*	0.60	7	RT	5	1	600	Pt grid	Bae [190]
Zn	−1.965*	−1.3926*	0.10	-	-	10	0.2	60	Pt	Nady [191]
	−1.965*	−1.6878*	0.20	-	-	10	0.2	60	Pt	
	−1.965*	−1.675*	0.40	-	-	10	0.2	60	Pt	
	−1.965*	−1.6476*	0.50	-	-	10	0.2	60	Pt	
Zn	−1.465*	−1.285*	0.60	-	30	-	-	0.6	Pt wire	Hamid [192]
Zn coating	−1.61*	−1.267*	0.60	-	RT	1	0.25	60	Pt plate	Li [193]
Galvanized Zn	−1.765*	−1.255*	0.51	-	-	2	0.785	-	Pt plate	Ünal [194]
Galvanized Zn, Cyclic voltammetry	−1.5	−1.33	0.60	8.2	25	33.3	-	0	Pt	Dutra [195]
Zn	−1.565*	−1.265*	0.51	-	-	2	1	0	Pt	Souza [196]
Zn electroplated	−1.485	−1.299	0.60	-	-	10	0.40	-	Pt	Zhao [197]
Zn	−1.565*	−1.165*	0.60	5.4	-	1	2.25	10	Graphite	Leidheiser [170]

[a] OCP time before starting the potentiodynamic polarization

* potentials corrected from SCE to Ag/AgCl

Table A–6: Comparison of electrochemical parameters obtained from potentiodynamic polarization with initial scan potential more positive than water reduction potential (−1.37 $V_{Ag/AgCl}$).

Material	Initial scan potential ($V_{Ag/AgCl}$)	E_{corr} ($V_{Ag/AgCl}$)	NaCl concentration (M)	pH	T (°C)	Scan rate (mV/s)	Electrode area (cm^2)	OCP time (min) [a]	Counter electrode	Autor
Galvanized Zn	−1	−1	0.20	-	-	1.00	0.01	360	Pt	Andreatta [198]
Zn	−1.05	−1.04	0.20	-	-	1.00	0.01	0	Pt	Andreatta [198]
Electrodeposited Zn, 130 μm thickness	−1.275*	−1.025*	0.60	-	RT	1.00	1.00	-	Pt plate	Hu [199]
Galvanized Zn	−1.3	−0.82	0.60	-	-	10.00	1.00	-	Graphite	Anwar [200]
Nano crystalline electrodeposited Zn	−1.253*	−1.053*	0.60		25	-	1.00	10	Pt wire	Onkrappa [201]
Zn	−1.015*	−0.965*	0.10	6.5	20	1.00	-	-	Pt	Shang [202]
Zn	−1.115	−0.915	0.60	-	-	-	1.00	-	Pt wire	Punith Kumar [203]
Zn	−1.319	−0.919	0.60	-	-	1.00	0.78	-	Pt	H Lee [204]
Zn	−1.215*	−1.015*	0.60	-	20	0.20	1.00	-	Pt plate	Wang [205]
Deposited Zn	−1.3	−1.072	0.10	-	-	10.00	2.40	30	Pt rod	Zhang [206]
Galvanized Zn	−1.215*	−1.011*	0.86	6.3	19	1.00	4.00	-	Pt plate	Bacharov [207]
Zn	−1.165*	−0.969*	0.62	-	RT		-	-	Graphite rod	Daniyan [208]
Zn	−1.3	−1	0.60	8.2	25	0.33		-	Pt	Dutra [195]
Zn, aerated solution	−1.27	−0.97	0.60	8.2	25	0.33		-	Pt	Dutra [195]
Zn, deaerated solution	−1.27	−1.17	0.60	8.2	25	0.33		-	Pt	Dutra [195]
Zn	−1.265*	−0.965*	0.50	-	30	0.33	0.28	-	Graphite rod	Abd-El-Naby [209]
Zn	−1.265*	−1.008*	0.60	-	-	-	-	-	Pt	Sherine [210]
Zn	−1.015*	−0.965*	0.10	-	-	1.00	0.10	-	Pt	Simões [211]
Zn	−1.015*	−1.015*	0.50	5	25	1.00	0.38	20	Pt sheet	Muñoz [212]
Zn	−1.015*	−1.025*	0.50	-	30	0.08	0.79	240	Pt	Aramaki [213]
Zn	−1.015*	−1.025*	0.50	-	30	0.08	0.79	240	Pt	Aramaki [213]

[a] OCP time before starting the potentiodynamic polarization

* potentials corrected from SCE to Ag/AgCl

Table A–7: Water solubility and physical characteristics of Zn and its reaction products in chlorinated solutions

Reaction product	Water solubility mg L^{-1}	Color	Specific volume^{a} cm^{3} g^{-1}	Volume expansion after reaction of metallic Zn %
Metallic Zn	-	Blue silvery	0.140	-
$Zn_5(OH)_8Cl_2{\cdot}H_2O$/ Simonkolleite	Insoluble [214]	White powder	0.303	216
ZnO	2.9 [215]	White powder	0.327	234
$Zn(OH)_2$	648 [216]	White powder	0.178	127

^{a} calculated as the inverse of the density

Figure A–14 shows the SEM images and EDX maps of Zn after 1 h of discharge at 1 mA cm^{-2} in the prepared electrolytes. The SEM image in Figure A–14a (no EDTA) shows two different areas: 1) a cracked film on the surface 2) a relatively flat Zn surface. The EDX phase maps in Figure A–14c (no EDTA) further confirms the existence of two different regions: one Zn phase and one Zn/O phase. The SEM image in Figure A–14b (0.1M EDTA) reveals a relative rough surface and the Zn grains from polishing cannot clearly be distinguished, but no film or reaction products is observed. The EDX maps in Figure A–14d (0.1M EDTA) reveals a homogeneous detection of only Zn.

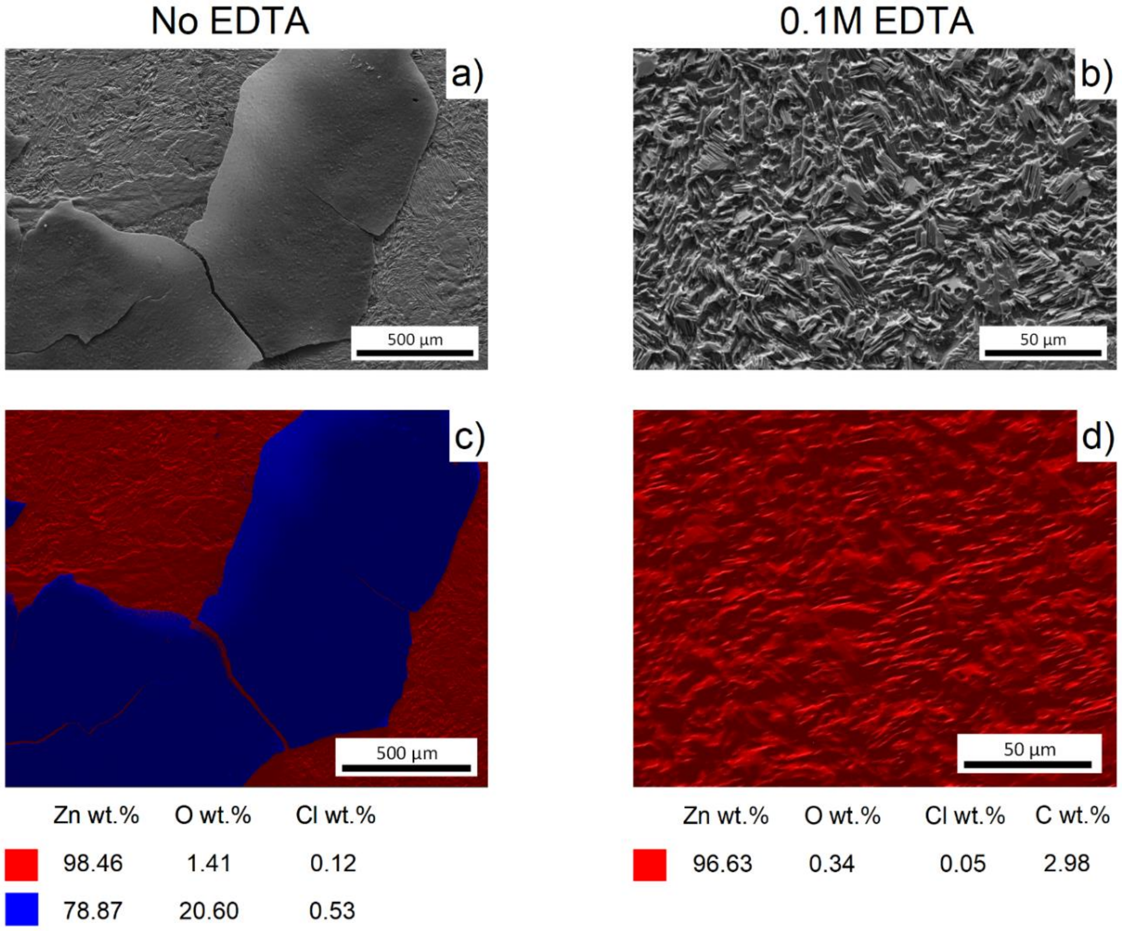

Figure A–14: SEM images and EDX elemental map of Zn discharged for 1 h at 1 mA cm^{-2} in 2M NaCl pH 10 without and with 0.1M EDTA

Figure A–15 shows the EDX mapping for each single element presented in Figure A–14.

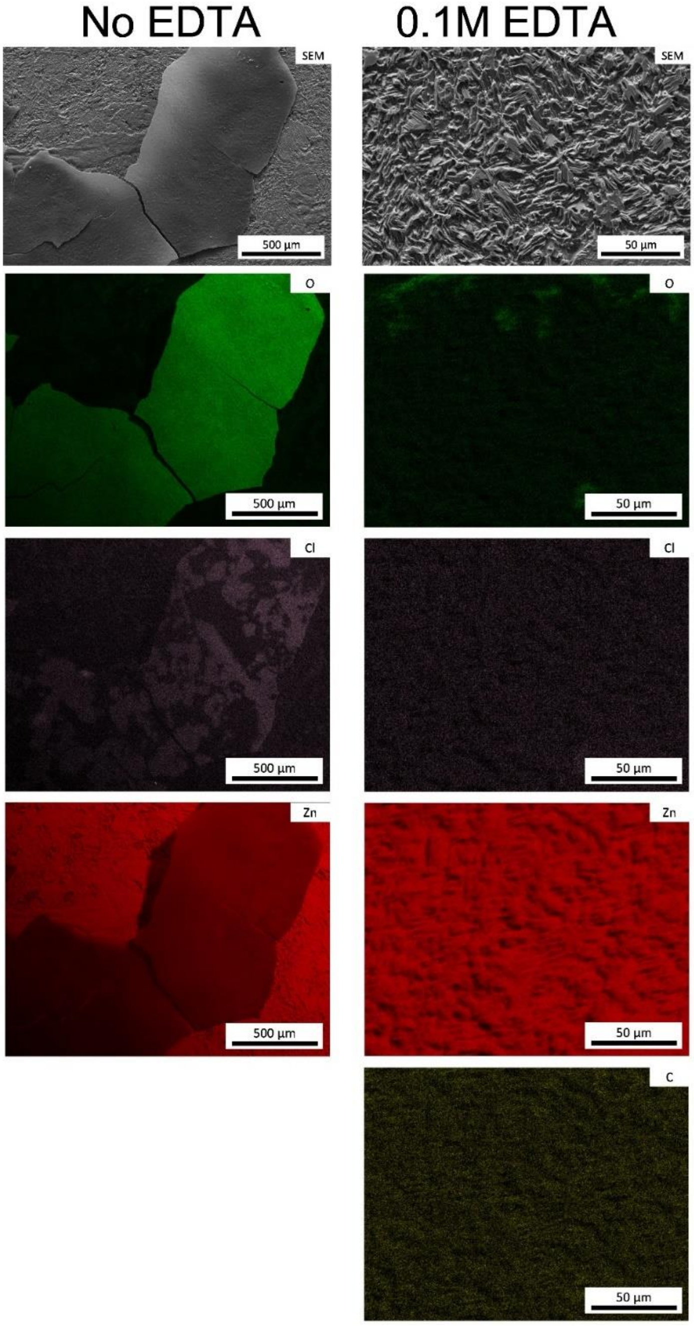

Figure A–15: SEM and EDX map of Zn discharged for 1 h at 1 mA cm^{-2} in 2M NaCl pH 10 without and with 0.1M EDTA.

Table A–8: Element weight percentage distribution of Zn corrosion products and elemental analysis of Zn after 1 h of discharge at 1 mA cm^{-2}.

		Zn wt%	O wt%	Cl wt%	C wt%
Theoretical	ZnO	80.34	19.66		
	$Zn(OH)_2$[a]	67.14	32.86		
	$Zn_5(OH)_8Cl_2\cdot H_2O$[a] (Simonkolleite)	60.33	26.58	13.09	
2M NaCl	Zn region (red)	98.46	1.41	0.12	
	Zn/O region (blue)	78.87	20.60	0.53	
2M NaCl + 0.1M EDTA	Zn region (red)	96.63	0.34	0.05	2.98

[a] The elemental weight distribution was calculated omitting the H, since EDAX cannot detect H

Figure A–16 shows the EDX mapping for each single element presented in Figure 5.8c,d of the main text.

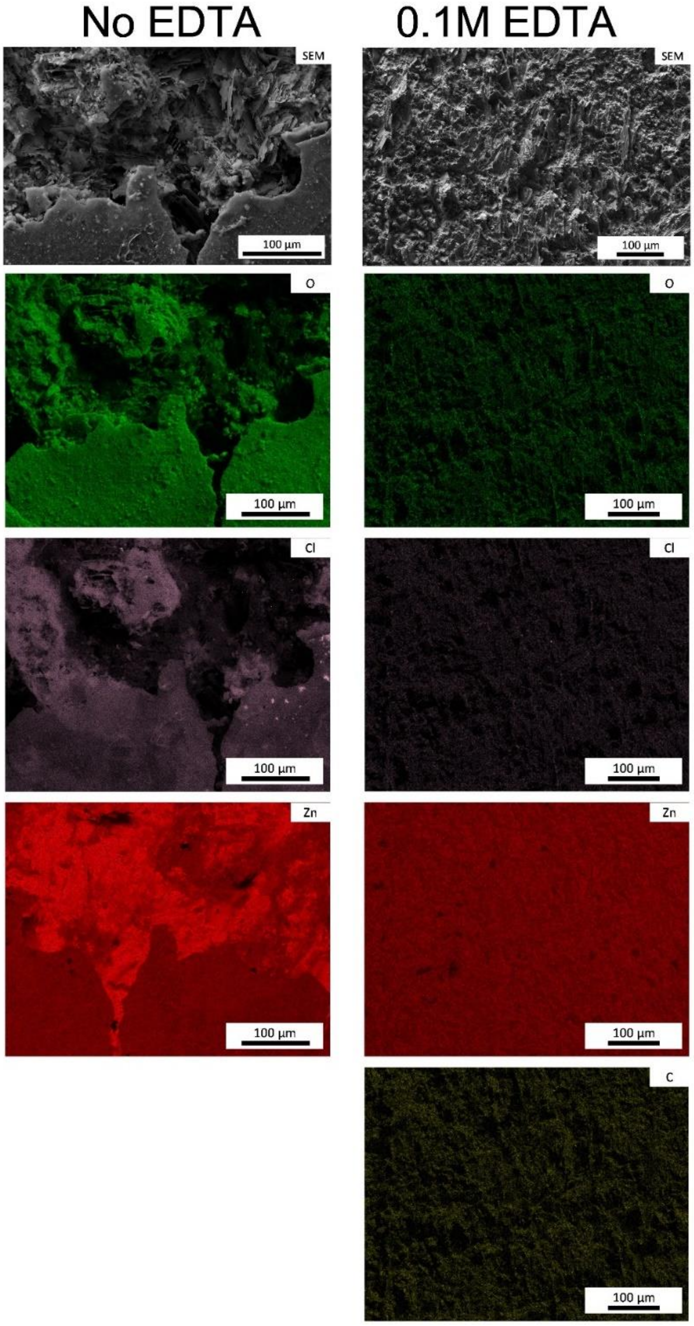

Figure A–16: SEM and EDX elemental map of Zn discharged for 24 h at 1 mA cm^{-2} in 2M NaCl pH 10 without and with 0.1M EDTA.

The limitation of the full–cell setup was further studied by doubling the reservoir volume from 20 to 40 mL. Figure A–17a shows an Open Circuit Voltage (OCV) of Zn in the neat 2M NaCl pH 10 (black curve) at around 1.06 V, then the voltage drops to 0.93 V under 1 mA cm^{-2} anodic current. The cell voltage continues decreasing down to 0.76 V and becomes irregular after 134 h. The cell still reached over 450 h of operation with voltages oscillating between 0.88 and 0.31 V. On the other hand, the OCV of Zn in the electrolyte with 0.1M EDTA (Figure A–17a, red curve) is around 1.42 V, whereas the cell voltage drops to 1.06 V under 1 mA cm^{-2} anodic current. The cell voltage slightly increases to 1.13 V and it decreases after 285 h to values around 1.07 to 0.86 V, which are similar to the discharge voltages of the cell discharged without EDTA. The cell voltage then oscillates between values of 0.88 and 0.71 V, whereas the cell breaks after 417 h. The total time of operation was drastically increased by just doubling the reservoir of the cell. The XRD analysis of the anode surface posterior to the discharge (Figure A–17b) reveals the presence of Simonkolleite, while the sample discharge in 0.1M EDTA shows no clear traces of Simonkolleite, ZnO or $Zn(OH)_2$.

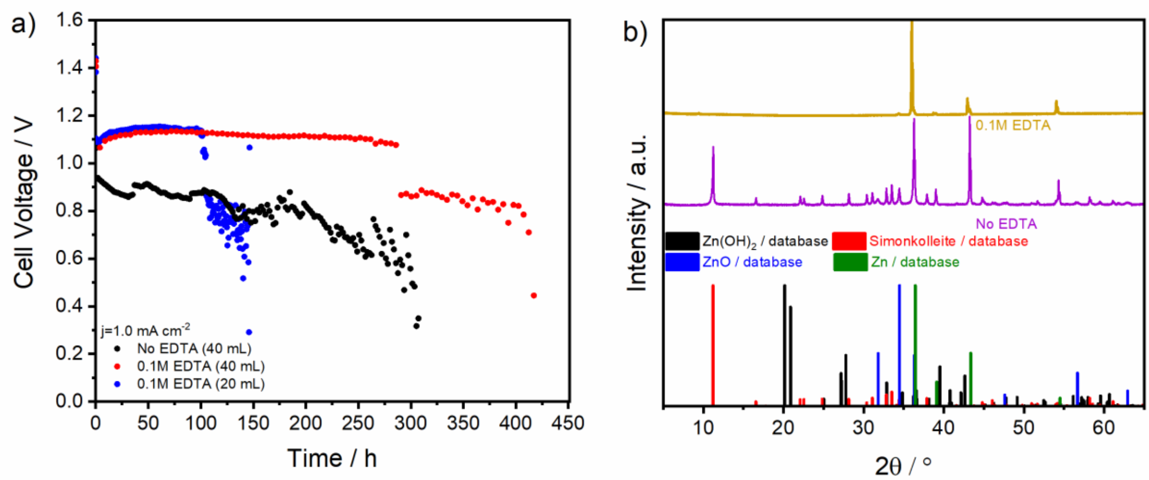

Figure A–17: a)Full–cell galvanostatic discharge profiles of Zn in 2M NaCl at pH 10 in absence (black curves) and presence (red curves) of 0.1M EDTA under 1 mA cm^{-2} with a 40 mL reservoir (blue curve corresponds to the experimental data with 20 mL from Figure 5.10) and b) XRD patterns after the discharge experiments.

Acknowledgement

In first and notable site, I would like to thank Prof. Rüdiger–A. Eichel for giving me the opportunity to carry out my PhD project at IEK–9 and for his absolute support on every step. I also owe my deepest gratitude to Prof. Stefan van Waasen, who has also given me unconditional guidance and more than enough hands on this venture.

To Dr. Hans Kungl and Dr. Hermann Tempel, I could not be more than grateful, and I owe them my deepest respects for their time, contributions, ideas, and supervision on every step of my work, besides being friendly and considerate listeners. They constantly bring motivation and order into the chaotic confusion of the inspiration. A remarkable big thanks to Dr. Yasin Emre Durmus, who has incarnated the figure of a guide and a big brother simultaneously. His continue questioning encourages the flourishment of his students, as I could testify with my colleagues and by myself.

I also appreciate the big contributions made by Christian Roth from ZEA–2, who incredibly supported this work. Many thanks to my colleagues Dr. Shay Robinson, Xin Lu, Li–Chung Kin, Krzysztof Dzieciol and Bernhard Schmidt for the unaccountable discussions and suggestions. To my students, “little” Selin Bulut, Volker Lewandowski, and Marie Heidler, thanks for your help in the lab and teaching me to listen. Same gratitude goes to all IEK–9 and their assistance.

Finally yet importantly, I am in eternal debt with my supporting and beloved family, with the ones who are still present and those who already departed. Three of five left the home, yet the other two keep them in their hearts alive. Thanks to my partner in crime Sandra, who not only gave me a new meaning of home, but an extended meaning of family.

List of Publications

Peer–reviewed publications:

[1] **S. S. Montiel Guerrero**, Y. E. Durmus, Hermann Tempel, Christian Roth, Hans Kungl, Stefan van Waasen, Yair Ein–Eli, and Rüdiger–A. Eichel, "Unveiling the Potential of Silicon–Air Batteries for Low-Power Transient Electronics : Electrochemical Insights and Practical Application", *Batteries & Supercaps*, 7 (2024), n/a, doi.org/10.1002/batt.202300573.

[2] Y. E. Durmus, **S. S. Montiel Guerrero**, Hermann Tempel, Florian Hausen, Hans Kungl, and Rüdiger–A. Eichel, "Influence of Al Alloying on the Electrochemical Behavior of Zn Electrodes for Zn–Air Batteries with Neutral Sodium Chloride Electrolyte", *Frontiers in Chemistry*, 7 (2019), 1–13, doi.org/10.3389/fchem.2019.00800.

[3] **S. S. Montiel Guerrero**, Y. E. Durmus, Krzysztof Dzieciol, Shibabrata Basak, Hermann Tempel, Stefan van Waasen, Hans Kungl, and Rüdiger–A. Eichel, "Improved Electrochemical Performance of Zinc Anodes by EDTA in Near–Neutral Zinc–Air Batteries", *Batteries & Supercaps*, 4 (2021), 1–14, doi.org/10.1002/batt.202100116.

Papers to be submitted:

[1] **S. S. Montiel Guerrero**, M. Heidler, Y. E. Durmus, Hermann Tempel, Stefan van Waasen, Hans Kungl, and Rüdiger–A. Eichel, "Investigation of electrolyte additives on the electrochemical performance of Near–Neutral Zinc–Air Batteries", to be submitted.

[2] **S. S. Montiel Guerrero**, M. Heidler, Y. E. Durmus, Hermann Tempel, Stefan van Waasen, Hans Kungl, and Rüdiger–A. Eichel, "Cyclability Improvement of Zn anodes in Near–Neutral Electrolytes by Addition of Chelating Agents", to be submitted.

DOI: 10.17185/duepublico/82241
URN: urn:nbn:de:hbz:465-20240814-072949-6